022872-1-F
ARO 22844.13-GS

THE UNIVERSITY OF MICHIGAN

COLLEGE OF ENGINEERING
DEPARTMENT OF ELECTRICAL ENGINEERING & COMPUTER SCIENCE
Radiation Laboratory

MILLIMETER WAVE RADAR CLUTTER PROGRAM

Fawwaz T. Ulaby

Radiation Laboratory
Department of Electrical Engineering
and Computer Science
The Unviersity of Michigan
Ann Arbor, MI 48109-2122

FINAL REPORT

U.S. Army Research Office
Box 12211
Research Triangle Park, NC 27709

Contract DAAG29-85-K-0220
October, 1989

Ann Arbor, Michigan

DISCLAIMER NOTICE

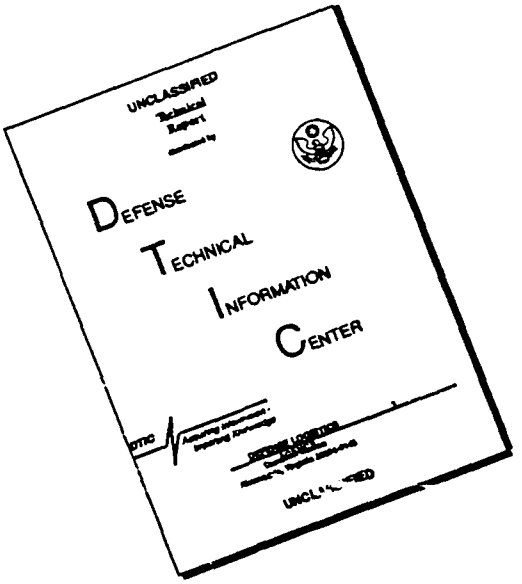

THIS DOCUMENT IS BEST QUALITY AVAILABLE. THE COPY FURNISHED TO DTIC CONTAINED A SIGNIFICANT NUMBER OF PAGES WHICH DO NOT REPRODUCE LEGIBLY.

MILLIMETER WAVE RADAR CLUTTER PROGRAM

FINAL REPORT
U.S. ARMY RESEARCH OFFICE
CONTRACT DAAG29-85-K-0220

Fawwaz T. Ulaby
Radiation Laboratory
Electrical Engineering and Computer Science
University of Michigan
Ann Arbor, Michigan 48109

October, 1989

UNCLASSIFIED MASTER COPY - FOR REPRODUCTION PURPOSES

SECURITY CLASSIFICATION OF THIS PAGE

REPORT DOCUMENTATION PAGE

1a. REPORT SECURITY CLASSIFICATION Unclassified	1b. RESTRICTIVE MARKINGS
2a. SECURITY CLASSIFICATION AUTHORITY	3. DISTRIBUTION / AVAILABILITY OF REPORT Approved for public release; distribution unlimited.
2b. DECLASSIFICATION / DOWNGRADING SCHEDULE	
4. PERFORMING ORGANIZATION REPORT NUMBER(S)	5. MONITORING ORGANIZATION REPORT NUMBER(S) ARO 22844.13-GS
6a. NAME OF PERFORMING ORGANIZATION Radiation Laboratory, University of Michigan, Ann Arbor, MI 48109 6b. OFFICE SYMBOL (If applicable)	7a. NAME OF MONITORING ORGANIZATION U. S. Army Research Office
6c. ADDRESS (City, State, and ZIP Code) Ann Arbor, Michigan 48109	7b. ADDRESS (City, State, and ZIP Code) P. O. Box 12211 Research Triangle Park, NC 27709-2211
8a. NAME OF FUNDING / SPONSORING ORGANIZATION U. S. Army Research Office 8b. OFFICE SYMBOL (If applicable)	9. PROCUREMENT INSTRUMENT IDENTIFICATION NUMBER DAAG29-85-K-0220
8c. ADDRESS (City, State, and ZIP Code) P. O. Box 12211 Research Triangle Park, NC 27709-2211	10. SOURCE OF FUNDING NUMBERS PROGRAM ELEMENT NO. / PROJECT NO. / TASK NO. / WORK UNIT ACCESSION NO.

11. TITLE (Include Security Classification)
Millimeter Wave Radar Clutter Program

12. PERSONAL AUTHOR(S)
Fawwaz T. Ulaby

13a. TYPE OF REPORT	13b. TIME COVERED	14. DATE OF REPORT (Year, Month, Day)	15. PAGE COUNT
Final	FROM 10/85 TO 9/89	1989, October 30	204

16. SUPPLEMENTARY NOTATION
The view, opinions and/or findings contained in this report are those of the author(s) and should not be construed as an official Department of the Army position, policy, or decision, unless so designated by other documentation.

17. COSATI CODES		
FIELD	GROUP	SUB-GROUP

18. SUBJECT TERMS (Continue on reverse if necessary and identify by block number)
Millimeter waves, Radar scattering, Terrain Clutter

19. ABSTRACT (Continue on reverse if necessary and identify by block number)

See Reverse side

20. DISTRIBUTION / AVAILABILITY OF ABSTRACT ☐ UNCLASSIFIED/UNLIMITED ☐ SAME AS RPT. ☐ DTIC USERS	21. ABSTRACT SECURITY CLASSIFICATION Unclassified
22a. NAME OF RESPONSIBLE INDIVIDUAL	22b. TELEPHONE (Include Area Code) / 22c. OFFICE SYMBOL

DD FORM 1473, 84 MAR 83 APR edition may be used until exhausted. All other editions are obsolete.

SECURITY CLASSIFICATION OF THIS PAGE
UNCLASSIFIED

ABSTRACT

This final report provides a summary of the results realized from the research activities conducted under the sponsorship of U.S. Army Research Office Contract DAAG29-85-K-0220, entitled "Millimeter Wave Radar Clutter Program". The overall goal of the progam was to conduct experimental measurments and develop theoretical models to improve our understanding of electromagnetic wave interaction with terrain at millimeter wavelengths. The work was divided into five major tasks. Tasks 1 involved the construction of calibrated scatterometer systems at 35, 94, and 140 GHz. In designing, constructing, and testing these systems, a great deal was learnt about system-design trade-offs and system stability requirements, and new calibration techniques were developed. The scatterometer systems were then used in support of the remaining tasks. The objective of Task 2 was to evaluate the effects of signal fading on the radar backscatter from terrain. Based on experiments conducted from asphalt and snow-covered surfaces, it was determined that the Rayleigh fading model is applicable at millimeter wavelengths, and a model was developed to show frequency averaging can be used to reduce signal fading fluctuations. Task 3 involved the development of a model that relates the transmission loss of dry snow to crystal size in the 18-90 GHz region. In Task 4, we examined the character of bistatic scattering from surfaces of various surface roughness and from two types of trees. The bistatic data for trees proved instrumental in the development of a radar model for scattering from tree foliage at millimeter wavelengths, which was one component of Task 5. The other component of Task 5 involved the development of a model for snow. (AW)

TABLE OF CONTENTS

1. INTRODUCTION

The "Millimeter Wave Radar Clutter Program" was funded by the U.S. Army Research Office in September, 1985 to answer a number of important questions related to millimeter-wave radar scattering from terrain. This Final Report provides a summary of the research conducted and the major results realized under this program. The program was organized in terms of the following five tasks.

Task 1 - Contruction of Millimeter-wave scatterometers: In order to develop valid models for radar scattering from terrain, it was imperative that we conduct careful measurements of various types of terrain under a variety of conditions. The experimental data serves to guide the development of the models as well as to verify their applicability. Hence, the first task of the program focused on the development of calibrated scatterometers with operating frequencies of 35, 94, and 140 GHz, which correspond to atmospheric-window frequencies. Under a seperate DOD-equipment grant, we also developed a system at 215 GHz.

Task 2 - Examination of Radar Signal Statistics: The literature contains several models for characterizing signal fading statistics of radar scatter from terrain. This task seeks to determine the nature of signal fading at millimeter wavelengths and to evaluate the relationship between the fading standard deviation and frequency bandwidth when frequncy averaging is used.

Task 3 - Modeling Extinction Loss of Dry Snow: Because snow is a dense medium and because the ice crystals are comparable to the wavelength in size in the millimeter-wavelength region, the models used at the lower microwave frequencies are inapplicable at millimeter wavelengths. The goal of this task is to develop a model for the extinction loss of dry snow and to verify its behavior with experimental measurement.

Task 4 - Examination of Bistatic Scattering from Surfaces and Volumes: Prior to this program, no millimeter-wave bistatic measurments of terrain had been reported in the literature. The purpose of this task is to examine the character of bistatic scattering and to use it in the development of radar scattering models. Even for monostatic radar, the backscattering return includes multiple-scattering contributions that are governed by bistatic scattering in the medium under observation.

Task 5 - Development of Radar Scattering Models for Terrain: Under this program, we concentrated on two types of terrain, snow-covered ground and tree foliage. The goal of this task is to develop electromagnetic models that can adequately describe millimeter-wave backscatter in terms of the physical properties of the medium.

Over the four-year duration of this program, numerous papers were published in the literature and several presentations were made at scientific symposia documenting the various results realized in support of the above five tasks. A subset comprised of the major papers generated under this program is included in Appendix A, and numbered 1 through 13.

In the next section, we shall focus on the major conclusions learnt from the research conducted under this program without going into the details of the experiments and models. We will refer the reader to the details by referencing the appropriate papers in Appendix A.

2. SUMMARY OF RESULTS

2.1 Task 1 - Construction of Millimeter-Wave Scatterometers

The basic approach used in designing the millimeter-wave scatterometers is described in paper [1]. The initial plan was to design and build three systems to operate at the atmospheric-windows frequencies of 35, 94, and 140 GHz. In 1989 we added a fourth channel at 215 GHz with funds provided by a DOD equipment grant. The salient features of the millimeter-wave system are given in Table 1. Examples of polarimetric measurements made at 35 GHz are given in paper [2], and example of observations made at 140 GHz are given in paper [3].

2.2 Examination of Radar Signal Statistics

Based on extensive radar measurements that were conducted for asphalt and snow-covered surfaces (see paper [5], the following results were obtained:

(1) The Rayleigh fading model provides excellent agreement with measurements for statistically homogeneous targets. The major cause responsible for the confusion that exists in the literature with regard to the question of which probability density function is appropriate for

Table 1. Parameters of the University of Michigan Millimeter Wave Polarimeter

FREQUENCIES:	35, 94, 140, 215 GHz		
IF BANDWIDTH:	0 to 2.0 GHz		
SWEEP RATE:	1 ms/freq., 51, 101, 201, 401 freq./sweep		
POLARIZATION:	HH, HV, VV, VH		
INCIDENCE ANGLES:	0 to 70 degrees		
PLATFORM HEIGHT:	3 meters minimum, to 18 meters maximum		
NOISE EQUIV. σ°:	35 GHz:	-22 dB	
	94 GHz:	-28 dB	
	140 GHz:	-21 dB	
	215 GHz:	-30 dB	
CROSSPOL ISOLATION:	35 GHz:	23 dB	
	94 GHz:	20 dB	
	140 GHz:	15 dB	
	215 GHz:	20 dB	
PHASE STABILITY:	35 GHz:	~1 degree/hour	
	94 GHz:	~1 degree/minute	
	140 GHz:	~10 to 50 degrees/second	
	215 GHz:	~20 degrees/hour	
NEAR FIELD DIST:	35 GHz:	2.7 m	
	94 GHz:	7.3 m	
	140 GHz:	2.7 m	
	215 GHz:	4.4 m	
BEAMWIDTH:	35 GHz:	R: 4.2 deg	T: 4.2 deg
	94 GHz:	R: 1.4 deg	T: 2.8 deg
	140 GHz:	R: 2.2 deg	T: 11.8 deg
	215 GHz:	R: 1.1 deg	T: 2.3 deg
ANTENNA DIAMETER:	35 GHz:	R: 6 inches	T: 6 inches
	94 GHz:	R: 6 inches	T: 3 inches
	140 GHz:	R: 3 inches	T: 0.36 inches
	215 GHz:	R: 3 inches	T: 1.5 inches

characterizing the statistical variability of the radar return from terrain is the fact that the data aquired with airborne programs includes two sources of variability, namely that due to fading and that due to the statistical inhomogeneity of the target scene. If we study these two types of variations seperately, we can easily compute the distribution for the combination.

(2) Examination of the standard deviation associated with the backscatter when frequency averaging over a bandwidth B is used, compared to the standard deviation when no frequency averaging is used (CW operation), led to the development of a model that shows the reduction in signal fluctuation with bandwidth. The model is in excellent agreement with experimental observations. The equivalent number of independent samples realized by frequency averaging is approximately

$$N = \frac{2DB}{c}$$

where D is the range resolution of the system and c is the velocity of light.

2.3 Task 3 - Modeling Extinction Loss of Dry Snow

A millimeter-wave model for the transmission loss of dry snow was developed taking into account both coherent loss due to scattering and absorption and multiple scattering effects [6, 7]. The model was compared with measurements made as a function of slab thickness for 18 different types of snow with crystal sizes varying from 0.2 mm to 2.0 mm. The measurements were made at 18, 35, 60, and 90 GHz. The results form the basis for modeling the backscatter from snow using the radiative transfer

approach because prior to this investigation it was not clear as to how to define crystal size in snow.

2.4 Task 4 - Examination of Bistatic Scattering from Surfaces and Volumes

Papers [8] - [10] describe experiments conducted and models developed to characterize millimeter-wave bistatic scattering from surfaces of varying surface roughness and from two distinctly different types of trees. The major findings were:

(1) For a smooth sand surface with rms height of less than 0.1 mm, bistatic scattering in the specular direction was found to be within a fraction of 1dB of theory for both horizontal and vertical polarizations. As the surface roughness was increased, the coherent specular component decreased and diffuse scattering increased. By making measurements as a function of both the azimuth angle and the elevation angle of the receiver, three dimensional scattering plots were generated for each polarization configuration.

(2) Bistatic scattering by trees can be modeled as the sum of a forward scattering narrow-lobed Gaussian function with a beamwidth on the order of 10° and an isotropic component, typically 20 dB lower in level than the peak of the forward pattern. Inspite of the complicated geometry of the tree architecture, insignificant differences were observed between the scattering patterns corresponding to horizontal and vertical polarizations. This result led to significant simplifications in the construction of a phase function for modeling multiple scattering effects in vegetation canopies.

2.5 Task 5 - Development of Radar Scattering Models for Terrain

Radiative transfer models were developed for tree canopies and snow-covered ground. Using the form of the scattering patterns measured in the bistatic scattering invetigations, a model was developed for the phase matrix of tree foliage and then used in a radiative transfer model to compute the radar backscatter. Three solutions were examined: (1) first order, (2) second order, and (3) numerical. It was found that the second-order solution provides accuracies within 1 dB for both like and cross polarization if the albedo is less than 0.6 (paper [12]). Upon comparing the model with data, excellent agreement was obtained at 35, 94, and 140 GHz.

A radiative transfer model with the quasi-crystalline approximation was developed for snow. The model accounts for snow surface roughness, crystal size, and liquid water content. Both model and data indicate that surface roughness is of secondary importance for dry snow but not for wet snow. The effect of liquid water content is most significant at 35 GHz and becomes smaller as we increase the frequency to 94 and 140 GHz.

Paper [13] provides a detailed description of the model. Comparison of the model results with experimental observations is the subject of a seperate paper which is in the final preparation stage but not yet ready for inclusion in this report. Both papers will be submitted for publication in a scientific journal in November, 1989.

3. LIST OF PUBLICATIONS

The following list contains papers published in scientific journals or symposia proceedings, or presented at technical symposia. Ail of these papers were generated in support of the Millimeter Wave Radar Clutter Progam.

[1] F.T. Ulaby, T.F. Haddock, J.R. East AND M.W. Whitt. A Millimeterwave Network Analyzer based Scatterometer. IEEE Transactions on Geoscience and Remote Sensing, Vol. 26(1). Jan. 1988.

[2] M.W. Whitt and F.T. Ulaby. Millimeter-Wave Polarimetric Measurements of Artificial and Natural Targets. IEEE Transactions on Geoscience and Remote Sensing, Vol. 26(5). Sept. 1988.

[3] T.F. Haddock and F.T. Ulaby. 140-GHz Scatterometer System and Measurements of Terrain. submitted for publication in IEEE Transactions on Geoscience and Remote Sensing.

[4] M.W. Whitt and F.T. Ulaby. Millimeter-wave Polarimetric Measurements of Artificial and Natural Targets. Proceedings of IGARSS '87 Symposium, Ann Arbor, May 1987.

[5] F.T. Ulaby, T.F. Haddock and R.T. Austin. Fluctuation Statistics of Millimeter-Wave Scattering from Distributed Targets. IEEE Transactions on Geoscience and Remote Sensing, Vol. 26(3), May 1988.

[6] M.T. Hallikainen, F.T. Ulaby and T.E. Van Deventer. Extinction Behavior of Dry Snow in the 18- to 90- GHz Range. IEEE Transactions on Geoscience and Remote Sensing, Vol. GE-25(6). Nov. 1987.

[7] M.T. Hallikainen, F.T. Ulaby and T.E. Van Deventer. Extinction Coefficient of Dry Snow at Microwave and Millimeterwave Frequencies. Proceedings of IGARSS '87 Symposium, Ann Arbor. May 1987.

[8] T.E. Van Deventer, J.R. East and F.T. Ulaby. Millimeter Transmission Properties of Foliage. Proceedings of IGARSS '87, Ann Arbor. May 1987.

[9] F.T. Ulaby, T.E. Van Deventer, J.R. East, T.F. Haddock and M.E. Coluzzi. Millimeter-wave Bistatic Scattering From Ground and Vegetation Targets. IEEE Transactions on Geoscience and Remote Sensing, Vol. 26(3). May 1988.

[10] F.T. Ulaby, T.F. Haddock and M.E. Coluzzi. Millimeter-wave Bistatic Radar Measurements of Sand and Gravel. Proceedings of IGARSS '87 Symposium, Ann Arbor. May 1987.

[11] K. Sarabandi, F.T. Ulaby, and T.B.A. Senior. Millimeter Wave Scattering Model for a Leaf. Accepted for publication in Radio Science.

[12] F.T. Ulaby, T.H. Haddock and Y. Kuga. Measurement and Modeling of Millimeter-wave Scattering from Tree Foliage. Submitted for publication in Radio Science.

[13] Y. Kuga, R.T. Austin, T.F. Haddock and F.T. Ulaby. Millimeter-wave Radar Scattering from Snow Part I--Radiative Transfer Model with Quasi-Crystalline Approximation. To be submitted for publication in IEEE Transactions on Geoscience and Remote Sensing.

[14] Y. Kuga, R.T. Austin, T.F. Haddock and F.T. Ulaby. Millimeter-wave Radar Scattering from Snow Part II - Experimental Measurements.

[15] Ulaby, F.T., T.E. Haddock, J. East and V. Liepa. Millimeterwave Network Analyzer-Based Scatterometer, IEEE International Geoscience and Remote Sensing Symposium (IGARSS '86) Digest, Zurich, Switzerland, Vol. 1, pp. 721-724, 8-11 September 1986.

[16] Ulaby, F.T., T.F. Haddock, and R.T. Austin. Fluctuation Statistics of Millimeter-wave Scattering from Distributed Targets, International Geoscience and Remote Sensing Symposium (IGARSS '87) URAI Digest, Ann Arbor, Michigan, pp. 1-2, 18-21 May 1987.

[17] Kuga, Y., R.T. Austin, T.F. Haddock, and F.T. Ulaby. Calculation of the Diurnal Backscattering Characteristics of Snow at 35 and 95 GHz, 1989 Progress in Electromagnetic Research Symposium (PIERS), July 25-26, 1989, Massachusetts Institute of Technology, Cambridge, Massachusetts.

[18] Sarabandi, K., F.T. Ulaby, and T.B.A. Senior. Millimeter Wave Scattering Model for a Leaf, 1989 International Geoscience and

Remote Sensing Symposium (IGARSS '89), July 10-14, 1989, Vancouver, Canada.

[19] Haddock, T.F. and F.T. Ulaby. 140 GHz Scatterometer Measurments, 1989 International Geoscience and Remote Sensing Sumposium (IGARSS '89), July 10-14, 1989, Vancouver, Canada.

[20] Ulaby, F.T. Millimeter-Wave Bistatic Scattering by Terrain, AGARD Conference Proceedings, Kopenhagen, Denmark, Sept. 9-13, 1985

[21] Ulaby, F.T., T.F. Haddock, and Y. Kuga. Measurments and Modeling of Millimeter-Wave Scattering from Tree Canopies. 1989 International Geoscience and Remote Sensing Symposium (IGARSS '89), July 10-14, 1989 Vancouver, Canada.

4. PARTICIPATING SCIENTIFIC PERSONNEL

The following people participated in The Millimeter Wave Radar Clutter Program:

Faculty and Research Scientists

Dr. Fawwaz T. Ulaby

Dr. Yasu Kuga

Dr. Thomas Senior

Dr. Jack East

Dr. Martti Hallikainen

Graduate Students

Dr. Kamal Sarabandi, Received M.S. (1986) and PhD (1989)

Mr. Michael Whitt, Received M.S. (1987), expected PhD completion in 1990

Ms. Emilie Van Deventer, Received M.S. (1987), expected PhD completion in 1990

Mr. Richard Austin, Received M.S. (1988), expected PhD completion in 1990

Mr. Jack Ross, no degree completed. Transferred to another university.

Mr. Vince Karasack, Received M.S. (1988)

Ms. Julie Hoffman, Received M.S. (1988)

Mr. Adib Nashashibi, expected PhD completion in 1991

Mr. Mike Colluzi, Received M.S. (1988)

5. CONCLUSIONS

Judging by both the quantity and quality of the work performed under this program and by the significance of the results achieved relative to the goals of the program, we believe that we have made important contributions towards understanding the nature of millimeter-wave interaction with terrain. This type of research should be continued with primary emphasis placed on the use of polarimetric data for characterizing the physical properties of the observed scene

APPENDIX A
LIST OF PERTINENT PUBLICATIONS

[1] F.T. Ulaby, T.F. Haddock, J.R. East AND M.W. Whitt. A Millimeterwave Network Analyzer based Scatterometer. IEEE Transactions on Geoscience and Remote Sensing, Vol. 26(1). Jan. 1988.

[2] M.W. Whitt and F.T. Ulaby. Millimeter-Wave Polarimetric Measurements of Artificial and Natural Targets. IEEE Transactions on Geoscience and Remote Sensing, Vol. 26(5). Sept. 1988.

[3] T.F. Haddock and F.T. Ulaby. 140-GHz Scatterometer System and Measurements of Terrain. submitted for publication in IEEE Transactions on Geoscience and Remote Sensing.

[4] M.W. Whitt and F.T. Ulaby. Millimeter-wave Polarimetric Measurements of Artificial and Natural Targets. Proceedings of IGARSS '87 Symposium, Ann Arbor, May 1987.

[5] F.T. Ulaby, T.F. Haddock and R.T. Austin. Fluctuation Statistics of Millimeter-Wave Scattering from Distributed Targets. IEEE Transactions on Geoscience and Remote Sensing, Vol. 26(3), May 1988.

[6] M.T. Hallikainen, F.T. Ulaby and T.E. Van Deventer. Extinction Behavior of Dry Snow in the 18- to 90- GHz Range. IEEE Transactions on Geoscience and Remote Sensing, Vol. GE-25(6). Nov. 1987.

[7] M.T. Hallikainen, F.T. Ulaby and T.E. Van Deventer. Extinction Coefficient of Dry Snow at Microwave and Millimeterwave Frequencies. Proceedings of IGARSS '87 Symposium, Ann Arbor. May 1987.

[8] T.E. Van Deventer, J.R. East and F.T. Ulaby. Millimeter Transmission Properties of Foliage. Proceedings of IGARSS '87, Ann Arbor. May 1987.

[9[F.T. Ulaby, T.E. Van Deventer. J.R. East. T.F. Haddock and M.E. Coluzzi. Millimeter-wave Bistatic Scattering From Ground and Vegetation Targets. IEEE Transactions on Geoscience and Remote Sensing, Vol. 26(3). May 1988.

[10] F.T. Ulaby, T.F. Haddock and M.E. Coluzzi. Millimeter-wave Bistatic Radar Measurements of Sand and Gravel. Proceedings of IGARSS '87 Symposium, Ann Arbor. May 1987.

[11] K. Sarabandi, F.T. Ulaby, and T.B.A. Senior. Millimeter Wave Scattering Model for a Leaf. Accepted for publication in Radio Science.

[12] F.T. Ulaby, T.H. Haddock and Y. Kuga. Measurement and Modeling of Millimeter-wave Scattering from Tree Foliage. Submitted for publication in Radio Science.

[13] Y. Kuga, R.T. Austin, T.F. Haddock and F.T. Ulaby. Millimeter-wave Radar Scattering from Snow Part I--Radiative Transfer Model with Quasi-Crystalline Approximation. To be submitted for publication in IEEE Transactions on Geoscience and Remote Sensing.

A Millimeterwave Network Analyzer Based Scatterometer

FAWWAZ T. ULABY, FELLOW, IEEE, THOMAS F. HADDOCK, MEMBER, IEEE, JACK R. EAST, MEMBER, IEEE, AND MICHAEL W. WHITT, STUDENT MEMBER, IEEE

Abstract—The Millimeterwave Polarimeter (MMP) is a network-analyzer based scatterometer and reflectometer system that has been developed in support of a program to characterize radar clutter at 35, 94, and 140 GHz. A HP 8510A network analyzer is employed in the MMP system as a signal conditioner and processor to facilitate real-time data reduction, to reduce the short time-delay leakage noise inherent in traditional FM/CW radar, and to further enhance the signal-to-noise ratio of the system through signal processing techniques. Operation of the system at millimeter wavelengths is achieved with up-conversion and harmonic downconversion. The use of harmonic down-converters permits low-frequency signal connections between components of the system and allows easy reconfiguration in either scatterometer, bistatic, or reflection/transmission modes.

I. Introduction

THE PRIMARY design objectives of the Millimeter-wave Polarimeter (MMP) is to achieve a system that can operate at 35, 94, and 140 GHz with full polarization and phase capability. It should operate from a truck platform as a scatterometer for backscatter measurements and in the laboratory for bistatic and transmission measurements, and should have ranging and real-time processing capabilities. The HP 8510A is an automatic vector network analyzer with a computer-control system that allows vector error correction of imperfections through the use of calibration standards. It provides the needed flexibility and signal conditioning and processing for our requirements.

The three configurations of the MMP are illustrated in Fig. 1. Fig. 1(a) illustrates the 94-GHz system in its backscatter mode. In this configuration it operates from a variable-angle mount on the end of an extendable boom mounted on a truck. The front end RF and IF components are mounted on the boom top, while the network analyzer and ancillary data processing and recording equipment are mounted in a control house on the bed of the truck. Fig. 1(b) shows the bistatic measurement configuration in which the transmitter and receiver sections are separated from one another and used to make bistatic measurements. Fig. 1(c) illustrates the transmitter and receiver subsystems, operating without the lens-horn antennas, to make transmission and reflection measurements. In this configuration the two subsystems directly face one another, so the transmitted signal passes directly through the sample.

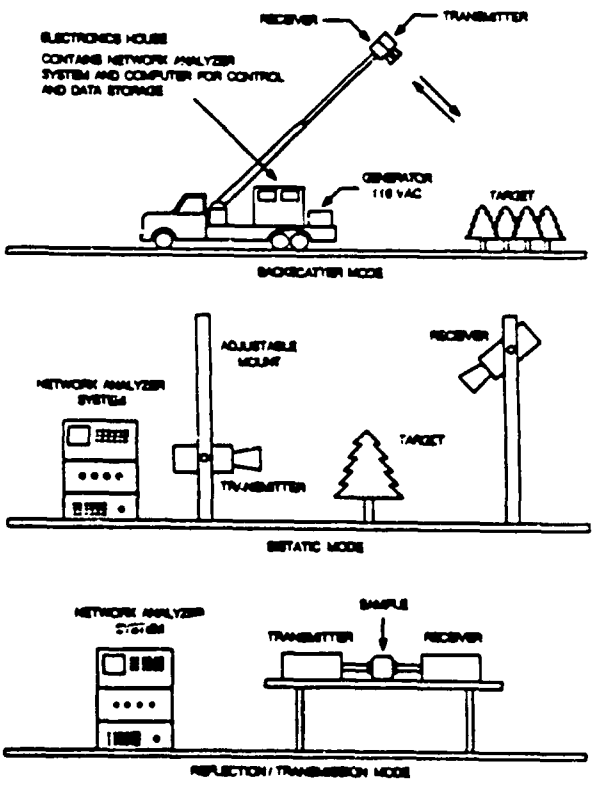

Fig. 1. The three operating configurations of the MMP.

Note that in the bistatic and reflection/transmission modes the receiver and transmitter sections must be positioned independently of each other. Scatterometer usage requires that the entire system be portable, with the front end moving remotely and independently from the HP 8510A back end. The MMP system illustrated in Fig. 2 addresses each of these goals, while providing standard operating procedures and data format for all three types of data acquisition.

II. MMP Design

The design goal was to produce a single versatile instrument with the ability to be configured in the three de-

Manuscript received January 13, 1987, revised July 30, 1987

The authors are with the Radiation Laboratory, Department of Electrical Engineering and Computer Science, The University of Michigan, Ann Arbor, MI 48109-2122.

IEEE Log Number 8717530.

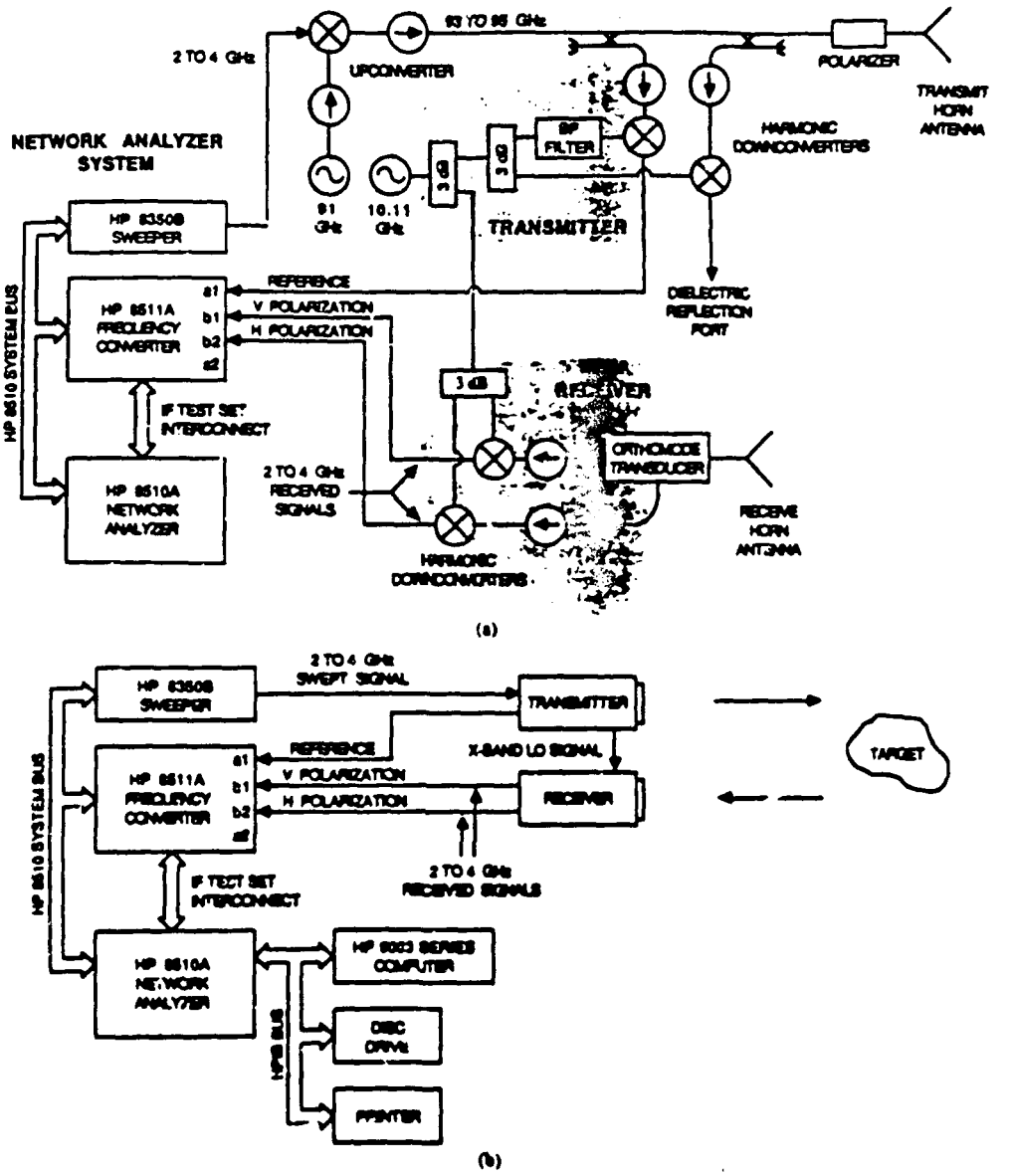

Fig. 2. Scattering configuration of the system, detail, and block diagrams. (a) System diagram in scatterometer mode. The 94-GHz system is illustrated. 35- and 140-GHz systems are analogous. (b) Scatterometer configuration of the system.

sired configurations. Discussion of each of the configurations follows.

A. Backscatter Mode

Fig. 2 illustrates the system in its backscatter mode, in detail (part a) and in block diagram form (part b). At each RF frequency a fixed-frequency Gunn source and mixer are used to upconvert a 2–4 GHz swept signal, controlled by the HP 8510A, to a swept 93–95 GHz signal. This signal is transmitted (in vertical or horizontal polarization) through a lens-horn antenna to the target. A sample of the transmitted signal is harmonically downconverted with a low-frequency LO (~ 10 GHz) and transmitted through flexible coaxial cable to the reference signal (a_1) port of the network analyzer. The reflected signal, picked up by a second antenna, is downconverted and fed into the return signal (b_1) port. The polarization switch allows the selection of either the horizontal or the vertical returned signal. Due to the low frequency (2–4 GHz and 10 GHz) coaxial interconnections between the various up and down converters, the transmitter and receiver subsystems are independently mobile.

In a traditional FM/CW radar [1]-[3] the noise floor is set by nonvarying leakages and reflections within the system. For short-range calibrated radars, or scatterometers, this level is typically about 30 to 35 dB above the thermal

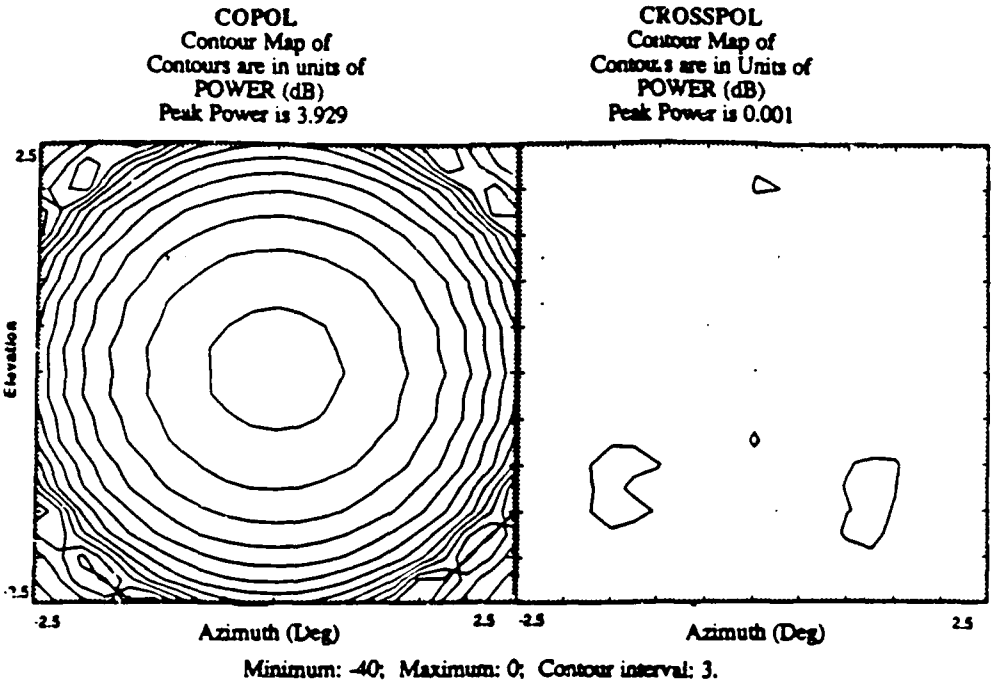

Fig. 3. Like- and cross-polarization traces for a typical MMP antenna.

noise floor of the system. The HP 8510A has error correction routines that correct for imperfections in the test circuitry through measurements of standard calibrators. By using an HP 8510A as a radar back-end, sources of system measurement error can be characterized and partially subtracted from the signal, hence, greatly increasing system sensitivity over that provided by a conventional design.

In addition, since the HP 8510A makes measurements by determining the phase and amplitude of returned signals over a series of stepped frequencies, all phase information is retained. When both horizontal and vertical modes of polarization are measured, complete polarization information can be obtained. This allows the reconstruction of any mode of polarization, linear or circular, thus making the system completely polarization agile. This capacity can be used to completely specify the scattering matrix of an object or target of interest.

The HP 8510A has the capability to perform complex binary math operations on pairs of swept signals. For example, a signal may be memorized and used to operate on subsequent signals to remove or reduce unwanted responses. This can be used to reduce reflection and leakage noise from within the system, as well as to reduce unwanted responses from outside the instrument.

The HP 8510A can perform real-time fast-Fourier transforms from the frequency domain, in which the data is taken, to the time domain. Range-gating capabilities in the time domain allow setting the response of the instrument to a specified time range. This can be used to reject signals reflected from targets outside of the desired range, as well as to measure the backscattered power as a function of range. In studying the scattering from vegetation canopies, for example, it is possible to record the differential scattering as a function of range from the top of the canopy down to the underlying ground surface.

TABLE I
TRUCK MOUNTED SCATTEROMETER PARAMETERS

Frequencies	35, 94, 140 GHz
RF Bandwidth	0 to 2.5 GHz
Sweep Rate	1 reading, 51, 101, 201, 401 frequencies
Polarization	HH, HV, VV, VH, magnitude and phase
Incidence Angles	0 to 70 degrees
Platform Height	3 meters minimum, to 15 meters maximum
Noise Equivalent σ^0	35 GHz: -30 dB * 94 GHz: -34 dB * 140 GHz: -37 dB *
(*These values for the 0 meters and 0 = 30 degrees - the actual values will vary with both parameters.)	
Near Field Distance	35 GHz: 5.83 m 94 GHz: 3.71 m 140 GHz: 1.20 m
Footprint	35 GHz: 0.035 to 16.9 sq. m 94 GHz: 0.032 to 4.76 sq. m 140 GHz: 0.004 to 0.32 sq. m
Signal Processing	HP 8510A/B11A based
Output Products	<received power versus range (dB = dBm) <received power versus frequency (at fixed R) <phase and amplitude for each frequency

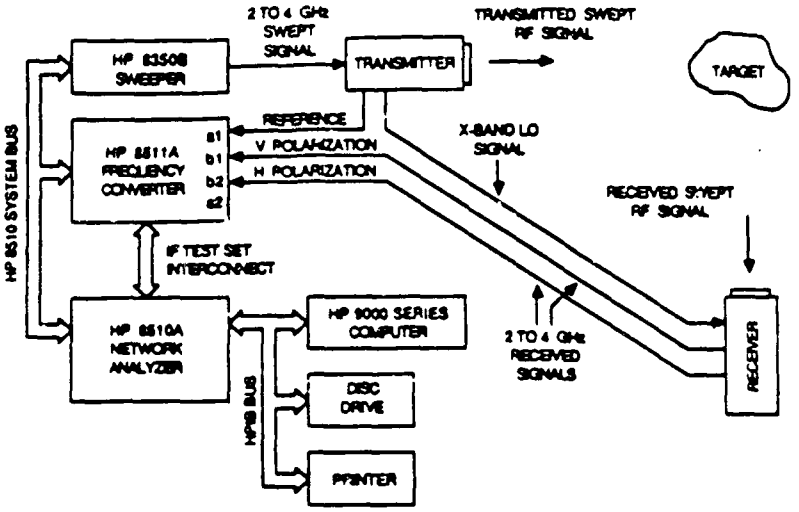

Fig. 4. Bistatic configuration of the system.

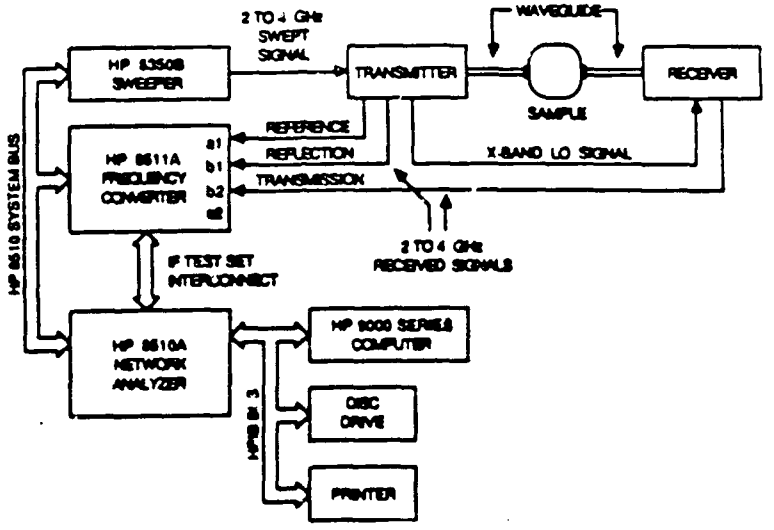

Fig. 5. Reflection/transmission configuration of the system.

equipment. The values for the noise-equivalent σ° for the 94- and 140-GHz systems were derived on the basis of tests in the laboratory.

The bandwidth of the MMP can range from 0 to 2 GHz, and can be changed in real-time. Narrow bandwidth allows the system to have high spectral resolution, and hence have good determination of frequency-dependent features of the targets. Wide bandwidth allows good temporal resolution and can be used to reduce and study the effects of fading.

Antenna patterns of a typical MMP antenna are given in Fig. 3. These antennas have corrugated conical feed horns with matched dielectric lenses. Note that the cross-polarization isolation is better than 40 dB.

B. Bistatic Mode

The bistatic configuration diagram is shown in Fig. 4. The operation is similar to that in the backscatter mode, only here the transmitter and receiver sections move independently of each other in making the measurements at various angles. Ease of movement of the two subsystems comes from the low-frequency IF (2 to 4 GHz) and LO (*X*-band) interconnections. Note that due to range-gating, bistatic measurements can take place anywhere, in the field, where the numerous unwanted reflections can be time-gated out, or in the usual anechoic chamber setting.

C. Transmission Mode

The transmission configuration diagram is shown in Fig. 5. Operation is as in the bistatic case, with the transmitter and receiver units positioned independently, only now the lens-horn antennas are removed and samples are placed directly against the waveguide probes. In this configuration the polarization switch is used to select either the response from the reflected signal or the transmitted signal.

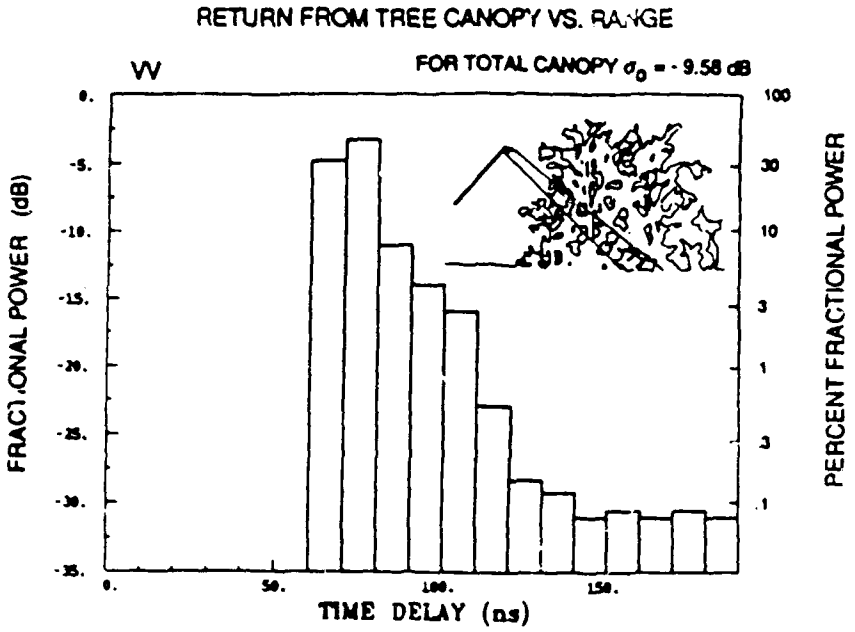

Fig. 6. Histogram of time-domain response of trees at 35 GHz.

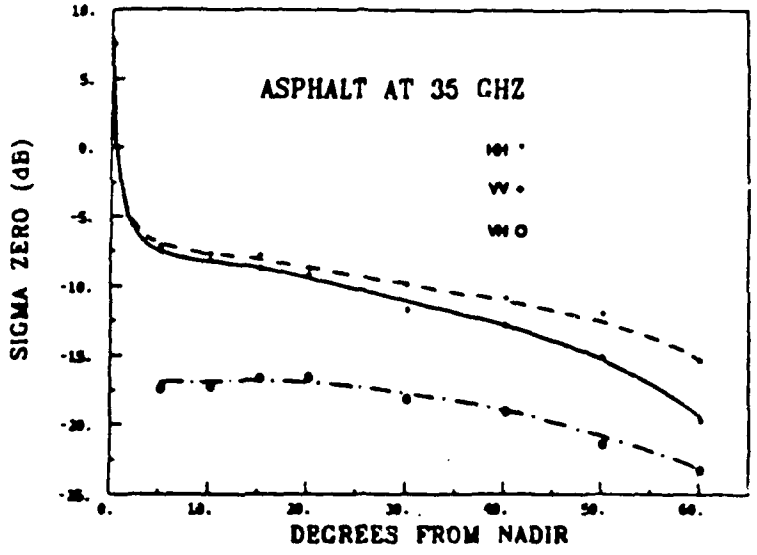

Fig. 7. Backscatter measurements on asphalt at 35 GHz.

III. Preliminary Results

Fig. 6 shows a histogram of the time-domain response of the system operating in the scatterometer mode at 35 GHz. The target was a dense stand of trees, and the data was taken with a full bandwidth of 2 GHz at an angle of approximately 45 degrees. Calibration was performed against a 15-in sphere, and the estimated 1-σ accuracy was 1 dB for the total canopy $\sigma^\circ = -9.6$ dB. The histogram shows the power, given as a percent of the total removed power, through the canopy in 10-ns bins.

Fig. 7 shows σ° measurements of an asphalt surface versus angle for H-H, V-V, and V-H polarizations. This data was taken at 35 GHz with a 2-GHz bandwidth.

Fig. 8 shows a plot of the radar-cross-section versus incidence angle for a leaf of cross section of approximately 40 cm^2, with 63-percent moisture content. This data was taken in an anechoic chamber at 35 GHz with the system operating in the backscatter mode.

IV. Conclusion

The HP 8510A network analyzer shows great promise as the back end of centimeter- and millimeter-wave FM/CW scatterometers and reflectometers. Use of its various error correction and signal processing capabilities should greatly improve signal-to-noise ratio over equivalent conventional systems. Furthermore, the versatility in

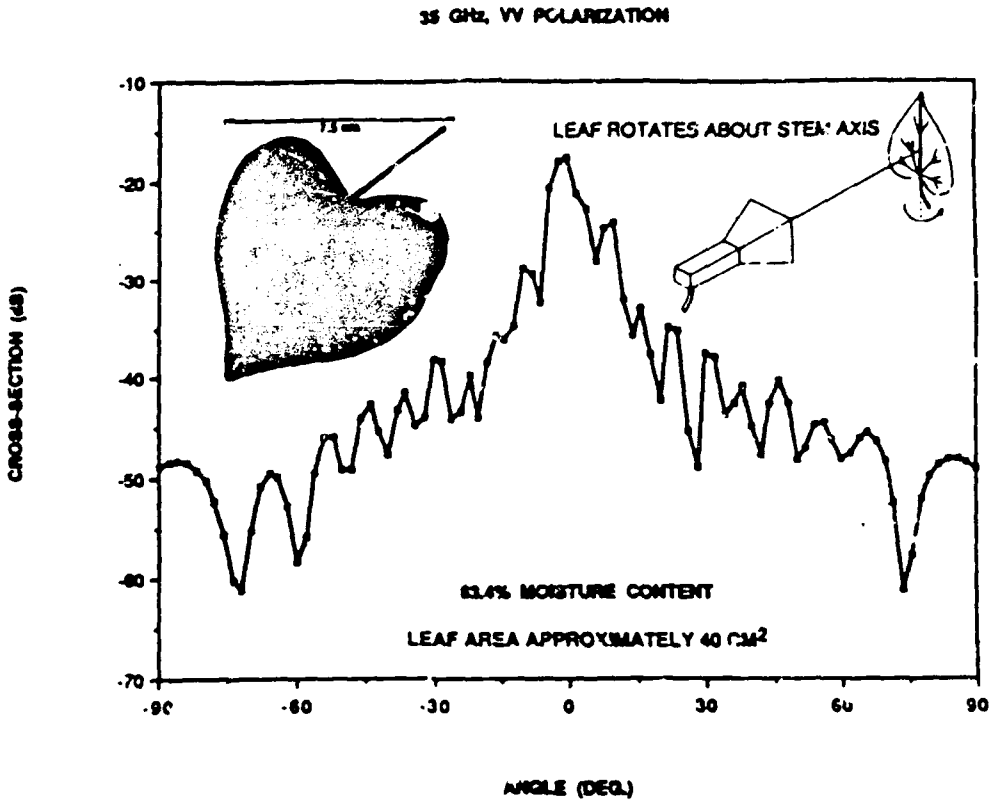

Fig. 8. *Leaf* backscatter cross section versus angle at 35 GHz for a leaf with 63.4-percent moisture content.

bandwidth, polarization, and configuration of the MMP allow for a flexible system for field as well as laboratory use.

REFERENCES

[1] W. K. Saunders, "CW and FM radar systems," in *Radar Handbook*, M. I. Skolnik, Ed. New York: McGraw-Hill, 1970.
[2] M. I. Skolnik, *Introduction to Radar Systems*. New York: McGraw-Hill, 1962.
[3] F. T. Ulaby, R. K. Moore, and A. K. Fung, *Microwave Remote Sensing: Active and Passive*, vol. I. Reading, MA: Addison-Wesley, 1981.

Fawwaz T. Ulaby (M'68–SM'74–F'80) was born in Damascus, Syria, on February 4, 1943. He received the B.S. degree in physics from the American University of Beirut, Lebanon, in 1964 and the M.S.E.E. and Ph.D. degrees in electrical engineering from the University of Texas, Austin, in 1966 and 1968, respectively.

From 1968 to 1984, he was with the Electrical Engineering Department at the University of Kansas, Lawrence, where he was the J. L. Constant Distinguished Professor, and the University of Kansas Center for Research, where he was Director of the Remote Sensing Laboratory. He is currently with the Radiation Laboratory and the Department of Electrical and Computer Engineering, University of Michigan, Ann Arbor. His current research interests involve microwave propagation and active and passive microwave remote sensing. Along with R. K. Moore and A. K. Fung, he is a coauthor of the three-volume series *Microwave Remote Sensing: Active and Passive* (Reading, MA: Addison-Wesley). In addition, he is coeditor of the *Manual of Remote Sensing*, 2nd ed., vol. I, American Society of Photogrammetry.

Dr. Ulaby is a member of Eta Kappa Nu, Tau Beta Pi, and Sigma Xi. He has been named the Executive Editor for IEEE TRANSACTIONS ON GEOSCIENCE AND REMOTE SENSING, 1984–1985, and was the Geoscience and Remote Sensing Society's Distinguished Lecturer for 1987. He was named an IEEE Fellow in 1980 "for contributions to the application of radar to remote sensing for agriculture and hydrology," received the GRS Society's Outstanding Service Award in 1982, and its Distinguished Service Award in 1983. In 1984, he also received a Presidential Citation for Meritorious service from the American Service of Photogrammetry. He received the University of Kansas Chancellor's Award for Excellence in Teaching in 1980, the University of Kansas Gould Award for "distinguished service to higher education" in 1973, and the Eta Kappa Nu MacDonald Award as an "outstanding electrical engineering professor in the United States of America" in 1975.

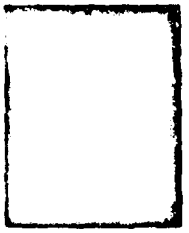

Thomas F. Haddock (M'86) was born in Washington, DC, on November 2, 1949. He received the B.A. degree in mathematics and the M.S. and Ph.D. degrees in physics from the University of Michigan, Ann Arbor, in 1972, 1977, and 1984, respectively.

From 1984 to 1985 he was Manager of Development Projects at Applied Intelligent Systems, a machine vision firm involved in real-time optical, infrared, and X-ray vision systems. He is currently with the Radiation Laboratory and the Department of Electrical Engineering and Computer Science, University of Michigan. He has conducted research in the fast flux density variations of quasi-stellar objects at a wavelength of 12.5 mm. Other research has included development of real-time alphanumeric character recognition algo-

rithms and ultrasonic weld inspection algorithms. Prior to receiving the Ph.D. degree, he worked as Applications Engineer for Sarns/3M, a manufacturer of heart-lung machines and cardiac assist devices, where he developed electrodes for manufacturing applications. Current research interests are millimeter-wave scattering and emission from natural targets.

Dr. Haddock is a member of the American Astronomical Society.

•

Jack R. East (S'70–M'72) received the B.S.E., M.S., and Ph.D. degrees from the University of Michigan, Ann Arbor.

He is now an Associate Research Scientist in the Solid-State Electronics Laboratory of the University of Michigan, working in the area of microwave- and millimeter-wave solid-state devices.

Michael W. Whitt (S'83) was born in St. Charles, MO, on December 3, 1962. He received the B.S. degree in electrical engineering from the University of Arkansas, Fayetteville, in 1985 and the M.S. degree in electrical engineering from the University of Michigan, Ann Arbor, in 1986. Since September 1985, he has been a Graduate Research Assistant at the University of Michigan Radiation Laboratory, where he is currently working toward the Ph.D. degree.

His research interests include millimeter-wave radar, radar polarimetry, and polarimetric scattering from terrain and vegetation canopies.

Millimeter-Wave Polarimetric Measurements of Artificial and Natural Targets

MICHAEL W. WHITT, STUDENT MEMBER, IEEE, AND FAWWAZ T. ULABY, FELLOW, IEEE

Abstract—The millimeter-wave polarimeter (MMP) is a scatterometer system that uses the HP 8510A vector network analyzer for coherent processing of the received signal. It operates at 35 and 94 GHz, and a third channel at 140 GHz is to be added in 1988. The MMP provides the polarization and phase measurement capability needed to measure the complete scattering matrix of a given target. This paper describes a calibration and measurement technique that was used with the MMP at 35 GHz to measure the scattering matrix for both distributed and point targets. An analysis of the measurement accuracy was performed by comparing theoretical and measured values for a set of conducting spheres and finite length conducting cylinders. As an extension of the analysis to natural targets, the scattering matrix was measured for a series of twigs and various smooth and rough surfaces.

I. Introduction

THE OVERWHELMING majority of scattering data reported in the literature for both distributed and point targets consists of incoherent power measurements conducted for specific polarization configurations. These measurements were generally limited to frequencies in the microwave range below 30 GHz. In recent years, the technology has advanced to the point where phase and polarization are being explored more extensively, and the frequency range of operating radar systems has been extended to the millimeter-wave region. Early work by Sinclair [1], Kennaugh [2], and Deschamps [3] showed that scattering from a radar target can be described in terms of a complex scattering matrix. The scattering matrix transforms the incident field into a scattered field and completely characterizes scattering from the target. Most of the early work relating to the scattering matrix concentrated on point targets. An extensive reference list for the work in this area is given in the papers by Huynen [4] and Guili [5]. Recent interest in its application to remote sensing has led to the development of polarimeter SAR systems, and quasi-calibrated polarimetric data have been obtained by the NASA/JPL *L*-band SAR for a variety of terrain surfaces [6], [7]. However, very little work has been conducted in measuring and characterizing the scattering matrices of distributed targets using calibrated polarimetric scatterometers. This is particularly the case at millimeter wavelengths.

Manuscript received March 21, 1988, revised May 12, 1988. This work was supported by the U. S. Army Research Office under Contract DAAG29-85-K-0220.

The authors are with the Radiation Laboratory, Department of Electrical Engineering, and Computer Science, The University of Michigan, Ann Arbor, MI 48109-2122.

IEEE Log Number 8822336

This paper will describe a technique developed at the University of Michigan to measure the scattering matrix of both distributed and point targets at millimeter wavelengths. The technique uses the millimeter-wave polarimeter (MMP), which is a coherent scatterometer developed to operate both in a laboratory setting and from a truck-mounted boom [8], [9]. With such a system, data can be produced under laboratory and natural conditions to facilitate the modeling of millimeter-wave scattering from natural targets.

II. Measurement System

The MMP system shown in Fig. 1 consists of an HP 8510A vector network analyzer, transmitter and receiver sections, and signal processing and recording equipment. The transmitter section produces a 34–36 GHz frequency swept RF signal by upconverting a 2–4 GHz signal supplied by the HP 8350B sweeper. A sample of the transmitted signal is harmonically downconverted and applied to the a_1 port of the HP 8511A frequency converter as a reference. A similar downconversion stage is used in the receiver section mounted directly below the transmitter. The receiver supplies both vertical and horizontal components of the returned signal. The vertical and horizontal components from the receiver are then applied to the b_1 and b_2 ports of the HP 8511A, respectively. A Faraday rotation polarizer is used to provide the desired polarization for transmission.

An anechoic chamber with a target mount was used for conducting the calibration tests and for measuring the scattering matrices of small targets. The target mount, shown in Fig. 2, was a large diameter circular wooden frame with a concentric inner ring (1-m diameter) that allowed variation of the target orientation angle. Monofilament line was used to suspend the target within the circular frame. Based on the 3.4° half-power beamwidths of the antennas, the 6-dB illuminated area at a 5-m target range is about 0.3 m in diameter, placing the illumination well within the diameter of the target mount frame. The target mount had both elevation and azimuth control to allow accurate target positioning. The measured noise-floor of the small target measurement configuration corresponded to a radar cross section of $\sigma = -40$ dBm^2 for co-polarized return and $\sigma = -50$ dBm^2 for cross-polarized return.

Backscatter measurements made for distributed surfaces (sand and rocks) were conducted in the laboratory.

0196-2892/88/0900-0562$01.00 © 1988 IEEE

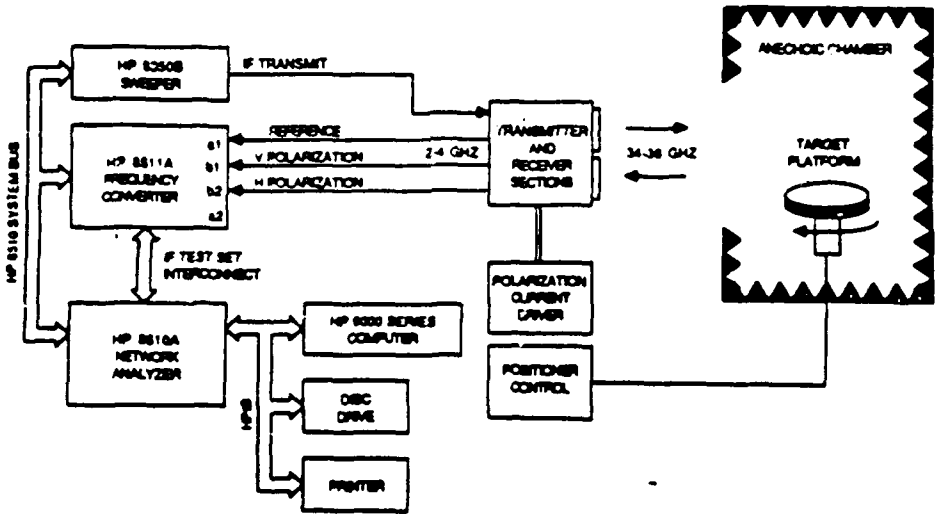

Fig. 1. Block diagram of the MMP system operating in the backscatter mode.

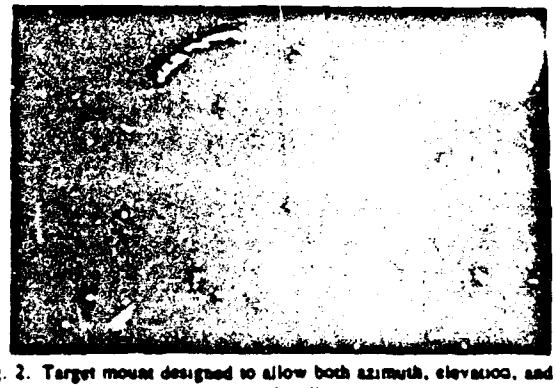

Fig. 2. Target mount designed to allow both azimuth, elevation, and on-station angle adjustment.

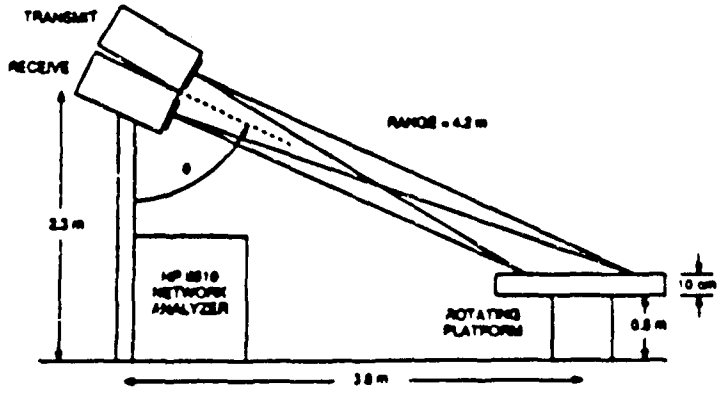

Fig. 3. Distributed surface measurement configuration.

but without an anechoic chamber (see Fig. 3). The measurement system has a range resolution of about 10 cm, so reflections from targets other than the one being measured were simply gated out. The noise-equivalent backscattering coefficient (σ^0) for the surface measurement configuration was less than -35 dB.

III. Measurement Procedure and Calibration

Using the HP 8510A vector network analyzer system as the IF processor provides the user with several features that can be used to improve the accuracy of the measurement. Complex math operations are available and can be

used to subtract out the response of the chamber and any other spurious but systematic errors. In addition, an internal real-time FFT processor is available to transform the frequency swept data to the time domain. Time-gating can then be used to select the target response and reduce spurious signals at ranges different from that corresponding to the target. The gated frequency response can be obtained by Fourier transforming the time-gated response. Another important feature of the HP 8510A is its averaging capability. Averaging of the returned signal reduces the system noise floor proportional to the square root of the averaging factor.

To make a measurement of a particular target, the time domain response of the target is displayed to allow the time-gate to be set for the proper target range. The time-gated frequency response for both the background and the target/background combination are then stored for all polarization combinations. The trace math feature of the HP 8510A is now used to subtract the gated frequency response of the chamber from that of the target/background combination, resulting in the frequency response for the target alone. To calibrate the system, a target of known radar cross section is measured in the same manner, thereby allowing the magnitude and relative phase of the scattered fields to be determined.

The procedure just described can also be implemented by using the internal calibration capabilities of the HP 8510A and an external controller [10]. The same error models developed for making network measurements may also be used to perform the error correction required for radar cross-section measurements. The errors in the measured frequency response of a given target can be modeled as a response error $E_R(f)$, which causes an error in the magnitude and phase of the measured signal, and an isolation error $E_I(f)$, which causes an error signal to arrive in parallel with the target signal. The response error is the gain and phase offset difference between the measurement and reference channels, and the isolation error is the response of the measurement configuration without the presence of the target. The isolation error contains the response of the chamber and target mount. The voltage $V_m(f)$ measured relative to the reference channel voltage is given by

$$V_m(f) = T(f)E_R(f) + E_I(f) \tag{1}$$

where $T(f)$ is the actual target response. By measuring the frequency response of a known target, then the background with the target removed, both the response and isolation errors can be determined and used in the internal HP 8510 one-port error correction procedure. The internal calibration method was preferred, since it overcomes some of the limitations of the trace math approach.

This calibration procedure can be used for measurements of both point targets and distributed targets. However, additional processing must be performed if the unknown target is at a different range than the calibration target. The magnitude of the measurement must be scaled by the ratio of the range dependence between the measurement and the calibration. The relative phase, however, is unaffected.

IV. The Scattering Matrix

For plane-wave incidence upon a target located at the origin and observed at a distance r, the vertical and horizontal components of the incident and scattered electric fields are related by the scattering matrix $[S]$ of the target

$$\begin{bmatrix} E_h^s \\ E_v^s \end{bmatrix} = \frac{e^{ikr}}{\sqrt{4\pi r^2}} \begin{bmatrix} S_{hh} & S_{hv} \\ S_{vh} & S_{vv} \end{bmatrix} \begin{bmatrix} E_h^i \\ E_v^i \end{bmatrix} \tag{2}$$

where $[S]$ is defined by

$$[S] = \begin{bmatrix} S_{hh} & S_{hv} \\ S_{vh} & S_{vv} \end{bmatrix} \tag{3}$$

and k is the wavenumber in free space. Using the relation between the elements of $[S]$ and their corresponding radar cross sections, namely

$$\sigma_{rt} = |S_{rt}|^2 \tag{4}$$

where the subscripts r and t denote the receive and transmit polarizations, the scattering matrix $[S]$ can be written as

$$[S] = e^{i\phi_{hh}} \begin{Bmatrix} \sqrt{\sigma_{hh}} & \sqrt{\sigma_{hv}}\, e^{i(\phi_{hv} - \phi_{hh})} \\ \sqrt{\sigma_{vh}}\, e^{i(\phi_{vh} - \phi_{hh})} & \sqrt{\sigma_{vv}}\, e^{i(\phi_{vv} - \phi_{hh})} \end{Bmatrix}. \tag{5}$$

We have factored out the phase of the S_{hh} term since we will only be able to measure relative phase. In this form, the scattering matrix can be determined from quantities that are independent of range.

V. RCS for a Finite-Length Conducting Cylinder

To calibrate the MMP for scattering matrix measurements, the seven independent quantities of $[S]$ must be measured for a known target. One target that was found to work well for calibration is a finite-length conducting cylinder. First, consider an infinite conducting cylinder oriented relative to the radar as in Fig. 4. Two coordinate systems are defined, primed and unprimed. The primed coordinates are local to the cylinder with the z' axis along the axis of the cylinder. The unprimed coordinates are fixed relative to the radar. The bistatic angle between the transmitter and receiver is about 3.4°, which is sufficiently small to assume that the measured cross section represents the backscattered case. The target was located at a distance of 5 m, which is slightly less than the $2D^2/\lambda$ far-field distance of 5.4 m.

For a vertically polarized incident wave, the electric field is

$$\bar{E}^i = \hat{z} E_0 e^{-ikx} \tag{6}$$

where an $e^{-i\omega t}$ time dependence has been assumed and suppressed. In terms of the primed coordinates, the incident electric field is

$$\bar{E}^i = (\hat{z}' \cos\theta - \hat{y}' \sin\theta) E_0 e^{-ikx} \tag{7}$$

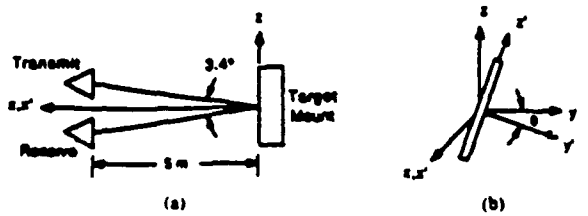

Fig. 4. Radar geometry relative to the target; (a) radar geometry and (b) target geometry.

The far-zone backscattered electric field due to this excitation for an infinite conducting cylinder with radius a [11, pp. 267-273] is given by

$$\bar{E}^s = E_0\sqrt{\frac{2}{\pi kx}}\, e^{j(kx-(\pi/4))}\left[\vartheta' \sin\theta \sum_{n=-\infty}^{\infty}(-1)^n C_n^{TE} + \ell' \cos\theta \sum_{n=-\infty}^{\infty}(-1)^n C_n^{TM}\right] \quad (8)$$

where

$$C_n^{TM} = -\frac{J_n(ka)}{H_n^{(1)}(ka)} = C_{-n}^{TM} \quad (9)$$

$$C_n^{TE} = -\frac{J_n'(ka)}{H_n^{(1)\prime}(ka)} = C_{-n}^{TE}. \quad (10)$$

In terms of the original unprimed coordinates, the backscattered electric field is

$$\bar{E}^s = E_0\sqrt{\frac{2}{\pi kx}}\, e^{j(kx-(\pi/4))}(\vartheta C_{hv} + \ell C_{vv}). \quad (11)$$

The complex coefficients C_{vv} and C_{hv} are functions of the orientation angle θ and can be written as

$$C_{vv} = \cos^2\theta \sum_{n=-\infty}^{\infty}(-1)^n C_n^{TM} - \sin^2\theta \sum_{n=-\infty}^{\infty}(-1)^n C_n^{TE} \quad (12)$$

$$C_{hv} = \cos\theta \sin\theta\left[\sum_{n=-\infty}^{\infty}(-1)^n C_n^{TM} + \sum_{n=-\infty}^{\infty}(-1)^n C_n^{TE}\right]. \quad (13)$$

Similarly, for a horizontally polarized incident wave, the incident and backscattered electric fields are

$$\bar{E}^i = \vartheta E_0 e^{-jkx} \quad (14)$$

$$\bar{E}^s = E_0\sqrt{\frac{2}{\pi kx}}\, e^{j(kx-(\pi/4))}(\vartheta C_{hh} + \ell C_{vh}). \quad (15)$$

In this case, the complex coefficients C_{hh} and C_{vh} are

$$C_{hh} = \sin^2\theta \sum_{n=-\infty}^{\infty}(-1)^n C_n^{TM} - \cos^2\theta \sum_{n=-\infty}^{\infty}(-1)^n C_n^{TE} \quad (16)$$

$$C_{vh} = C_{hv}. \quad (17)$$

The scattering width for the infinite cylinder is defined as

$$\sigma_{rt}^c = 2\pi \lim_{\rho\to\infty} \rho \frac{|\bar{E}_r^s|^2}{|\bar{E}_t^i|^2} \quad (18)$$

where the subscripts r and t are the receive and transmit polarizations, respectively. Using this definition, the scattering widths for the infinite conducting cylinder are

$$\sigma_{vv}^c = \frac{4}{k}|C_{vv}|^2 \quad (19)$$

$$\sigma_{hv}^c = \frac{4}{k}|C_{hv}|^2 = \sigma_{vh}^c \quad (20)$$

$$\sigma_{hh}^c = \frac{4}{k}|C_{hh}|^2. \quad (21)$$

The relative phases of the hv, vh, and vv scattered fields are

$$\phi_{hv} - \phi_{hh} = \tan^{-1}\left[\frac{\mathrm{Im}\,(C_{hv}/C_{hh})}{\mathrm{Re}\,(C_{hv}/C_{hh})}\right] = \phi_{vh} - \phi_{hh} \quad (22)$$

$$\phi_{vv} - \phi_{hh} = \tan^{-1}\left[\frac{\mathrm{Im}\,(C_{vv}/C_{hh})}{\mathrm{Re}\,(C_{vv}/C_{hh})}\right]. \quad (23)$$

For cylinder lengths much larger than a wavelength, the radar cross section σ_{rt} can be written in terms of the scattering width of the infinite cylinder with the same diameter [11, pp. 302-305]

$$\sigma_{rt} = \frac{kL^2}{\pi}\sigma_{rt}^c \quad (24)$$

where L is the length of the cylinder. The relative phases for the finite-length cylinder at normal incidence were assumed to be the same as those for the infinite cylinder. Using these expressions in (5), we can readily compute the scattering matrix for the finite cylinder versus the rotation angle θ

$$[S] = \frac{2L}{\sqrt{\pi}}\, e^{jkx}\begin{bmatrix} |C_{hh}| & |C_{hv}|e^{j(\phi_{hv}-\phi_{hh})} \\ |C_{vh}|e^{j(\phi_{vh}-\phi_{hh})} & |C_{vv}|e^{j(\phi_{vv}-\phi_{hh})} \end{bmatrix} \quad (25)$$

with C_{vv}, $C_{hv} = C_{vh}$, C_{hh}, $\phi_{hv} - \phi_{hh} = \phi_{vh} - \phi_{hh}$, and $\phi_{vv} - \phi_{hh}$ given by (12), (13), (16), (22), and (23), respectively.

VI. Measurement Results for Small Targets

Three types of small targets were measured: conducting spheres, conducting cylinders, and natural evergreen twigs. A photograph of these targets is shown in Fig. 5. Radar cross-section measurements were first conducted for eight conducting spheres ranging in diameter from 0.787 to 6.35 cm. One of the spheres (d = 6.35 cm) was used for calibration, and the measured normalized cross sections of the others were compared to Mie calculations. The results, displayed in Fig. 6, show very good agreement for all spheres. It is worth noting that the measurements covered a wide dynamic range for σ, extending from −45.7 to −25.2 dBm^2. The rms error of the difference between the calculated and measured values of σ was 0.7 dB.

A conducting sphere is a convenient target to use for evaluating the linearity of the measurement system; it has geometrical symmetry and σ can be computed exactly. However, a sphere cannot be used to calibrate the cross-polarized (hv and vh) channels of the measurement system. Instead, a dihedral corner reflector may be used. When the axis of the dihedral is rotated by an angle θ in the $y - z$ plane (as in Fig. 4(b) with the cylinder representing the common axis of the dihedral reflector), the scattering matrix contains nonzero terms for hv and vh [12]

$$[S] = \frac{4\sqrt{\pi}ab}{\lambda}\begin{bmatrix} -\cos 2\theta & \sin 2\theta \\ \sin 2\theta & \cos 2\theta \end{bmatrix} \qquad (26)$$

where a and b are the dimensions of a single plane of the dihedral. The elements of $[S]$ measured for the dihedral were found to be different from those calculated on the basis of (26) by several decibels. This was attributed to scattering contributions from the unbeveled edges of the dihedral planes and to the difficulty of positioning the dihedral relative to the radar.

A conducting cylinder is an alternate target for calibrating the amplitude and relative phase of the hv and vh channels of the measurement system. Its scattering matrix was derived in Section IV and is given by (25). First, the error coefficients were computed by measuring the amplitude and phase of the backscattered signal as a function of frequency for all four linear polarization configurations with the conducting cylinder oriented at θ = 45°. The cylinder was 7.62 cm in length (L/λ = 8.89) and 0.1168 cm in diameter ($2a/\lambda$ = 0.273). Then, the system performance was evaluated at other values of θ by comparing the amplitudes of σ_{hh}, σ_{hv}, and σ_{vv}, and the relative phases $\phi_{hv} - \phi_{vv}$ and $\phi_{hh} - \phi_{vv}$ with the values computed using the theoretical expressions given in Section IV. The results presented in Fig. 7 show excellent agreement between theory and experiment. Similar tests were conducted for several other conducting cylinders, all 7.62 cm in length, but with diameters ranging from 0.0533 to 0.957 cm. The results were equally good in all cases. Fig. 8 shows the results for a cylinder with a diameter of 0.3175 cm.

Fig. 5. Targets measured using the small target measurement configuration.

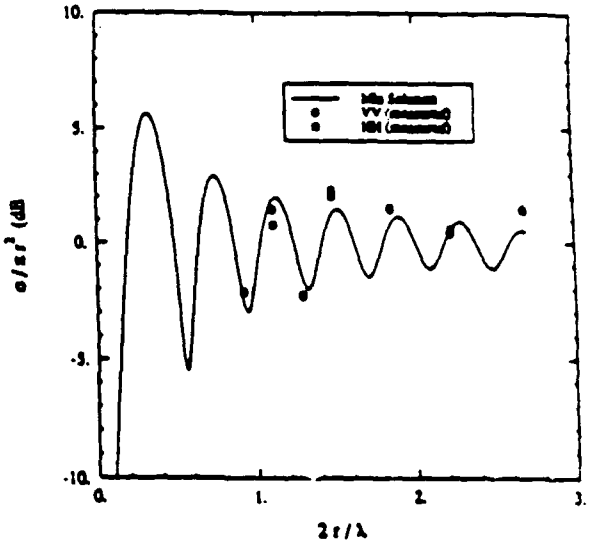

Fig. 6. Measured versus theoretical comparison of σ for a set of conducting spheres.

Based on the preceding analysis, the standard deviation characterizing the measurement precision of the MMP for all channels was computed to be about 0.9 dB for amplitude and 8.6° for phase. This precision reflects the error in positioning the target as well as the error introduced by the measurement system. The positioning error was found to be the most significant. Notice in Fig. 7(b) for the 0.1168-cm diameter cylinder that over the range $0° \le \theta \le 90°$, the measured phase fits the theoretical very closely. Since calibration was made with the same cylinder at θ = 45°, the positioning error is minimized. Based on an analysis of this region, the precision of the measurement system without positioning error is on the order of 0.5 dB for amplitude and 2.5° for phase.

Next, scattering matrix measurements were conducted on three small twigs at orientation angles of θ = 0°, −45°, and −90° where θ is defined as in Fig. 4(b) with the stem of the twig along the z' axis. The twigs were shown in Fig. 5, and we will refer to them as (from left to right) twigs A, B, and C. Notice that twig C has an asymmetric shape with the needles connected to the

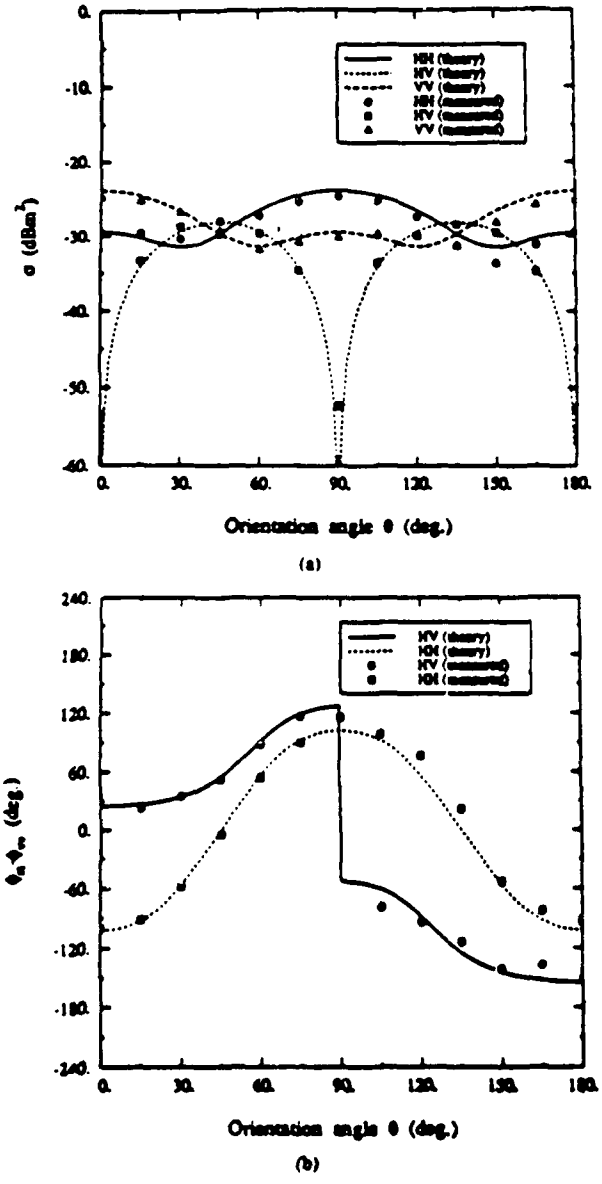

Fig. 7. Measured versus theoretical comparison of scattering from a conducting cylinder as a function of orientation angle θ (L = 7.62 cm, d = 0.1158 cm); (a) amplitude and (b) relative phase.

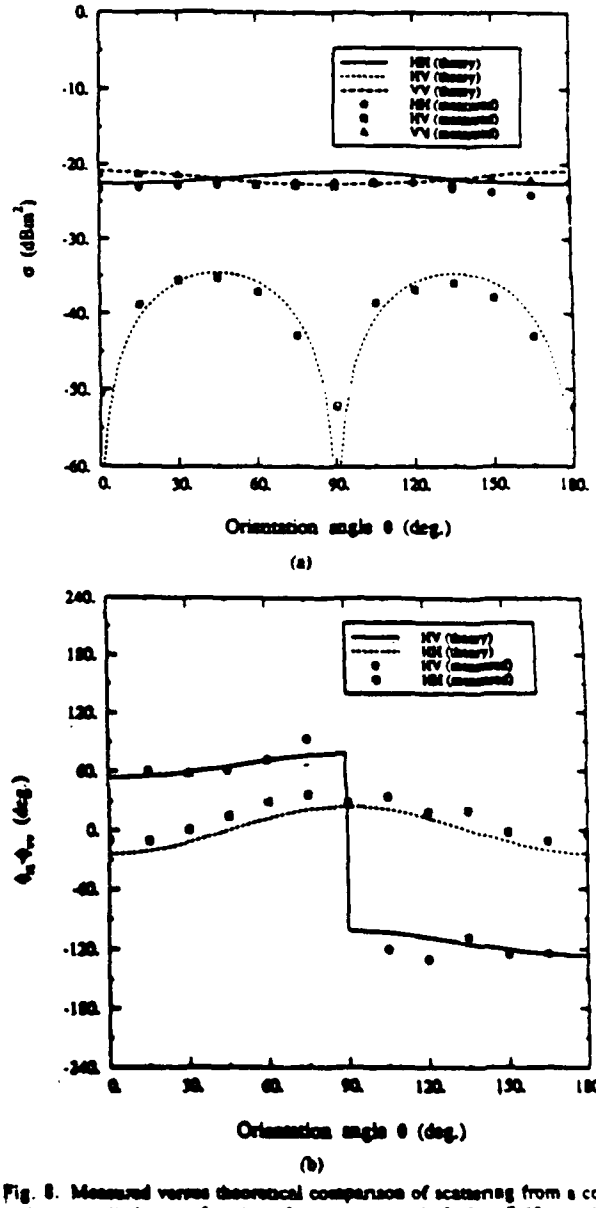

Fig. 8. Measured versus theoretical comparison of scattering from a conducting cylinder as a function of orientation angle θ (L = 7.62 cm, d = 0.3175 cm); (a) amplitude and (b) relative phase.

branch at about a 45° angle. As an example of the results, let us examine twig C at an orientation angle of $\theta = -45°$, with its needles oriented below the branch at an angle of $\theta = 0°$. The measured scattering matrix for this configuration was

$$[S] = e^{j\phi_{hh}} \begin{bmatrix} 0.0178 & 0.00902\, e^{j158.4°} \\ 0.0156\, e^{j157.3°} & 0.0220\, e^{-j1.95°} \end{bmatrix}. \quad (27)$$

The difference between the amplitudes of S_{hv} and S_{vh} is within the measurement precision for a signal-to-background ratio of 9.1 dB [13], where we have taken the background to be $\sigma = -50$ dBm^2 and the target level to be σ_{hv}. Notice also that the vv and hh returns from the twig are essentially in phase, but the cross-polarized hv and vh returns are shifted in phase to approximately 160° relative to the co-polarized return.

Once the scattering matrix of the target is known, the scattering cross section can be synthesized for any combination of transmit and receive polarization. In general, an elliptically polarized wave can be defined in terms of two angles, ψ and χ, as shown in Fig. 9. The angle ψ is the orientation angle of the ellipse, and the angle χ is the ellipticity. Notice that $\psi = 90° - \theta$. The normalized cross section can now be displayed as a function of polarization in a plot called the polarization signature that was intro-

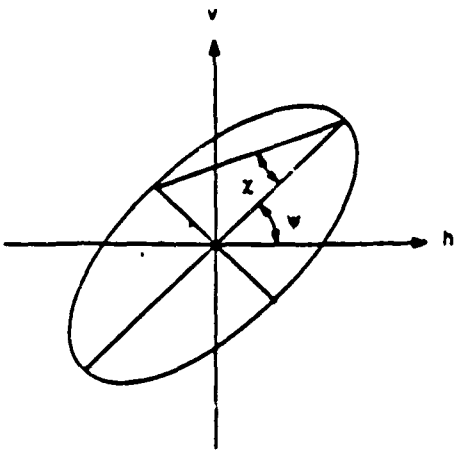

Fig. 9. Polarization ellipse.

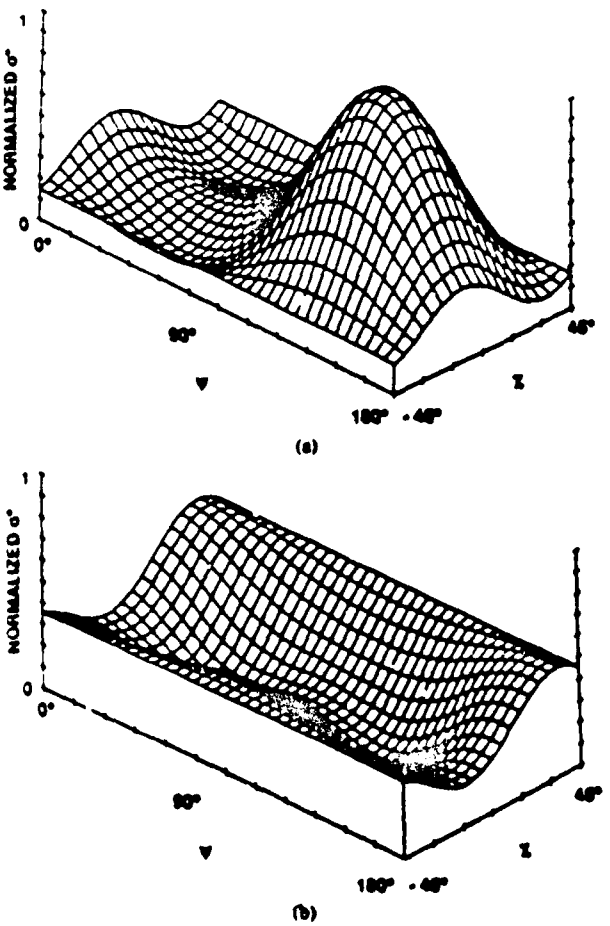

Fig. 10. Polarization signature for twig C at an orientation angle of $\psi = 135°$ ($\theta = -45°$). (a) co-polarized signature and (b) cross-polarized signature.

duced by Zebker *et al.* [6] and van Zyl *et al.* [7]. The co-polarized and cross-polarized signatures for twig C, based on the scattering matrix given in (27), are shown in Fig. 10. Linear polarizations are located on the line $\chi = 0°$, with vv polarization at $\psi = 90°$ and hh polarization at $\psi = 0°, 180°$. Right- and left-handed circular polarizations are located along the lines $\chi = -45°$ and $\chi = 45°$, respectively. For twig C, we see that the co-polarized signature has a maximum at $\psi = 130°$ ($\theta = -40°$) indicating that the backscatter from the branch is dominating the return from the needles.

VII. Measurement Results for Distributed Targets

In the second phase of this study, we examined scattering from distributed targets. For distributed surfaces, we can define the differential scattering matrix $[S^0]$ as

$$[S^0] = e^{i\phi_{hh}} \begin{Bmatrix} \sqrt{\sigma^0_{hh}} & \sqrt{\sigma^0_{hv}}\, e^{i(\phi_{hv}-\phi_{hh})} \\ \sqrt{\sigma^0_{vh}}\, e^{i(\phi_{vh}-\phi_{hh})} & \sqrt{\sigma^0_{vv}}\, e^{i(\phi_{vv}-\phi_{hh})} \end{Bmatrix} \quad (28)$$

where σ^0_{rt} is the differential scattering coefficient of the surface for rt polarization. For the configuration previously shown in Fig. 3, the received power for rt polarization is given by

$$P_{rt} = \frac{P_t G_{0r} G_{0t} \lambda^2}{(4\pi)^3} \iint_A \frac{1}{R^4} g_r(\theta_r) g_t(\theta_t) \sigma^0_{rt}\, dA \quad (29)$$

where P_t is the transmit power, G_{0r} and G_{0t} are the gains of the receive and transmit antennas along their respective boresight directions, $g_r(\theta_r)$ and $g_t(\theta_t)$ are the normalized gains of the receive and transmit antennas as a function of the angles θ_r and θ_t relative to boresight, R is the range to a given point on the surface, and A is the area of illumination. The transmit and receive antennas had circular beams, both with a half-power beamwidth of 3.4°, allowing σ^0_{rt} to be treated as constant over such a narrow angular range. With this assumption, (29) can be written as

$$P_{rt} = \left[\frac{P_t G_{0r} G_{0t} \lambda^2}{(4\pi)^3}\right] \sigma^0_{rt} I(h, \theta_0) \quad (30)$$

where $I(h, \theta_0)$ is the illumination integral

$$I(h, \theta_0) = \iint_A \frac{1}{R^4} g_r(\theta_r) g_t(\theta_t)\, dA \quad (31)$$

at antenna height h and incidence angle θ_0. The quantity inside the square bracket in (30) is determined from the conducting cylinder calibration described in Section III, and the illumination integral is computed from knowledge of the antenna patterns and the illumination geometry. Hence, σ^0_{rt} can be determined from the measured power P_{rt}. The relative phases $\phi_{hv} - \phi_{hh}$, $\phi_{vh} - \phi_{hh}$, and $\phi_{vv} - \phi_{hh}$ are measured directly by referencing the phase of the respective signal to ϕ_{hh}.

The differential scattering matrix $[S^0]$ was measured for three surfaces: a rock surface, a visually smooth sand surface, and a visually rough sand surface, all at an incidence angle of 64° relative to normal incidence. The range to the center of the illuminated cell was 4.2 m, which is slightly shorter than the 5.4-m far-field distance for the antenna. The illuminated cell was approximately 5° cm

long in the range direction and 25 cm wide in the azimuth direction. The platform used for containing the target material (sand and rocks) consisted of a square wooden box 1.7 m on a side. Prior to conducting the measurements, the radar was positioned directly above the box at a height of 4 m. The backscattered signal at normal incidence was then measured for a layer of sand as a function of layer depth. This test was conducted to determine the penetration depth of the sand medium, and thus establish the depth necessary for the target to appear semi-infinite at 35 GHz. The penetration depth of dry sand was found to be around 7.5 cm. For the measurements reported in this study, the box was filled with the sand or rock material to a depth of 10 cm, which insures that the backscatter contribution from the base of the box is at least 30 dB lower than that from the target surface. The target platform was placed on a rotatable positioner, which allowed the acquisition of data from spatially independent footprints by rotating the platform in discrete steps over a full circle. A total of 100 spatially independent samples were taken for each surface target. Fig. 11 shows the three surfaces with the target platform that was used.

The distributions of σ^0 for the rock surface at *hh*, *hv*, and *vv* polarizations are shown in Fig. 12, and the phase distributions of *hv* and *vv* relative to *hh* are shown in Fig. 13. For all targets and polarizations, the standard deviation-to-mean ratio of σ^0 was about 1, which is as expected for Rayleigh fading. This means that the standard deviation associated with the mean values of the distributions given in Fig. 12 is ± 0.4 dB. The mean value of σ^0_{vv} was 0.5 dB higher than the mean value of σ^0_{hh} and 7.7 dB higher than the mean value of σ^0_{hv}. The distribution of $\phi_{hv} - \phi_{hh}$ was approximately uniform between $-180°$ and $180°$ while the distribution of $\phi_{vv} - \phi_{hh}$ was gaussian-like with a mean value of $8.48°$ and a standard deviation of $65.5°$.

The σ^0 results obtained for the smooth sand surface and the rough sand surface were significantly lower in level than those for the rocks, and the differences $\sigma^0_{vv} - \sigma^0_{hh}$ and $\sigma^0_{vv} - \sigma^0_{hv}$ were larger than those for rocks (see Table I). However, the shapes of the σ^0 and relative phase distributions were very similar. The distributions of $\phi_{vv} - \phi_{hh}$ for the three surfaces differ only with respect to their mean values, which are shown in Table II. For the rough sand surface, the mean of the distribution for $\phi_{vv} - \phi_{hh}$ was $-30.31°$ (see Fig. 14), which is a significant shift from $0°$ based on the standard error $\sigma/\sqrt{N} = 7°$ for the three surfaces. For all three distributed targets, the distribution of $\phi_{hv} - \phi_{hh}$ was approximately uniform between $-180°$ and $180°$, and the standard deviation was between $106°$ and $110°$. For a uniform phase distribution, the calculated standard deviation is $104°$.

Fig. 15 shows the co-polarized and cross-polarized signatures for the rocks, rough sand, and smooth sand surfaces. These signatures were obtained by converting each of the 100 scattering matrix samples to a Stokes matrix (or Stokes scattering operator), and then computing the average Stokes matrix representing the target. For the rock surface, the co-polarized signature shown in Fig. 15(a)

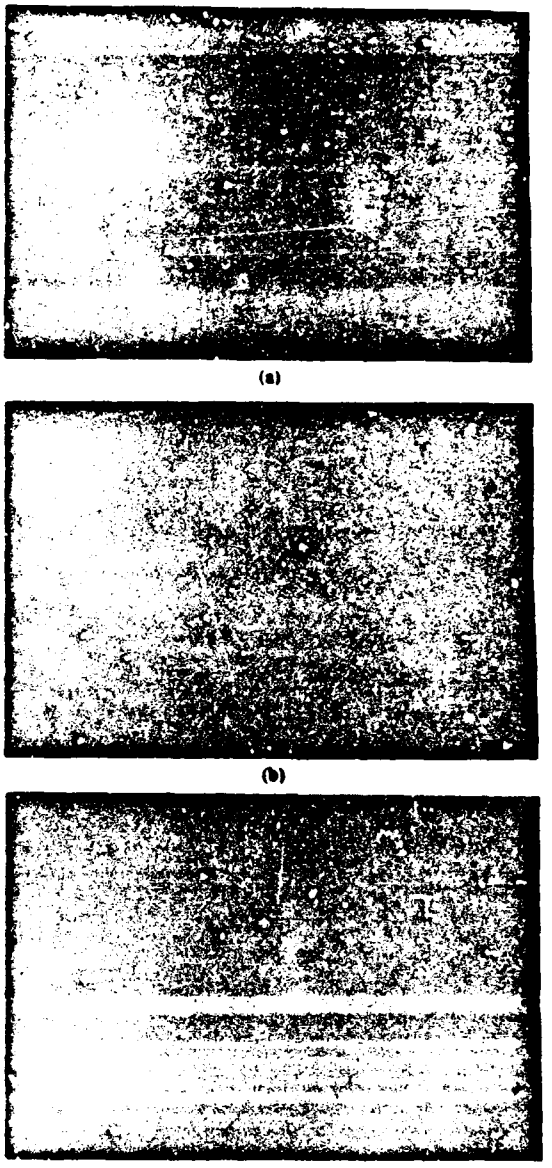

Fig. 11. Surfaces measured using the distributed surface measurement configuration: (a) rocks, (b) rough sand, and (c) smooth sand

has a maximum at the linear polarizations ($\chi = 0°$) with σ^0_{vv} only 0.4 dB higher than σ^0_{hh} as predicted by the mean values in Table I. The minimum in the co-polarized signature occurs at the circular polarizations ($\chi = \pm 45°$). The cross-polarized signature in Fig. 15(b) has a minimum at the linear polarizations and a maximum at circular. This type of polarization signature is characteristic of specular reflection from a smooth dielectric surface at normal incidence [7]. The rock surface is not smooth, but the scattering is dominated by specular reflection from smooth facets where the local surface normal is oriented toward the radar.

The smooth sand surface and the rough sand surface

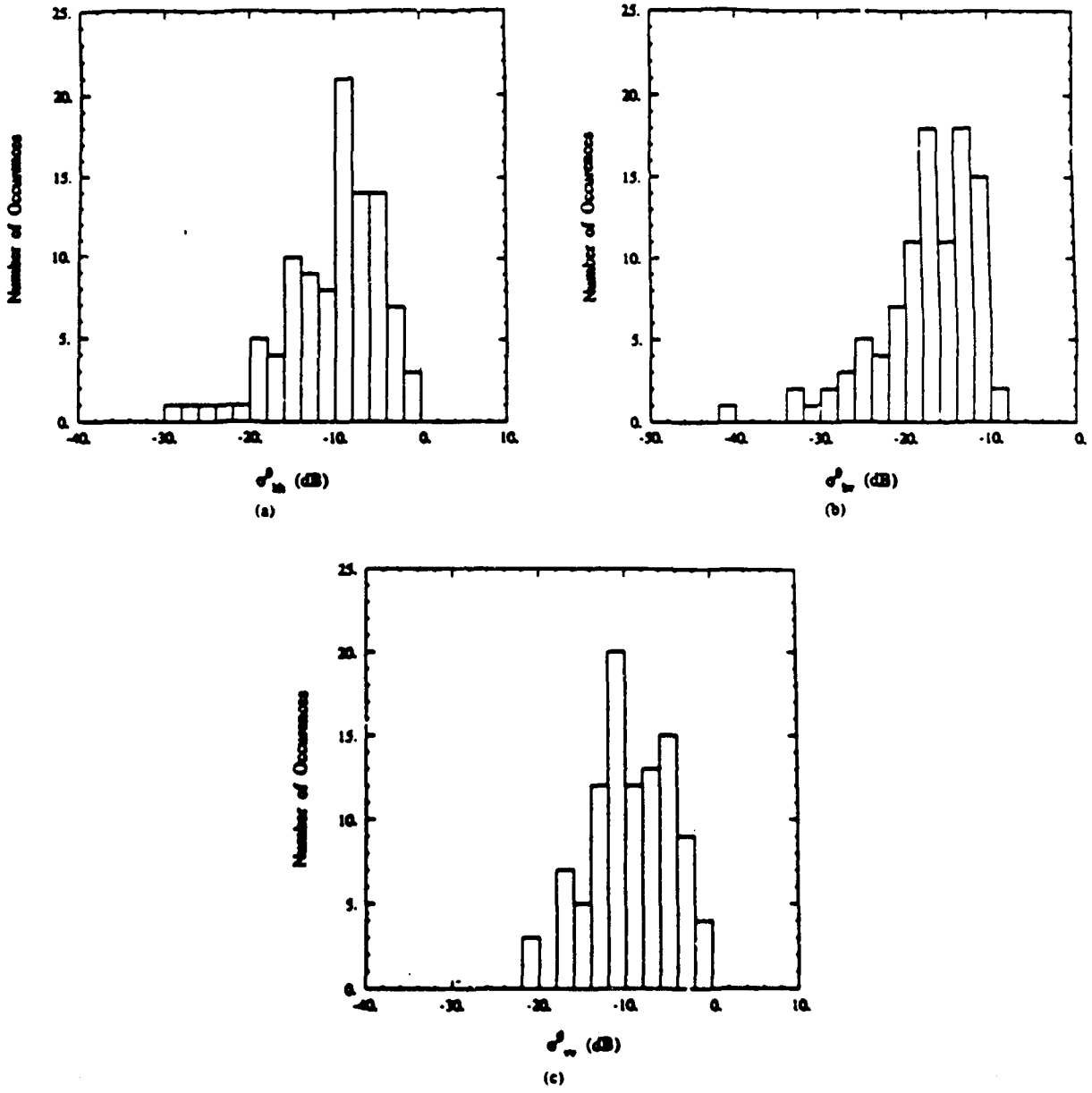

Fig. 12. Distributions for σ^0 for the rock surface: (a) σ^0_{hh}, (b) σ^0_{hv}, and (c) σ^0_{vv}.

have polarization signatures similar to the rock surface. For both sand surfaces, however, the normalized co-polarized σ^0 is maximum at vv polarization. Since the polarization signature is an average power representation of the target, the difference between vv and hh is equal to the difference in the mean values as given in Table II. In contrast to the rock surface, the minima (maxima) for the co-polarized (cross-polarized) signature are at elliptical polarizations instead of circular. Notice that the maximum (minimum) σ^0 for each value of ψ in the co-polarized (cross-polarized) signature does not follow the $\chi = 0°$ line as with the rock surface. In fact, when the ellipticity χ for maximum σ^0 is plotted as a function of the orientation angle ψ as in Fig. 16, we find that even the rock surface exhibits this effect to a small degree. This curvature in the polarization signature arises at least in part from the mean phase shift between S_{vv} and S_{hh}.

The polarization signatures for all three surfaces show the presence of an unpolarized component of the scattered field in the form of a pedestal (nonzero minimum level), which is approximately the same for all surfaces. The pedestal can arise from various effects, including multiple scattering, which is probably a significant mechanism at 35 GHz for all three surfaces measured.

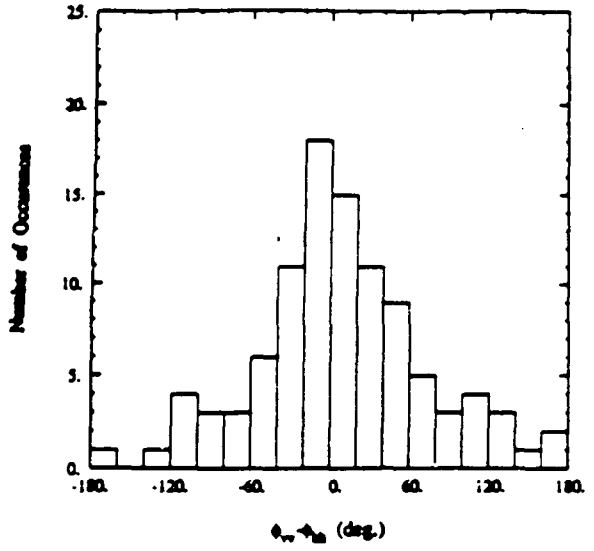

(a)

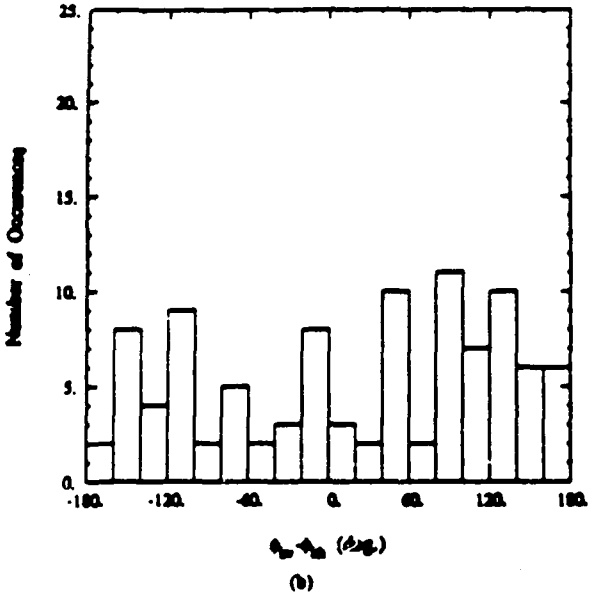

(b)

Fig. 13. Distributions of relative phase for the rock surface: (a) $\phi_{vv} - \phi_{hh}$ and (b) $\phi_{hv} - \phi_{hh}$.

TABLE I
MEAN VALUES OF σ^0_{pq} IN DECIBELS FOR THE THREE SURFACES MEASURED

Surface	σ^0_{hh}	σ^0_{vv}	σ^0_{hv}
Rocks	-7.5	-14.6	-7.1
Smooth Sand	-13.2	-22.3	-12.6
Rough Sand	-13.1	-20.4	-12.1

VIII. Conclusions

The results presented in this paper satisfy the first phase of a two-phase experiment. The ability of the MMP to measure the complete scattering matrix of both distributed and point scatterers has been demonstrated. The amplitude and phase measurement precisions were found to be 0.5 dB and 2.5°, respectively, over the range of cylinders measured. The noise level of the system corresponds to a radar cross section on the order of -40 dBm^2 for co-polarized signals and -50 dBm^2 for cross-polarized signals. These levels are realized by the ability of the network analyzer to subtract out the effects of the target mount. It is estimated that with a more carefully developed technique to mount small targets, the noise level can be improved by at least 10 dB. At the same time a new mounting technique will also improve the precision of amplitude and phase measurements on asymmetric targets such as cylinders where the orientation is critical.

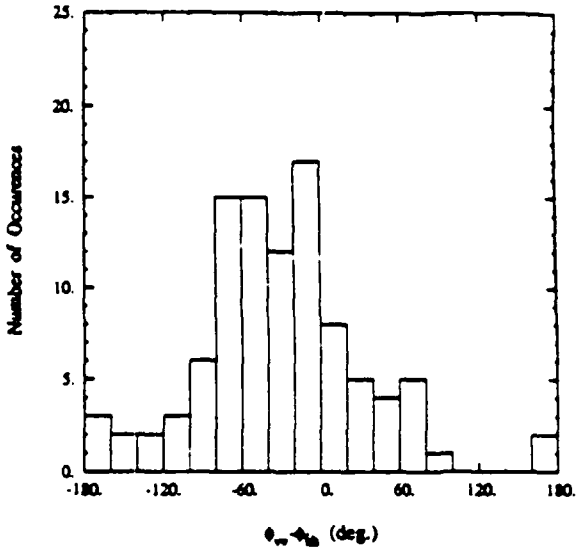

Fig. 14. Distribution of $\phi_{vv} - \phi_{hh}$ for the rough sand surface.

TABLE II
$\phi_{vv} - \phi_{hh}$ FOR THE THREE SURFACES MEASURED

Surface		Mean (°)	Std. Dev. (°)
Rocks	vv	8.48	65.5
	hv	18.72	106.2
Smooth Sand	vv	-11.13	69.1
	hv	16.31	108.7
Rough Sand	vv	-30.31	62.6
	hv	8.15	110.4

The second phase of the project involves measuring the scattering matrix of natural targets. Preliminary results on a series of twigs and three surfaces were shown in this paper. These results demonstrated the ability of the MMP to measure the complete scattering matrix for distributed targets. Now that the performance of the system has been demonstrated, measurements will be conducted to determine the polarimetric scattering behavior for a variety of

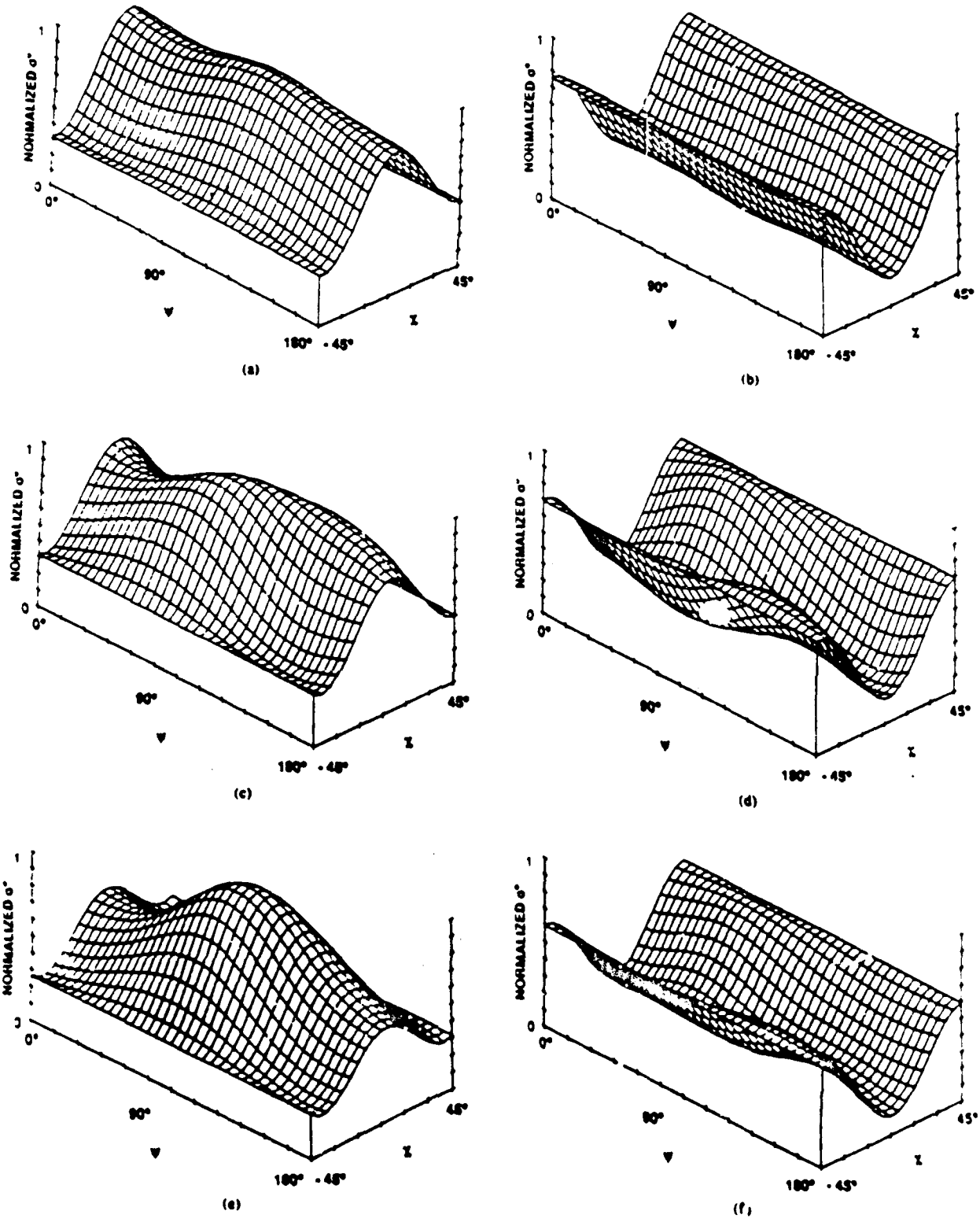

Fig. 15. Polarization signatures for the three surfaces measured: (a) co-polarized signature for rocks, (b) cross-polarized signature for rocks, (c) co-polarized signature for rough sand, (d) cross-polarized signature for rough sand, (e) co-polarized signature for smooth sand, and (f) cross-polarized signature for smooth sand.

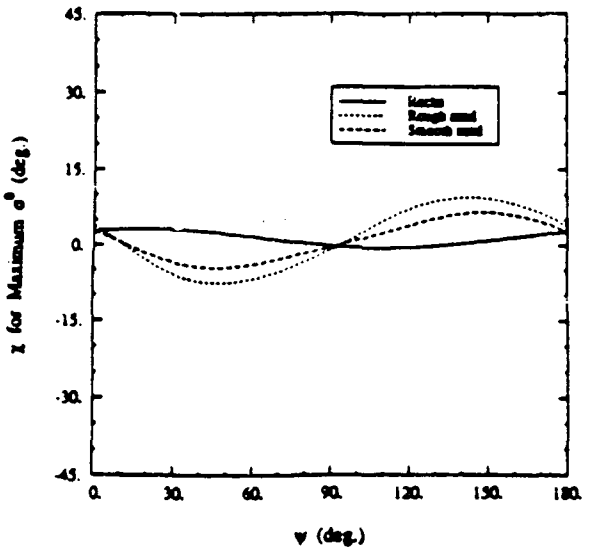

Fig. 16. Ellipticity χ for maximum σ^0 as a function of the orientation angle ψ.

natural targets including soil and rock surfaces and vegetation canopies.

The technique for making polarimetric measurements described in this paper can be used at any frequency, provided the proper RF equipment is available. This would require a change in the transmitter and receiver sections, but all other aspects of the method would remain the same. Moreover, the technique can be used to measure the polarimetric scattering properties of distributed targets under natural conditions using truck-mounted platforms. In fact, such measurements have been made for bare ground, grass, and tree canopies, and the results will be reported in a forthcoming paper.

References

[1] G. Sinclair, "The transmission and reception of elliptically polarized waves," *Proc. IRE*, vol. [illegible], pp. 148-[illegible], Feb. 1950.

[2] E. M. Kennaugh, "Effects of the type of polarization on echo characteristics," Rep. 389-9, Antenna Lab., Ohio State Univ., Columbus, 1951.

[3] G. A. Deschamps, "Part II—Geometrical representation of the polarization of a plane electromagnetic wave," *Proc. IRE*, vol. 39, pp. 540-544, May 1951.

[4] J. R. Huynen, "Measurement of the target scattering matrix," *Proc. IEEE*, vol. 53, pp. 936-946, 1965.

[5] D. Guili, "Polarization diversity in radars," *Proc. IEEE*, vol. 74, no. 2, pp. 245-269, Feb. 1986.

[6] H. A. Zebker, J. J. van Zyl, and D. N. Held, "Imaging radar polarimetry from wave synthesis," *J. Geophys. Res.*, vol. 92, no. B1, pp. 683-701, Jan. 1987.

[7] J. J. van Zyl, H. A. Zebker, and C. Elachi, "Imaging radar polarization signatures: Theory and observation," *Radio Sci.*, vol. 22, no. 4, pp. 529-543, July-Aug. 1987.

[8] M. W. Whitt, F. T. Ulaby, and T. F. Haddock, "The development of a millimeter-wave network analyzer based scatterometer," Rep. 022872-1-T, Radiation Lab., Univ. Michigan, Ann Arbor, Jan. 1987.

[9] F. T. Ulaby, T. F. Haddock, J. East, and M. W. Whitt, "A millimeter-wave network analyzer based scatterometer," *IEEE Trans. Geosci. Remote Sensing*, vol. 26, no. 1, pp. 75-81, Jan. 1988.

[10] "Radar cross-section measurements with the HP 8510 network analyzer," HP product note 8510-2, Apr. 1985.

[11] G. T. Ruck, D. E. Barrick, W. D. Stuart, and C. K. Krichbaum, *Radar Cross Section Handbook*, vol. I. New York: Plenum, 1970.

[12] H. Mott, *Polarization in Antennas and Radar*. New York: Wiley Interscience, 1986.

[13] F. T. Ulaby, R. K. Moore, and A. K. Fung, *Microwave Remote Sensing: Active and Passive*, vol. I. Reading, MA: Addison-Wesley, 1981, pp. 768-770.

[14] J. R. Huynen, "Phenomenological theory of radar targets," Ph.D. dissertation, Drukkerij Bronder-Offset, N.V., Rotterdam, 1970.

[15] M. W. Whitt and F. T. Ulaby, "Millimeter-wave polarimetric measurements of artifical and natural targets," in *Proc. IGARSS Symp.* (Ann Arbor, MI), pp. 537-543, 1987.

Michael W. Whitt (S'83) was born in St. Charles, MO, on December 3, 1962. He received the B.S. degree in electrical engineering from the University of Arkansas, Fayetteville, in 1985 and the M.S. degree in electrical engineering from the University of Michigan, Ann Arbor, in 1986. Since September 1985, he has been a Graduate Research Assistant at the University of Michigan Radiation Laboratory, where he is currently working toward the Ph.D. degree.

His research interests include millimeter-wave radar, radar polarimetry, and polarimetric scattering from terrain and vegetation canopies.

Fawwaz T. Ulaby (M'68-SM'74-F'80) was born in Damascus, Syria, on February 4, 1943. He received the B.S. degree in physics from the American University of Beirut, Lebanon, in 1964 and the M.S.E.E. and Ph.D. degrees in electrical engineering from the University of Texas, Austin, in 1966 and 1968, respectively.

From 1968 to 1984, he was with the Electrical Engineering Department at the University of Kansas, Lawrence, where he was the J. L. Constant Distinguished Professor, and the University of Kansas Center for Research, where he was Director of the Remote Sensing Laboratory. He is currently with the Radiation Laboratory and the Department of Electrical and Computer Engineering, University of Michigan, Ann Arbor. His current research interests involve microwave propagation and active and passive microwave remote sensing. Along with R. K. Moore and A. K. Fung, he is a coauthor of the three-volume series *Microwave Remote Sensing: Active and Passive* (Reading, MA: Addison-Wesley). In addition, he is coeditor of the *Manual of Remote Sensing*, 2nd ed., vol. I, American Society of Photogrammetry.

Dr. Ulaby is a member of Eta Kappa Nu, Tau Beta Pi, and Sigma Xi. He has been named the Executive Editor for IEEE TRANSACTIONS ON GEOSCIENCE AND REMOTE SENSING, 1984-1988, and was the Geoscience and Remote Sensing Society's Distinguished Lecturer for 1987. He was named an IEEE Fellow in 1980 "for contributions to the application of radar to remote sensing for agriculture and hydrology," received the GRS Society's Outstanding Service Award in 1982, and its Distinguished Service Award in 1983. In 1984, he also received a Presidential Citation for Meritorious service from the American Service of Photogrammetry. He received the University of Kansas Chancellor's Award for Excellence in Teaching in 1980, the University of Kansas Gould Award for "distinguished service to higher education" in 1973, and the Eta Kappa Nu MacDonald Award as an "outstanding electrical engineering professor in the United States of America" in 1975.

Submitted for publication in IEEE Transactions on Geoscience and Remote Sensing.

140-GHz SCATTEROMETER SYSTEM AND MEASUREMENTS OF TERRAIN

T. F. Haddock and F. T. Ulaby
Radiation Laboratory
University of Michigan
Ann Arbor, MI
USA

Abstract - **The goal of the University of Michigan millimeter-wave radar program is to characterize terrain scattering at 35, 94 and 140 GHz. The 140-GHz channel of a truck-mounted scatterometer system has recently been added to give the full desired operating capability. Two injection-locked 45.33-GHz Gunn oscillators use triplers to supply the up- and down-converters. Full polarization capability is obtained through the use of rotatable quarter-wave plates. Real-time signal processing and data reduction takes place in an HP 8510A automatic network analyzer on the truck-mounted platform. Sample measurements of millimeter-wave radar backscattering from vegetation and snow are given.**

I. INTRODUCTION

Millimeter-wave systems offer the inherent advantages of high resolution, large bandwidth and small antenna size. In recent years significant advances have been realized in the development of millimeter-wave components for the construction and operation of imaging airborne radar systems at the atmospheric window frequencies of 35, 94, 140, and 215 GHz. Hence, there is much interest in measuring terrain scattering at these frequencies, and in the associated development of theoretical and empirical scattering models. While recent work has been carried out at millimeter-wavelengths on trees [1] and snow [2, 3], such data is still sparce, particularly at 140 GHz.

The University of Michigan 140-GHz scatterometer system is the latest addition to the network-analyzer based millimeter-wave scatterometer system, a truck-mounted full-polarization scatterometer that has been developed in support of a program to characterize radar scattering from

terrain at 35, 94, and 140 GHz. Basic operation of the scatterometer system has been described in detail elsewhere [4, 5]. Conversion from a swept 2 to 4 GHz intermediate frequency (IF) to the millimeter-wave RF frequencies is made in the front-end, allowing flexible real-time signal processing by the remotely-located HP 8510A automatic network analyzer. An outline of the system is given in Fig. 1. An HP 8350B sweep oscillator is swept from 2 to 4 GHz by the HP 8510A network analyzer. After a portion of this IF signal is taken off and fed to the a_1 reference port of the HP 8511 frequency converter, it is up-converted within the 140-GHz radar and transmitted to the target. The returned signal is down-converted to the 2 to 4 GHz range and fed to the b_1 port of the frequency converter. Signal processing of the return and reference signals takes place within the network analyzer, and is sent on the HPIB bus to the HP 9920S computer where final data reduction takes place, and the results are printed out and saved on disk. The HP 8510 computer-control system allows vector error correction of system imperfections through its calibration algorithms. The system has previously operated in this mode at 35 and 94 GHz, and the 140-GHz channel is its latest extension in frequency capability.

II. 140-GHZ SCATTEROMETER DESIGN

A block diagram of the 140-GHz front-end is shown in Fig. 2. The transmit portion across the top and the receive portion across the bottom are driven by a common local oscillator (LO) chain. The LO consists of a 45.33 GHz free-running Gunn oscillator, two circulator-coupled 45.33 GHz injection-locked Gunn oscillators acting as amplifiers and two third-harmonic frequency multipliers. This combination provides a nominal output power of 10 dBm from each multiplier to power the up- and down-converters. Other combinations of fundamental oscillators, amplifiers or frequency multipliers are possible. This particular combination provided the best combination of performance and cost. Wave polarization is controlled by a fixed quarter-wave plate followed by a rotatable quarter-wave plate. A 90-degree rotation of the movable wave-plate moves the electric field vector through 90 degrees to give either vertical or horizontal polarization. The polarized signal is transmitted though a conical standard-gain horn with a half-power beamwidth of

11.8 degrees. The received RF signal passes though a 3.0 inch diameter lens-corrected horn antenna with a half-power beamwidth of 2.2 degrees. Hence the antennas' product pattern is essentially controlled by the receive-antenna pattern, resulting in an effective beamwidth of 2.1 degrees. Receive polarization is determined by movable and fixed quarter-wave plates, in the same manner as the transmit section. The RF signal is down-converted using a tripled 45.33 GHz LO. Since the conversion processes must be phase-coherent, the up- and down-converter LOs are each injection-locked from a central dual-ended Gunn oscillator running at 45.33 GHz. This arrangement gives a phase-coherent LO of sufficient power to supply both up- and down-converters.

III. CALIBRATION AND PERFORMANCE

For each data set, measurement of a sphere of known size and range is used to generate the 401 VV and HH calibration constants for each of the 401 frequencies in the 2 to 4 GHz IF band. A calibration target with known cross-polarization response is used for VH and HV calibration. For an incident signal consisting of either pure vertical (or pure horizontal) polarization, a return signal oriented at 45 degrees to vertical is generated by a calibrator consisting of a rectangular standard-gain horn followed by a 38.1 cm long section of WR6 waveguide with a short on the end. This calibrator is placed in the far-field of the 140-GHz radar, and pointed toward the radar with the rectangular aperture of the horn oriented at 45 degrees to horizontal. While a portion of the incident radiation is reflected from the horn, another portion passes from the horn into the waveguide and propagates in the TE_{10} mode with the electric field in line with the short axis of the waveguide, which is oriented at 45 degrees to the horizontal. This signal, comprised of equal amplitude vertical and horizontal components, is reflected by the short, and returns to the radar. It can be distinguished from the return from the horn aperture by its longer time delay. The waveguide and short are encased in a metal cylinder to prevent return from the outside of the guide and flange at the range of the short. Figure 3 illustrates the VV, HH, VH and HV responses of the cross-polarization calibration target. While the return from the horn is complex, the return from the short

gives a known cross-polarization response. At the range of the horn in Fig. 3 the like- and cross-polarized responses differ by approximately 5 dB. At the range of the short, where for a perfect radar all four responses would be the same, all returns fall within a +/- 1 dB range (within experimental uncertainties). Measurement of this signal is used to generate the 401 cross-polarization calibration constants.

Sphere calibration is made on a daily basis, but the standard-gain horn cross-polarization calibration is more cumbersome and is made less frequently. Cross-polarization isolation of the system is typically about 15 dB, and this is checked at each use of the system by making cross-polarization measurements of the sphere. For most natural targets, the cross-polarized return at 140 GHz is only 3 to 6 dB below the like-polarized return. Hence the cross-polarization isolation of the system is quite adequate at 140 GHz. Noise performance of the system is checked after each calibration by making measurements of the sky at typical target ranges. Table I lists the measured system performance parameters.

TABLE I

Parameters of Truck-Mounted 140-GHz Scatterometer

RF Frequencies:	138 to 140 GHz
Transmit power:	-4 dBm
RF Bandwidth:	0 to 2.0 GHz
Sweep Rate:	1 ms/freq., 51, 101, 201, 401 freq./sweep
Polarization:	VV, VH, HV HH
Product-Gain Beamwidth:	2.1 degrees
Incidence Angles:	0 to 70 degrees
Platform Height:	2.7 meters minimum, to 18 meters maximum
Noise Equivalent σ^0:	~ -20 dB
Stability:	~ 0.2 dB/hour
Measurement Repeatability:	~ 1 dB

Near Field Distance:	2.7 m
Footprint:	min.: 0.013 m^2 max.: 16.8 m^2
Signal Processing:	HP 8510A/8511A based
Output Products:	received power verses range ($\Delta R = c/2B$) received power verses frequency (at fixed R)

Figure 4 illustrates the combined effects of stability and repeatability of calibration of the 140-GHz system over a diurnal cycle. Repeatability of sphere measurements due to pointing only is typically within $\pm$ 0.5 dB. Variations are the cumulative result of system gain variations and sphere pointing errors. Installation of a controlled heater on the triple LO unit was required to achieve the excellent system stability observed in Fig. 4 (+/- 0.8 dB).

For most terrain measurements, a data set consists of measurements of the backscattering coefficient σ^o as a function of incidence angle for VV, HH, and VH (or HV) polarizations. The incidence angle is set by an elevation positioner located at the top of the truck-mounted boom. The target is scanned in azimuth to obtain spatially independent samples. For each polarization configuration the number of independent samples, including bandwidth averaging, is at least 50, which corresponds to a measurement precision of about +/- 0.66 dB [6]. Data is tabulated as it is recorded and examined in real time.

IV. SAMPLE RESULTS

Several types of terrain surfaces and covers were observed by the 140-GHz scatterometer in 1988 and 1989. Sample results are shown next for grasses, trees and snow.

A. Backscatter from Grasses

The backscatter plots shown in Figs. 5 and 6 correspond to a field of Amaranthus Retroflexus, a spiny weed about 50 centimeters tall, commonly known as Pigweed, over ground

cover of Stellaria Media, a low ground-hugging weed, commonly known as Chick Weed. Figure 5 shows the 140-GHz backscatter response as a function of incidence angle (measured relative to normal incidence) for VV, HH, and HV. Throughout this paper the "receive-transmit" convention is used. As expected for such a medium, volume scattering effects predominate and the VV and HH returns are comparable to one another at all incidence angles. The cross-polarized return is approximately 6 dB lower than the like-polarized returns.

Figure 6 shows the HH backscatter response from the same target at all three of the scatterometer operating frequencies: 35, 94, and 140 GHz. The target shows a weak sensitivity to frequency, exhibiting a maximum spread of 5 dB between the three curves.

B. Backscatter from Trees

Figure 7 shows 140 GHz measurements of the backscattering coefficient, plotted as a function of incidence angle, for a uniform tree canopy of Thuja Occidentalis, commonly known as Arbor Vitae. The trees were approximately 10m in height and the average water content of the needles was measured to be 56.3%. The like-polarization components (HH and VV) are essentially identical in level and exhibit an approximately cos θ dependence between 20° and 70°. The HV component, on the other hand, increases with increasing incidence angle and its level approaches those of the like-polarization components at 70°.

In a separate investigation, the backscattering coefficient at 35 GHz was observed as a function of time over a two-week period for a canopy of deciduous trees (Bur Oaks). The observation period covered the autumn senescence stage during which the moisture content of the trees decreased. The temporal response of the backscattering coefficient (Fig. 8) exhibited a 3-dB change in level between October 2 and October 4 as the leaves underwent a rapid change is moisture content.

C. Backscatter from snow

In February and March of 1989, the University of Michigan millimeter-wave system was used to measure the backscatter from snow at a site near Ann Arbor, Michigan. Figures 9 and 10 illustrate the angular variation of σ^o for wet and dry snow. Figure 9 shows the response of dry, metamorphosed snow with a crystal size of approximately 2.2 millimeters, and Fig. 10 corresponds to fresh, wet, unmetamorphosed snow, with crystal size of approximately 1.0 millimeter and a gravimetric water content of approximately 1.9 %.

While the angular dependence of the two plots is similar, there is a 4 to 5 dB level shift between the like-polarized responses of the dry and wet snow targets. At these frequencies snow is predominantly a volume-scattering medium, and the presence of liquid water in the snow medium leads to increased attenuation and decreased albedo. For the dry snow, the cross-polarized response is lower than the like-polarized response by about 4 dB, while for the wet snow the difference in level is about 6 dB.

Figure 11 shows 140 GHz backscatter measurements made at an incidence angle of 40 degrees as a function of time over a 12-hour interval extending from noon to midnight on February 27, 1989. The liquid water content measured with a freezing calorimeter for the top 5-cm snow layer and the air temperature are also shown. The backscattering coefficient is observed to exhibit a 3-dB change in level at around 14:30 in response to the decrease in temperature and liquid water content. At 140 GHz, the penetration depth is on the order of 1 cm, particularly when the snow is wet. As the air temperature drops below 0 C, the snow layer starts to freeze from the top surface downward. Hence, although the liquid water content of the top 5-cm layer may still be greater than zero, the radar responds only to the top 1-2 cm layer and therefore exhibits a time response that leads the temporal variation exhibited by the measured liquid water content. This dependance on penetration depth is illustrated further by the data in Fig. 12 which was measured by the 35-GHz channel. Because of the greater penetration depth, the 35-GHz system exhibits a much more gradual change in level between 14:00 hours and 24:00 hours. Also, the magnitude of the change is level is 12 dB at 35 GHz, compared to only 3 dB at 140 GHz. At 94 GHz, the measured diurnal

pattern (not shown) exhibited a response similar to the 35 GHz data, but with a total change in level of 8 dB. This observed decrease in sensitivity (of the backscattering coefficient to liquid rate content) with increasing frequency is in agreement with earlier observations reported at 35 GHz and lower frequencies [7,8].

VI. CONCLUSIONS

This paper describes the operation of a 140-GHz scatterometer system with a measured accuracy of 1 dB. Sample measurements of terrain backscatter at 35, 94, and 140 GHz are shown for grasses, trees, and snow. In all cases, the angular dependence is approximately as cos θ. The two like-polarized components (HH and VV) exhibit essentially identical levels, and the cross-polarized response is anywhere from 1 dB to 6 dB below the like-polarized responses, depending on target type. At 140 GHz, the backscatter from snow exhibits a dynamic range of about 3 dB, in response to change in liquid water content.

This work was supported by ARO contract DAAG 29-85-K-0220.

REFERENCES

[1] Narayanan, R. M., Borel, C. C., and McIntosh, R. E., "Radar Backscatter Characteristics of Trees at 215 GHz," pp. 217-228, IEEE Trans Geo. and Rem. Sens., Vol. 26, No. 3, May 1988.

[2] Baars, E. P., and Essen, H., "Millimeter-Wave Backscatter Measurements on Snow-Covered Terrain," pp. 282-299, IEEE Trans Geo. and Rem. Sens., Vol. 26, No. 3, May 1988.

[3] Williams, L. D., Gallagher, J. G., Sugden, D. E., and Birnie, R. V., "Surface Snow Properties Effects on Millimeter-Wave Backscatter," pp. 300-306, IEEE Trans Geo. and Rem. Sens., Vol. 26, No. 3, May 1988.

[4] Ulaby, F. T., Haddock, T. F., East, J. R., and Whitt, M. W., "A Millimeterwave Network Analyzer Based Scatterometer," pp. 75-81, IEEE Trans Geo. and Rem. Sens., Vol. 26, No. 1, January 1988.

[5] Whitt, M. W., and Ulaby, F. T., "Millimeter-Wave Polarimetric Measurements of Artificial and Natural Targets," pp. 562-573, IEEE Trans Geo. and Rem. Sens., Vol. 26, No. 5, September 1988.

[6] Ulaby, F. T., Haddock, T. F., and Austin, R. T., "Fluctuation Statistics of Millimeter-Wave Scattering From Distributed Targets," pp. 268-281, IEEE Trans Geo. and Rem. Sens., Vol. 26, No. 3, May 1988.

[7] Stiles, W. H., and Ulaby, F. T., "The Active and Passive Microwave Response to Snow Parameters: Part 1 - Wetness," pp. 1037-1044, J. Geophys Res., Vol. 85, No. C2, February 1980.

[8] Ulaby, F. T., and Stiles, W. H., "The Active and Passive Microwave Response to Snow Parameters: Part 2 - Water Equivalent of Dry Snow," pp. 1045-1049, J. Geophys Res., Vol. 85, No. C2, February 1980.

FIGURES

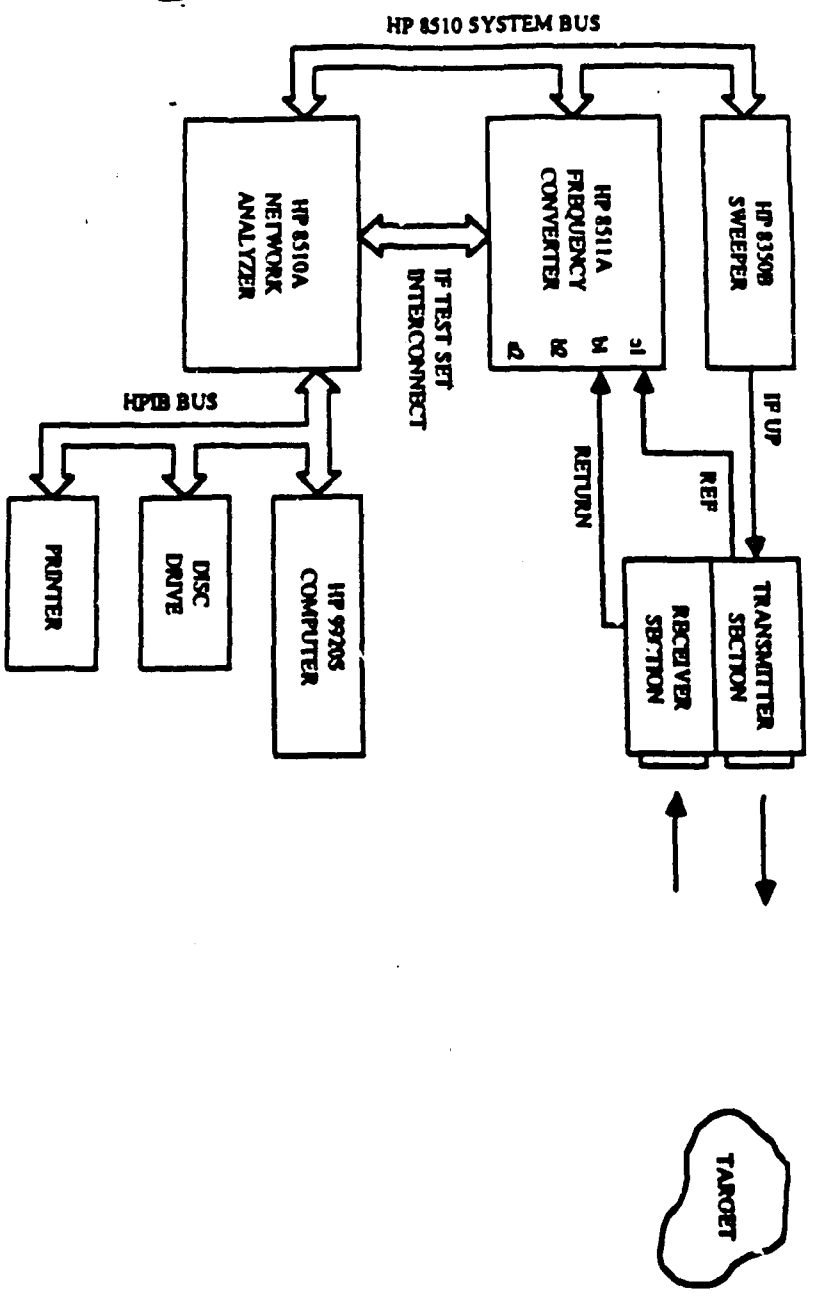

Fig. 1 Block diagram of millimeter-wave scatterometer system.

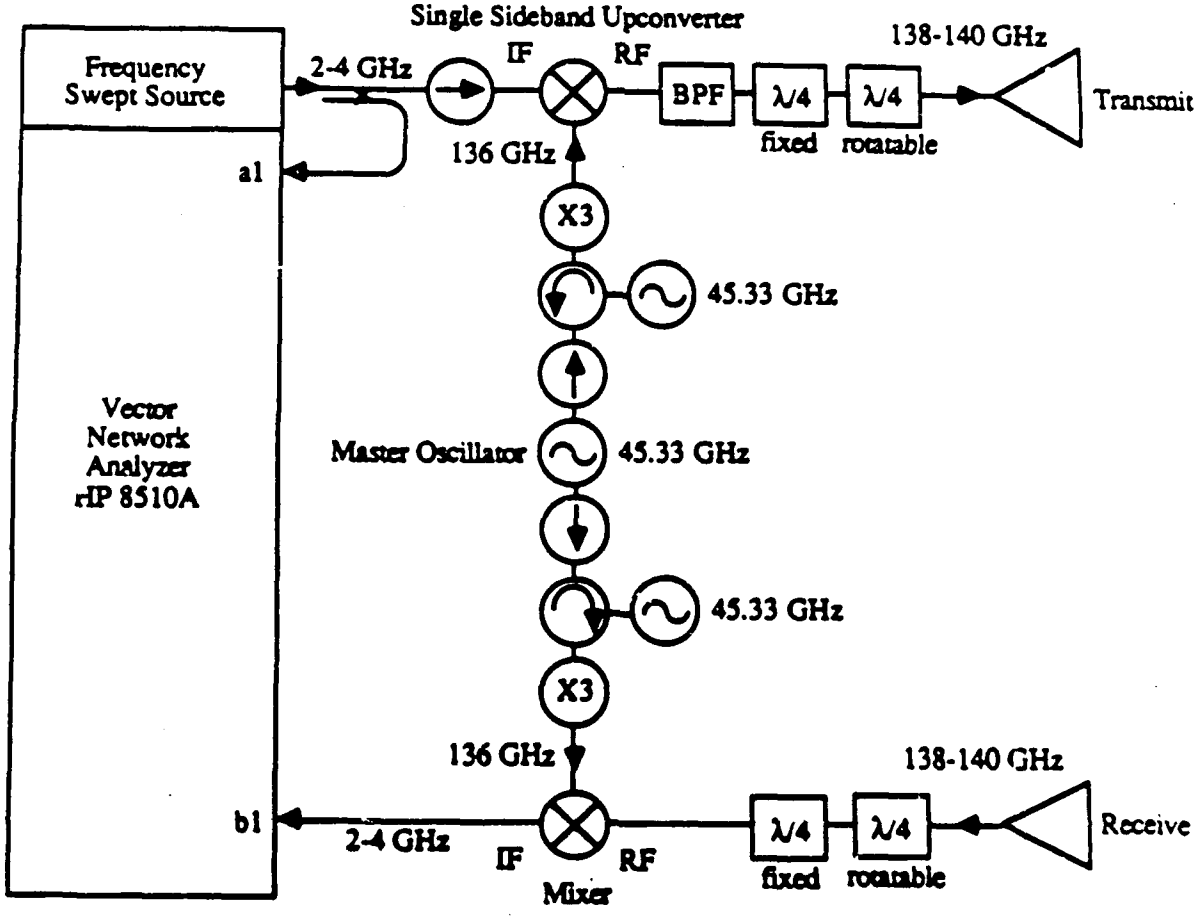

Fig. 2 Block diagram of 140-GHz scatterometer front-end.

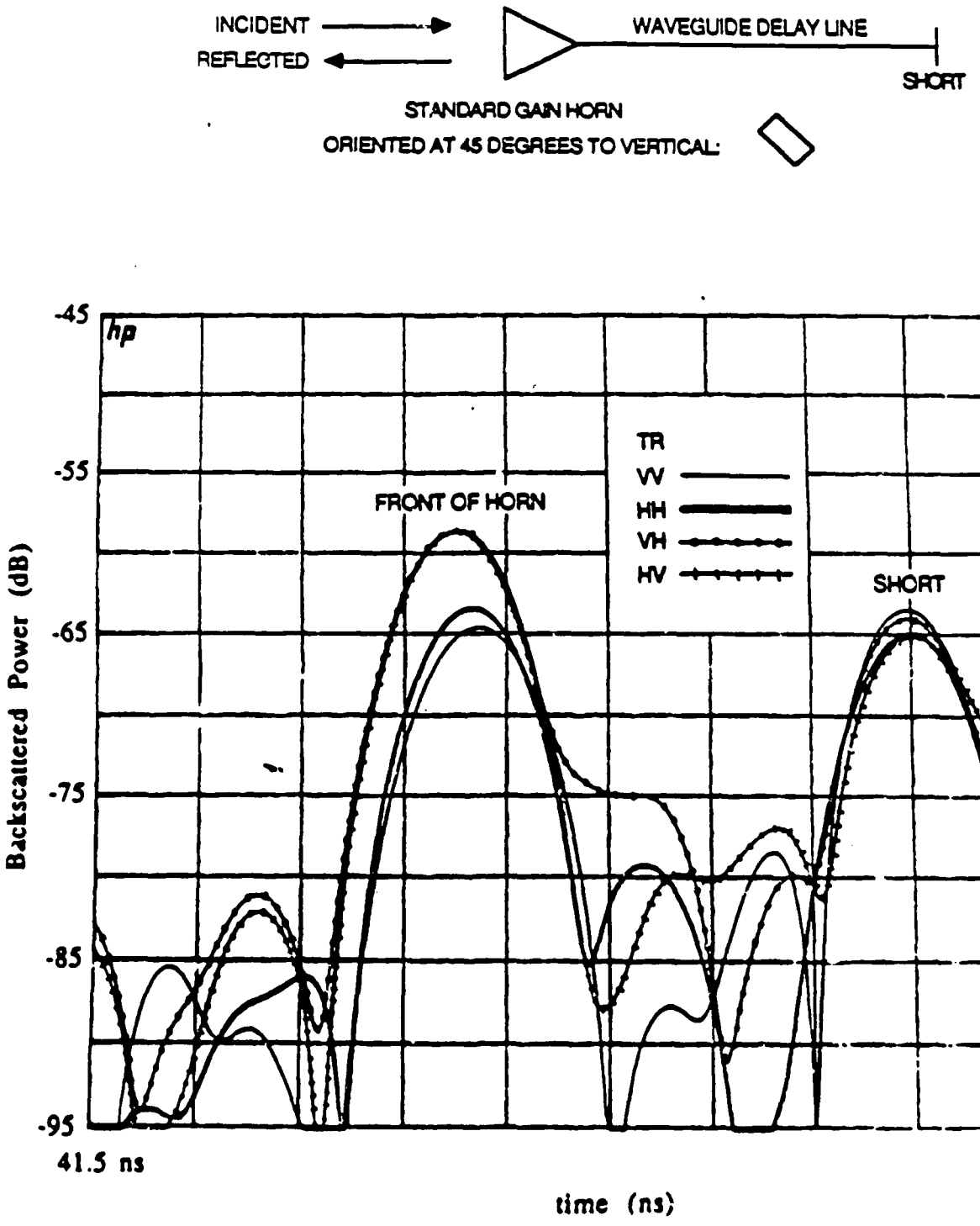

Fig. 3 Measured backscatter response of 140-GHz system when observing a horn antenna connected to a short through a 38.1-cm long waveguide section.

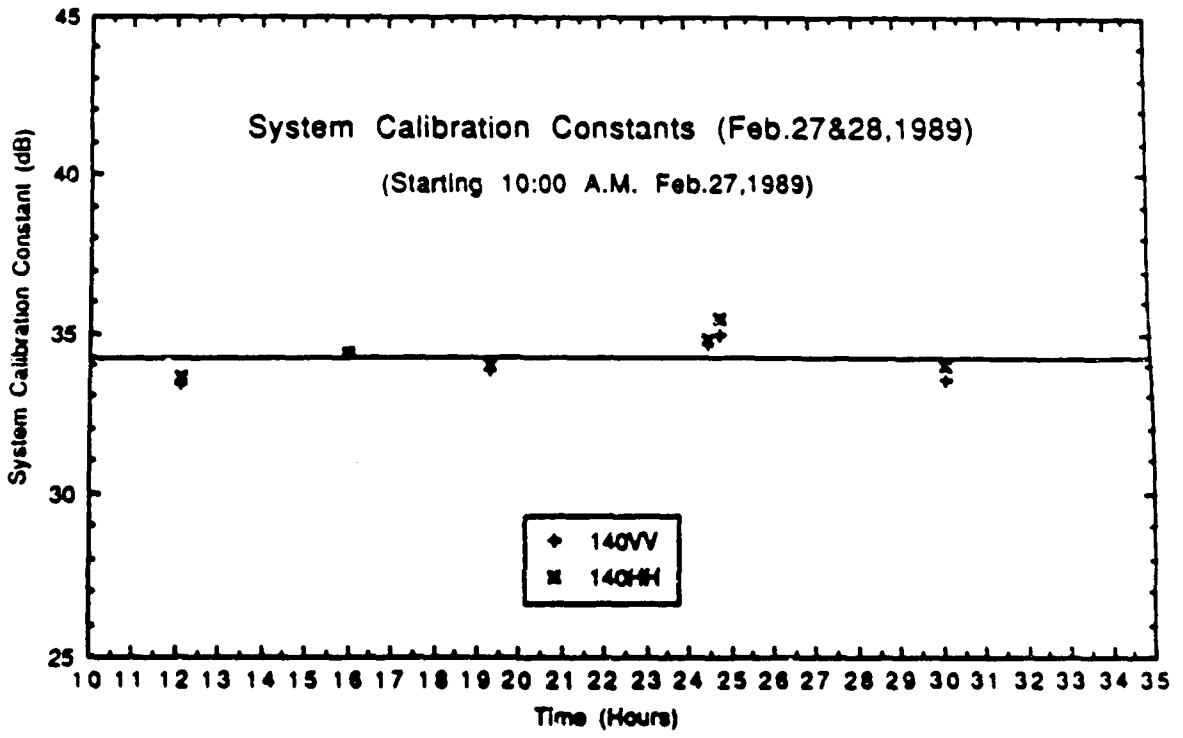

Fig. 4 System calibration was established by measuring system calibration constant over a diurnal cycle.

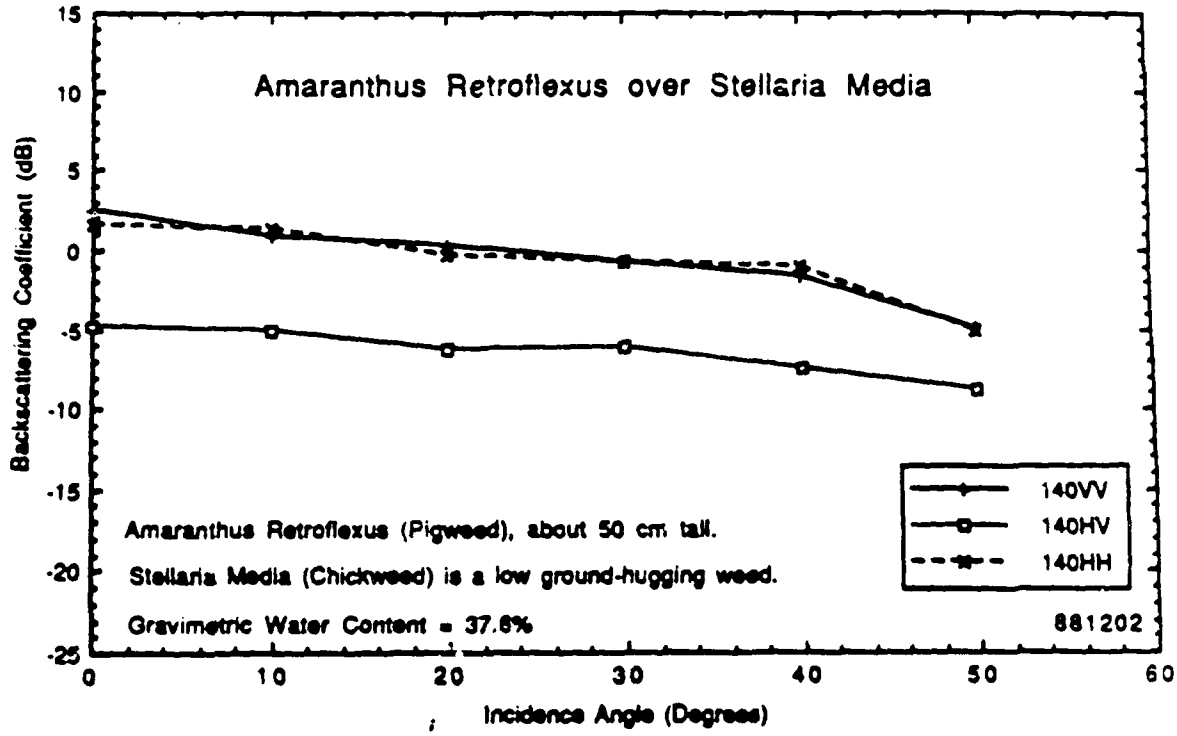

Fig. 5 Measured backscatter angular response of pigweed grass at 140 GHz.

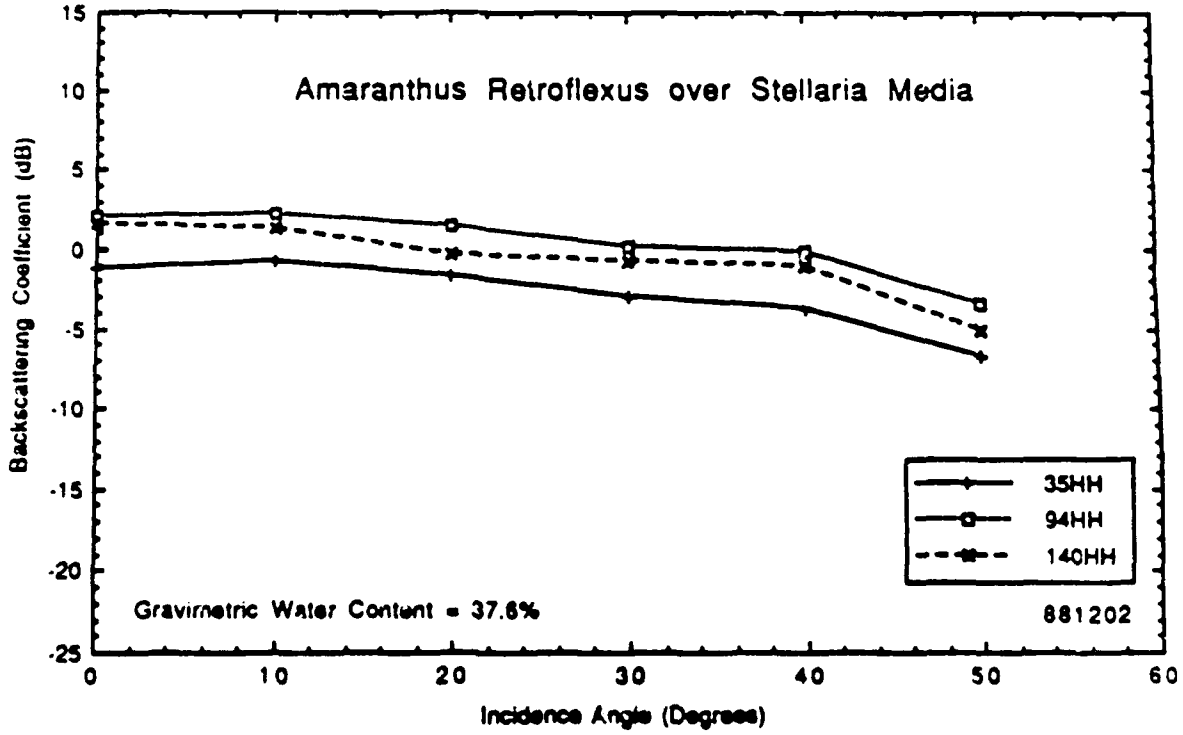

Fig. 6 Measured angular response of pigweed grass at 35, 94, and 140 GHz for HH polarization.

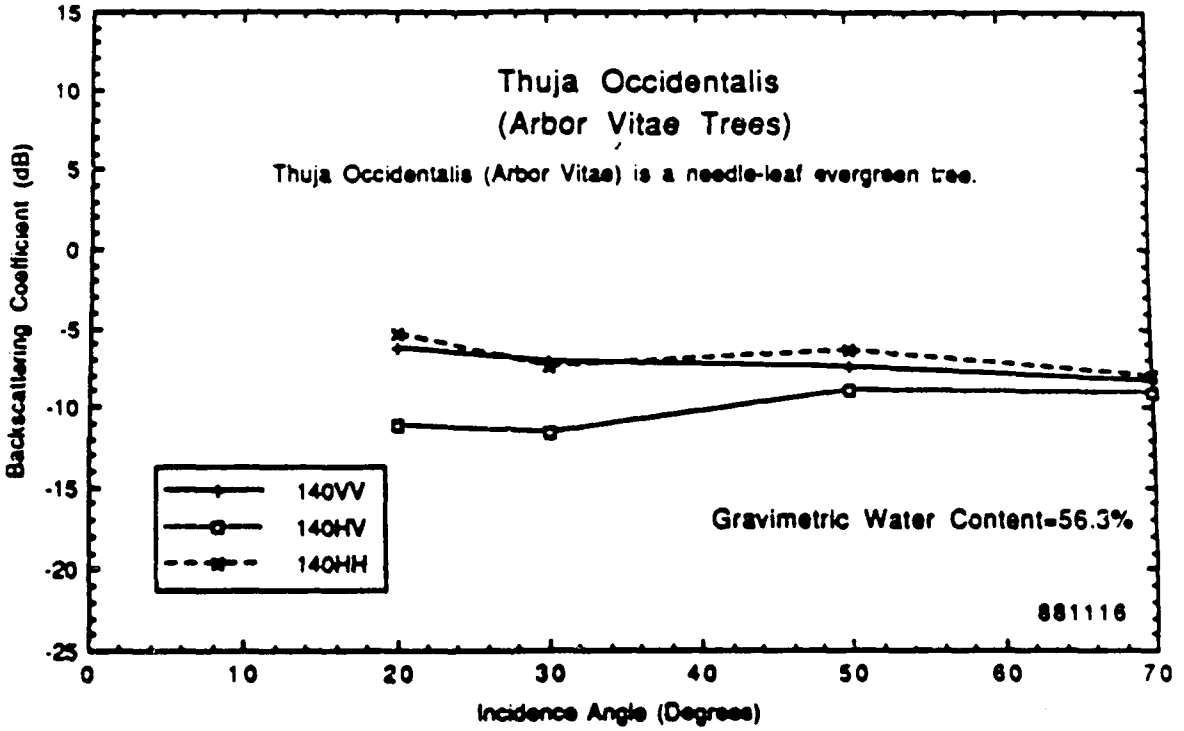

Fig. 7 Measured angular response of Arbor Vitae trees at 140 GHz

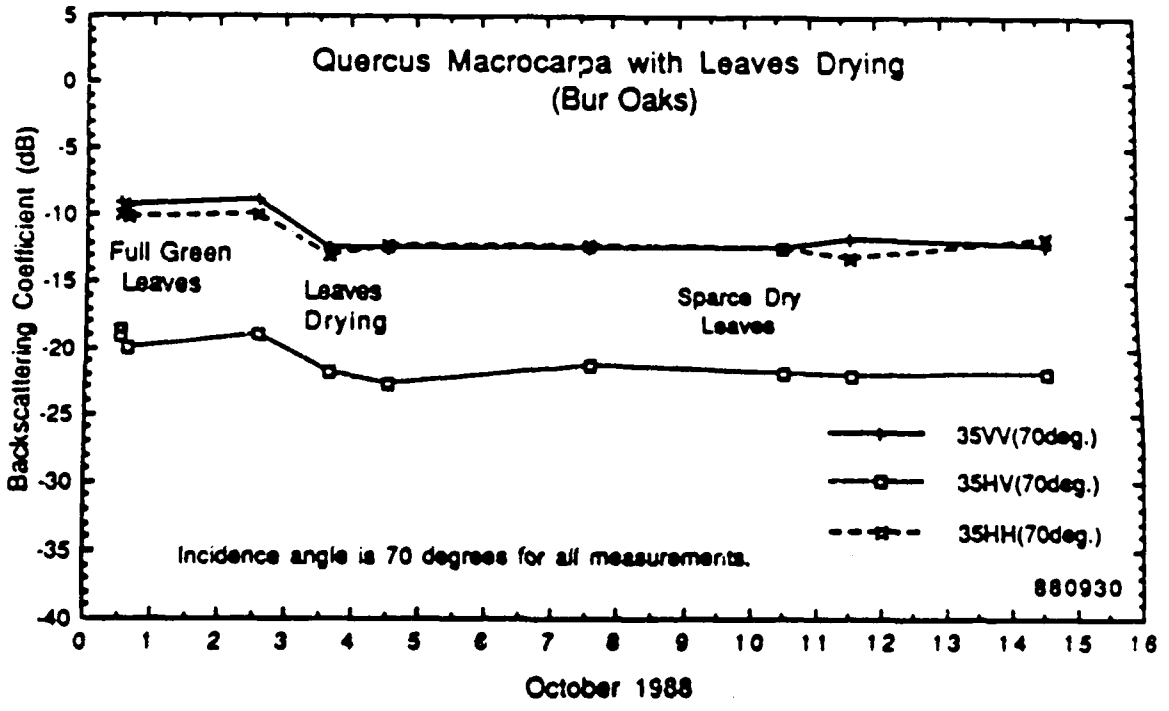

Fig. 8 Two-week temporal response of the 35-GHz backscatter from Bur Oak trees at 70 degrees.

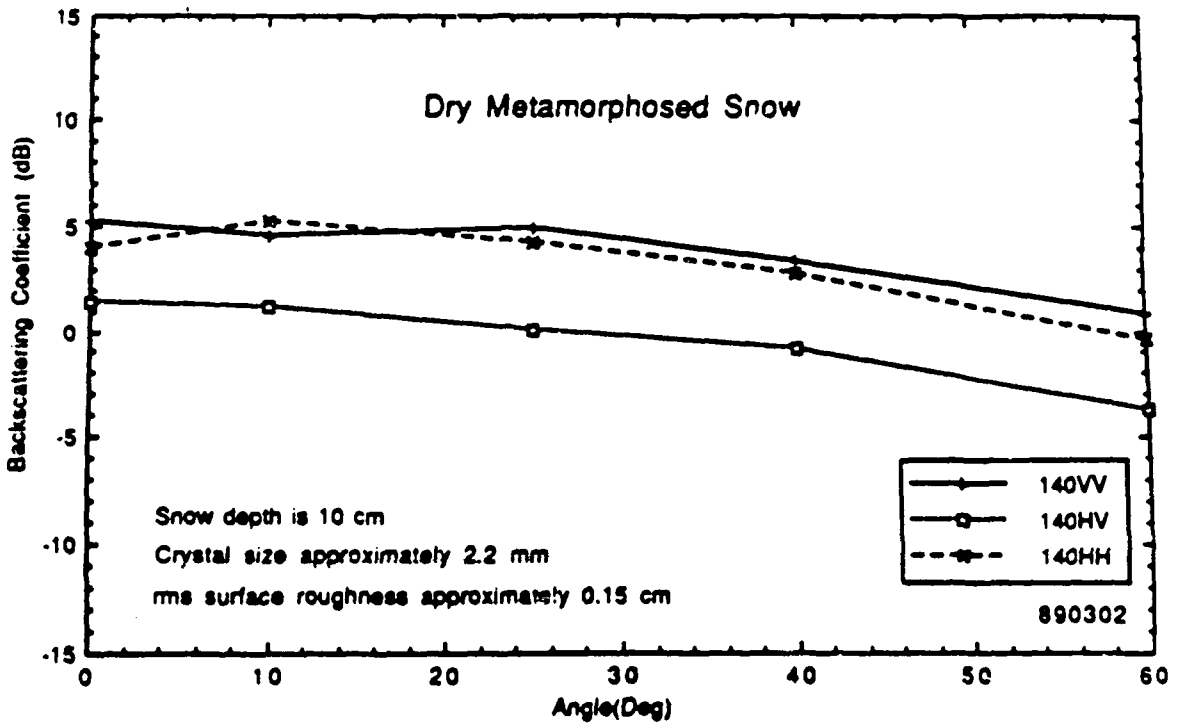

Fig. 9 Angular response of the backscatter from dry metamorphosed snow at 140 GHz.

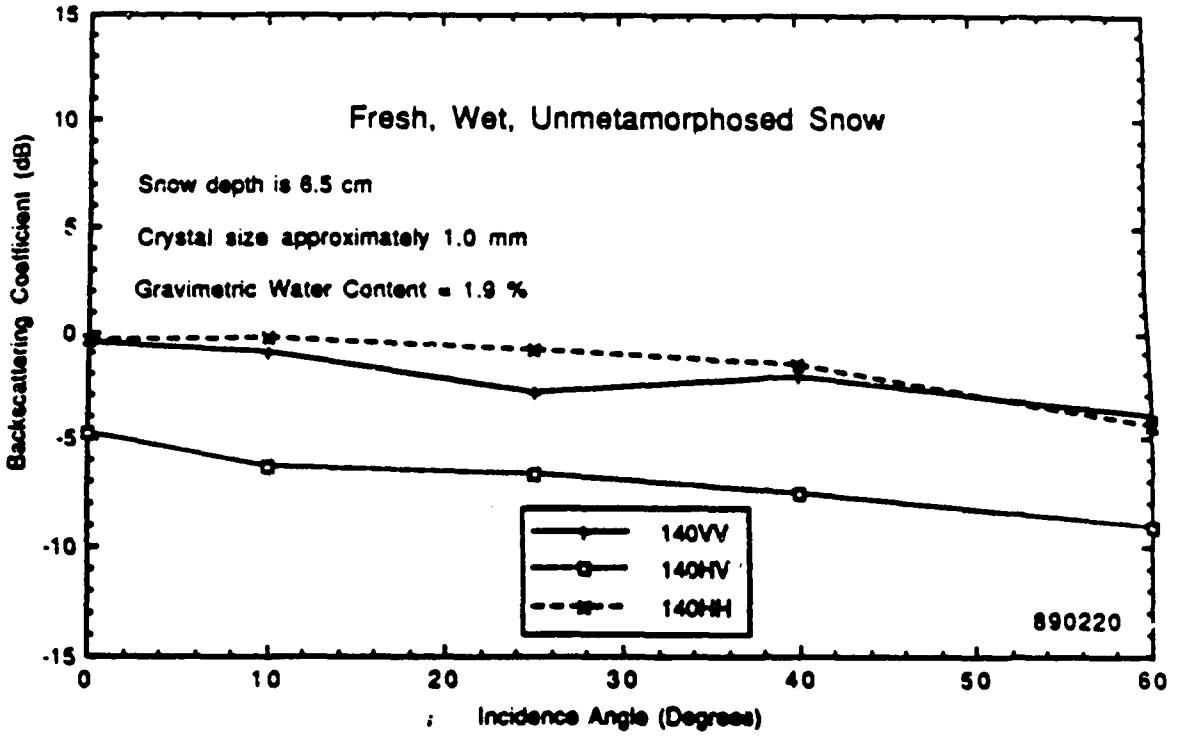

Fig. 10 Angular response of the backscatter from fresh, wet unmetamorphosed snow at 140 GHz.

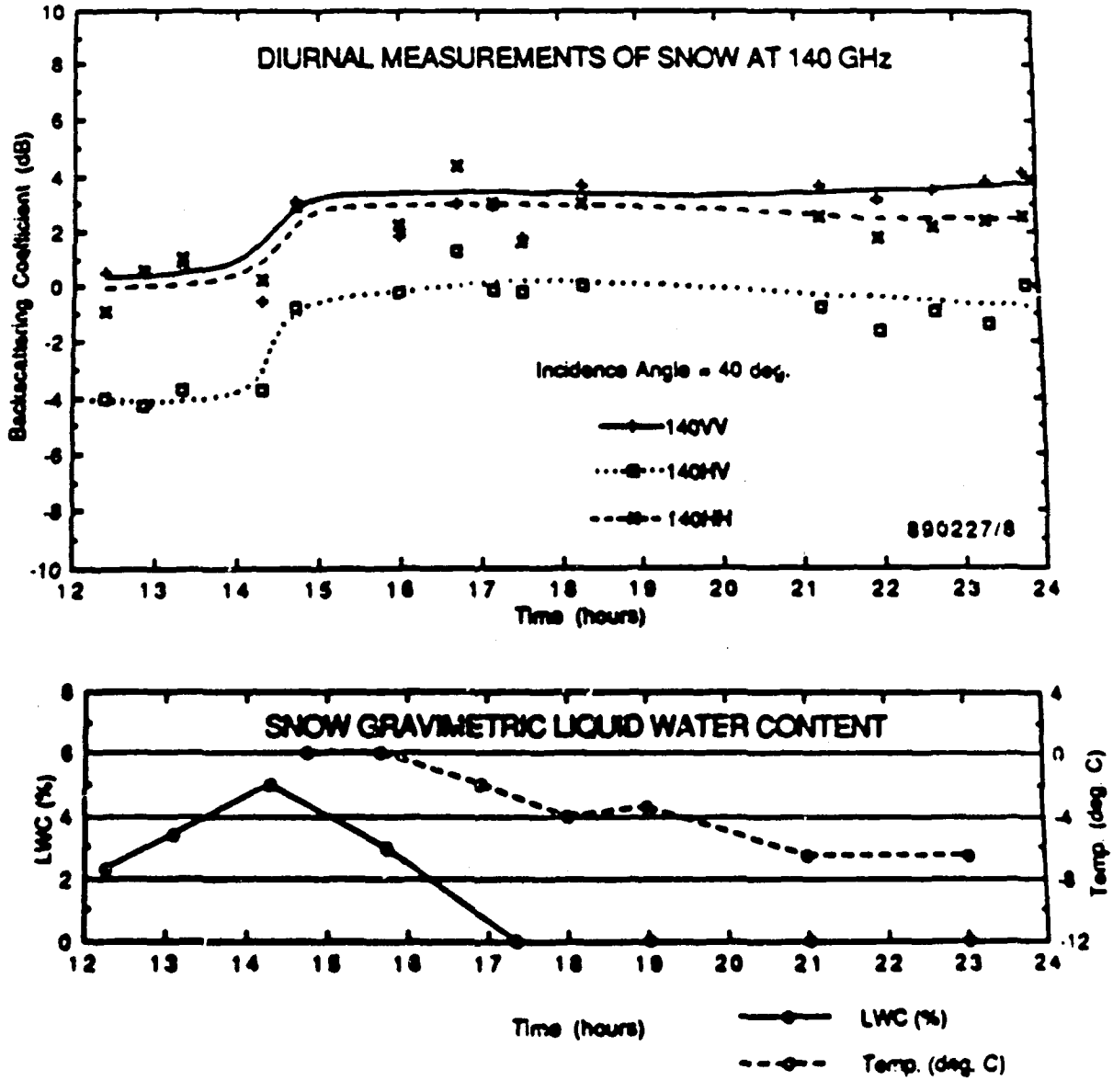

Fig. 11 Measured temporal variation of the 140-GHz radar backscatter, air temperature, and snow liquid water content (of the top 5-cm layer).

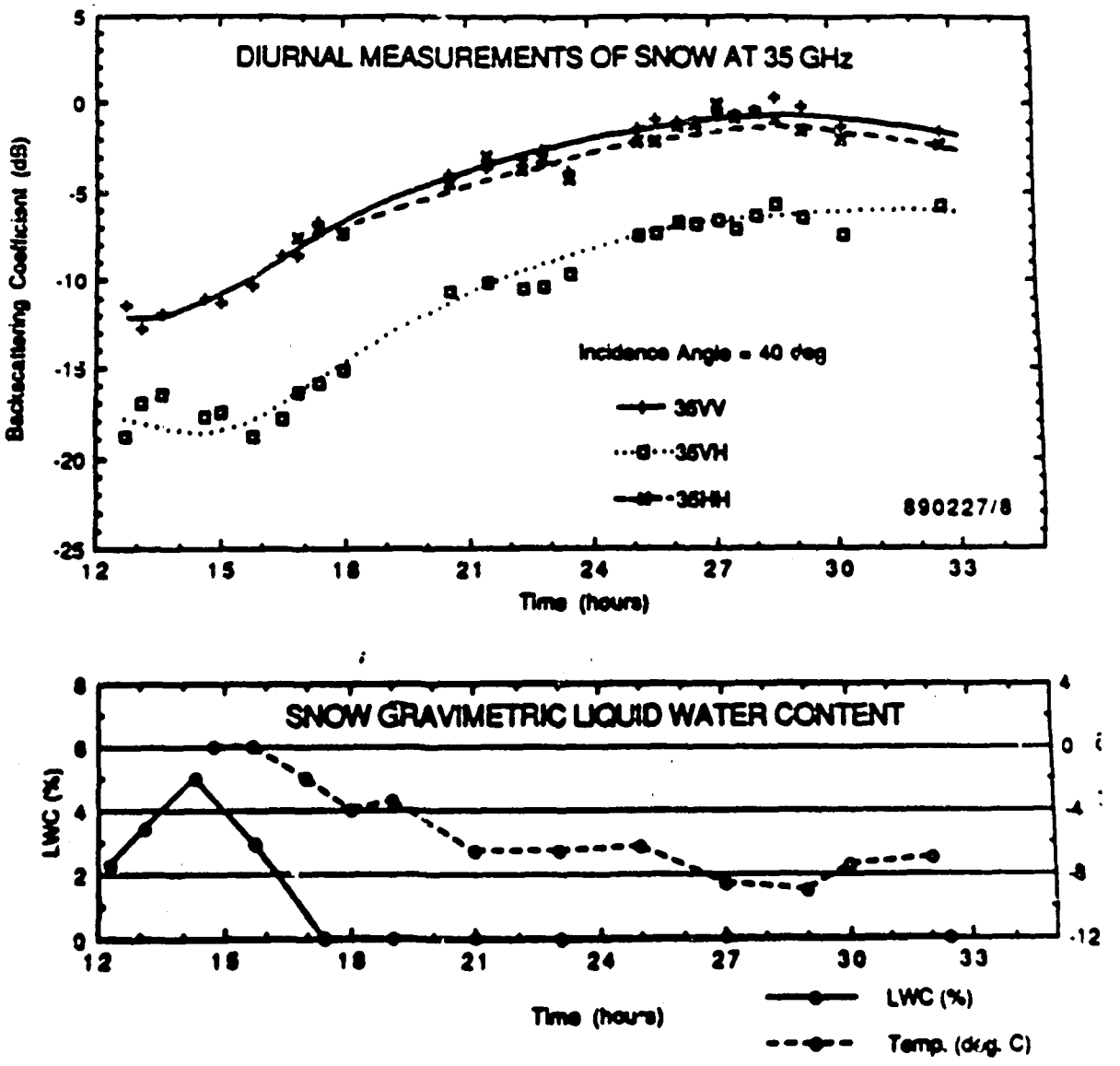

Fig. 12 Measured temporal variation of the 35-GHz radar backscatter, air temperature, and snow liquid water content (of the top 5-cm layer).

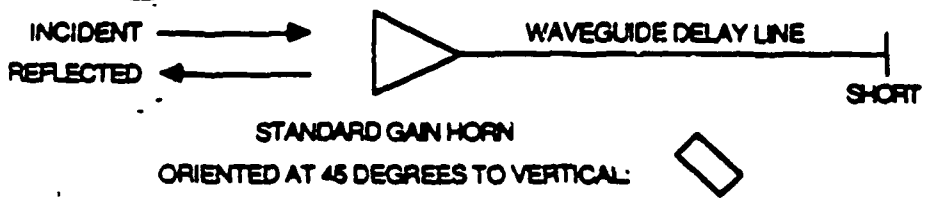
INCIDENT
REFLECTED
WAVEGUIDE DELAY LINE
SHORT
STANDARD GAIN HORN
ORIENTED AT 45 DEGREES TO VERTICAL:

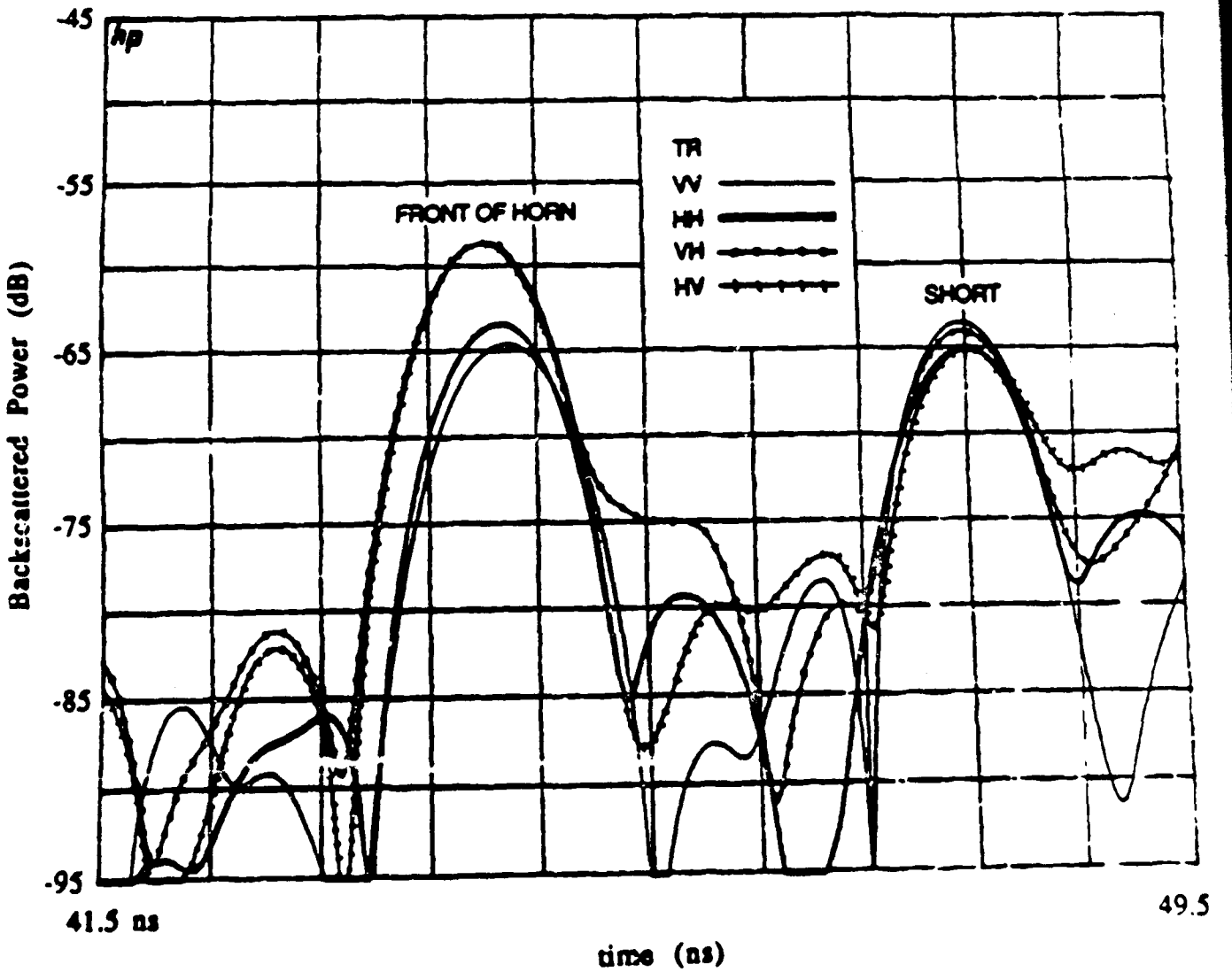
-45
-55
-65
-75
-85
-95
hp
TR
VV
HH
VH
HV
FRONT OF HORN
SHORT
Backscattered Power (dB)
41.5 ns
49.5
time (ns)

MILLIMETER-WAVE POLARIMETRIC MEASUREMENTS OF ARTIFICIAL AND NATURAL TARGETS

M. W. Whitt and F. T. Ulaby

Radiation Laboratory
Department of Electrical Engineering
and Computer Science
The University of Michigan
Ann Arbor, MI 48109-2122

ABSTRACT

The Millimeter-Wave Polarimeter is a scatterometer system that uses the HP 8510A vector network analyzer for coherent processing of the received signal. It operates at 35 GHz and 94 GHz, and a third channel at 140 GHz is to be added in 1987. The MMP provides full polarization and phase capabilities to allow measurement of the complete scattering matrix of both distributed and point targets. This paper describes the calibration techniques used at 35 GHz to measure the scattering matrix and presents some sample data. An analysis of the measurement accuracy was performed by comparing the measured values with theoretical calculations for conducting spheres and finite-length conducting cylinders. As an extension of the analysis to natural targets, the scattering matrices of a series of twigs were examined, and preliminary results are presented.

I. INTRODUCTION

In the past, much of the scattering data for both distributed and point targets consisted of incoherent power measurements for only a limited range of polarizations. Very little data at millimeter-wave frequencies has been taken at all. In recent years, however, remote sensing has developed to the point where phase and polarization are being explored more extensively. Early work by Sinclair, Kennaugh, Gent, et al. has shown that a radar target acts as a polarization transformer. The transformation was expressed by Sinclair in the form of a scattering matrix. An extensive reference list for the work in this area is given in the papers by Huynen [1] and Guill [2]. Much of the work relating to the scattering matrix has been done for point targets. Recent interest in its application to remote sensing has grown, but very little work has been done in measuring the scattering matrices of distributed targets. It is the purpose of this paper to describe a technique to measure the scattering matrix of either distributed or point targets at millimeter-wave frequencies. The technique utilizes the Millimeter-Wave Polarimeter (MMP), which is a coherent scatterometer developed at the University of Michigan [3, 4]. With such a system, a comprehensive data set can be produced to facilitate the modelling of millimeter-wave scattering from natural targets. The results from individual target measurements (leaves, branches, rocks, etc.) can be integrated into a comprehensive model for terrain surfaces and canopies. Additional data taken for distributed targets (soil surfaces, tree canopies, vegetation, etc.) could be used to further improve these models.

II. MILLIMETER-WAVE POLARIMETRY

A. Measurement Setup

The measurement system consists of an HP 8510 vector network analyzer, transmitter and receiver sections, and an anechoic chamber with a styrofoam target mount. A block diagram is shown in Figure 1. The transmitter produces a 34-36 GHz frequency swept RF signal by upconverting a 2-4 GHz signal supplied by the network analyzer. A sample of the transmitted signal is harmonically downconverted and applied to the a_1 port of the HP 8511A frequency converter as a reference. A similar downconversion stage is employed in the receiver section, which is mounted directly below the transmitter, for both vertically and horizontally polarized signals. The received V-polarized and H-polarized signals are then applied to the b_1 and b_2 ports of the HP 8511A, respectively. A Faraday rotation polarizer is used to provide both polarizations for transmission. A photograph of the measurement setup is shown in Figure 2.

The target mount consists of a styrofoam frame with the edges cut at a variety of angles to allow rotation of the target relative to the radar. The target is attached to the mount with nylon string as shown in Figure 3 where a cylinder is mounted as an example. The measured noise-floor of the system corresponds to a radar cross-section of approximately -50 dBm^2 and the radar cross-section of the target mount was determined to be below this level. The orientation of the target relative to the radar is defined in terms of the coordinate systems shown in Figures 4(a) and b

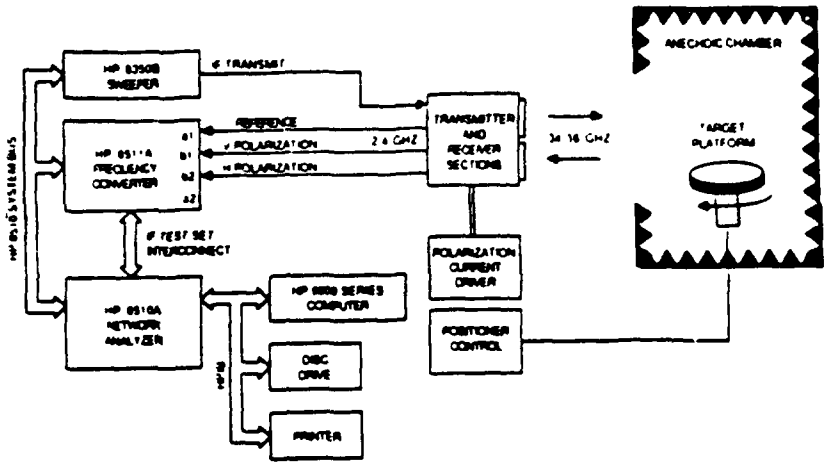

Figure 1. Block diagram of the MMP system operating in the backscatter mode.

Figure 2. Photograph of the measurement system operating in the backscatter mode.

Figure 3. Target mount.

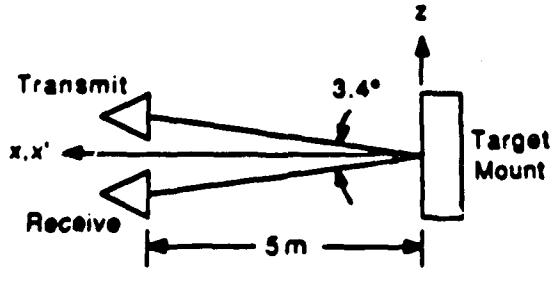

(a) Radar geometry

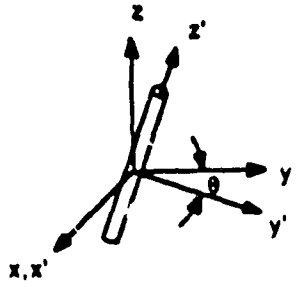

(b) Target geometry

Figure 4. Geometry associated with the target orientation relative to the radar

B. Measurement Procedure

Using the HP8510 network analyzer system as the IF processor provides the user with several features that can be used to improve the accuracy of the measurement. Complex math operations are available and can be used to subtract out the response of the chamber and any other spurious but systematic errors. In addition, an internal real-time FFT processor is available to transform the frequency swept data to the time domain where time-gating can be used to select the target response and reduce spurious signals at ranges different from that corresponding to the target. The gated frequency response can be obtained by Fourier transforming the time-gated response.

To make a measurement of a particular target, the time-domain response of the target is displayed to allow the time gate to be set. The target is then removed and the time-gated frequency response of the chamber is stored for all polarization combinations. The target is then replaced and the complex math feature is used to subtract the gated frequency response of the chamber from that of the target/chamber combination. To calibrate the system, a target of known radar cross-section is measured in the same manner, thereby allowing the magnitude and relative phase of the scattered fields to be determined.

III. THE SCATTERING MATRIX

We can define the scattering matrix [S] for a target in terms of the vertical and horizontal components of the incident and scattered electric fields by the following matrix equation:

$$\begin{bmatrix} E_V^S \\ E_H^S \end{bmatrix} = [S] \begin{bmatrix} E_V^i \\ E_H^i \end{bmatrix}. \tag{1}$$

where

$$[S] = \begin{bmatrix} S_{VV} & S_{VH} \\ S_{HV} & S_{HH} \end{bmatrix}. \tag{2}$$

If we define the radar cross-section of the target to be

$$\sigma_{RT} = 4\pi r^2 \, |S_{RT}|^2, \tag{3}$$

where subscripts T and R are the transmit and receive polarizations, the scattering matrix [S] can be written in terms of the radar cross-section. By factoring out the phase of the S_{VV} term, we have

$$[S] = \frac{e^{i\phi_{VV}}}{\sqrt{4\pi r^2}} \begin{bmatrix} \sqrt{\sigma_{VV}} & \sqrt{\sigma_{VH}}\, e^{i(\phi_{VH}-\phi_{VV})} \\ \sqrt{\sigma_{HV}}\, e^{i(\phi_{HV}-\phi_{VV})} & \sqrt{\sigma_{HH}}\, e^{i(\phi_{HH}-\phi_{VV})} \end{bmatrix} \tag{4}$$

In this form, the scattering matrix can be determined from quantities that are independent of range.

IV. RCS FOR A FINITE-LENGTH CONDUCTING CYLINDER

The performance of the system can be evaluated by measuring the scattering matrix of a conducting cylinder as a function of its orientation relative to the radar. Figure 4(b) shows the geometry associated with the orientation of the cylinder. Two coordinate systems are defined; the unprimed coordinates are fixed relative to the radar, and the primed coordinates are local to the cylinder as it is rotated. The bistatic angle between the transmitter and receiver is approximately 3.4 degrees, which is sufficiently small to assume that the measured cross-section represents the backscattered case.

For a vertically polarized incident wave, the fields are given by

$$\bar{E}^i = \hat{z}\, E_0 \exp\left[-ik_0 x\right] \tag{5}$$

$$\bar{H}^i = \hat{y}\, \frac{E_0}{\eta} \exp\left[-ik_0 x\right], \tag{6}$$

where an $e^{-j\omega t}$ time dependence has been assumed and suppressed. In terms of the primed coordinates, we have for the incident fields

$$\bar{E}^i = \left(\hat{z}' \cos\theta - \hat{y}' \sin\theta\right) E_0 \exp\left[-ik_0 x\right] \tag{7}$$

$$\bar{H}^i = \left(\hat{y}' \cos\theta + \hat{z}' \sin\theta\right) \frac{E_0}{\eta} \exp\left[-ik_0 x\right] \tag{8}$$

The far-zone backscattered fields due to this excitation for an infinitely long perfectly conducting cylinder with diameter 2a are given by [5]:

$$\bar{E}^s = \hat{y} \sqrt{\frac{2}{\pi}} \frac{E_0 \sin\theta}{\sqrt{k_0 x}} \exp\left[i\left(k_0 x - \frac{\pi}{4}\right)\right] \sum_{n=-\infty}^{\infty} (-1)^n C_n^{TE}$$

$$+ \hat{z}' \sqrt{\frac{2}{\pi}} \frac{E_0 \cos\theta}{\sqrt{k_0 x}} \exp\left[i\left(k_0 x - \frac{\pi}{4}\right)\right] \sum_{n=-\infty}^{\infty} (-1)^n C_n^{TM} \tag{9}$$

$$\bar{H}^s = \frac{1}{\eta}\left(\hat{x} \times \bar{E}^s\right). \tag{10}$$

where

$$C_n^{TM} = -\frac{J_n(k_0 a)}{H_n^{(1)}(k_0 a)} = C_{-n}^{TM} \tag{11}$$

$$C_n^{TE} = -\frac{J_n'(k_0 a)}{H_n^{(1)'}(k_0 a)} = C_{-n}^{TE}. \tag{12}$$

In terms of the original unprimed coordinates, the backscattered fields are given by

$$\bar{E}^s = \hat{y}\sqrt{\frac{2}{\pi}}\frac{E_0}{\sqrt{k_0 x}}\exp\left[i\left(k_0 x - \frac{\pi}{4}\right)\right] C_{VH} + \hat{z}\sqrt{\frac{2}{\pi}}\frac{E_0}{\sqrt{k_0 x}}\exp\left[i\left(k_0 x - \frac{\pi}{4}\right)\right] C_{VV} \tag{13}$$

$$\bar{H}^s = \frac{1}{\eta}\left(\hat{x} \times \bar{E}^s\right). \tag{14}$$

The complex coefficients C_{VH} and C_{VV} are a function of the rotation angle and can be written as

$$C_{VH} = \cos\theta \sin\theta \left[\sum_{n=-\infty}^{\infty} (-1)^n C_n^{TM} + \sum_{n=-\infty}^{\infty} (-1)^n C_n^{TE}\right] \tag{15}$$

$$C_{VV} = \sin^2\theta \sum_{n=-\infty}^{\infty} (-1)^n C_n^{TM} - \cos^2\theta \sum_{n=-\infty}^{\infty} (-1)^n C_n^{TE}. \tag{16}$$

Similarly, for a horizontally polarized incident wave, the incident and backscattered fields are given by

$$\bar{E}^i = \hat{y} E_0 \exp\left[-ik_0 x\right] \tag{17}$$

$$\bar{H}^i = -\hat{z}\frac{E_0}{\eta}\exp\left[-ik_0 x\right] \tag{18}$$

$$\bar{E}^s = \hat{y}\sqrt{\frac{2}{\pi}}\frac{E_0}{\sqrt{k_0 x}}\exp\left[i\left(k_0 x - \frac{\pi}{4}\right)\right] C_{HH} + \hat{z}\sqrt{\frac{2}{\pi}}\frac{E_0}{\sqrt{k_0 x}}\exp\left[i\left(k_0 x - \frac{\pi}{4}\right)\right] C_{HV} \tag{19}$$

$$\bar{H}^s = \frac{1}{\eta}\left(\hat{x} \times \bar{E}^s\right). \tag{20}$$

In this case, the complex coefficients C_{HV} and C_{HH} are given by

$$C_{HV} = C_{VH} \tag{21}$$

$$C_{HH} = \cos^2\theta \sum_{n=-\infty}^{\infty} (-1)^n C_n^{TM} - \sin^2\theta \sum_{n=-\infty}^{\infty} (-1)^n C_n^{TE} \tag{22}$$

The scattering width for the infinite cylinder is defined as

$$\sigma_{RT}^c = 2\pi \lim_{r\to\infty} \frac{|E_R^s|^2}{|E_T^i|^2}. \tag{23}$$

where subscripts T and R are the transmit and receive polarizations, respectively. Using this definition, the scattering widths for the infinitely long conducting cylinder are given by

$$\sigma_{VV}^c = \frac{4}{k_0}|C_{VV}|^2 \tag{24}$$

$$\sigma_{VH}^c = \frac{4}{k_0}|C_{VH}|^2 = \sigma_{HV}^c \tag{25}$$

$$\sigma_{HH}^c = \frac{4}{k_0}|C_{HH}|^2. \tag{26}$$

The relative phase of the VH, HV, and HH scattered fields can also be found from the following expressions

$$\phi_{VH} - \phi_{VV} = \tan^{-1}\left[\frac{\mathrm{Im}\left(C_{VH}/C_{VV}\right)}{\mathrm{Re}\left(C_{VH}/C_{VV}\right)}\right] = \phi_{HV} - \phi_{HH}.$$

$$\phi_{HH} - \phi_{VV} = \tan^{-1}\left[\frac{\mathrm{Im}\left(C_{HH}/C_{VV}\right)}{\mathrm{Re}\left(C_{HH}/C_{VV}\right)}\right] \quad (28)$$

For finite cylinder lengths much larger than a wavelength, the radar cross-section can be written in terms of the scattering width for an infinitely long cylinder of the same diameter. The radar cross-section derived in this manner is given by

$$\sigma_{RT} = \frac{k_0 L^2}{\pi}\,\sigma^c_{RT} \quad (29)$$

where L is the length of the cylinder. The relative phases for the finite cylinder at normal incidence for a finite cylinder can be approximated by those for the infinitely long cylinder. With expressions for σ_{RT} and $\phi_{RT} - \phi_{VV}$, we can compute the scattering matrix for a finite-length conducting cylinder versus rotation angle θ.

V. MEASUREMENT RESULTS

Three types of targets were measured: a set of conducting spheres, conducting cylinders, and natural evergreen twigs. A photograph of these targets is shown in Fig. 5 along with the dihedral reflector used for calibration.

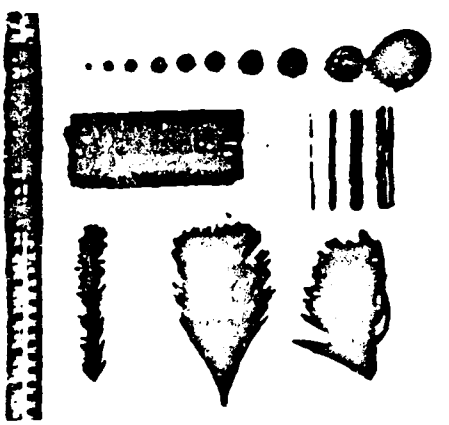

Figure 5. Measured targets.

A. Artificial Targets

Radar cross-section measurements were conducted for eight spheres ranging in diameter from 0.787 cm to 6.35 cm. One of the spheres (d = 6.35 cm) was used for calibration, and the measured normalized cross-sections of the others were compared to Mie calculations. The results, displayed in Fig. 6, show good agreement for all spheres. The maximum and minimum error bounds for the measured sphere cross-sections range from +0.48 dB and -0.5 dB for the 6.35 cm diameter sphere to +3.9 dB and -7.2 dB for the 0.787 cm diameter sphere [6]. It is worth noting that the measurements covered a wide dynamic range for σ, extending from -45.7 dBm^2 to -25.2 dBm^2.

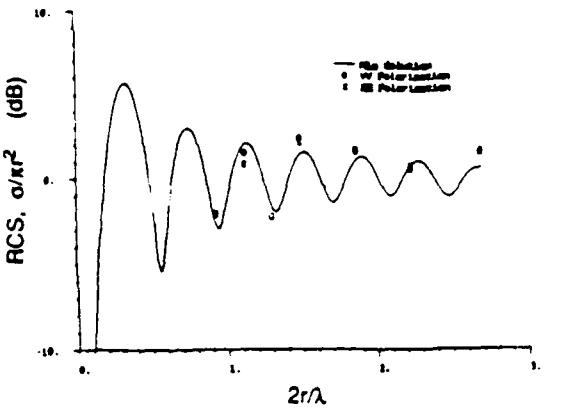

Figure 6. Normalized radar cross-section for a conducting sphere versus diameter.

The phase performance was evaluated by measuring the scattering matrix of a series of conducting cylinders approximately 7.62 cm in length and ranging from 0.0533 cm to 0.957 cm in diameter. Calibration was made by measuring a dihedral as a reference target. The scattering matrix for a dihedral is given by [7]:

$$[S] = \frac{2ab}{\lambda r}\begin{bmatrix} -\cos 2\theta & \sin 2\theta \\ \sin 2\theta & \cos 2\theta \end{bmatrix}, \quad (30)$$

where a and b are the dimensions of a single plane of the dihedral, and θ is the rotation angle. The relative phase of the scattered fields for VH, HV, and HH polarizations were compared to the theoretical values as developed in this paper. The relative phase versus rotation angle for two different cylinder diameters (0.0533 cm and 0.1168 cm) are given in Figures 7 and 8. The standard deviation in relative phase for these two cylinders was 9.7 degrees for all polarizations.

The radar cross-section of the cylinders was also measured, and an example of the measured and theoretical data versus rotation angle is given in Figure 9 for the 0.0838 cm diameter cylinder. The degradation in accuracy for the magnitude measurement is due primarily to difficulty in positioning the target within the antenna beam. The length of the cylinders (~9 wavelengths) made the azimuth and elevation orientation very critical for accurate radar cross-section measurements.

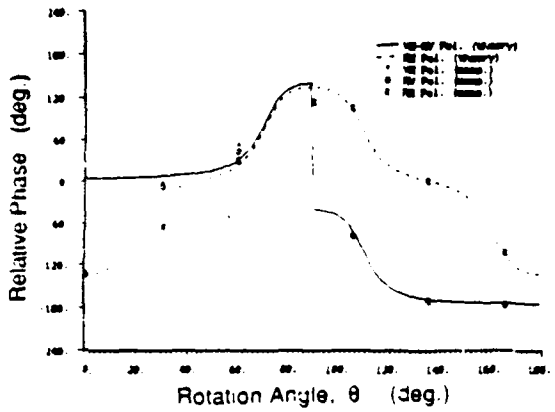

Figure 7. Relative phase for a finite-length conducting cylinder versus rotation angle (0.0533 cm diameter, 7.62 cm length).

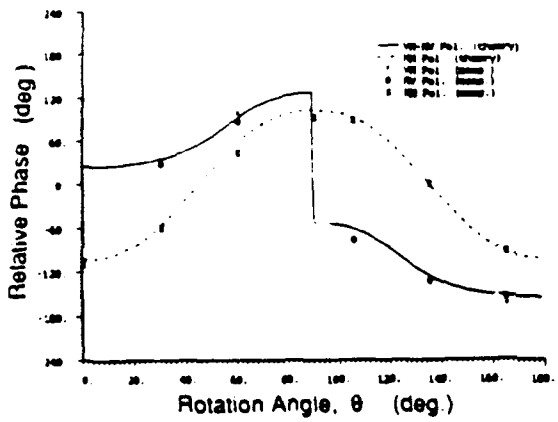

Figure 8. Relative phase for a finite-length conducting cylinder versus rotation angle (0.1168 cm diameter, 7.62 cm length).

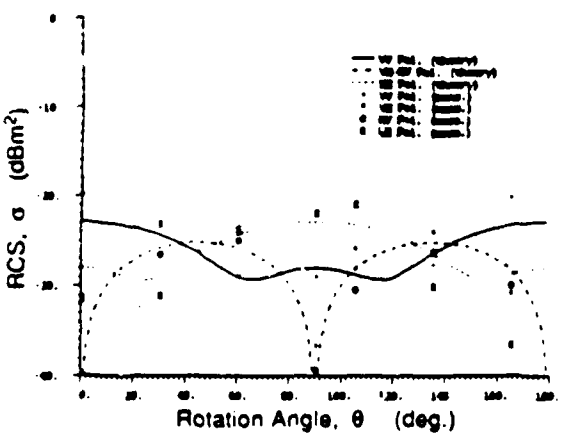

Figure 9. Backscatter for a finite-length conducting cylinder versus rotation angle (0.0838 cm diameter, 7.62 cm length).

B. Natural Targets

A set of three types of evergreen twigs were measured at angles of 0, -45, and 90 degrees relative to vertical. These twigs were shown in Figure 5 along with the conducting spheres and cylinders. As an example, the scattering matrix for a pine twig at a -45 degree angle of rotation was measured to be

$$[S] = \frac{e^{i\phi_{VV}}}{\sqrt{4\pi r^2}} \begin{bmatrix} 0.047 & 0.016\, e^{-i22.8^\circ} \\ 0.018\, e^{-i21.9^\circ} & 0.034\, e^{i31.4^\circ} \end{bmatrix} \quad (11)$$

where the relative phase terms are given in degrees. Preliminary results show a reasonable accuracy in both the magnitude and phase associated with the scattering matrix.

VI. CONCLUSIONS

The results presented in this paper satisfy the first phase of a two phase experiment. The capability of the MMP to measure the complete scattering matrix of point scatterers has been demonstrated. The relative phase accuracy for a single measurement was found to be ±9.7 degrees, and based on sphere measurements, the magnitude accuracy was found to correspond well with that predicted from the measurement signal-to-noise ratio as given in [6]. The noise level of the present system corresponds to a radar cross-section on the order of -50 dBm^2. This level is realized by the ability of the network analyzer to subtract out the effects of the target mount. It is estimated that with a more carefully developed technique to mount the point targets, the noise level can be improved by at least 10 dB. At the same time a new mounting technique will also improve the accuracy of magnitude measurements on assymetric targets such as cylinders where the orientation is very critical.

The second phase of the project involves measurements of the scattering matrix for natural targets. Preliminary results on a series of twigs have been obtained, and an example of a measured scattering matrix was shown in this paper. Now that the performance of the system has been demonstrated, measurements will be conducted to determine the scattering matrices for a variety of natural targets including soil and rock surfaces and vegetation canopies.

This work was supported by Army Research Office Contract DAAG29-85-K-0220.

VII. REFERENCES

[1] Huynen, J.R., "Measurement of the Target Scattering Matrix," *Proc. IEEE*, vol. 53, pp. 936-946, August 1965.

[2] Guili, D., "Polarization Diversity in Radars," *Proc. IEEE*, vol. 74, No. 2, pp. 245-269, February 1986.

[3] Whitt, M.W., F.T. Ulaby, and T.F. Haddock, "The Development of a Millimeter-wave Network Analyzer Based Scatterometer," University of Michigan Radiation Laboratory Technical Report, Contract DAAG29-85-K-0220, Ann Arbor, MI, January, 1987.

[4] Ulaby, F.T., T.F. Haddock, J. East, and M.W. Whitt, "A Millimeter-wave Network Analyzer Based Scatterometer," Submitted for publication in *IEEE Trans. on Geosci. and Rem. Sens.*, 1987.

[5] Ruck G.T., D.E. Barnick, W. D. Stuart, and C.K. Krichbaum, Radar Cross Section Handbook, vol. I, Plenum Press, New York, pp. 267-273, 1970.

[6] Ulaby, F.T., R.K. Moore, A.K. Fung, Microwave Remote Sensing: Active and Passive, vol. II, Reading MA: Addison-Wesley, pp. 768-770, 1970.

[7] Mott, H., Polarization in Antennas and Radar, John Wiley and Sons, New York, pp. 240-242, 1986.

Fluctuation Statistics of Millimeter-Wave Scattering From Distributed Targets

FAWWAZ T. ULABY, FELLOW, IEEE, THOMAS F. HADDOCK, MEMBER, IEEE, AND RICHARD T. AUSTIN, STUDENT MEMBER, IEEE

Abstract—The applicability of the Rayleigh fading model for characterizing radar scattering from terrain is examined at 35 GHz for both backscattering and bistatic scattering. The model is found to be in excellent agreement with experimental observations for single-frequency observations of uniform targets such as asphalt and snow-covered ground. The use of frequency averaging to reduce signal fading variations was examined experimentally by sweeping the radar signal from 34–36 GHz in 401 steps. The results show that the formulation based on the Rayleigh model relating the reduction in signal fluctuation to the bandwidth used provides a reasonable estimate of the improvement provided by frequency averaging.

I. Introduction

To *fade*, as defined in Webster's dictionary [1], is "to change gradually in loudness, strength, or visibility, when used (in connection) with a motion picture image or an electronics signal." In radio communications [2], *signal fading* refers to fluctuations in the received signal caused by multipath interference, and in radar sensing of terrain the terms *fading*, *scintillation*, and *fluctuation* have all been used interchangeably to describe random-like intensity variations corresponding to signals backscattered from cells at different locations on a distributed target [3, pp. 463–495, 1803–1804]. If the radar is of the imaging type, the random variations produce a "speckle" pattern or appearance on the image, which complicates the image interpretation problem and reduces the effectiveness of information extraction algorithms.

Consider, for example, the two image segments shown in Fig. 1. These two segments, one of which corresponds to a corn field and the other to a forest parcel and which were part of the same strip of *X*-band radar imagery, have different average *tones*, exhibit significantly different *textures*, and both exhibit large pixel-to-pixel intensity variations. The average tone of an image is the average value of the image intensity for all pixels contained in that image. (Each image segment contains approximately 10^4 pixels.) This average tone is proportional to the average received power, which, in turn, is directly proportional to the *backscattering coefficient* σ^0 of the imaged target. In other words, σ^0 of the imaged target is, by definition, the mean value of the random process characterizing the intensity variations in the image. Texture refers to the low spatial-frequency variations of intensity across the image [4]; the corn field, being more spatially uniform than the forest parcel, exhibits the same type of random variations in all regions of the image, whereas the image of the forest parcel contains "clumps" of dark and bright regions, on which the random variation is superimposed. If we adopt the strict definition that the concept of "a backscattering coefficient for a distributed target" is meaningful only for targets with *uniform* electromagnetic properties, then texture becomes the spatial variation of σ^0 from one region of an image to another. In the case of the forest parcel, these variations are related to the spatial nonuniformity of tree density.

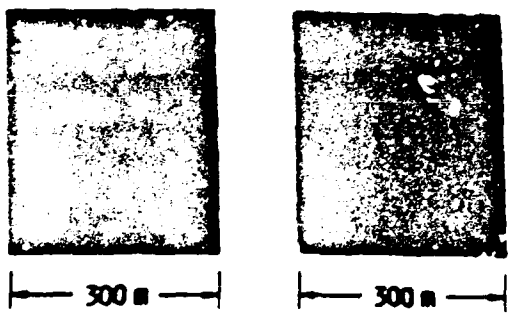

Fig. 1. *X*-band SAR images of (a) a corn field and (b) a forested area. Note the textural differences between the two images.

Unlike textural variations, which may or may not have specific directional properties and which are governed by the spatial variation of the target scattering properties relative to the dimensions of the radar resolution cell, the random variations that give the image its speckled appearance are due to phase-interference effects and are a characteristic feature of the scattering pattern for any distributed target (provided the target satisfies certain conditions, as we shall discuss later). Image speckle is simply a visual manifestation of fading statistics, which is the central topic of this paper.

Thus, there are three types of intensity variations that one may observe in a radar image: (1) variations in average tone from one distributed target (such as a bare soil field) to

Manuscript received October 6, 1987.

The authors are with the Radiation Laboratory, EECS Department, The University of Michigan, Ann Arbor, MI 48109-2122.

IEEE Log Number 8820718.

0196-2892/88/0500-0268$01.00

to another (such as a forest parcel), 2) textural variations from one region of a distributed target to another, and 3) random fading variations at the pixel-to-pixel scale. These variations are governed by different processes and are characterized by different probability density functions (pdf's).

In some radar applications, these three types of variations are lumped together, treated as a single variation, and characterized as terrain *clutter*. To determine the statistics of the clutter random variable for a given terrain type or geographic area, the area is imaged and then a pdf of the received voltage or power is generated. Next, the data is tested against theoretical pdf's to determine which fits best. Such an empirical approach may produce a statistical description appropriate to the imaged area, but it has some severe limitations. The empirically generated pdf is, in essence, a convolution of the three pdf's characterizing the three types of variations referred to above. Hence, it is both target-specific and sensor-specific. It is target-specific in that it pertains to the specific mix of terrain categories and the specific conditions of those categories at the time the radar observations were made. Most terrain surfaces exhibit dynamic variations with time of day, season, and weather history. The pdf is sensor-specific because one of the underlying variations, namely that due to signal fading, is governed by the detection scheme used in the receiver (linear or square-law) and the type of filtering or smoothing technique employed in the signal processor. Filtering techniques are used to reduce fading variations; they may include spatial averaging and/or frequency averaging schemes and may be performed coherently or incoherently [4]–[9].

To characterize the fading statistics associated with a terrain surface of uniform electromagnetic properties, the usual approach is to model the surface as an ensemble of independent, randomly located scatterers, all of comparable scattering strengths. Such a model leads to the result that the amplitude of the backscattered signal is Rayleigh-distributed [3, pp. 476–481]. If the return is dominated by backscatter from one or a few strong scatterers, the fading process is characterized by the Nakagami–Rice distribution [10]. Some experimental observations support the Rayleigh behavior [4], [11], [12] while others, particularly those measured for complex terrain categories, are in closer agreement with the lognormal or the Weibull pdf's [13]–[17], or other more complicated distributions [18].

The purpose of this paper is to:

1) examine the applicability of Rayleigh fading at 35 GHz for both backscattering and bistatic scattering from uniform terrain media,

2) examine the statistics associated with the use of frequency averaging to reduce fading variations, and

3) determine if the statistical character of the backscatter is affected by the size of the ground cell (antenna footprint) illuminated by the radar.

To this end, both experimental measurements and theoretical analyses were performed.

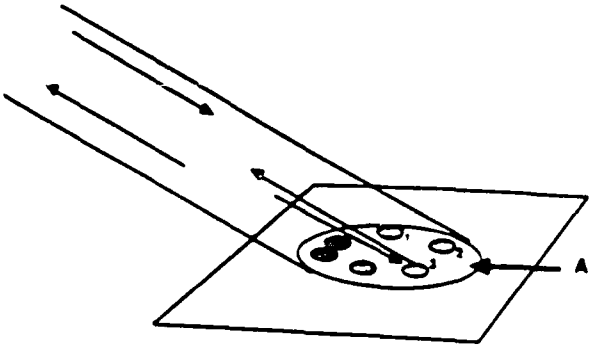

Fig. 2. The illuminated area A contains N_t randomly distributed scatterers.

II. Rayleigh Fading Statistics

A. Underlying Assumptions

The Rayleigh fading model used for describing radar scattering from an area-extended (distributed) target is essentially the same as the model used for random noise and is based on the same mathematical assumptions. A review of these assumptions will prove useful in later sections.

The sketch shown in Fig. 2 depicts a radar beam illuminating an area A of an area-extended target. The illuminated area contains N_t point scatterers designated by the index $i = 1, 2, \cdots, N_t$. For simplicity, we shall confine our present discussion to the backscatter case. The field intensity at the input of the receiving antenna due to backscatter by the ith scatterer may be expressed as

$$E_i = K_i E_{i0} \exp\left[j(\omega t - 2kr_i + \theta_i)\right] \tag{1}$$

where E_{i0} is the scattering amplitude and θ_i is the scattering phase of the ith scatterer; r_i is the range from the antenna to the scatterer; $k = 2\pi/\lambda$ is the wavenumber; and K_i is a system constant that accounts for propagation losses to and from the scatterer, antenna gain, and other radar system factors. The expression given by (1) may be abbreviated as

$$E_i = K_i E_{i0} e^{j\phi_i} \tag{2}$$

where

$$\phi_i = \omega t - 2kr_i + \theta_i \tag{3}$$

is the instantaneous phase of E_i.

Assumption 1: The scatterers are statistically independent. This assumption allows us to express the total instantaneous field due to the N_t scatterers contained in the area A as a simple sum

$$E = \sum_{i=1}^{N_t} K_i E_{i0} e^{j\phi_i} \tag{4}$$

and it implies that interaction effects between adjacent scatterers may be ignored.

Assumption 2: The maximum range extent of the target $\Delta r = |r_i - r_j|_{max}$ is much smaller than the mean range to the target area A, and the antenna gain is uniform across A. This allows us to set $K_i = K$ for all i. For convenience

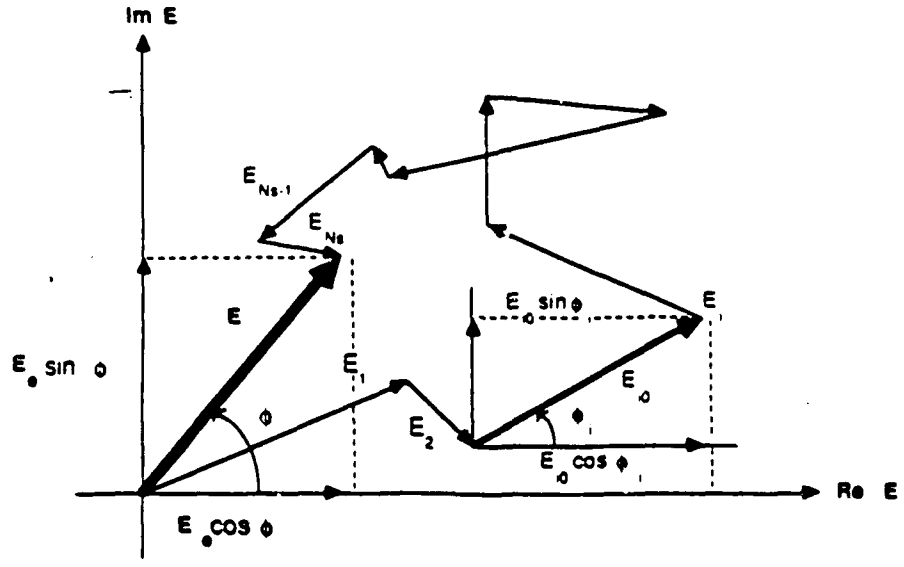

Fig. 3. The vector E is the phasor sum of N_s fields.

we shall set $K = 1$. Hence

$$E = \sum_{i=1}^{N_s} E_{i0} e^{j\phi_i} \tag{5}$$

The total field E is a vector sum of N_s phasors. If we express these phasors graphically (Fig. 3) with the first one starting at the origin and the successive one starting each at the tip of the preceding one, the resultant is a vector from the origin to the tip of the last phasor. The length of this vector and its phase angle are denoted E_s and ϕ, respectively. That is

$$E = E_s e^{j\phi}. \tag{6}$$

Assumption 3: N_s is a large number. This assumption allows us to use the central-limit theorem, which, in turn, allows us to assume that the x- and y-components of E, E_x, and E_y, are normally distributed. However, it can be shown through computer simulation that this condition can be satisfied (approximately) for N_s as small as 10. (The same conclusion was reached by Kerr [19] in the 1940's.)

Assumption 4: The scattering amplitude E_{i0} and the instantaneous phase ϕ_i are independent random variables. This condition is easily satisfied if E_{i0} is independent of the range r_i, which would be the case if the scatterers are randomly distributed in range.

Assumption 5: The phase ϕ_i is uniformly distributed over the range $[0, 2\pi]$. To satisfy this condition it is not only necessary that the scatterers be randomly distributed in range, but the maximum range extent of the target Δr must be several wavelengths across also.

Assumption 6: No one individual scatterer produces a field intensity of magnitude commensurate with the resultant field from all scatterers. In other words, the field E is not dominated by one (or few) very strong scatterer(s). If this condition is not satisfied, the Rayleigh noiselike statistics do not apply and the statistics developed by Rice [20] for one or more large signals contained in a background of noise should be used instead.

Use of Assumptions 3–6 can be shown to lead to the following properties [3, p. 479]:

$$p(E_s) = \frac{E_s}{s^2} \exp\left(-E_s^2/2s^2\right), \quad E_s \geq 0 \tag{7}$$

$$p(\phi) = 1/(2\pi) \tag{8}$$

$$\overline{E}_s = \left(\frac{\pi}{2}\right)^{1/2} s \tag{9}$$

$$\overline{E_s^2} = 2s^2 \tag{10}$$

where $p(E_s)$ and $p(\phi)$ denote the pdf's of E_s and ϕ, respectively, $\overline{E}_s$ is the ensemble average (mean value) of E_s, and s is the standard deviation of E_x and E_y. Equation (7) is known as the Rayleigh distribution.

B. Output Voltage

1) Linear Detection: If the receiver uses a linear detector, its output voltage V_L is directly proportional to E_s

$$\begin{aligned} V_L &= K_1 E_s \\ &= K_1 \overline{E}_s \frac{E_s}{\overline{E}_s} \\ &= K_1 K_2 (\sigma^0)^{1/2} f \\ &= \overline{V}_L f \end{aligned} \tag{11}$$

where K_1 is a system constant, K_2 relates the mean field $\overline{E}_s$ to the backscattering coefficient of the target σ^0 (actually, σ^0 is directly proportional to $\overline{E^2}$, but $\overline{E} = k\sqrt{\overline{E^2}}$), and f is the normalized *fading random variable*

by

$$f = E_r / \bar{E}_r \tag{12}$$

Using the relation $p(E_r)\,dE_r = \bar{p}(f)\,df$, we obtain

$$p(f) = \frac{\pi f}{2} \exp\left(-\pi f^2/4\right), \quad f \geq 0 \tag{13}$$

$$\bar{f} = 1 \tag{14}$$

$$s_f = s_{V_L}/\bar{V}_L = 0.523. \tag{15}$$

Because the output voltage V_L is a product of its mean value $\bar{V}_L = K_1 K_2 (\sigma^0)^{1/2}$ and the random variable f, the process is sometimes referred to as a *multiplicative* noise model.

2) Square-Law Detection: The voltage output of a square-law detector is directly proportional to the power of the input signal rather than to its field intensity E_r. Thus

$$\begin{aligned} V_S &= K_3 P \\ &= K_3 K_4 \overline{E_r^2} \frac{E_r^2}{\overline{E_r^2}} \\ &= K_3 K_4 K_5 \sigma^0 F \end{aligned} \tag{16}$$

where

$$F = E_r^2/\overline{E_r^2} \tag{17}$$

is the normalized fading random variable for power. The pdf characterizing F is the exponential distribution [3, p. 480]

$$p(F) = e^{-F}, \quad F \geq 0 \tag{18}$$

with

$$\bar{F} = 1 \tag{19}$$

and

$$s_F = s_P/\bar{P} = 1. \tag{20}$$

C. Interpretation

What do these statistics tell us? To answer this question we start by examining Fig. 4(a), which shows plots of $p(f)$ and $p(F)$ for the Rayleigh and exponential distributions, respectively, and Fig. 4(b), which shows the corresponding cumulative distributions. We observe that the range of fading associated with these distributions is very large. That is, if one takes a single sample of the signal from a Rayleigh-distributed or exponentially distributed ensemble, one has very little chance of selecting a value close to the mean. To illustrate this with a specific example, according to the Rayleigh distribution in Fig. 4(b) the value of f that exceeded 5 percent of the time is 1.95 (relative to the mean) and that exceeded 95 percent of the time is 0.25. In decibels, these levels correspond to +5.8 and −11.9 dB, respectively. If we select a sample at random, the probability is 90 percent (95 to 5 range) that its value will be within the range extending from 11.9 dB below the mean to 5.8 dB above the mean. We may think

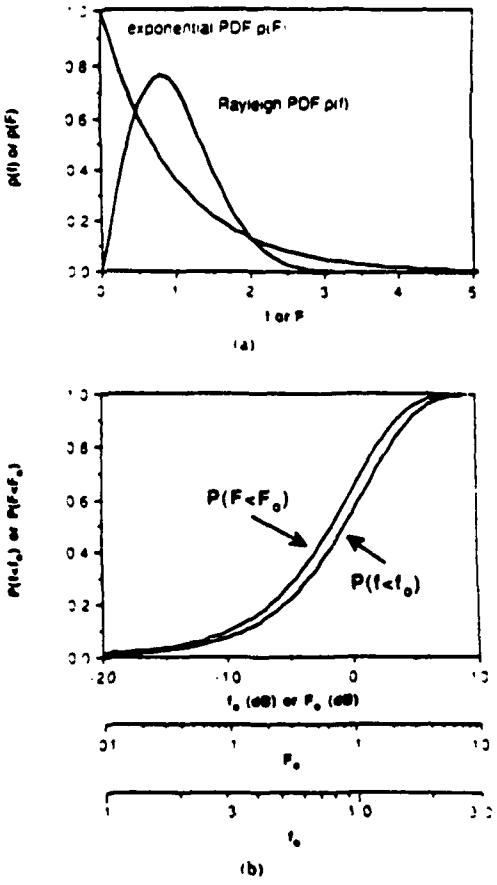

Fig. 4. Plots of (a) probability density functions and (b) cumulative distributions for f and F.

of this as the 90-percent confidence interval associated with our measurement. The important point to note here is the fact that this interval (17.7 dB) is very large indeed. The situation is not much different when square-law detection is used; the 5- and 95-percent levels of the cumulative distribution for the exponential pdf are +4.8 and −12.9 dB, also totalling to 17.7 dB.

Now let us illustrate the fading behavior with measured data. Fig. 5(b) presents a trace of radar backscatter measurements made by a 35-GHz truck-mounted scatterometer as the truck was driven across an asphalt surface with the radar beam pointing downward along the aft direction at an incidence angle of 40° relative to normal incidence (Fig. 5(a)). The antennas were mounted atop a telescopic boom at a height of 10.3 m above the asphalt surface. The sampling rate was such that the footprints (on the asphalt surface) corresponding to adjacent samples were totally independent (no overlap). More detailed information on the system and measurement procedure is given in Section IV.

The vertical axis in Fig. 5(b) represents F, the ratio of the received power to the average value computed for a 1000 measurements, expressed in decibels. (It is associ-

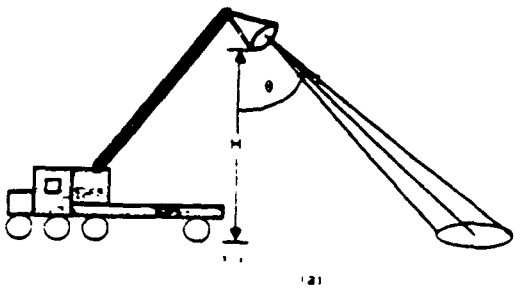

(a)

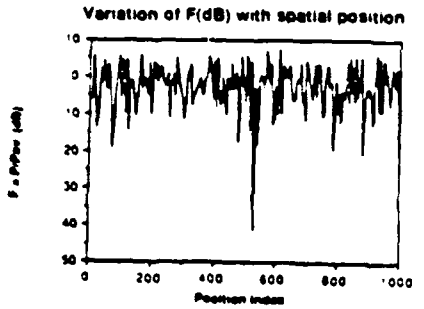

(b)

Fig. 5. The sketch in (a) shows how the measurement of the backscattering from asphalt (shown in (b)) were acquired. The incidence angle was 40°, the platform height 10.3 m, and the polarization VV. The measured backscattering coefficient (corresponding to $\bar{P}$) was −5.25 dB.

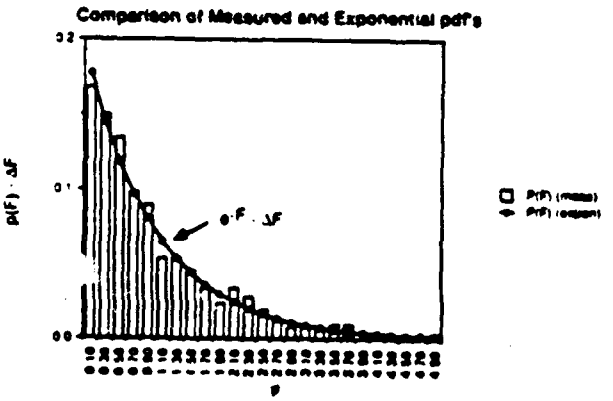

Fig. 6. Comparison of the measured pdf's with the exponential pdf. The quantity $F = 0.2$ is the bin size.

that the mean of 1000 independent samples is a good estimate of the true mean.) We observe that

1) The measured values of F extend over a range of 50.2 dB, and that 90.8 percent of these data points are within the −12.9- to +4.8-dB range (which corresponds to the 90-percent interval for the exponential distribution).

2) The standard deviation $s_F = 0.97$, which is in close agreement with the value of 1 predicted by (20).

3) The measured pdf of F closely resembles the exponential distribution (Fig. 6), an acceptance hypothesis test using the chi-square goodness of fit test shows agreement with a probability of 86 percent.

D. Independent Samples

To improve the uncertainty of a radar measurement of the backscatter from a terrain surface, it is necessary to average many independent samples together. An easy way to increase the number of independent samples N contained in an estimate of the radar backscatter is through spatial averaging, which amounts to trading spatial resolution for improved radiometric resolution. Other ways to increase N are discussed in Section III.

1) Linear Detection: If N randomly selected samples of a Rayleigh-distributed voltage V_L are averaged together, the average value V_{LN} has the following properties:

$$V_{LN} = \frac{1}{N}\sum_{i=1}^{N} V_{Li} = K_1 K_2 (\sigma^0)^{1/2}\left[\frac{1}{N}\sum_{i=1}^{N} f_i\right] = K_1 K_2 (\sigma^0)^{1/2} f_N \quad (21)$$

where we defined

$$f_N = \frac{1}{N}\sum_{i=1}^{N} f_i \quad (22)$$

as the fading random variable corresponding to the average of N independent samples. Its properties are

$$\bar{f}_N = 1, \qquad s_{f_N} = \frac{0.523}{\sqrt{N}} \quad (23)$$

and its pdf may be obtained by N-successive convolutions of the Rayleigh distribution (13). Plots of $p(f_N)$ are shown in Fig. 7(a) for several values of N. As expected, as N increases the distribution becomes more peaked and narrow (the standard deviation decreases as $N^{-1/2}$).

2) Square-Law Detection: If the receiver uses square-law detection

$$V_{SN} = K_3 K_4 K_5 \sigma^0 F_N \quad (24)$$

with

$$F_N = \frac{1}{N}\sum_{i=1}^{N} F_i \quad (25)$$

The mean value of F_N is 1, its standard deviation is

$$s_{F_N} = \frac{s_{P_N}}{\bar{P}} = \frac{1}{\sqrt{N}} \quad (26)$$

and its pdf is a χ^2 distribution with $2N$ degrees of freedom [3, p. 1914]

$$p(F_N) = \frac{F_N^{N-1} N^N e^{-NF_N}}{(N-1)!}, \quad F_N \geq 0 \quad (27)$$

Plots of $p(F_N)$ are shown in Fig. 7(b).

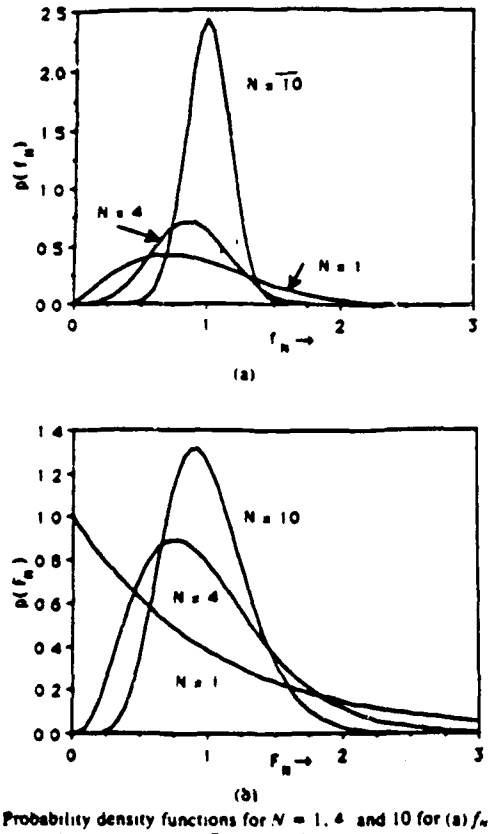

Fig. 7 Probability density functions for $N = 1$, 4 and 10 for (a) f_N (linear detection) and (b) F_N (square-law detection).

E. Applicability of the Rayleigh Model

Does the Rayleigh fading model provide an appropriate approach for characterizing the statistics of radar backscatter from terrain? The answer is a qualified yes. If the assumptions underlying the Rayleigh fading model are reasonably satisfied, the available experimental evidence suggests that the Rayleigh model is quite applicable [4], [11], [12]. Terrain targets satisfying the Rayleigh assumptions include bare ground surfaces, agricultural fields, dense forest canopies, and snow-covered ground. In all cases the target has to have stationary statistics, which requires that its "local-average" electromagnetic properties be uniform across the extent of the target.

Rayleigh fading is inapplicable for a sparse forest observed by a high-resolution radar because the high spatial variations in tree density at the scale of the radar resolution violate the stationarity assumption. Thus, a very important parameter governing applicability of Rayleigh statistics to backscatter from terrain is the size of the radar resolution cell relative to the spatial frequency spectrum characterizing the scattering from the terrain target under consideration.

An urban scene is another target class/condition for which Rayleigh statistics may not apply. If the resolution cell size is such that the backscatter is likely to be dominated by the return from one or a few strong scatterer(s), such as a building or a corner reflector formed by two intersecting flat surfaces, the Rayleigh pdf is no longer applicable.

In a recent study on image texture [4], Seasat SAR data was examined for five land use categories in a test site in Northeastern Oklahoma. Comparison of pdf's based on the data from the digital SAR image with the Rayleigh pdf revealed a good fit between data and theory for backscatter from a lake surface, a fair fit for grasslands and cultivated terrain, and poor agreement for forests and urban areas, particularly for the latter.

III. Ways to Increase the Number of Independent Samples

According to the preceding section, if a radar is used to measure the backscattering from a uniform, randomly distributed target with backscattering coefficient σ^0, the voltage observed at the receiver output will be proportional to $(\sigma^0)^n$, with $n = 1/2$ for linear detection and $n = 1$ for square-law detection. However, associated with the measurement process there will be a *multiplicative* error represented by the random variable f_N (for linear detection) or F_N (for square-law detection). These random variables both have means of 1 and standard deviations proportional to $N^{-1/2}$. Hence, the key to improving the precision of the measurement process is to make N as large as possible.

Fundamentally, increasing N is equivalent to trading off spatial resolution for improved radiometric resolution. This statement is true when discrete measurements (corresponding to discrete resolution cells) are averaged together after detection, as well as when the averaging process is an integral part of the detection process (as we shall discuss later).

A. Spatial Averaging

1) Discrete Samples: If N measurements corresponding to statistically independent nonoverlapping footprints are averaged together, then the number of independent samples characterizing the average value is simply N. Statistical independence requires that the spacing between adjacent footprints be greater than the spatial correlation length of the random surface L_s. Thus, reflections from two nonoverlapping footprints on a very smooth surface are not considered independent because the correlation length of a smooth surface is very long (it is infinite for a specular surface). Conversely, for a random surface the returns from two footprints may be considered independent even if the footprints do overlap, provided that the spacing between the centers of the two footprints is greater than a certain distance which we shall call the *fading decorrelation distance* L_d. Expressions for L_d are given in succeeding sections for specific antenna pointing configurations. In all cases the condition $L_d > L_s$ has to be satisfied in order for the samples to be statistically independent.

2) Continuous Averaging in Azimuth: Consider the

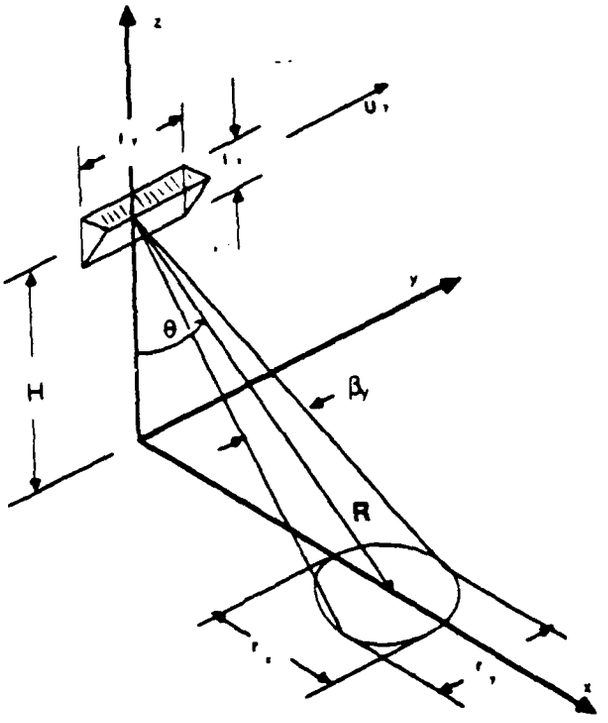

Fig. 8 Antenna with effective beamwidth β_y illuminating a target at range R and incidence angle θ

tenna beam shown in Fig. 8; the boresight direction is in the x–z plane, pointing at an angle θ, and the effective beamwidth is β_y in the y-direction. The antenna is moving along the y-direction (azimuth) at a velocity u_y, the nominal range to the antenna footprint is R, and the nominal azimuth resolution (width of the footprint in the y direction is)

$$r_y = \beta_y R. \tag{28}$$

If the radar output voltage is recorded as a function of time as the beam traverses the ground surface at the velocity u_y, the beam performs a form of continuous averaging equivalent to low-pass filtering. From considerations of the time it takes to travel over a distance r_y and the Doppler bandwidth of the signal backscattered from the illuminated cell, it can be shown [3, pp. 585–586] that the output voltage represents an average of N_y-equivalent discrete independent samples, and that N_y is given by the approximate expression

$$N_y \cong r_y/(l_y/2) \tag{29}$$

where l_y is the length of the antenna along the y-direction. The above result, which is independent of u_y, may be interpreted as saying that the fading signal decorrelates whenever the antenna moves a distance $l_y/2$ in the y-direction, and therefore a resolution cell of width r_y contains $r_y/(l_y/2)$ independent samples. Thus, the fading decorrelation distance is simply

$$L_d \cong l_y/2. \tag{30}$$

The result given in (29) is equally applicable to a pencil-beam scatterometer and to a fan-beam side-looking real-aperture-radar (RAR). In the case of a side-looking fully focused synthetic aperture radar (SAR), the Doppler bandwidth is used to improve the azimuth resolution from $r_y = \beta_y R$ to the resolution $r_y = l_y/2$ corresponding to a synthetic aperture of length $l_y = \beta_y R$. Thus, for the fully focused SAR

$$N_y = r_y/(l_y/2)$$
$$= 1.$$

Looked at another way, N_y represents the degradation in spatial resolution from the best achievable $(l_y/2)$ *down* to r_y.

3) Continuous Averaging in Range: For a narrow pencil-beam scatterometer traveling in the x-direction, consideration of the time-bandwidth product leads to

$$N_x \cong r_x/L_d \tag{31}$$

and

$$L_d \cong (l_e/2)\sec^2\theta \tag{32}$$

where r_x is the ground resolution in the x-direction, and l_e is the height of the antenna in the elevation plane.

B. Frequency Averaging

The criteria used to decide whether or not a pair of signals V_1 and V_2 backscattered from two ground footprints may be treated as statistically independent observations is based on the magnitude of the correlation coefficient between them, $\rho(V_1, V_2)$. If, on the average, ρ is smaller than some specified value, such as 0.2, the two observations may be regarded as statistically independent. Decorrelation is a consequence of differences in the instantaneous phases of the scatterers present in the observed cells. The phase of a given scatterer, as given by (3)

$$\phi_i = \omega t - 2kr_i + \theta_i$$
$$= \omega t - \frac{4\pi}{c}\nu r_i + \theta_i$$

may be changed by altering the range r_i between the scatterer and the antenna, or by changing the wave frequency ν. Birkemeier and Wallace [21] derived an expression for the correlation function for two signals (one at frequency ν_1 and the other at frequency ν_2) scattered from the same randomly distributed target as a function of the illumination geometry and the frequency separation $\Delta\nu = \nu_2 - \nu_1$. If V_S is the output voltage after square-law detection (i.e., $V_S = KP$, where P is the input power), the autocorrelation function for $V_S(\nu_1)$ and $V_S(\nu_2)$ is given by

$$R(\nu_1, \nu_2) = \overline{V_S(\nu_1)\,V_S(\nu_2)}$$
$$= \overline{P(\nu_1)\,P(\nu_2)}$$

where K has been set equal to unity for convenience. For the randomly distributed target depicted in Fig. 9, Birkemeier and Wallace [21] argued that the process is stationary; i.e., $R(\nu_1, \nu_2) = R(\Delta\nu)$, and showed that the autocovariance function, defined as

$$R_r(\Delta\nu) = R(\Delta\nu) - \bar{P} \tag{34}$$

is given by

$$R_r(\Delta\nu) = \bar{P}^2 \left| \frac{\sin \alpha\Delta\nu}{\alpha\Delta\nu} \right|^2 \tag{35}$$

where $\bar{P} = \bar{P}(\nu_1) = \bar{P}(\nu_2)$ is the mean value of the input power (assumed constant over the frequency separation $\Delta\nu$), and

$$\alpha = \frac{2\pi D}{c} = \frac{2\pi}{c} r_g \sin\theta. \tag{36}$$

The correlation coefficient is the normalized autocovariance function

$$\rho(\Delta\nu) = \frac{R_r(\Delta\nu)}{R_r(0)} = \left(\frac{\sin \alpha\Delta\nu}{\alpha\Delta\nu} \right)^2. \tag{37}$$

The two signals $P(\nu_1)$ and $P(\nu_2)$ may be regarded as statistically uncorrelated, and therefore independent, if the separation $\Delta\nu$ corresponds to the first zero of $\rho(\Delta\nu)$, which occurs at $\alpha\Delta\nu = \pi$. This was called the critical frequency change by Birkemeier and Wallace [21], but we shall refer to it as the *decorrelation bandwidth* $\Delta\nu_d$, and it is given by

$$\Delta\nu_d = \frac{c}{2D} \cong \frac{150}{D} \text{ MHz} \tag{38}$$

with D in meters.

For continuous integration over a swept-frequency bandwidth B extending from ν_1 to ν_2, the variance of

$$P(B) = \frac{1}{B} \int_{\nu_1}^{\nu_2} P(\nu)\, d\nu \tag{39}$$

is given by [20]

$$\sigma_P^2(B) = \frac{2}{B} \int_0^B \left(1 - \frac{\xi}{B}\right) R_r(\xi)\, d\xi \tag{40}$$

where ξ is $\Delta\nu$. Use of (35) in (40) leads to

$$\sigma_P^2(B) = \frac{2\bar{P}^2}{B} \int_0^B \left(1 - \frac{\xi}{B}\right) \left(\frac{\sin \alpha\xi}{\alpha\xi} \right)^2 d\xi. \tag{41}$$

The effective number of independent samples realized as a result of frequency averaging may be obtained by relating the variance of P to its mean value as in (26)

$$N = \left(\frac{\bar{P}}{\sigma_P} \right)^2 = \frac{B}{2} \left| \int_0^B \left(1 - \frac{\xi}{B}\right) \left(\frac{\sin \alpha\xi}{\alpha\xi} \right)^2 d\xi \right|^{-1} \tag{42}$$

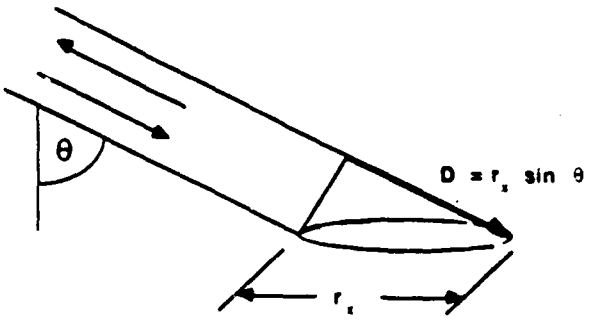

Fig. 9. Backscattering geometry for an illuminated cell with ground-range dimension r_g.

This result will be evaluated in Section V through comparison with measured data.

If $\alpha B \gg 1$, the term ξ/B is negligible over the region where the autocovariance function is of significant size in the integrand, which allows us to integrate the function analytically and obtain the approximate solution

$$N \cong \frac{2D}{c} B \cong B/\Delta\nu_d. \tag{43}$$

Here D is the slant-range resolution of the radar system. We may show the equivalence of the above result to the chirped pulse-radar case (as in a RAR or SAR) by noting that B is the chirp bandwidth and $2D/c$ is the de-chirped pulse length τ. Hence

$$N \cong B\tau \cong B/B_r \tag{44}$$

where $B_r = 1/\tau$ is the receiver bandwidth. If the transmitted pulse is de-chirped in the receiver to obtain the narrowest possible pulse length, the receiver bandwidth B_r has to be equal to the modulation bandwidth B. Hence, $N = 1$. However, if it is desired to have N be larger than 1, the pulse may be de-chirped only partially, thereby using the excess bandwidth to provide frequency averaging. This is referred to as coherent frequency averaging [8], in contrast with incoherent frequency averaging wherein the averaging operation is performed after the detection and sampling operations. That is, full de-chirping is performed to retrieve the best possible range resolution possible, and then after the image is produced, several range pixels are averaged together to increase N.

IV. Experiment Description

Two types of experiments were conducted in support of this study, one involving backscatter measurements using a truck-mounted platform and another experiment involving bistatic scattering measurements conducted in the laboratory. To maintain continuity in this presentation, only the backscatter measurement system will be described in this section, and description of the bistatic configuration will be deferred to Section VI.

The backscattered data analyzed in succeeding sections was measured by a 35-GHz scatterometer that was mounted on a truck-mounted telescopic boom as depicted in Fig. 5(a). The system, which is part of The University of Michigan's millimeter wave polarimeter [22], uses an HP8510A vector network analyzer to sweep frequency from 34 to 36 GHz in 401 discrete steps. Subsequent to calibration against a metal sphere of known radar cross section, the output is presented in the form of a frequency spectrum of the measured backscattering cross section per unit illuminated area (i.e., σ^0) or in the form of a plot of the received power versus round-trip delay. A more detailed description of the system's operation and signal processing capabilities is given in Ulaby *et al.* [22].

The scatterometer uses a pair of 15-cm diameter lens-corrected horn antennas mounted onto a common positioner one above the other in the elevation plane. The antenna far-field distance is approximately 5.2 m and the effective beamwidth of the product gain pattern is 3°. The antenna positioner may be set at an angle of incidence θ from 0° (nadir) to 90°, and the platform height may be extended up to a maximum of 20 m above the ground surface.

Two types of terrain targets were selected: 1) an asphalt surface, as a representative of targets from which the backscatter is due primarily to surface scattering, and 2) a layer of dry snow over a soil surface, as a representative of media from which the backscatter is due primarily to volume scattering. Several experiments were conducted for each of these targets to evaluate the statistical variability of the backscattered power for various combinations of incidence angle and platform height. The measurements for asphalt were acquired with the antennas pointing in the aft direction as shown in Fig. 5(a). To insure that measurements from adjacent footprints were statistically independent, the truck was moved a distance greater than the extent of the antenna footprint between successive measurements. The arrangement for snow was similar to that employed for asphalt except that the truck remained stationary and the boom was made to move in azimuth in order to avoid disturbing the snow surface. The rms height of the asphalt surface was measured to be 0.4 mm (from a surface mold), and the snow was 15 cm deep and had an average temperature of −1°C.

To limit the scope of the data-collection segment of this investigation, all observations were made with the VV polarization only.

In addition to the scatterometer system, the truck-mounted platform carried three microwave radiometers that were mounted on the same platform and their beams pointed along the same direction as that of the scatterometer. Their center frequencies were 35, 94, and 140 GHz, and all three had temperature resolutions better than 1 K. At the time of this investigation, however, only the two upper-frequency radiometers were in operating condition. These instruments proved extremely useful in verifying that 1) the targets were uniform, and 2) the snow was dry (i.e., it contained no water in liquid form).

Table I provides a summary of the statistics of the radiometric observations. At 94 GHz, the mean value of the brightness temperature T_B based on measurements from 10 spatially independent footprints was 252.8 K and the standard deviation was only 1.2 K, which is an excellent indicator that the asphalt surface was electromagnetically uniform. For snow, the radiometric observations were made at both 94 and 140 GHz, and from heights of 11 and 19 m. The two 94-GHz sets of observations (each consisting of 50 measurements from spatially independent footprints) had mean value that were within 1 K of one another and standard deviations of only a few kelvins each. In spite of the slighly greater difference between the mean values of the 140-GHz observations (which is attributed to the greater sensitivity of the 140-GHz radiometer (relative to the 94-GHz radiometer) to variations in cloud conditions between the times corresponding to the 11- and 19-m experiments), the results again indicate that the snow medium was fairly uniform from one location to another. The magnitude of $\bar{T}_B \cong 166$ K at 94 GHz is characteristic of dry snow [23], and considering that a change in liquid water content by only 2 percent would cause $\bar{T}_B$ to increase by about 100 K [23], the measured standard deviation of only a few kelvins is a clear indicator that the snow layer was indeed dry everywhere. By way of comparisons, we show in Fig. 10 radiometric observations that were made later in the season for wet snow. We observe that $\bar{T}_B$ of wet snow is about 266 K at 94 GHz (compared to 166 K for dry snow) and 270 K at 140 GHz (compared to about 208 K for dry snow), and again the standard deviations are only on the order of 1–2 K.

A. Single-Frequency Observations

As was mentioned in the previous section, the scatterometer measures the backscattered power at 401 equally spaced frequencies (channels) extending from 34 to 36 GHz. In this section we shall consider only the statistics associated with single-frequency measurements, namely the 35-GHz channel. It should be noted, however, that the results and conclusions realized at 35 GHz are statistically indistinguishable from those found at lower and higher frequencies in the 34–36 GHz range.

Our first example showing the variability of the backscattered power as a function of spatial position was presented earlier in Fig. 5(b) for an asphalt surface, and the associated probability density function was compared to the exponential distribution in Fig. 6. Similar results were obtained for snow and a summary of the observed statistics is given in Table II.

The asphalt results given in Table II are divided into two groups: (a) the near-nadir group (0° and 4°), and (b) the higher-incidence-angle group (20° and 40°). This division is necessary because the mechanics of signal fading are different in these two angular regions. At incidence angles near normal incidence, the backscattered power consists of a coherent component P_c and an incoherent component P_i [3, p. 1812], and only the latter exhibits

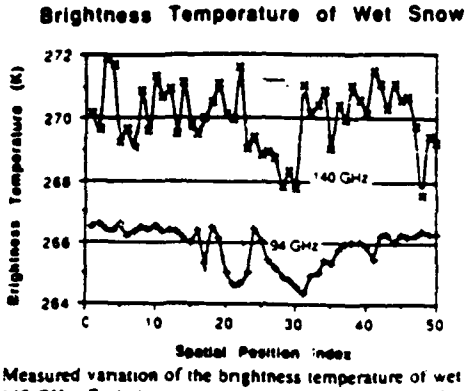

Fig. 10. Measured variation of the brightness temperature of wet snow at 94 and 140 GHz. Each data point represents an independent footprint

TABLE I
SUMMARY OF VERTICALLY POLARIZED RADIOMETRIC OBSERVATIONS MADE CONTEMPORANEOUSLY WITH THE RADAR OBSERVATIONS
(The incidence angle was 40°, and the statistics are based on observations of N spatially independent footprints. s_{T_B} is the measured standard deviation of T_B.)

TARGET	FREQUENCY	HEIGHT	N	T_B	sT_B
Asphalt	94 GHz	5 m	10	252.8	1.2
Snow	94 GHz	11 m	50	186.8	3.5
Snow	94 GHz	19 m	50	185.8	1.9
Snow	140 GHz	11 m	50	208.8	1.3
Snow	140 GHz	19 m	50	210.8	1.2

TABLE II
SUMMARY OF THE STATISTICS ASSOCIATED WITH THE BACKSCATTERING MEASUREMENTS FROM ASPHALT AND SNOW (INDEPENDENT FOOTPRINTS).

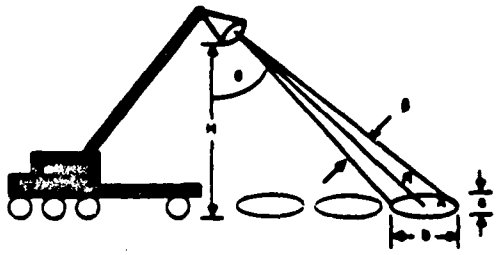

ASPHALT

Incidence Angle	Height(m)	a x b (cm x cm)	Area(m^2)	$s_p / \bar{P}$
0°	4.0	28 x 28	0.07	0.35
4°	8.8	71 x 72	0.41	0.58
20°	4.1	31 x 33	0.08	0.99
20°	9.9	76 x 82	0.50	1.31
40°	4.2	38 x 52	0.16	0.82
40°	10.3	80 x 129	1.01	1.07

SNOW

Incidence Angle	Height(m)	a x b (cm x cm)	Area(m^2)	$s_p / \bar{P}$
40°	4.2	40 x 52	0.16	1.10
40°	10.7	101 x 134	1.06	1.21
40°	18.5	175 x 231	3.24	1.00

to signal fading fluctuations. Thus

$$\bar{P} = P_c + \bar{P}_i \tag{45}$$

$$s_P = s_{P_i} \tag{46}$$

and

$$\frac{s_P}{\bar{P}} = \frac{s_P}{P_c + \bar{P}_i}. \tag{47}$$

For the incoherent component, Rayleigh fading suggests that $s_{P_i} = \bar{P}_i$ (20). Hence

$$\frac{s_P}{\bar{P}} = \bar{P}_i/(P_c + \bar{P}_i) \tag{48}$$

which is always significantly smaller than 1 if P_c is significant in magnitude relative to $\bar{P}_i$.

The coherent component P_c is largest at $\theta = 0$, decreases exponentially with increasing θ, and becomes negligible in comparison with $\bar{P}_i$ (for most natural surfaces) at angles greater than a few degrees [24]. Consequently, the value of $s_P/\bar{P}$ computed on the basis of the experimental data was found to be 0.35 at $\theta = 0°$, 0.59 at $\theta = 4°$, and close to 1 at 20° and 40°.

The major conclusions reached on the basis of the single-frequency observations are

1) The Rayleigh model is a reasonable descriptor of signal fading for uniform targets. This is supported by the good agreement shown in Fig. 6 between the measured pdf and the exponential distribution and by the result that $s_P/\bar{P} \cong 1$ for both asphalt and snow (the deviation from an exact value of 1 is attributed to the fact that the sample size is only 50, and therefore the values of s_P and $\bar{P}$ given in Table II are merely measured estimates of the true values).

2) No discernable difference between the statistics for the backscatter from snow and those for asphalt is observed.

3) No discernable dependence on footprint size is observed over the range of values examined in this study, which varied in footprint area from 0.07 to 3.24 m^2. The corresponding dimensions of the major and minor axes of the elliptically shaped footprint were 0.29 m × 0.29 m for the smallest footprint and 1.75 m × 2.31 m for the largest.

B. Frequency Averaging

Fig. 11 displays a typical example of the frequency spectrum of the measured power for a given footprint. We observe that P varies relatively slowly as a function of frequency, implying high correlation between adjacent frequency points, but the overall variation across the 34-36 GHz band is on the order of 23 dB.

The improvement (reduction) in spatial variability of the return provided by frequency averaging is demonstrated in Fig. 12, which shows both single-frequency measurements and the 2-GHz averaged measurements of the return from snow as a function of spatial position. The

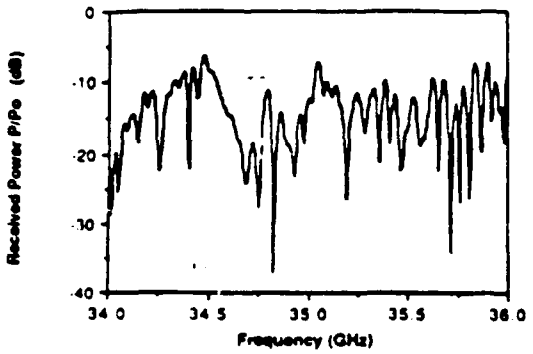

Fig. 11. Typical trace of the frequency variation from 34 to 36 GHz of the received power for a given footprint of snow.

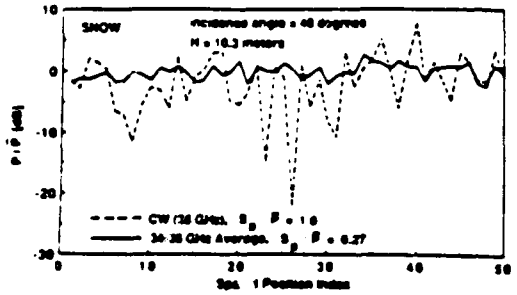

Fig. 12. Reduction of signal variability through frequency averaging.

associated normalized standard deviation is 1.0 for the single-frequency data, compared to 0.27 for the frequency-averaged data.

1) Correlation Function: Now we shall examine the role of frequency averaging relative to the theoretical expectations presented in Section III-B. We have 50 traces corresponding to 50 independent footprints, each consisting of measurements at 401 frequencies. Let us denote $P_i(\nu_j)$ as the measured power corresponding to spatial position i (with $i = 1, 2, \cdots, 50$) and frequency ν_j, where $\nu_1 = 34$ GHz, $\nu_j = [34 + 0.005(j-1)]$ GHz, and $j = 1, 2, \cdots, 401$. For each position i, we compute the autocovariance

$$R_{ii}(\Delta\nu) = \frac{1}{N_f}\sum_{j=1}^{N_f}\left[P_i(\nu_j) - \bar{P}\right]\left[P_i(\nu_{j+k}) - \bar{P}\right] \quad (49)$$

and the correlation coefficient

$$\rho_i(\Delta\nu) = \frac{R_{ii}(\Delta\nu)}{R_{ii}(0)} \quad (50)$$

where k is the displacement index, $N_f = 401 - k$, $\Delta\nu = 0.005k$ (GHz), and $\bar{P}$ is the mean value of $P_i(\nu_j)$ averaged over both i and j. The correlation coefficient is computed for integer values of k from 0 to 200, corresponding to a range of $\Delta\nu$ from 0 to 1 GHz. Once this process has been completed for each position i, the correlation function $\rho_i(\Delta\nu)$ is averaged over all i to obtain a better estimate of its frequency spectrum. Thus, the measured correlation coefficient is given by

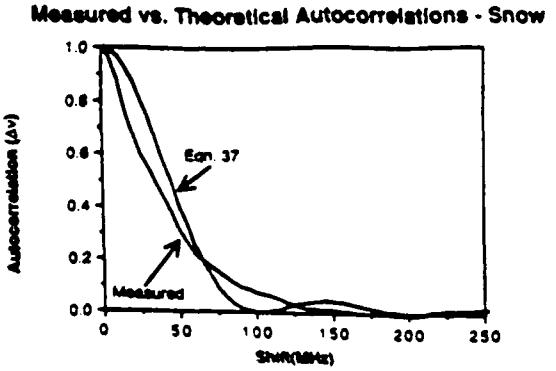

Fig. 13. Comparison of theoretical autocorrelation function given by (37) with that computed on the basis of the spectral measurements of the radar backscatter.

$$\rho_m(\Delta\nu) = \frac{1}{50}\sum_{i=1}^{50}\rho_i(\Delta\nu). \quad (51)$$

A plot of $\rho_m(\Delta\nu)$ is shown in Fig. 13 for snow. The figure also includes a plot of the expression given by (37). We observe that the measured correlation coefficient decreases with increasing frequency shift $\Delta\nu$ in an exponential-like manner and at a rate somewhat faster than the theoretical function. Similar results were observed for asphalt.

2) Normalized Standard Deviation: From (37) and (40), the normalized standard deviation associated with the received power P, when averaged over a bandwidth B, is given by

$$\frac{s_P(B)}{\bar{P}} = \left[\frac{2}{B}\int_0^B\left(1 - \frac{\xi}{B}\right)\rho(\xi)\,d\xi\right]^{1/2} \quad (52)$$

where $\xi = \Delta\nu$. Fig. 14 shows plots of the normalized standard deviation as given by (52) with $\rho(\Delta\nu) = \rho_m(\Delta\nu)$, the measured correlation function, and with $\rho(\Delta\nu)$ as given by (37). The figure also includes a plot of the normalized standard deviation as computed directly from measured data. For a given bandwidth B, s_P is based on the values of P measured at all frequencies between $B/2$ below and $B/2$ above 35 GHz. We observe that the "measured" normalized standard deviation is close to the curve calculated using the theoretical expression for $\rho(\Delta\nu)$ given by (37) and that using the experimental function $\rho_m(\Delta\nu)$.

To provide a simple formula for estimating $s_P(B)/\bar{P}$, we propose to use

$$\frac{s_P}{\bar{P}} = \begin{cases} \dfrac{1}{\sqrt{N}} = \sqrt{\dfrac{\Delta\nu_d'}{B}}, & \text{for } B \geq \Delta\nu_d' \\ 1, & \text{for } B \leq \Delta\nu_d' \end{cases} \quad (53)$$

with $\Delta\nu_d'$ selected to provide a good fit to the data. This process led to

$$\Delta\nu_d' = 138/D, \text{ (in megahertz)} \quad (54)$$

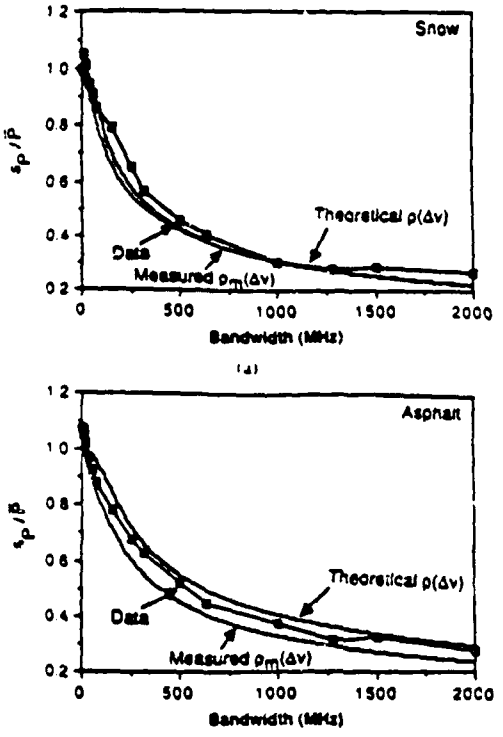

Fig. 14. Normalized standard deviation versus bandwidth B. "Theoretical" refers to (52) with $\rho(\Delta\nu)$ given by (37). "Measured" refers to (52) with $\rho(\Delta\nu) = \rho_m(\Delta\nu)$. (a) Snow and (b) asphalt.

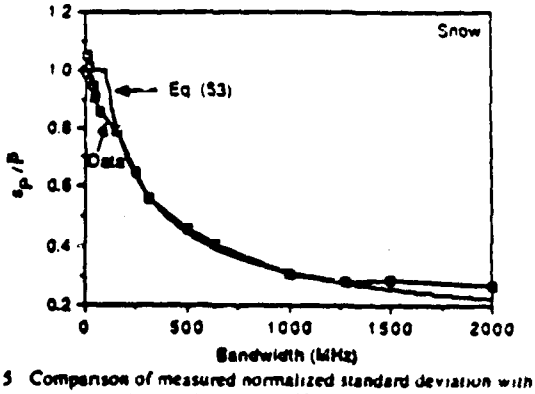

Fig. 15. Comparison of measured normalized standard deviation with single model given by (53) and (54).

and is shown graphically in Fig. 15. In the above expressions, B is in megahertz and D (the slant-range resolution defined in Fig. 9) is in meters.

These formulas, which provide an excellent fit to the measured normalized standard deviation for $N \geq 2$, indicate that the effective decorrelation bandwidth is approximately equal to the theoretical value predicted by (38).

VI. Results of the Bistatic Scattering Observations

The scatterometer system that was used to acquire the backscattering data reported in the preceding section had been designed to operate in a bistatic mode as well [22]. Bistatic scattering measurements were made for several sand and gravel surfaces using the arrangement shown in Fig. 16. Details of the results and their significance are given elsewhere [25]; our present interest pertains to the variability of the bistatically scattered signal only. Moreover, we shall limit the discussion to a typical example.

In one of the bistatic scattering experiments, the received power was measured at many azimuth angles ϕ ranging between 10° and 180° for fixed and equal values of the incidence angle θ_i and scattered elevation angle θ_s, namely $\theta_i = \theta_s = 66°$. The configuration with $\phi = 180°$ corresponds to the specular case. At each angle ϕ [illegible]

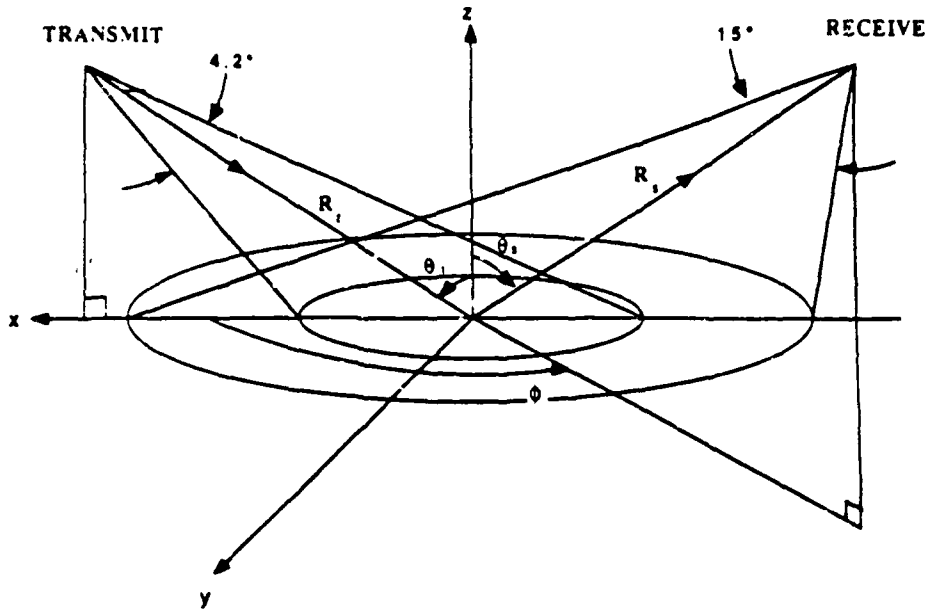

Fig. 16. Bistatic arrangement.

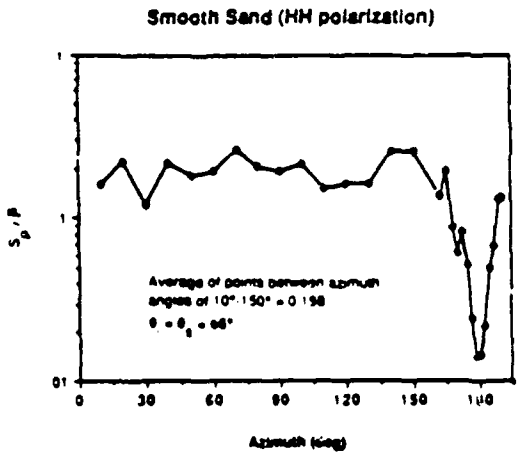

Fig. 17. Standard-deviation to mean ratio versus the azimuth angle for the bistatic scattering measurements for smooth sand. Each data point is based on measurements of 10 spatial positions (footprints).

received power was measured for 10 independent (nonoverlapping) footprints on the target surface. This was accomplished by partially rotating the target platform between successive measurements. In each case the recorded power was the received power averaged over the 34–36 GHz band.

Fig. 17 presents a plot of $s_p/\bar{P}$ as a function of ϕ. At each value of ϕ, s_p, and $\bar{P}$ were calculated using the 10 observations described above. Except for the near-specular directions ($\phi \approx 180°$), the normalized standard deviation exhibited an approximately constant value of 0.2. The equivalent total number of independent samples is $N = (1/0.2)^2 = 25$. Thus, frequency averaging provides about 2.5 independent samples per spatial sample. The power scattered in the specular direction was dominated by coherent scattering that is not subject to fading. Consequently, the measured normalized standard deviation was found to be only 0.015. This result is analogous with the backscattering result for the normal incidence case (see (48) and Table II).

VII. Conclusions

This paper has shown that the Rayleigh fading model is indeed appropriate for characterizing the fluctuation statistics associated with radar scattering from terrain, *provided* the target's properties satisfy the model's underlying assumptions. One of these properties is spatial uniformity. If the terrain target is an asphalt surface, snow-covered ground, or a grass surface, the Rayleigh model gives results in good agreement with experimental observations at 35 GHz for both backscattering and bistatic scattering. When frequency averaging is used to reduce the variability of the radar return, however, the formulations based on the Rayleigh model provide a good estimate of the improvement provided by frequency averaging.

References

[1] *Webster's New Collegiate Dictionary*. Springfield, MA: G. and C. Merriam Pub. Co., 1975, p. 411.

[2] R. L. Freeman, *Telecommunication Transmission Handbook*. New York: Wiley, 1975, pp. 197–198.

[3] F. T. Ulaby, R. K. Moore, and A. K. Fung, *Microwave Remote Sensing: Active and Passive, Vols. I–III*. Reading, MA: Addison Wesley Artech House, 1981–1987.

[4] F. T. Ulaby, F. Kouyate, B. Brisco, and T. H. L. Williams, "Textural information in SAR images," *IEEE Trans. Geosci. Remote Sensing*, vol. GE-24, no. 2, pp. 235–245, 1986.

[5] J. S. Zelenka, "Comparison of continuous and [illegible]

grator processors," *J. Opt. Soc. Amer.*, vol. 66, pp. 1295–1304, 1976.
[6] L. J. Porcello, N. G. Massey, R. B. Innes, and J. M. Marks, "Speckle reduction in synthetic aperture radar," *J. Opt. Soc. Amer.*, vol. 66, pp. 1305–1311, 1976.
[7] L. J. Cutrona, E. N. Leith, C. J. Palermo, and L. J. Porcell, "Optical data processing and filtering systems," *IEEE Trans. Inform. Theory*, vol. 2, no. 6, pp. 386–400.
[8] F. K. Li, C. Croft, and D. N. Held, "Comparison of several techniques to obtain multiple-look SAR imagery," *IEEE Trans. Geosci. Remote Sensing*, vol. GE-21, pp. 370–375.
[9] C. Y. Chi, D. G. Long, and F. K. Li, "Radar backscatter measurement accuracies using digital Doppler processors in spaceborne scatterometers," *IEEE Trans. Geosci. Remote Sensing*, vol. GE-24, pp. 426–437, 1986.
[10] P. Beckmann, *Probability in Communication Engineering*. New York: Harcourt, Brace, and World, 1967, p. 122.
[11] W. W. Weinstock, "Radar cross-section target models," and "Illustrative problems in radar detection analysis," in *Modern Radar Analysis, Evaluation, and System Design*, R. S. Berkowitz, Ed. New York: Wiley, 1965.
[12] T. F. Bush and F. T. Ulaby, "Fading characteristics of panchromatic radar backscatter from selected agricultural targets," *IEEE Trans. Geosci. Electron.*, vol. GE-13, no. 4, pp. 149–157, Oct. 1975.
[13] G. R. Valenzuela and M. B. Laing, "Point-scatterer formulation of terrain clutter statistics," *Naval Res. Lab. Rep. 7459*, Washington, DC, Sept. 27, 1972.
[14] M. P. Warden, "An experimental study of some clutter characteristics," in *AGARD Conf. Proc. No. 66 Advanced Radar Systems*, Nov. 1970.
[15] R. R. Boothe, "The Weibull distribution applied to the ground clutter backscatter coefficient," in *Automatic Detection and Radar Data Processing*, D. C. Schleher, Ed. Dedham, MA: Artech House, 1980.
[16] D. C. Schleher, "Radar detection in log normal clutter," presented at the IEEE Int. Radar Conf., Washington, DC, 1975.
[17] H. Kashihara, K. Nakada, M. Murata, M. Hiroguchi, and H. Abia, "A study of amplitude distribution of space-borne synthetic aperture radar (SAR) data," in *Proc. ISNCR Symp.* (Tokyo), Oct. 22–24, 1984.
[18] J. K. Jao, "Amplitude distribution of composite terrain radar clutter and the *K*-distribution," *IEEE Trans. Antennas Propagat.*, vol. AP-32, pp. 1049–1062, 1984.
[19] D. E. Kerr, Ed., *Propagation of Short Radio Waves*. New York: McGraw-Hill, 1951, p. 554.
[20] S. O. Rice, "Mathematical analysis of random noise," *Bell Syst. Tech. J.*, vol. 23, p. 282, 1944.
[21] W. P. Birkemeier and N. D. Wallace, "Radar tracking accuracy improvement by means of pulse-to-pulse frequency modulation," *IEEE Trans. Commun. Electron.*, pp. 571–575, Jan. 1963.
[22] F. T. Ulaby, T. F. Haddock, J. East, and M. Whitt, "A millimeter-wave network analyzer based scatterometer," *IEEE Trans. Geosci. Remote Sensing*, vol. GE-26, Jan. 1988.
[23] R. Hofer and W. Good, "Snow parameter determination by multichannel microwave radiometry," *Remote Sensing Environ.*, vol. 8, pp. 211–224, 1979.
[24] F. T. Ulaby, C. T. Allen, and A. K. Fung, "Method for retrieving the true backscattering coefficient from measurements with real antenna," *IEEE Trans. Geosci. Remote Sensing*, vol. GE-21, no. 3, pp. 308–313, July 1983.
[25] F. T. Ulaby, T. E. van Deventer, T. F. Haddock, M. Coluzzi, and J. R. East, "Millimeter-wave bistatic scattering from ground and vegetation targets," *IEEE Trans. Geosci. Remote Sensing*, vol. GE-26, May 1988.

Fawwaz T. Ulaby (M'68–SM'74–F'80) was born in Damascus, Syria, on February 4, 1943. He received the B.S. degree in physics from the American University of Beirut, Lebanon, in 1964 and the M.S.E.E. and Ph.D. degrees in electrical engineering from the University of Texas, Austin, in 1966 and 1968, respectively.

From 1968 to 1984, he was with the Electrical Engineering Department at the University of Kansas, Lawrence, where he was the J. L. Constant Distinguished Professor and the University of Kansas Center for Research, where he was Director of the Remote Sensing Laboratory. He is currently with the Radiation Laboratory and the Department of Electrical and Computer Engineering, University of Michigan, Ann Arbor. His current research interests involve microwave propagation and active and passive microwave remote sensing. Along with R. K. Moore and A. K. Fung, he is a coauthor of the three-volume series *Microwave Remote Sensing: Active and Passive* (Reading, MA: Addison-Wesley). In addition, he is coeditor of the *Manual of Remote Sensing*, 2nd ed., vol. I, American Society of Photogrammetry.

Dr. Ulaby is a member of Eta Kappa Nu, Tau Beta Pi, and Sigma Xi. He has been named the Executive Editor for IEEE TRANSACTIONS ON GEOSCIENCE AND REMOTE SENSING, 1984–1985, and was the Geoscience and Remote Sensing Society's Distinguished Lecturer for 1987. He was named an IEEE Fellow in 1980 "for contributions to the application of radar to remote sensing for agriculture and hydrology." He received the GRS Society's Outstanding Service Award in 1982, and its Distinguished Service Award in 1983. In 1984, he also received a Presidential Citation for Meritorious service from the American Service of Photogrammetry. He received the University of Kansas Chancellor's Award for Excellence in Teaching in 1980, the University of Kansas Gould Award for "distinguished service to higher education" in 1973, and the Eta Kappa Nu MacDonald Award as an "outstanding electrical engineering professor in the United States of America" in 1975.

•

Thomas F. Haddock (M'86) was born in Washington, DC, on November 2, 1949. He received the B.A. degree in mathematics and the M.S. and Ph.D. degrees in physics from the University of Michigan, Ann Arbor, in 1972, 1977, and 1984, respectively.

From 1984 to 1985 he was Manager of Development Projects at Applied Intelligent Systems, a machine vision firm involved in real-time optical, infrared, and X-ray vision systems. He is currently with the Radiation Laboratory and the Department of Electrical Engineering and Computer Science, University of Michigan. He has conducted research in the fast flux density variations of quasi-stellar objects at a wavelength of 12.5 mm. Other research has included development of real-time alphanumeric character recognition algorithms and ultrasonic weld inspection algorithms. Prior to receiving the Ph.D. degree, he worked as Application Engineer for Sams/3M, a manufacturer of heart-lung machines and cardiac assist devices, where he developed electrodes for manufacturing applications. His current research interests are millimeter-wave scattering and emission from natural targets.

Dr. Haddock is a member of the American Astronomical Society.

•

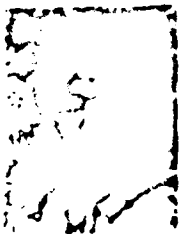

Richard T. Austin (S'84) was born in Maryville, TN, on September 2, 1964. He received the B.S. degree in electrical engineering from the University of Kentucky, Lexington, in 1986 and the M.S. degree in electrical engineering from the University of Michigan, Ann Arbor, in 1987. He is currently working toward the Ph.D. degree in the Radiation Laboratory at the University of Michigan. He holds a National Science Foundation Graduate Fellowship.

His research interests include millimeter-wave radiometry, millimeter-wave radar, and scattering and emission from natural targets.

Extinction Behavior of Dry Snow in the 18- to 90-GHz Range

MARTTI T. HALLIKAINEN, SENIOR MEMBER, IEEE, FAWWAZ T. ULABY, FELLOW, IEEE, AND TAHERA EMILIE VAN DEVENTER

Abstract—The extinction properties of several dry snow types were examined in the 18- to 90-GHz range. The snow types ranged from newly fallen snow to refrozen snow, and the density and mean grain size varied from 0.17 to 0.39 g/cm³ and from 0.2 to 1.6 mm, respectively. From measurements of the transmission loss as a function of sample thickness at a temperature of −15°C, the extinction coefficient and the surface scattering loss (due to surface roughness at the front and back surfaces of the snow slab) were determined for each snow type. The experimental values were compared against theoretical results computed according to the strong fluctuation theory. In general, good agreement with the experimental data was obtained at 18, 35, and 60 GHz when the grain size used in the theoretical calculations was chosen to be slightly smaller than the observed snow-particle size. However, the extinction coefficient of large-grained refrozen snow as predicted by the strong fluctuation theory is much larger at 90 GHz than the values determined experimentally. The attenuation in snow was observed to increase only slightly with increasing temperature in the −35 to −1°C range.

I. Introduction

THE FEASIBILITY of microwave radiometers and radars to provide information on seasonal snow cover has been evaluated in several experimental programs, including both ground-based [1]–[7] and satellite [8]–[10] investigations. Recently, the frequency range of the experimental programs has been extended to 90 GHz [3], [4], [7]. However, the basic tools to interpret the results from those measurements, namely the dielectric and scattering properties of snow, are not known with adequate accuracy. At present, experimental microwave dielectric data combined with verified dielectric models (the real and imaginary part of the complex dielectric constant $\epsilon_s = \epsilon_s' - j\epsilon_s''$) are available as follows: $\epsilon_s' - j\epsilon_s''$ for wet snow and ϵ_s' for dry snow at frequencies up to 37 GHz [11], and ϵ_s'' for dry snow at frequencies up to 13 GHz [12], [13]. Using a radiometric technique, ϵ_s'' was recently measured up to 94 GHz for two snow densities by eliminating the effect of scattering [7]. The temperature dependence of ϵ_s' is very small, whereas ϵ_s'' increases with increasing temperature. Since one of the primary uses of microwave sensors for snow measurements will be retrieval of the water equivalent of dry snow cover, high-frequency data on the dielectric and scattering loss of dry snow are needed.

The total loss of dry snow is expressed by the extinction coefficient, which includes both absorption loss and scattering loss. At low microwave frequencies (snow-particle size is much smaller than the wavelength) absorption is the primary loss process, whereas at high microwave and all millimeterwave frequencies (snow-particle size is of the same order of magnitude as wavelength) scattering dominates over absorption. According to Mie theory calculations for a snow particle with a diameter of 1 mm, scattering dominates at frequencies above 15 GHz [14].

Few experimental investigations on the attenuation of dry snow have been reported at millimeter wave frequencies [2], [7], [15], [16]. The snow parameters were not documented in a detailed manner to allow the derivation of any quantitative expressions for the extinction coefficient and the surface loss as a function of snow properties.

In the present investigation, the extinction coefficient and the surface loss for several snow types were obtained from transmission-loss measurements of snow slabs as a function of sample thickness. The effects of frequency, snow-particle size, snow metamorphism, and temperature were investigated in a detailed manner. The experimental results were compared with theoretical values obtained from the strong fluctuation theory [17]. Recent evaluations of this theory suggest that it can be applied to calculate the effective dielectric constant and the extinction coefficient of snow, as well as the brightness temperature of snow-covered terrain [18].

II. Transmission Model for Snow Slab

The following discussion concerning the transmission of a plane wave through a slab of scatterers is mainly based on a representation available in the literature [19]. Since a detailed derivation of an approximate solution to the problem has been given previously [20], only a brief discussion is included in this paper.

The geometry of the problem is depicted in Fig. 1. The total intensity incident on the slab is denoted by $I(0)$, $I = I_0$. The intensity transmitted through the air-snow interface is reduced by T, the Fresnel power transmission coefficient, and by S, a surface roughness factor that accounts

Manuscript received January 22, 1987, revised July 10, 1987. This work was supported in part by the Army Research Office under Contract DAAG29-85-K-0210.

M. T. Hallikainen is with the Helsinki University of Technology, Radio Laboratory, Otakaari 5A, 02150 Espoo, Finland.

F. T. Ulaby and T. E. van Deventer are with the University of Michigan, Radiation Laboratory, Ann Arbor, MI 49109.

IEEE Log Number 8716816.

0196-2892/87/0600-0737$01.00 © 1987 IEEE

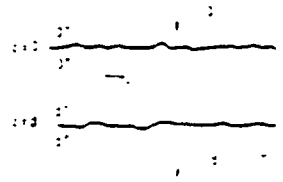

Fig. 1. Transmission of electromagnetic wave through a slab of scatterers.

for scattering by a nonspecular surface. Thus

$$I(0^+) = I_0 TS. \tag{1}$$

A relatively simple model for S that has been used in connection with soil-surface scattering [21] takes the form

$$S = \exp\left[-(2k_0 s)^2\right] \tag{2}$$

where $k_0 = 2\pi/\lambda_0$ and s is the effective rms height of the surface fluctuation. In practice, this model is reasonably adequate, although the value of s needed to match experimental data usually is smaller than the measured rms height of the surface. Combining (1) and (2) leads to

$$I(0^+) = I_0 T \exp\left[-(2k_0 s)^2\right]. \tag{3}$$

In the snow medium, the total intensity consists of a coherent component I_c and an incoherent component I_i

$$I(z) = I_c(z) + I_i(z). \tag{4}$$

The coherent intensity attenuates due to both absorption and scattering

$$I_c(z) = I(0^+)\, e^{-\kappa_e z} \tag{5}$$

where the extinction coefficient κ_e is the sum of the absorption coefficient κ_a and the scattering coefficient κ_s

$$\kappa_e = \kappa_a + \kappa_s. \tag{6}$$

The forward-scattered incoherent intensity is given by Ishimaru [20, pp. 268–274], assuming that the scattering is mostly concentrated in the forward direction, as

$$I_i(z) = I(0^+)\, q\left[e^{-\kappa_a z} - e^{-\kappa_e z}\right] \tag{7}$$

where q represents the fraction of the total scattered power intercepted by the beam angle of the receiving antenna. The total power transmitted across the boundary at $z = d$ is

$$\begin{aligned} I(d^+) &= \left[I_c(d^-) + I_i(d^-)\right] TS \\ &= I_0 T^2 S^2\left[e^{-\kappa_e d} + q\left(e^{-\kappa_a d} - e^{-\kappa_e d}\right)\right]. \end{aligned} \tag{8}$$

The loss factor $L(dB)$ is defined as

$$\begin{aligned} L(dB) &= -10 \log\left[\frac{I(d^+)}{I_0}\right] \\ &= 34.72 k_0^2 s^2 - 10 \log\left[e^{-\kappa_e d}\right. \\ &\quad \left. + q\left(e^{-\kappa_a d} - e^{-\kappa_e d}\right)\right]; \qquad T^2 = 1. \end{aligned} \tag{9}$$

For a small slab thickness d such that $\exp(-\kappa_e d) >> q[\exp(-\kappa_a d) - \exp(-\kappa_e d)]$, the coherent intensity is the dominant contributor to I and (9) may be approximated as

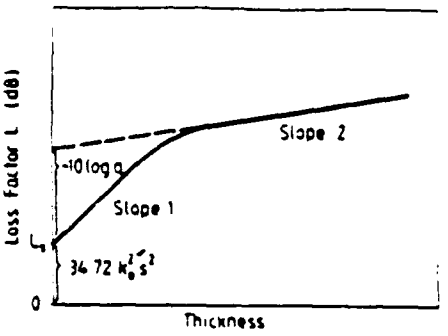

Fig. 2. Plot of the transmission loss.

$$L(dB) \cong L_s(dB) + 4.34\kappa_e d \tag{10}$$

where $L_s(dB) = 34.72 k_0^2 s^2$ is the loss factor attributed to surface roughness at the two slab boundaries. For a large slab thickness such that $\exp(-\kappa_e d) << q[\exp(-\kappa_a d) - \exp(-\kappa_e d)]$, the incoherent intensity modified by q becomes the only significant remaining component of the original incident power, and (9) may be approximated as

$$L(dB) \cong L_s(dB) - 10 \log q + 4.34\kappa_a d. \tag{11}$$

Thus, because of multiple scattering, the rate of attenuation for propagation through a thick sample becomes proportional to κ_a rather than κ_e, because the loss due to scattering is approximately equal to the generation of incoherent intensity by scattering.

According to the preceding model, if we measure the transmission-loss factor $L(dB)$ as a function of the slab thickness d, the following four parameters can be determined: 1) the extinction coefficient κ_e (from Slope 1 in Fig. 2), 2) the absorption coefficient κ_a (from Slope 2 in Fig. 2), 3) the effective rms height of the surface s (from L_s), and 4) the parameter q (from the absolute level of the curve).

Equation (11) was not used to determine κ_a in the present investigation. This would have required the measurement system to be able to measure transmission losses as high as about 70 dB. Hence, the accuracy of (11) could not be evaluated either. It is relevant to note that the total attenuation of tree foliage (observed range: 11 to 30 dB) has been found to follow a behavior similar to that shown in Fig. 2 [22].

III. Experimental Arrangement

A. Snow Samples

All snow measurements were conducted under laboratory conditions at the Radio Laboratory, Helsinki University of Technology. The snow samples were acquired from natural snow cover, including both the top and the bottom layers. Extreme care was taken not to destroy the structure of the samples. The extra snow around the essential sample (diameter 38 cm, maximum thickness

TABLE I
PROPERTIES OF SNOW SAMPLES

No.	Date (1985)	Depth in Snowpack	Observed Mean Grain Size (mm)	Surface Roughness (mm)	Melt-Freeze Cycles	Clustering	Density (g/cm³)	Dielectric Constant at 10 GHz	Comments
1	Feb. 5	Top	0.2	0	None	None	0.172	1.31	One-hour old snow
2	Feb. 15	Near Top	0.5	0	None	None	0.194	1.34	Newly fallen snow
3	Feb. 16	Near Top	0.7	0	None	None	0.217	1.39	Newly fallen snow
4	Feb. 18	Top	0.2	0	None	None	0.322	1.58	Wind-driven 5-day old snow
5	March 12	Top	0.3	0	None	None	0.277	1.52	
6	March 12	Middle	0.9	0	None	None	0.268	1.49	Separate grains
7	March 18	Near Top	0.6	0	None	None	0.235	1.41	Newly fallen snow
8	March 21	Near Bottom	1.0	1	None	None	0.315	1.58	
9	March 29	Top	1.0	1	Few	None	0.385	1.75	Hard snow
10	March 29	Near Bottom	1.0	1	None	None	0.276	1.50	Separate grains
11	April 7	Top	1.3	2 to 3	Some	Some	0.307	1.61	
12	April 11	Top	1.2	3	Some	Some	0.304	1.61	
13	April 11	Near Bottom	1.3	1 to 3	None	None	0.293	1.54	
14	April 13	Top	1.5	2 to 3	Some	Some	0.345	1.64	
15	April 13	Middle	1.1	1 to 2	Few	None	0.332	1.63	
16	April 16	Bottom	1.1	1 to 2	None	None	0.361	1.77	Separate grains; no continuous structure
17	April 17	Top	1.5	2 to 4	Some	Some	0.390	1.79	
18	April 30	Near Top	1.6	2 to 3	Several	Some	0.351	1.66	
19	March 18	Near Top	0.4	0	None	None	0.240	1.43	Acquired 1 m away from No. 7
20	March 29	Near Bottom	1.0	1	None	None	0.271	1.46	Acquired 1 m away from No. 10
21	April 7	Top	1.3	2 to 3	Some	Some	0.311	1.64	Acquired 1 m away from No. 11
22	April 13	Top	1.5	2 to 3	Some	Some	0.350	1.68	Acquired 1 m away from No. 14
23	April 17	Top	1.5	2 to 4	Some	Some	0.380	1.72	Acquired 1 m away from No. 17

Samples 1 to 18 were measured as a function of sample thickness and samples 19 to 23 as a function of temperature.

was removed, the upper surface was smoothed with a straight edge, and the sample holder was placed upside down on top of the sample; the sample was then cut, turned right-side up, and its lower surface was smoothed.

A total of 23 snow samples were acquired between February 5 and April 30, 1985 (Table I). Samples 1 to 18 were used to determine the extinction coefficient and surface loss for different snow types at −15°C, whereas samples 19 to 23 were used to investigate the temperature dependence of the extinction coefficient. The samples acquired in February were new snow, whereas those acquired in late March and April were refrozen snow. The melt-freeze period (warm days, cold nights) in late March and April was exceptionally long in 1985, allowing the development of a thick crust layer on the snow surface. Consequently, the samples acquired even from the topmost snow layers in April were reasonably homogeneous in terms of grain size and density, which is not the case during a normal winter.

The density of a sample was determined from its volume and mass. For cases 1 to 18 in Table I, these parameters were determined for every thickness of each snow sample in order to check for density variations. The density range among all the samples was 0.17 to 0.39 g/cm³.

The average grain size and the surface roughness were determined from photographs taken with a macro lens. For photographs, small samples of each snow type were placed on a glass plate equipped with a millimeter scale. It is emphasized that, although extreme care was taken to provide accurate grain-size estimates, the absolute values may have a bias. However, it is believed that the relative accuracy of the grain-size estimates is good. For nonspherical snow particles, the mean grain diameter estimate is based on volume. In case of clustering, the particle-size estimate is for individual crystals.

B. Measurement Procedure

The transmission loss for cases 1 to 18 (Table I) was measured at 10, 18, 35, 60, and 90 GHz using free-space transmission systems. In free-space transmission measurements, a sample is placed between the transmitting and receiving antennas and an electromagnetic plane wave is transmitted through the sample. The use of the free-space technique for dielectric measurements is discussed in [23] and [11]. In addition, the phase shift due to the sample was measured at 10 GHz for each sample thickness to provide ϵ_r'. Since ϵ_r' and the dry snow density ρ are related [11] by

$$\epsilon_r' = 1 + 1.9\rho \qquad (12)$$

in the microwave range, the measured ϵ_r' can be used to verify the density values.

After completing the measurement in the 10- to 90-GHz range each sample was cut thinner and the measurement procedure was repeated. The minimum sample thickness used in this investigation was 1.5 cm. For cases 19 to 23, the transmission loss at each frequency was measured as a function of temperature in the −35 to −1°C range. The sample thickness in each case was 10 cm. The first set of measurements was made at −35°C; the temperature then was increased to the next desired value and the measurements were repeated. One temperature step per day was used to guarantee stabilization of the temperature within the sample. In order to avoid damage to the sample surfaces in the environmental chamber (from air blowers, etc.), the styrofoam sample holder was always covered with a styrofoam lid.

Upon completion of the transmission-loss measurements at −1°C, three of the samples were cooled down to −15°C and the transmission loss was measured for

sample thicknesses of 7, 5, 3, and 1.5 cm. This allowed the loss behavior for each snow type to be compared with that of the neighboring sample (see Table I). For example, sample nos. 7 and 19 were acquired simultaneously from the same place (1 m apart) and depth.

During the measurements, the samples were handled and stored at −15°C. The sample holder and the lid (both made of styrofoam) provided the necessary thermal insulation during the measurement (the free-space transmission systems were at room temperature).

The distance between the transmitting and receiving antennas varied from 60 cm (60 GHz) to 75 cm (90 GHz). Horn antennas were employed in all free-space systems. The maximum loss that the measurement system could handle was about 55 dB at 90 GHz, 47 dB at 60 GHz, and 40 dB at 35 and 18 GHz. Since the transmission loss of snow samples increases with increasing frequency, the sample thickness was limited by the maximum loss that the 90- and 60-GHz systems could measure.

IV. Experimental Results

A. Transmission Loss

Due to the structural variations within each snow sample, the transmission loss was found to depend substantially (the largest observed variation was ±5 dB for an average loss of 50 dB) on the location of the sample between the transmitting and receiving antennas. Consequently, the loss at each frequency was measured as a function of the sample location. The sample was moved systematically both across (to some extent) and in the direction of power propagation; the loss was recorded using a pen recorder. The loss value used in this paper for a given snow sample is the average value of the recorded signal. The results of the transmission-loss measurements for different sample thicknesses are given in Fig. 3. The sample numbers refer to those in Table I, giving the temporal order of measurements. The precision of the results in Fig. 3 is estimated to be ±0.3 dB for the lowest values (~1 dB) and ±2 dB for the highest values (~50 dB). The measured loss values at 10 GHz are practically zero for all samples; hence, they are not shown.

The main observations from Fig. 3 are: 1) the transmission loss increases with increasing frequency and increasing grain size (see Table I), 2) the loss depends linearly on sample thickness at 18 and 35 GHz; at 60 and 90 GHz the nonlinearity of the relationship increases with increasing snow-particle size, 3) the surface loss factor L_s (estimated by extrapolating the transmission loss down to zero sample thickness) is, in most cases, negligible at 18 and 35 GHz, but it may be as large as 20 dB at 60 and 90 GHz for refrozen snow.

Comparison of the experimental results shown in Fig. 3 with the model behavior in Fig. 2 indicates that slope 1 (extinction coefficient) can be estimated easily from the data in Fig. 3, but that is not the case for slope 2 (absorption coefficient). In order to obtain the absorption coefficient, the measurements should extend over a much larger range of the sample thickness. This would have required the measurement system to be able to measure transmission losses as high as about 70 dB. The maximum loss the present free-space system at 90 GHz can measure is 55 dB.

The temperature dependence of the transmission loss was observed to be negligible in the −35 to −10°C range (cases 19 to 23 in Table I). Between −10 and −1°C the experimental loss increases with increasing temperature. The measured loss values are compared with theoretical results from the strong fluctuation theory in Section V.

B. Extinction Coefficient and Surface Loss

The extinction coefficient and the surface loss were determined for each case by fitting a straight line to the measured transmission loss. For snow types exhibiting a quasi-linear relationship between L and d, all the data points were used. This was the case for practically all 18- and 35-GHz results and low-loss types at 60 and 90 GHz. For snow types exhibiting a nonlinear variation between L and d, only the data points falling on the first linear part of the curve (see Fig. 2) were employed. Typically, the number of data points used in that case was three. The intercept of the straight line gives the surface loss factor L_s (in decibels).

The values of the extinction coefficient and the surface loss factor determined using the above procedure are listed in Table II. For convenience, the values are given in decibels instead of nepers. To convert decibels to nepers, the values must be divided by 4.34.

It is evident from Table II that both the extinction coefficient and the surface loss factor exhibit strong variations with snow type. For newly fallen snow, the extinction coefficient at 90 GHz is only 10 to 20 dB/m, compared to −400 dB/m for some samples of refrozen snow.

The following empirical expressions were developed to relate κ_e (in decibels per meter) to the observed snow-particle diameter d_0:

$$\kappa_e = 1.5 + 7.4 d_0^{2.3}; \quad \text{in decibels per meter at 18 GHz} \tag{13a}$$

$$\kappa_e = 30 d_0^{2.1}; \quad \text{in decibels per meter at 35 GHz} \tag{13b}$$

$$\kappa_e = 180 d_0^{2.0}; \quad \text{in decibels per meter at 60 GHz} \tag{13c}$$

$$\kappa_e = 300 d_0^{1.9}; \quad \text{in decibels per meter at 90 GHz.} \tag{13d}$$

The observed particle diameter d_0 is in millimeters.

Equations (13a) to (13c) can be combined into a single equation of the form

$$\kappa_e = 0.0018 f^{1.8} d_0^{2.0}; \quad \text{in decibels per meter for 18-60 GHz} \tag{14}$$

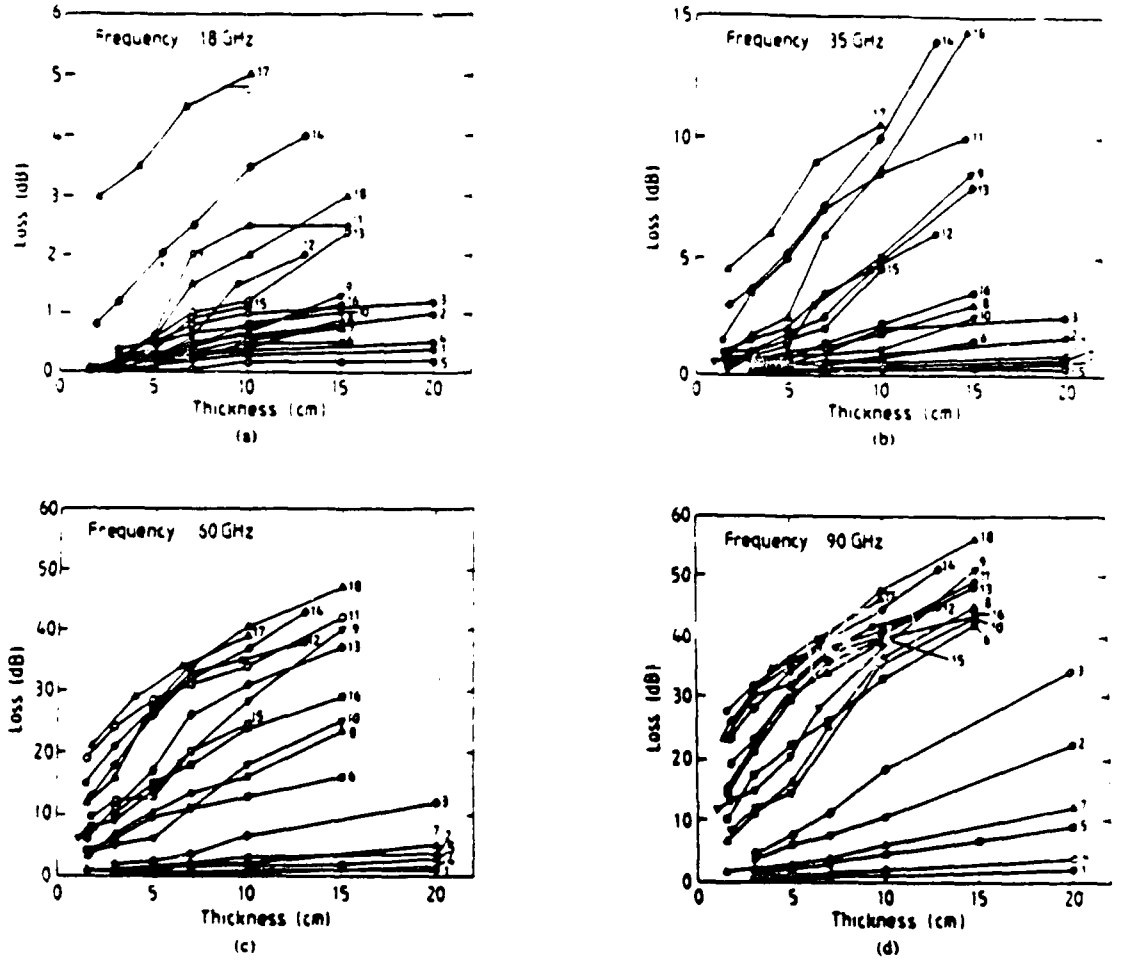

Fig. 3. Measured transmission loss for snow samples. Sample numbers refer to those in Table I.

In (14), f is in gigahertz and d is in millimeters. Equation (14) holds for particle sizes below 1.6 mm in the 18- to 60-GHz range. For 90 GHz, (13d) should be used instead.

From the surface loss values in Table II, the effective rms height was calculated from

$$s = \left[\frac{L_s}{34.72k_0^2}\right]^{1/2} \qquad (15)$$

where L_s is the surface loss in decibels and k_0 is the wave number in free space. The experimental surface loss values at 60 GHz are compared with those at 90 GHz in Fig. 4(a), and the corresponding effective rms heights are compared in Fig. 4(b). The effective rms heights at the two frequencies are strongly correlated ($R = 0.863$) with

$$s_{60} = 0.019 + 0.958 s_{90} \text{ (in millimeters)} \qquad (16)$$

where s_{60} and s_{90} are the rms heights at 60 and 90 GHz, respectively. This relationship is very close to $s_{60} = s_{90}$, which is what the model in (2) would predict. Comparison between the observed (Table I) and calculated (Fig. 4) values for the surface roughness shows that the calculated values are much smaller.

The surface loss at 90 and 60 GHz was observed to be negligible for new snow and to increase linearly with increasing observed grain size for refrozen snow types

$$L_s \text{ (90 GHz)} \cong \begin{cases} 0 \text{ dB}, & \text{for } d_0 < 0.6 \text{ mm} \\ -10.87 + 18.63 d_0, & \text{for } d_0 \geq 0.6 \text{ mm} \end{cases} \qquad (17)$$

$$L_s \text{ (60 GHz)} \cong \begin{cases} 0 \text{ dB}, & \text{for } d_0 < 0.7 \text{ mm} \\ -6.86 + 10.27 d_0, & \text{for } d_0 \geq 0.7 \text{ mm}. \end{cases} \qquad (18)$$

V. Comparison of Experimental and Theoretical Results

The strong fluctuation theory was applied by Stogryn [17], [18] to calculate the effective complex dielectric

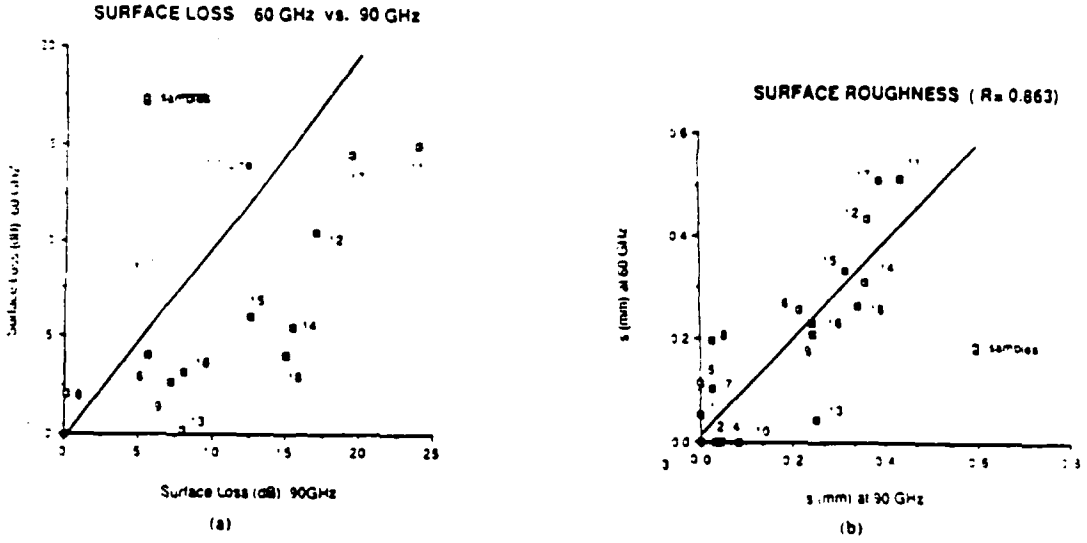

Fig. 4. Comparison of (a) experimental surface loss values (from Table II), and (b) corresponding effective surface roughness values (from (15)) at 60 and 90 GHz.

TABLE II
EXPERIMENTAL EXTINCTION COEFFICIENT AND SURFACE SCATTERING LOSS FOR DIFFERENT SNOW TYPES

Sample No.	Extinction Coefficient κ_e (dB/m)				Surface Scattering Loss L_s (dB)			
	18 GHz	35 GHz	60 GHz	90 GHz	18 GHz	35 GHz	60 GHz	90 GHz
1	2.2	2.5	5.1	10.2	0.0	0.0	0.2	0.0
2	4.3	8.3	32.8	108.1	0.2	0.0	-0.1	0.2
3	4.9	13.1	63.3	175.8	0.3	0.1	-0.5	-0.6
4	1.6	2.9	7.9	16.5	0.2	0.1	0.0	0.2
5	1.4	1.1	9.0	44.3	0.0	0.2	0.8	-0.1
6	4.2	10.1	87.6	337.8	-0.1	0.0	3.8	5.6
7	3.9	2.7	22.5	58.6	0.0	0.3	0.3	0.1
8	6.4	18.4	144.1	358.6	-0.1	0.1	2.2	0.1
9	10.2	58.8	247.2	304.0	-0.3	-0.7	2.6	7.1
10	6.7	14.1	173.8	334.3	0.0	0.1	-0.3	0.8
11	21.2	61.9	269.9	241.9	-0.2	1.6	15.3	24.0
12	19.0	44.7	332.0	437.5	-0.5	0.2	10.6	16.9
13	18.1	56.5	363.4	471.6	-0.3	-0.5	0.1	7.9
14	29.2	98.5	416.7	416.7	0.4	0.6	5.5	15.5
15	13.9	46.6	181.6	346.9	-0.2	-0.6	6.0	12.5
16	8.0	23.0	263.6	456.7	-0.1	-0.2	3.1	7.2
17	25.4	76.3	363.6	363.6	2.6	3.2	14.4	19.5
18	22.3	104.6	464.9	533.3	-0.3	-1.6	3.9	15.0

constant of dry snow ϵ_s using an exponential correlation function with a correlation length given by

$$l = \tfrac{3}{2}(1 - v_i)\, d \tag{19}$$

where v_i is the volume fraction of ice in the snow and d is the average grain diameter [18]. The assumption of an exponential correlation function is supported by experimental data discussed in [24]. The formulation [18] for the effective dielectric constant ϵ_s accounts for both scattering and absorption by the ice particles in the snow medium. The extinction coefficient can be obtained readily from

$$\kappa_e = 2k_0 |\mathrm{Im}\,(\epsilon_s^{1/2})|. \tag{20a}$$

The expression in (20a) is analogous to that for the absorption coefficient

$$\kappa_a = 2k_0 |\mathrm{Im}\,(\epsilon_s^{1/2})|. \tag{20b}$$

In order to calculate ϵ_s, we need to know ϵ_s', the quasi-static value of the dielectric constant of dry snow. The real part of ϵ_s has been observed to follow (12) in the 1 to 37-GHz range. Since ϵ' for ice is practically constant in the 1- to 100-GHz range [25], (12) can be assumed to hold in the 1- to 100-GHz range also. For ϵ_s'', however, experimental data exist only for frequencies below 13 GHz [12]. For the purposes of this paper, we shall adopt the following mixing model [14]:

$$\epsilon_s'' \approx 3v_i\epsilon_i'' \frac{\epsilon_s'^2(2\epsilon_s' + 1)}{(\epsilon_s' + 2\epsilon_s')(\epsilon_s' + 2\epsilon$$

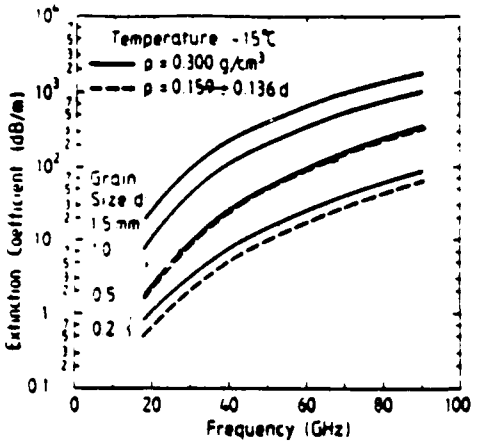

Fig. 5. Theoretical extinction coefficient for dry snow, with snow density ρ and grain size d as parameters.

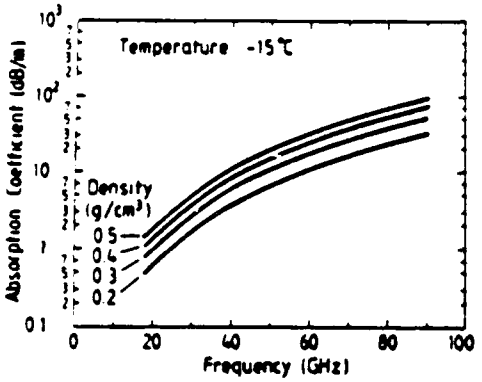

Fig. 6. Calculated absorption coefficient for dry snow with snow density as a parameter.

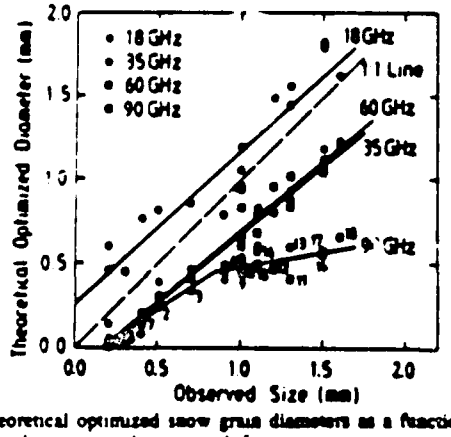

Fig. 7. Theoretical optimized snow grain diameters as a function of observed snow particle size, with frequency as a parameter.

where v_i is the volume fraction of ice in the snow medium and subscripts s and i refer to snow and ice, respectively. Data for ϵ_i'' as a function of frequency and temperature were obtained from [13].

Fig. 5 shows plots of κ_e that were computed using (20a) after computing ϵ_s using the formulation given in [18]. Because the assumption of no correlation between the snow density and the average grain size is not realistic, a regression analysis between the measured densities and estimated grain sizes in the present data was performed resulting in

$$\rho = 0.159 + 0.136 d_0 \tag{22}$$

where ρ is the density in grams per cubic centimeters and d_0 is the observed grain size in millimeters. Fig. 5 shows theoretical κ_e values for both $\rho = 0.3$ g/cm³ and for ρ from (22). The effect of density on κ_e is significant only for small particle sizes. For comparison, Fig. 6 shows the absorption coefficient for snow, calculated from (20b) and (21).

Comparison of Fig. 5 with Fig. 6 indicates that at 35, 60, and 90 GHz, the scattering coefficient ($\kappa_s = \kappa_e - \kappa_a$) is much larger than the absorption coefficient for all realistic grain sizes. At 18 GHz, absorption and scattering losses are comparable in magnitude for small-grained snow.

In order to compare values of κ_e from the strong fluctuation theory with the experimental data, theoretical values were computed for the 18 snow types. In each case, the snow density was kept constant, and the grain size was treated as a free parameter whose value was chosen such that it gave a theoretical extinction coefficient equal to the measured value. By repeating this for each of the 18 snow types, a set of model-derived grain sizes was obtained at each frequency.

Fig. 7 is a scatter diagram of d_m, the model-derived grain sizes, versus the observed grain sizes d_0. The model-derived values at 18 GHz are larger and those at 35, 60, and 90 GHz are smaller than the observed values. The linear expressions shown in Fig. 7 are given by

$$d_m = 0.26 + 0.91 d_0 \text{ at 18 GHz} \tag{23a}$$

$$d_m = -0.15 + 0.82 d_0 \text{ at 35 GHz} \tag{23b}$$

$$d_m = -0.15 + 0.83 d_0 \text{ at 60 GHz} \tag{23c}$$

$$d_m = \begin{cases} -0.11 + 0.67 d_0, \\ \quad \text{for } d_0 \le 0.9 \text{ mm, at 90 GHz} \\ 0.31 + 0.18 d_0, \\ \quad \text{for } d_0 > 0.9 \text{ mm, at 90 GHz.} \end{cases} \tag{23d}$$

The slopes of the linear equations at 18, 35, and 60 GHz in (23) are reasonably close to 1. The experimental values of κ_e at 18 GHz may be biased, due to the low values of the transmission loss L (mostly below 1 dB even for thick snow samples. It is remarkable that the expressions for d_m at 35 and 60 GHz are almost identical. This, combined with the similar slope at 18 GHz, strongly suggests that the strong fluctuation theory provides reasonably accurate results in the 18- to 60-GHz range for all realistic grain sizes, and also at 90 GHz for grain sizes smaller than 0.9 mm.

At the present time, we do not have a good explanation

for the observed departure of the 90-GHz results for refrozen snow ($d_0 > 0.9$ mm). This behavior may be due to the fact that at 90 GHz the wavelength in ice is about 1.8 mm, which is comparable in size to the ice particles in refrozen snow; such a condition is conducive to resonant scattering and absorption.

The following method was used to obtain an estimate to the temperature dependence of the extinction coefficient from the measured transmission-loss values in the -35 to -1°C range. It is assumed that the surface scattering loss does not depend on temperature. This assumption is supported by the fact that the surface roughness is constant and the measured ϵ' for each case (19 to 23) was found to vary only ± 0.01 between -35 and -1°C. Further, it is assumed that the surface scattering loss for each case is equal to that measured for its neighboring sample. For example, samples 19 and 7 were acquired from the same area (1 m apart) and from the same depth (Table I). Hence, the surface scattering loss can be subtracted from the transmission loss resulting in a value that accounts for the volume effects only

$$L_v = L - L_s \text{ (in decibels)} \qquad (24)$$

In (24), L and L_s are the experimental transmission loss and the surface scattering loss, respectively. Although L_v divided by the sample thickness is equal to the extinction coefficient only when the data point is located on Slope 1 in Fig. 2, the temperature behavior of L_v should give a reasonably good estimate for that of κ_e.

L_v for cases 19 to 23 was calculated from (24) for each temperature used in the experiment. Since the values for -35 and -20°C were practically the same for each case, the value observed for -20°C is used as a reference. The observed average increase from L at -20°C is depicted for 35, 60, and 90 GHz in Fig. 8. The experimental values are slightly smaller than the theoretical behavior obtained from (20).

The present theoretical and experimental values in Fig. 8 are substantially smaller than the experimental increase of 100 percent reported for L_v at 35 GHz in [15].

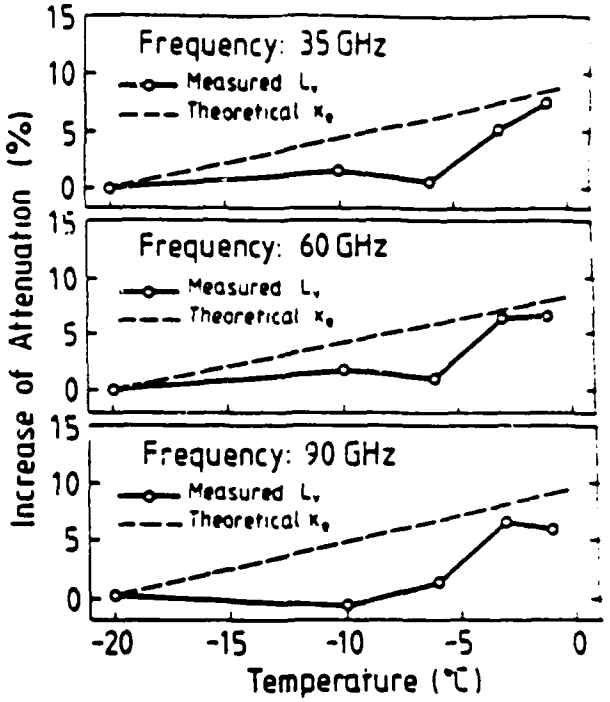

Fig. 8. Snow attenuation as a function of temperature, with -20°C as a reference point. Experimental data: average values for snow types 19 to 23 (Table I).

VI. Conclusions

The extinction coefficient and the surface loss factor for 18 dry snow types, ranging from newly fallen snow to refrozen snow, were measured in the 18- to 90-GHz range. The experimental results indicate that the extinction coefficient increases rapidly with increasing frequency and increasing average snow-particle size. However, the extinction coefficient at 90 GHz exhibits a weaker dependence on grain size for snow with grains larger than 0.9 mm in diameter than for snow with smaller grains. The effect of temperature was examined in the -35 to -1°C range; only a slight increase in snow attenuation with increasing temperature was observed. The surface loss factor (including both surface scattering and reflection loss) was found to be negligible at 18 and 35 GHz and quite substantial at 60 and 90 GHz. The magnitude of the surface loss factor was observed to be highly correlated with grain size.

The measured values of the experimental extinction coefficient were compared with theoretical values obtained using strong fluctuation theory. By matching the theoretical values (with grain size as a free parameter) to the measured values in each of the 18 cases, a set of model-derived grain sizes was obtained for each frequency. In general, the model-derived grain sizes are slightly smaller than the observed ones. It is emphasized that, although the absolute accuracy of the observed grain sizes is difficult to establish, their relative accuracy is believed to be good, based on macro photographs of each snow type. Good agreement between 1) the model-derived grain sizes at 35 and 60 GHz, 2) the slopes of the model-derived grain size versus observed grain size at all frequencies (only nonmetamorphosed snow at 90 GHz), and 3) the observed and calculated temperature dependence of the loss suggests that the streng fluctuation theory provides fairly accurate estimates of the extinction coefficient of dry snow at microwave and millimeterwave frequencies

References

[1] A. T. Edgerton, A. Stogryn, and G. Poe, "Microwave radiometric investigation of snowpacks," Aerojet Gen. Corp., Microwave Div., El Monte, CA, Final Rep. 1285-R4, 1971

[2] R. Hofer and C. Mätzler, "Investigation of snow parameters [illegible] diometry in the 3- to 60-mm wavelength region," [illegible], vol. 85, pp. 453–460, 1980

[3] W. H. Stiles and F. T. Ulaby, "The active and passive microwave response to snow parameters. I. Wetness," *J. Geophys. Res.*, vol. 85, no. C2, pp. 1037–1044, 1980.
[4] F. T. Ulaby and W. H. Stiles, "The active and passive microwave response to snow parameters. 2. Water equivalent of dry snow," *J. Geophys. Res.*, vol. 85, no. C2, pp. 1045–1049, 1980.
[5] M. Tiuri, "Theoretical and experimental studies of microwave emission signatures of snow," *IEEE Trans. Geosci. Remote Sensing*, vol. GE-20, pp. 51–57, 1982.
[6] C. Matzler, E. Schanda, and W. Good, "Toward the definition of optimum sensor specification for microwave remote sensing of snow," *IEEE Trans. Geosci. Remote Sensing*, vol. GE-20, pp. 57–66, 1982.
[7] C. Matzler, "Interaction of microwaves with the natural snow cover," *Habilitationsschrift*, Univ. Bern, 1985.
[8] A. Rango, A. T. C. Chang, and J. L. Foster, "The utilization of spaceborne microwave radiometers for monitoring snowpack properties," *Nord. Hydrol.*, vol. 10, pp. 25–40, 1979.
[9] K. Künzi, S. Patil, and H. Rott, "Snow-cover parameters retrieved from Nimbus-7 scanning multichannel microwave radiometer (SMMR) data," *IEEE Trans. Geosci. Remote Sensing*, vol. GE-20, pp. 452–467, 1982.
[10] M. T. Hallikainen and P. A. Jolma, "Retrieval of the water equivalent of snow cover in Finland by satellite microwave radiometry," *IEEE Trans. Geosci. Remote Sensing*, vol. GE-24, no. 6, pp. 855–862, 1986.
[11] M. Hallikainen, F. T. Ulaby, and M. Abdelrazik, "Dielectric properties of snow in the 3- to 37-GHz range," *IEEE Trans. Antennas Propagat.*, vol. AP-34, pp. 1329–1340, 1986.
[12] M. Tiuri, A. Sihvola, E. Nyfors, and M. Hallikainen, "The complex dielectric constant of snow at microwave frequencies," *IEEE J. Ocean. Eng.*, vol. OE-9, pp. 377–382, 1984.
[13] W. H. Stiles and F. T. Ulaby, "Dielectric properties of snow," The University of Kansas Center for Research, Inc., Remote Sensing Laboratory, Lawrence, Kansas, RSL Tech. Rep. 527-1, 1981.
[14] F. T. Ulaby, R. K. Moore, and A. K. Fung, *Microwave Remote Sensing: Active and Passive*, vols. I and III. Dedham, MA: Artech House, 1985.
[15] J. W. Battles and D. E. Crane, "Millimeter wave attenuation through snow," U.S. Naval Ordnance Lab., Corona, CA, NAVWEPS Rep. 8816, July 1965.
[16] N. C. Currie, F. B. Dyer, and G. W. Ewell, "Radar millimeter backscatter measurements from snow," Engineering Experiment Station, Georgia Tech., Atlanta, Georgia, Final Rep., Jan. 1977.
[17] A. Stogryn, "The bilocal approximation for the electric field in strong fluctuation theory," *IEEE Trans. Antennas Propagat.*, vol. AP-31, no. 6, pp. 985–986, Nov. 1983.
[18] ——, "A study of the microwave brightness temperature of snow from the point of view of strong fluctuation theory," *IEEE Trans. Geosci. Remote Sensing*, vol. GE-24, no. 2, pp. 220–231, 1986.
[19] V. Twersky, "On propagation in random media of discrete scatterers," in *Proc. Am. Math. Soc. Symp. Stochas. Proc. Math. Phys. Eng.*, vol. 16, pp. 84–116, 1964.
[20] A. Ishimaru, *Wave Propagation and Scattering in Random Media*, vols. I–II. New York: Academic, 1978.
[21] B. J. Choudhury, T. J. Schmugge, A. Chang, and R. W. Newton, "Effect of surface roughness on the microwave emission from soils," *J. Geophys. Res.*, vol. 84, pp. 5699–5706, 1979.
[22] E. J. Violette, R. H. Espeland, and P. Schwering, "Vegetation loss measurements at 9.6, 28.8, and 57.6 GHz through a pecan orchard in Texas," U.S. Army Communications-Electronics Command, Fort Monmouth, NJ, CECOM-83-2, 1983.
[23] M. T. Hallikainen and F. T. Ulaby, "A free-space system for dielectric measurements in the 3- to 18-GHz frequency range," Remote Sensing Laboratory, Univ. Kansas Center for Research, Inc., Lawrence, Ks., RSL Tech. Rep. 545-3.
[24] A. Stogryn, "Correlation functions for random granular media in strong fluctuation theory," *IEEE Trans. Geosci. Remote Sensing*, vol. GE-22, pp. 150–154, 1984.
[25] S. Evans, "Dielectric properties of ice and snow—A review," *J. Glaciol.*, vol. 5, pp. 773–792, 1965.
[26] M. Hallikainen, "Retrieval of snow water equivalent from Nimbus-7 SMMR data. Effect of land-cover categories and weather conditions," *IEEE J. Ocean. Eng.*, vol. OE-9, pp. 372–376, 1984.

Martti T. Hallikainen (M'83–SM'85) received the Engineering Diploma and the Doctor of Technology degree from the Helsinki University of Technology in 1971 and 1980, respectively.

He was a Post-Doctoral Fellow at the University of Kansas Remote Sensing Laboratory in Lawrence, KS, from 1981 to 1983, where his research involved microwave remote sensing and dielectric measurements of natural media. He is currently Professor of Aerospace Engineering (Remote Sensing), Helsinki University of Technology, where his research interests include passive and active microwave remote sensing and dielectric modeling of natural media.

Dr. Hallikainen is Secretary of the URSI National Committee in Finland.

•

Fawwaz T. Ulaby (M'68–SM'74–F'80) was born in Damascus, Syria, on February 4, 1943. He received the B.S. degree in physics from the American University of Beirut, Lebanon, in 1964 and the M.S.E.E. and Ph.D. degrees in electrical engineering from the University of Texas, Austin, in 1966 and 1968, respectively.

From 1968 to 1984, he was with the Electrical Engineering Department at the University of Kansas, where he was the J. L. Constant Distinguished Professor, and the University of Kansas Center for Research, where he was Director of the Remote Sensing Laboratory. He is currently Professor of Electrical Engineering and Computer Science, The University of Michigan, Ann Arbor. His current research interests involve microwave propagation and active and passive microwave remote sensing. Along with R. K. Moore and A. K. Fung, he is a coauthor of the three-volume series *Microwave Remote Sensing: Active and Passive* (Reading, MA: Addison-Wesley). In addition, he is coeditor of the *Manual of Remote Sensing*, 2nd ed., vol. I (American Society of Photogrammetry).

Dr. Ulaby is a member of Eta Kappa Nu, Tau Beta Pi, and Sigma Xi. He is the Executive Editor for the IEEE TRANSACTIONS ON GEOSCIENCE AND REMOTE SENSING, 1984–1988, and was the Geoscience and Remote Sensing Society's Distinguished Lecturer for 1986–1987. He received the GRS Society's Outstanding Service Award in 1982, and its Distinguished Service Award in 1983. In 1984, he also received a Presidential Citation for Meritorious service from the American Service of Photogrammetry and the IEEE Centennial Medal. He received the University of Kansas Chancellor's Award for Excellence in Teaching in 1980, the University of Kansas Gould Award for "distinguished service to higher education" in 1973, and the Eta Kappa Nu MacDonald award as an "outstanding electrical engineering professor in the United States of America" in 1975, the University College of Engineering Research Excellence Award in 1986, and the Kuwait Prize in applied science for 1986.

•

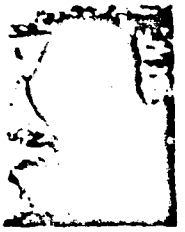

Tahera Emilie van Deventer was born in Hillerod, Denmark, on October 3, 1961. She received the Diplome Universitaire de Technologie from the Institut Universitaire de Technologie de Marseille (I.U.T.), France, in 1982, and the B.S.E. and M.S.E. degrees in electrical engineering from the University of Michigan, Ann Arbor, in 1985 and 1986, respectively. She is currently working toward the Ph.D. degree on the subject of scattering and attenuation by nonlinear media such as vegetation and snow.

She worked in the acoustic field for Bruel and Kjar from 1982 to 1985. Ms. van Deventer is a member of Tau Beta Pi and Eta Kappa Nu.

EXTINCTION COEFFICIENT OF DRY SNOW AT MICROWAVE AND MILLIMETERWAVE FREQUENCIES

Martti T. Hallikainen

Helsinki University of Technology
Radio Laboratory
Otakaari 5 A, 02150 Espoo, Finland

Fawwaz T. Ulaby, T. Emilie van Deventer

The University of Michigan
Radiation Laboratory
Ann Arbor, MI 48109, USA

Abstract

The extinction properties of several dry snow types were examined in the 18 to 90 GHz range. The snow types ranged from newly fallen snow to refrozen snow, and the density and mean grain size varied from 0.17 to 0.39 g/cm^3 and from 0.2 mm to 1.6 mm, respectively. From measurements of the transmission loss as a function of sample thickness at a temperature of -15°C, the extinction coefficient and the surface scattering loss (due to surface roughness at the front and back surfaces of the snow slab) were determined for each snow type. The experimental values were compared against theoretical results computed according to the strong fluctuation theory. In general, good agreement with the experimental data was obtained at 18, 35, and 60 GHz when the grain size used in the theoretical calculations was chosen to be slightly smaller than the observed snow particle size. However, the extinction coefficient of large grained refrozen snow as predicted by the strong fluctuation theory is much larger at 90 GHz than the values determined experimentally. The attenuation in snow was observed to increase only slightly with increasing temperature in the -35°C to -1°C range.

Keywords: Extinction coefficient, Snow, Attenuation

1. Introduction

At the present, experimental microwave dielectric data (real and imaginary part of the complex dielectric constant $\varepsilon_s = \varepsilon_s' - j\varepsilon_s''$) are available as follows: $\varepsilon_s' - j\varepsilon_s''$ for wet snow and ε_s' for dry snow at frequencies up to 37 GHz [1], and ε_s'' for dry snow at frequencies up to 13 GHz [2,3]. The temperature dependence of ε_s' is very small, whereas ε_s'' increases with increasing temperature. Since the frequency range of microwave sensors has been recently extended to 90 GHz, high-frequency data on the dielectric and scattering loss of dry snow are needed.

The total loss of dry snow is expressed by the extinction coefficient, which includes both absorption loss and scattering loss. At low microwave frequencies (snow particle size is much smaller than the wavelength) absorption is the primary loss process, whereas at high microwave and all millimeterwave frequencies (snow particle is of the same order of magnitude as wavelength) scattering dominates over absorption. According to Mie theory calculations for a snow particle with a diameter of 1 mm, scattering dominates at frequencies above 15 GHz [4].

Few experimental investigations on the attenuation of dry snow have been reported at millimeterwave frequencies [5,6]. However, the snow parameters were not documented in a detailed manner to allow the derivation of any quantitative expression for the extinction coefficient and the surface loss as a function of snow properties.

In the present investigation, the extinction coefficient and the surface loss for several snow types were obtained from transmission loss measurements of snow slabs as a function of sample thickness. The effects of frequency, snow particle size, snow metamorphism, and temperature were investigated in a detailed manner. The experimental results were compared with theoretical values obtained from the strong fluctuation theory [7]. Recent evaluations of this theory suggest that it can be applied to calculate the effective dielectric constant and the extinction coefficient of snow as well as the brightness temperature of snow-covered terrain.

2. Transmission Model for Snow Slab

The transmission of a plane wave through a slab of scatterers has been discussed previously [9,10]. The geometry of the problem is depicted in Figure 1. The total intensity incident on the slab is denoted by $I(0^-) = I_0$. The intensity transmitted through the air-snow interface is reduced by τ, the Fresnel power transmission coefficient, and by S, a surface roughness factor that accounts for scattering by a non-specular surface. A relatively simple model for S that has been used in connection with soil-surface scattering [11] takes the form

$$S = \exp[-(2k_0 s)^2] \quad , \qquad (1)$$

where $k_0 = 2\pi/\lambda_0$ and s is the effective rms height of the surface fluctuation. In practice, this model is reasonably adequate, although the value of s needed to match experimental data usually is smaller than the measured rms height of the surface.

Proceedings of IGARSS '87 Symposium, Ann Arbor, 18-21 May 1987

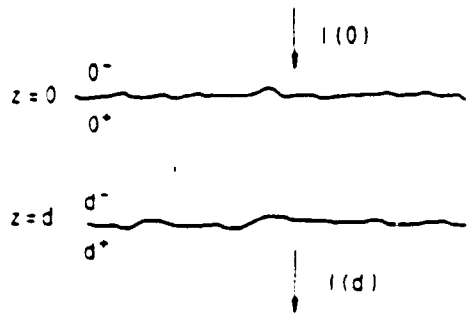

Figure 1. Transmission of electromagnetic wave through a slab of scatterers.

The total power transmitted across the boundary at z = d is

$$I(d^+) = I_0 T^2 S^2 [e^{-\kappa_e d} + q(e^{-\kappa_a d} - e^{-\kappa_e d})] \quad , \quad (2)$$

where q represents the fraction of the total scattered power intercepted by the beam angle of the receiving antenna, and κ_e, the extinction coefficient, is the sum of the absorption coefficient κ_a and the scattering coefficient κ_s,

$$\kappa_e = \kappa_a + \kappa_s \quad . \quad (3)$$

The loss factor L(dB) is defined as

$$L(dB) = -10 \log\left[\frac{I(d^+)}{I_0}\right]$$

$$= 34.72 k_0^2 s^2 - 10 \log[e^{-\kappa_e d} + q(e^{-\kappa_a d} - e^{-\kappa_e d})]; \quad T^2 = 1 \quad . \quad (4)$$

For a small slab thickness d such that $\exp(-\kappa_e d) >> q[\exp(-\kappa_a d) - \exp(-\kappa_e d)]$ the coherent intensity is the dominant contributor to I and (4) may be approximated as

$$L(dB) \approx L_s(dB) + 4.34\, \kappa_e d \quad , \quad (5)$$

where $L_s(dB) = 34.72 k_0^2 s^2$ is the loss factor attributed to surface roughness at the two slab boundaries. For a large slab thickness such that $\exp(-\kappa_e d) << q[\exp(-\kappa_a d) - \exp(-\kappa_e d)]$, the incoherent intensity modified by q becomes the only significant remaining component of the original incident power, and (4) may be approximated as

$$L(dB) \approx L_s(dB) - 10 \log q + 4.34\, \kappa_a d \quad . \quad (6)$$

Thus, because of multiple scattering, the rate of attenuation after propagation through a thick sample becomes proportional to κ_a rather than κ_e because the loss due to scattering is approximately equal to the generation of incoherent intensity by scattering.

According to the preceding model, if we measure the transmission loss factor L(dB) as a function of the slab thickness d, the following four parameters can be determined: (a) the extinction coefficient κ_e (from Slope 1 in Figure 2), (b) the absorption coefficient κ_a (from Slope 2 in Figure 2), (c) effective rms height of the surface s (from L_s), and (d) the parameter q (from the absolute level of the curve). It is relevant to note that the total attenuation of tree foliage has been observed to follow a behavior similar to that shown in Figure 2 [12].

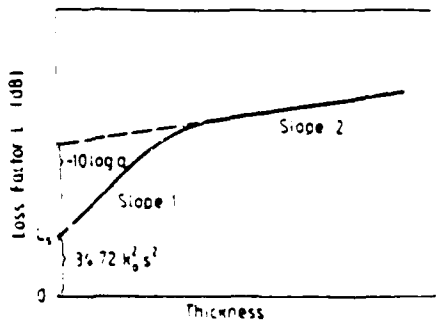

Figure 2. Plot of the transmission loss.

3. Experimental Arrangement

3.1 Snow Samples

All snow measurements were conducted under laboratory conditions at the Radio Laboratory of the Helsinki University of Technology. The snow samples were acquired from natural snow cover, including both the top and the bottom layers. Extreme care was taken not to disturb the structure of the samples. A total of 23 snow samples were acquired between February 5 and April 30, 1985 (Table I). The samples acquired in February were new snow, whereas those acquired in late March and April were refrozen snow.

The density of a sample was determined from its volume and mass. For cases 1 to 18 in Table I, these parameters were determined for every thickness of each snow sample in order to check for density variations. The density range among all the samples was 0.17 to 0.39 g/cm^3.

The average grain size and the surface roughness were determined from photographs taken with a macro lens. For photographs, small samples of each snow type were placed on a glass plate equipped with a millimeter scale. It is emphasized that, although extreme care was taken to provide accurate grain size estimates, the absolute values may have a bias. However, it is believed that the relative accuracy of the grain size estimates is good. For non-spherical snow particles, the mean grain diameter estimate is based on volume. In case of clustering, the particle size estimate is for individual crystals.

3.2 Measurement Procedure

The transmission loss for cases 1 to 18 (Table I) was measured at 10, 18, 35, 60, and 90 GHz using free-space transmission systems. In free-space transmission measurements, a sample is placed between the transmitting and receiving antennas and an electromagnetic plane wave is transmitted through the sample. The use of free-space [illegible]

Table I. Properties of snow samples. Samples 1 to 18 were measured as a function of sample thickness and samples 19 to 23 as a function of temperature.

No.	Date (1985)	Depth in Snowpack	Observed Mean Grain Size (mm)	Surface Roughness (mm)	Melt-Freeze Cycles	Clustering	Density (g/cm^3)	Dielectric Constant at 10 GHz	Comments
1	Feb. 5	Top	0.2	0	None	None	0.172	1.31	One-hour old snow
2	Feb. 15	Near Top	0.5	0	None	None	0.194	1.34	Newly fallen snow
3	Feb. 16	Near Top	0.7	0	None	None	0.217	1.39	Newly fallen snow
4	Feb. 19	Top	0.2	0	None	None	0.322	1.58	Wind-driven 5-day old snow
5	March 12	Top	0.3	0	None	None	0.277	1.52	
6	March 12	Middle	0.9	0	None	None	0.268	1.49	Separate grains
7	March 18	Near Top	0.4	0	None	None	0.235	1.41	Newly fallen snow
8	March 21	Near Bottom	1.0	1	None	None	0.215	1.58	
9	March 29	Top	1.0	1	Few	None	0.385	1.75	Hard snow
10	March 29	Near Bottom	1.0	1	None	None	0.276	1.50	Separate grains
11	April 7	Top	1.3	2 to 3	Some	Some	0.307	1.61	
12	April 11	Top	1.2	3	Some	Some	0.304	1.61	
13	April 11	Near Bottom	1.3	1 to 3	None	None	0.293	1.54	
14	April 13	Top	1.5	2 to 3	Some	Some	0.345	1.64	
15	April 13	Middle	1.1	1 to 2	Few	None	0.332	1.63	
16	April 16	Bottom	1.1	1 to 2	None	None	0.361	1.77	Separate grains; no continuous structure
17	April 17	Top	1.5	2 to 4	Some	Some	0.390	1.79	
18	April 30	Near Top	1.6	2 to 3	Several	Some	0.351	1.66	
19	March 18	Near Top	0.4	0	None	None	0.240	1.43	Acquired 1 m away from No. 7
20	March 29	Near Bottom	1.0	1	None	None	0.271	1.46	Acquired 1 m away from No. 10
21	April 7	Top	1.3	2 to 3	Some	Some	0.311	1.64	Acquired 1 m away from No. 11
22	April 13	Top	1.5	2 to 3	Some	Some	0.350	1.68	Acquired 1 m away from No. 14
23	April 17	Top	1.5	2 to 4	Some	Some	0.380	1.72	Acquired 1 m away from No. 17

for dielectric measurements is discussed in detail in [13]. In addition, the phase shift due to the sample was measured at 10 GHz for each sample thickness to provide ϵ_s'. Since ϵ_s' and the dry snow density ρ are related [1] by

$$\epsilon_s' = 1 + 1.9\rho \qquad (7)$$

in the microwave range, the measured ϵ_s' can be used to verify the density values.

After completing the measurement in the 10 to 90 GHz range each sample was cut thinner and the measurement procedure was repeated. The minimum sample thickness used in this investigation was 1.1 cm. During the measurements, the samples were handled and stored at -15°C. For cases 19 to 23, the transmission loss at each frequency was measured as a function of temperature in the -35°C to -1°C range. The sample thickness in each case was 10 cm. The first set of measurements was made at -35°C; the temperature was then increased to the next desired value and the measurements were repeated.

The sample holder and the lid (both made of styrofoam) provided the necessary thermal insulation during the measurement (the free-space transmission systems were at room temperature).

4. Experimental Results

4.1 Transmission Loss

The results of transmission loss measurements for different sample thicknesses are given in Figure 3. The sample numbers refer to those in Table I, giving the temporal order of measurements. The precision of the results in Figure 3 is estimated to be ±0.3 dB for the lowest values (~1 dB) and ±2 dB for the highest values (~50 dB). The measured loss values at 10 GHz are practically zero for all samples; hence, they are not shown.

The main observations from Figure 3 are (a) the transmission loss increases with increasing frequency and increasing grain size (see Table I), (b) the loss depends linearly on sample thickness at 18 and 35 GHz; at 60 and 90 GHz the nonlinearity of the relationship increases with increasing snow particle size, (c) the surface loss factor L_s (estimated by extrapolating the transmission loss down to zero sample thickness) is, in most cases, negligible at 18 and 35 GHz, but it may be as large as 20 dB at 60 and 90 GHz for refrozen snow.

Comparison of the experimental results shown in Figure 3 with the modal behavior in Figure 2 indicates that Slope 1 (extinction coefficient) can be easily estimated from the data in Figure 3, but that is not the case for Slope 2 (absorption coefficient). In order to obtain the absorption coefficient, the measurements should extend over a much larger range of sample thickness. This would have required the measurement system to be able to measure transmission losses as high as about 70 dB. The maximum loss the present free-space system at 90 GHz can measure is 55 dB.

The temperature dependence of the transmission loss was observed to be negligible in the -35°C to -10°C range (cases 19 to 23 in Table I). Between -10°C and -1°C the experimental loss increases with increasing temperature. The measured loss values are compared with theoretical results from the strong fluctuation theory in Section 5.

4.2 Extinction Coefficient and Surface Loss

The extinction coefficient and the surface loss were determined for each case by fitting a straight line to the measured transmission loss. For snow

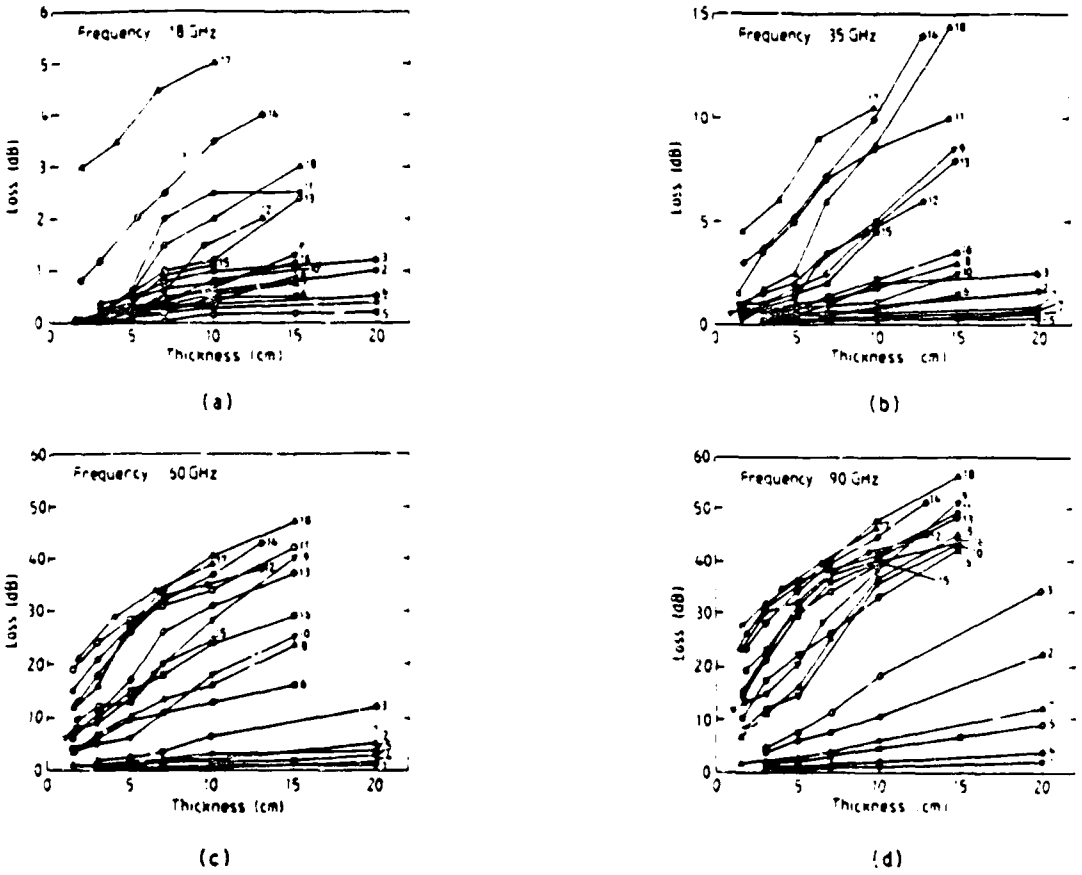

Figure 3. Measured transmission loss for snow samples. Sample numbers refer to those in Table I.

types exhibiting a quasi-linear relationship between L and d, all the data points were used. This was the case for all 18 and 35 GHz results and low-loss snow types at 60 and 90 GHz. For snow types exhibiting a nonlinear variation between L and d, only the data points falling on the first linear part of the curve (see Figure 2) were employed. Typically, the number of data points used in that case was three. The intercept of the straight line gives the surface loss factor L_s(dB).

The values of the extinction coefficient and the surface loss factor determined using the above procedure are listed in Table II. The values are given in decibels instead of nepers. To convert dB to Np, the values must be divided by 4.34.

The following empirical expressions were developed to relate κ_e(dB/m) to the observed snow particle diameter d_0:

$$\kappa_e = 1.5 + 7.4 d_0^{2.3} \quad ; \quad \text{(dB/m)} \quad \text{at 18 GHz} \quad (8a)$$

$$\kappa_e = 30\, d_0^{2.1} \quad ; \quad \text{(dB/m)} \quad \text{at 35 GHz} \quad (8b)$$

$$\kappa_e = 180\, d_0^{2.0} \quad ; \quad \text{(dB/m)} \quad \text{at 60 GHz} \quad (8c)$$

$$\kappa_e = 300\, d_0^{1.9} \quad ; \quad \text{(dB/m)} \quad \text{at 90 GHz} \quad (8d)$$

Table II. Experimental extinction coefficient and surface scattering loss for different snow types.

Sample no.	Extinction Coefficient κ_e(dB/m)				Surface Scattering Loss L_s(dB)			
	18 GHz	35 GHz	60 GHz	90 GHz	18 GHz	35 GHz	60 GHz	90 GHz
1	2.2	2.5	5.1	10.2	0.0	0.0	0.2	0.2
2	4.3	6.3	12.8	168.1	0.2	0.3	0.1	0.2
3	4.9	13.1	63.3	179.8	0.3	0.1	0.5	0.5
4	1.6	2.9	7.9	16.5	0.2	0.1	0.2	0.2
5	1.4	1.1	9.0	44.3	0.0	0.2	0.8	0.2
6	4.2	10.1	97.6	337.8	0.1	0.3	1.8	5.5
7	3.9	2.7	22.5	58.6	0.0	0.3	0.3	0.3
8	6.4	18.6	144.1	358.6	0.1	0.1	2.2	0.2
9	10.2	54.8	247.2	304.0	0.3	0.7	2.6	0.2
10	6.7	14.1	173.8	336.3	0.0	0.1	2.3	0.2
11	21.2	61.9	269.9	241.9	0.2	1.8	5.3	24.3
12	19.0	64.7	332.0	637.5	0.5	0.2	10.8	15.2
13	18.1	54.5	361.4	671.6	0.3	0.5	3.1	0.4
14	29.2	90.5	416.7	416.7	0.6	2.8	5.5	15.5
15	13.9	46.6	181.6	346.9	0.2	0.8	9.0	0.2
16	9.0	23.0	241.6	454.7	0.1	3.2	1.1	0.2
17	24.4	76.1	363.6	363.6	2.6	1.2	4.4	0.2
18	22.3	104.8	464.9	533.3	0.3	1.9	1.9	0.2

The observed grain diameter d_0 is in millimeters.

Equations (8a) to (8c) can be combined into a single equation of the form

$$\kappa_e = 0.0018 f^{2.8} d_0^{2.0} \quad \text{(dB/m)} \quad \text{for 18-60 GHz.} \quad (9)$$

In (9), f is in GHz and d_0 in millimeters. Equation (9) holds for particle sizes below 1.6 mm in the 18 to 60 GHz range. For 90 GHz, (8d) should be used instead.

From the surface loss values in Table II, the effective rms height was calculated from

$$s = \left[\frac{L_s}{34.72\ k_0^2}\right]^{1/2} , \qquad (10)$$

where L_s is the surface loss in dB and k_0 is the wave number in free space. The effective rms heights at 60 and 90 GHz are strongly correlated with

$$s_{60} = 0.019 + 0.958\ s_{90}\ (\text{mm}) , \qquad (11)$$

where s_{60} and s_{90} are the rms heights at 60 and 90 GHz, respectively. This relationship is very close to $s_{60} = s_{90}$, which is what the model in (2) would predict.

5. Comparison of Experimental and Theoretical Results

The strong fluctuation theory [7,8] was applied to calculate the effective complex dielectric constant of dry snow, ϵ_e, using an exponential correlation function [8,14]. The formulation for the effective dielectric constant ϵ_e accounts for both scattering and absorption by the ice particles in the snow medium. The extinction coefficient can be readily obtained from

$$\kappa_e = 2k_0 |\mathrm{Im}(\epsilon_e^{1/2})| . \qquad (12)$$

In order to calculate ϵ_e, we need to know ϵ_s, the quasistatic value of the dielectric constant of dry snow. For ϵ_s'', a mixing model from [4, E84] was adopted and for ϵ_s', (7) was assumed to hold in the present frequency range.

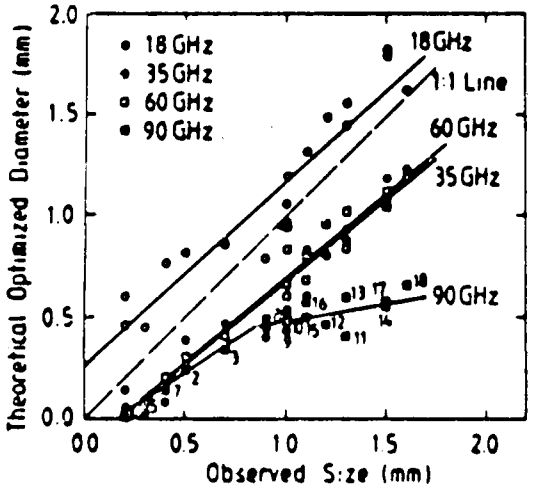

Figure 4. Theoretical optimized snow grain diameters as a function of observed snow particle size, with frequency as a parameter.

In order to compare the theoretical values of κ_e from the strong fluctuation theory with experimental data, theoretical values were computed for the 18 snow types. In each case, the snow density was kept constant, and the grain size was treated as a free parameter whose value was chosen such that it gave a theoretical extinction coefficient equal to the measured value. By repeating this for each of the 18 snow types, a set of model-derived grain sizes was obtained for each frequency.

Figure 4 is a scatter diagram of d_m, the model-derived grain sizes, versus the observed grain sizes, d_0. The model-derived values at 18 GHz are larger and those at 35, 60 and 90 GHz are smaller than the observed values. The linear expressions shown in Figure 4 are given by

$$d_m = 0.26 + 0.91\ d_0 \qquad \text{at 18 GHz} \qquad (13a)$$

$$d_m = -0.15 + 0.82\ d_0 \qquad \text{at 35 GHz} \qquad (13b)$$

$$d_m = -0.15 + 0.83\ d_0 \qquad \text{at 60 GHz} \qquad (13c)$$

$$d_m = \begin{cases} -0.11 + 0.67\ d_0 & \text{for } d_0 < 0.9 \text{ mm at 90 GHz} \\ 0.31 + 0.18\ d_0 & \text{for } d_0 > 0.9 \text{ mm at 90 GHz} \end{cases} \qquad (13d)$$

The slopes of the linear equations at 18, 35, and 60 GHz in (13) are reasonably close to 1. The experimental values of κ_e at 18 GHz may be biased, due to the low values of the transmission loss L (mostly below 1 dB) even for thick snow samples. It is remarkable that the expressions for d_m at 35 and 60 GHz are almost identical. This, combined with the similar slope at 18 GHz, strongly suggests that the strong fluctuation theory provides reasonably accurate results in the 18 to 60 GHz range for all realistic grain sizes, and also at 90 GHz for grain sizes smaller than 0.9 mm. The observed departure of the 90 GHz results for refrozen snow ($d_0 > 0.9$ mm) may be due to the fact that at 90 GHz the wavelength in ice is about 1.8 mm. This is comparable in size to the ice particles in refrozen snow; such a conditions is conducive to resonant scattering and absorption.

The following method was used to obtain an estimate to the temperature dependence of the extinction coefficient from the measured transmission loss values in the -35°C to -1°C range. It is assumed that (a) the surface scattering loss does not depend on temperature and (b) the surface scattering loss for each case is equal to that measured for its neighboring sample. For example, samples 19 and 7 were acquired from the same area (one meter apart) and from the same depth (Table I). Hence, the surface scattering loss can be subtracted from the transmission loss resulting in a value that accounts for the volume effects only,

$$L_v = L - L_s \ \text{(dB)} . \qquad (14)$$

In (14), L and L_s are the experimental transmission loss and the surface scattering loss, respectively. Although L_v divided by the sample thickness is equal to the extinction coefficient only when the data point is located on Slope 1 in Figure 2, the temperature behavior of L_v should give a reasonably good estimate for that of κ_e.

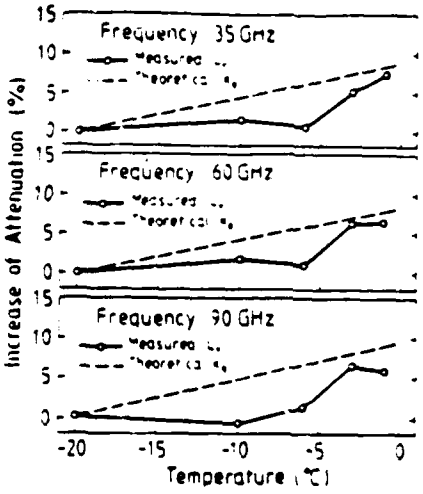

Figure 5. Snow attenuation as a function of temperature, with -20°C as a reference point. Experimental data: average values for snow types 19 to 23 (Table I).

L_v for cases 19 to 23 was calculated from (14) for each temperature used in the experiment. Since the values for -35°C and -20°C were practically the same for each case, the value observed for -20°C is used as a reference. The observed average increase from L at -20°C is depicted for 35, 60, and 90 GHz in Figure 5. The experimental values are slightly smaller than the theoretical behavior obtained from (12). The present values in Figure 5 are substantially smaller than the previously reported experimental increase of 100 % for L_v at 35 GHz [5].

6. Conclusions

The extinction coefficient and the surface loss factor for 18 dry snow types, ranging from newly fallen snow to refrozen snow, were measured in the 18 to 90 GHz range. The experimental results indicate that the extinction coefficient increases rapidly with increasing frequency and increasing average snow particle size. However, the extinction coefficient at 90 GHz exhibits a weaker dependence on grain size for snow with grain larger than 0.9 mm in diameter than for snow with smaller grains. The effect of temperature was examined in the -35°C to -1°C range; only a slight increase in snow attenuation with increasing temperature was observed. The surface loss factor (including both surface scattering and reflection loss) was found to be negligible at 18 and 35 GHz and quite substantial at 60 and 90 GHz. The magnitude of the surface loss factor was observed to be highly correlated with grain size.

The measured values of the experimental extinction coefficient were compared with theoretical values obtained using strong fluctuation theory. By matching the theoretical values (with grain size as a free parameter) to the measured values in each of the 18 cases, a set of model-derived grain sizes was obtained for each frequency. It is emphasized that, although the absolute accuracy of the observed grain sizes is difficult to establish, their relative accuracy is believed to be good. Good agreement between (a) the model-derived grain sizes at 35 and 60 GHz, (b) the slopes of the model-derived grain size versus observed grain size at all frequencies (only nonmetamorphosed snow at 90 GHz), and (c) the observed and calculated temperature dependence of the loss suggests that the strong fluctuation theory provides fairly accurate estimates of the extinction coefficient of dry snow at microwave and millimeterwave frequencies.

References

1 M Hallikainen, F T Ulaby, M Abdelrazik: Dielectric properties of snow in the 3 to 37 GHz range. IEEE Trans. Ant. Propagat. Vol. AP-34, pp. 1329-1340.

2 M Tiuri, A Sihvola, E Nyfors, M Hallikainen: The complex dielectric constant of snow at microwave frequencies. IEEE J. Oceanic Eng., Vol. OE-9, pp. 377-382, 1984.

3 W Stiles, F T Ulaby: Dielectric properties of snow. RSL Technical report 527-1, The Univ. of Kansas Center for Research, Inc., Remote Sensing Lab., Lawrence, Kansas, 1981.

4 F T Ulaby, R K Moore, A K Fung: Microwave Remote Sensing: Active and Passive. Vols. I and III. Addison-Wesley/Benjamin-Cummings, 1982, Dedham, MA: Artech House, 1985.

5 J W Battles, D E Crane: Millimeter wave attenuation through snow. U.S. Naval Ordnance Lab., NAVWEPS Report 8816, Corona, California, 1965.

6 N C Currie, F B Dryer, G W Ewell: Radar millimeter backscatter measurements from snow. Final Report, Engineering Experiment Station, Georgia Tech., Atlanta, Georgia, January 1977.

7 A Stogryn: The bilocal approximation for the electric field in strong fluctuation theory. IEEE Trans. Antennas Propagat., Vol. AP-31, No. 6, pp. 985-986, 1986.

8 A Stogryn: A study of the microwave brightness temperature of snow from the point of view of strong fluctuation theory. IEEE Trans. Geosci. Remote Sensing, Vol. GE-24, pp. 220-231, 1986.

9 V Twersky: On propagation in random media of discrete scatterers. Proc. Am. Math. Soc. Symp. Stochas, Proc. Math. Phys. Eng., Vol. 16, pp. 84-116, 1964.

10 A Ishimaru: Wave Propagation and Scattering in Random Media, Vols. I-II, Academic Press, New York, 1978.

11 B J Choudhury, T J Schmugge, A Chang, R W Newton: Effect of surface roughness on the microwave emission from soils. J. Geophys. Res., 84, pp. 5699-5706, 1979.

12 E J Vinlette, R H Espeland, F Schwering: Vegetation loss measurements at 9.6, 28.8 and 57.6 GHz through a Pecan Orchard in Texas. ECEOM-83-2, U.S. Army Communications-Electronics Command, Fort Monmouth, NJ, March 1983.

13 M Hallikainen, F T Ulaby: A free-space system for dielectric measurements in the 3- to 18-GHz frequency range. RSL Tech. Rep. 545-3, Remote Sensing Laboratory, Univ. of Kansas Center for Research, Inc., Lawrence, KS 66044, 1983.

14 A Stogryn: Correlation functions for random granular media in strong fluctuation theory. IEEE Geosci. Remote Sensing, Vol. GE-22, pp. 150-154, 1984.

MILLIMETER TRANSMISSION PROPERTIES OF FOLIAGE

T. E. van Deventer, J. R. East, and F. T. Ulaby

Radiation Laboratory
Department of Electrical Engineering and Computer Science
The University of Michigan
Ann Arbor, MI 48109-2122, USA

ABSTRACT

A compact indoor measurement system has been developed to study the transmission properties of foliage at 35 GHz. The system uses an up-converter and mixer-downconverter to extend the operating frequency range of a computer-controlled HP 8510 network analyzer to millimeter-wave frequencies. The system has been used to measure the transmission and scattering properties of two different types of trees for horizontal, vertical, and cross polarization.

Keywords: Radar scattering from trees, attenuation, bistatic scattering.

I. INTRODUCTION

Accurate models for microwave scattering by complex random structures, such as a tree canopy, are not existant. This is due, in part, to the lack of accurate scattering and extinction data for single scatterers (such as a leaf) and single trees. This is especially true in the millimeter-wave part of the spectrum. Relevant studies reported in the literature are given in [1] - [4]. This paper documents an attempt to examine some aspects of wave extinction and scattering by trees at 35 GHz. Using separate antennas for transmission and reception, a calibrated transmission system was used to measure the attenuation of individual trees as a function of azimuth position and of several trees placed in series. The measurements were conducted for two types of trees of markedly different structure. The system was also used to measure the bistatic radar cross-section of a tree as a function of the azimuth angle between transmitter and receiver. The combination of the direct transmission measurements and the bistatic scattering measurements provide a picture of the relative levels of coherent and incoherent scattering by the tree. Such measurements are strong indicators of the relative importance of diffuse scattering and how multiple scattering may be incorporated in volume scattering models.

II. EXPERIMENTAL SET-UP

The system used to measure the transmission and bistatic scattering properties of foliage is a Millimeter-Wave Polarimeter (MMP) [5]. The MMP is a network analyzer based scatterometer system that operates at 35 GHz. It was designed to be used in three configurations: backscatter mode, bistatic mode and transmission/reflection mode. In this laboratory experiment, the MMP is used in the bistatic mode. The transmitter and receiver sections are mounted as two independent units on poles of variable height and can be placed at the desired locations with respect to the target. The set-up is shown in Fig. 1 for the transmission mode.

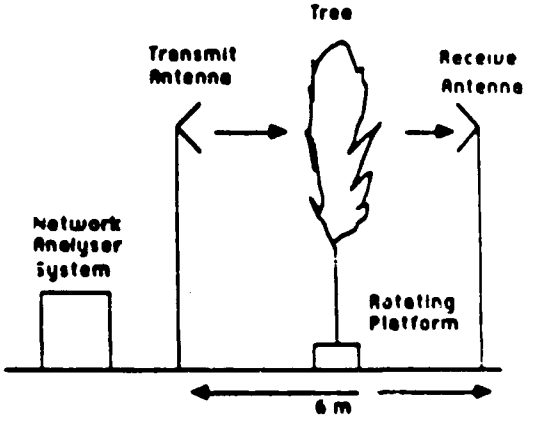

Fig. 1 - Transmission Measurement Set-Up

The MMP includes a swept-frequency source driven by the HP 8510 network analyzer. It sweeps in frequency from 2 to 4 GHz. The signal is sent to the transmitter section and is upconverted to 34-36 GHz using a mixer and fixed-frequency Gunn source operating at 32 GHz. The RF signal is transmitted via a lens-corrected horn antenna with a beamwidth. Part of the transmitted signal is sampled via a directional coupler and is downconverted to be the reference signal. The receiver section consists another horn antenna. Since the beamwidth

the receive and transmit antennas were of the order of 3°, an infrared beam was used to insure proper antenna alignment. The received signal is mixed down to the 2-4 GHz range and then sent to the test port of the HP 8510. The main characteristics of the system are summarized in Table 1.

Frequency	35 GHz
IF Bandwidth	1-2 GHz
Polarization	HH, HV, VV
Platform Height	1.75 m
Antenna Beamwidth	3°
Polarization Isolation	> 24 dB

Table 1 - MMP System Characteristics

Calibration of the system is accomplished by referencing the received power level with the target between transmitter and receiver to that received for free-space. The system is calibrated for each polarization configuration. Calibration for HH (both transmit and receive antennas horizontally polarized) and VV polarization configurations is straight forward, but calibration of HV polarization is not so straight forward for the transmission mode. The ratio of the free space measurements in the HV mode to that in the HH (or VV) mode provides a measure of the polarization isolation of the two antennas in combination. If we regard the transmission problem as a forward-scattering problem, rather than as an extinction problem, the received power in the HV mode in the presence of a tree should be compared to the received power in the HH mode under free-space conditions in order to determine the forward scattering cross-section of the tree.

Measurements were conducted for two different types of trees, ficus and pine trees. They were chosen because they are distinctly different in appearance and geometrical structure. The ficus tree (Ficus Nitida-Green Gem) has small flat, untoothed pine leaves approximately 10 cm^2 in area (see Fig. 2(a)). The pine tree is an eastern Arbor Vitae with a branched trunk and a conical crown of short, spreading branches in the vertical direction. It has narrow needles approximately 1.5 to 3mm in length (see Fig 2(b)). More detailed information about the trees examined in this study is given in Table 2 and shown in Fig 3. The dielectric constant of the leaves and trunk were measured up to 20 GHz using the coaxial line method. The results were compared to a dielectric model for vegetation [6], where the input parameters are the frequency of operation and the gravimetric moisture. The trees were kept in their pots and did not undergo any major changes during the experiment. However differences as large as ±5 dB were observed for some of the trees between measurements taken a week apart. This is attributed to the fact that these trees lost some leaves during that period of time, and the moisture content of the remaining leaves may have changed also.

Fig. 2(a) - Photograph of the Crown of the ficus tree

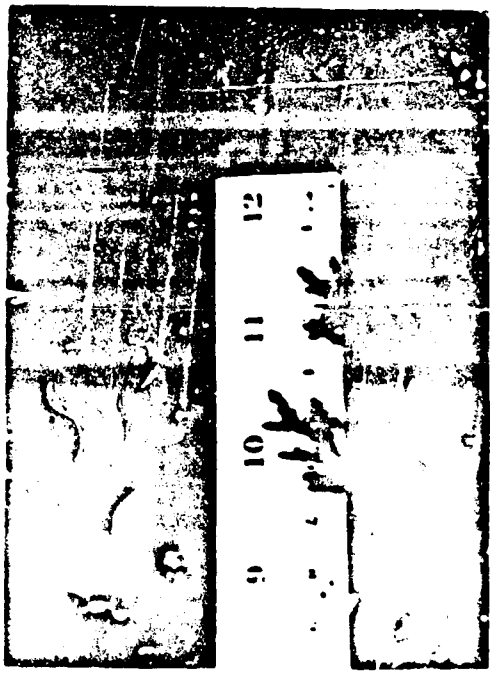

Fig. 2(b) - Close-Up Photograph of the pine tree

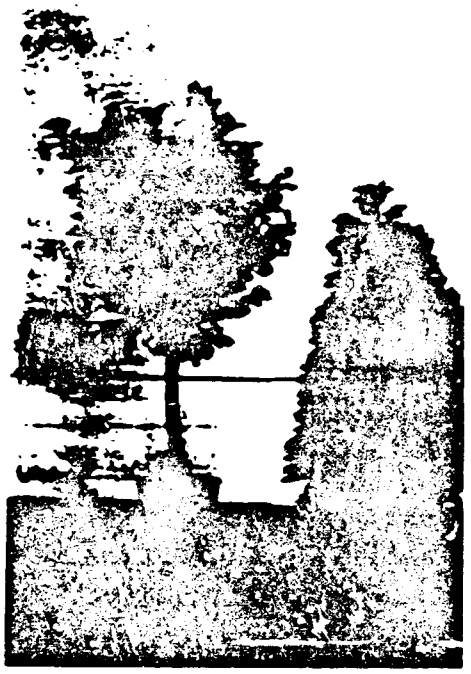

Fig. 3 - Photograph of the Relative Height of the trees

	Ficus	Pine
Tree Height	1.6 m	1.4 m
Tree width (crown)	> 1 m	80 cm
Trunk Diameter	4 cm	2 cm (*)
Leaf/ Needle area	10 cm2	15 cm2
Gravimetric moisture (leaves)	0.74	0.55

* for the pine tree, no main trunk, but vertical stems of diameter 1.4"

Table 2 - Tree Information

III. RESULTS

3.1 Transmission Measurements

For the single-tree experiments, the tree was placed on a rotating platform at 3 m from the transmit and receive antennas. That distance corresponded to the far field of the antennas. The transmission loss did not seem to depend on the tree's location between the two antennas. The transmit antenna, the receive antenna, and the tree crown were at the same height and arranged such that the receive antenna was an azimuth angle of 180°. The received signal was measured as a function of rotation angle over 360°. The area covered by the beam on the tree was about 0.02 m^2 and therefore was well within the crown of the tree.

A statistics test was performed to determine the number of samples N necessary to obtain a standard deviation S_N for the average μ_N of N samples such that $S_N / \mu_N \simeq 0.2$. If the samples are statistically independent, $S_N = S / \sqrt{N}$ where S is the standard deviation associated with a single measurement. The number of samples N is equal to $360^\circ / \Omega$, where Ω is the spacing between measurements in degrees. From N transmission measurements, the mean μ_N and standard deviation S are readily computed and then used to determine S_N. The plot shown in Fig. 4 is based on measurements made for various sampling intervals extending from one sample every 5° (i.e., a total of 72 samples per rotation) to one sample every 180° (i.e., 2 samples per rotation). From Fig. 4 one can see that sampling every 5° around the tree gives the desired precision. Hence, most of the data acquired in this study represents averages of 72 samples obtained by rotating the tree about its axis.

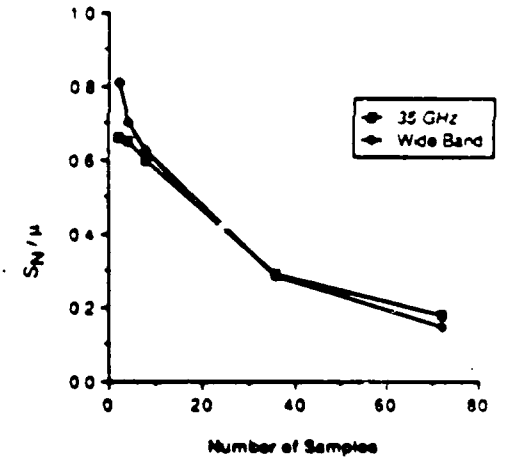

Fig. 4 - Statistics test on the ficus

The output data of the system was in terms of the magnitude of the received power calibrated with respect to free-space attenuation. The total tree attenuation includes absorption loss and scattering loss. At lower frequencies, absorption is the main contribution, but at millimeter-wave frequencies scattering loss becomes an important factor because leaves are of the same order of magnitude as the wavelength.

Frequency averaging over the 2 GHz bandwidth of the MMP system was used to reduce fading effects, whenever applicable. Plots of the attenuation versus rotation angle are shown in Fig. 5(a) for the pine and in Fig. 5(b) for the ficus. The difference between the single-frequency attenuation data and the 2-GHz averaged attenuation data is on the order of only 0.3 dB. This indicates that the transmitted wave is essentially totally coherent. In contrast, for bistatic scattering at $\phi = 90^{0}$, frequency averaging produces results that are significantly different from single-frequency results because the scattered signal is essentially incoherent in nature.

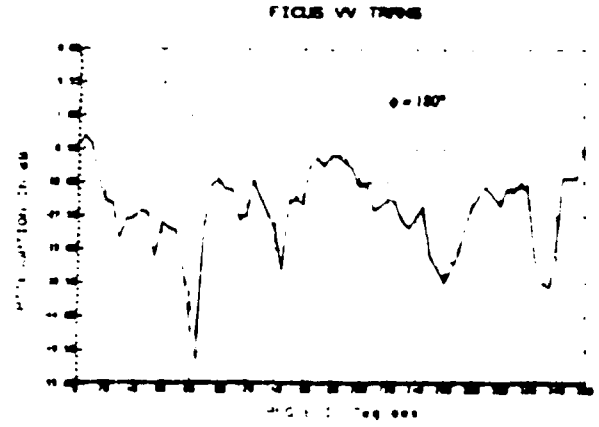

Fig. 5(a) - Attenuation vs. rotating angle for the ficus tree ($\phi = 180°$) showing the physical asymetry of the tree

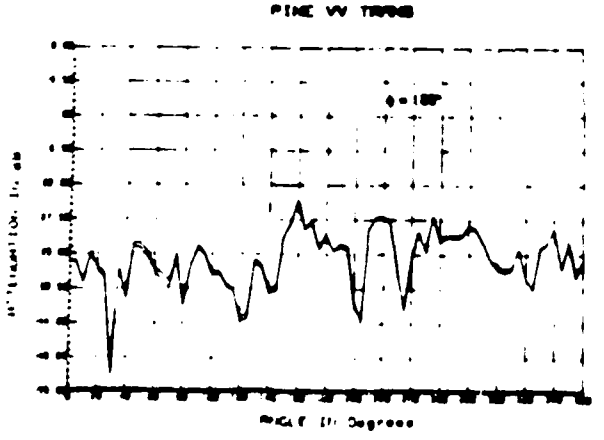

Fig. 5(b) - Attenuation vs. rotating angle for the pine tree ($\phi = 180°$)

Polarization information gives an insight into the geometry of the tree. At lower frequencies, one would expect the VV return to be stronger than other polarizations because of the orientation of the main branch (continuation of the trunk). At millimeter frequencies no major difference have been detected when comparing the two types of trees for HH polarization (0.4 dB). However the two trees exhibit very different attenuation values for VV polarization (7.5 dB). This is due to the vertical structure of the branches (see Table 3).

	FICUS	PINE
HH	-28.5 dB	-28.1 dB
VV	-27.1 dB	-34.6 dB

Table 3 - Transmission loss for the types of trees

For cross polarization (horizontal transmission, vertical reception), the depolarization ratio of the system was of the order of -24 dB. With the tree present, the received signed level for HV polarization was 19.4 dB below that received for VV polarization for the ficus. This difference in level is indicative of the degree of multiple scattering that takes place in the foliage. If the medium consists of randomly oriented scatterers and strong multiple scattering takes place in it, the HV-polarized signal would approach the like-polarized signal if the path length is sufficiently long to allow incoherent scattering to become the dominant component. In contrast to the ficus tree, the received HV - polarized signal for the pine tree was greater than the VV - polarized signal (15 dB) indicating that depolarization is more pronounced in pine than in ficus.

Attenuation measurements versus foliage depth were also performed by adding some trees in the transmission path. The penetration depth at a certain frequency is dependent upon the geometry of the tree, the volume percentage of foliage and the water content of the tree. The power level was recorded while the trees were rotated about their axis of symmetry for N positions of the two trees. The N positions were selected by a random number generator from 360° of 360° possible positions. The same procedure was used for three trees. From Fig. 6, it is possible to observe the nonlinear behavior of attenuation versus foliage depth; i.e., the attenuation in decibels increases with foliage depth at a rate slower than linear. This is in agreement with data obtained by Violette et al. [6]. Moreover, similar trends have been observed for transmission loss through snow [7].

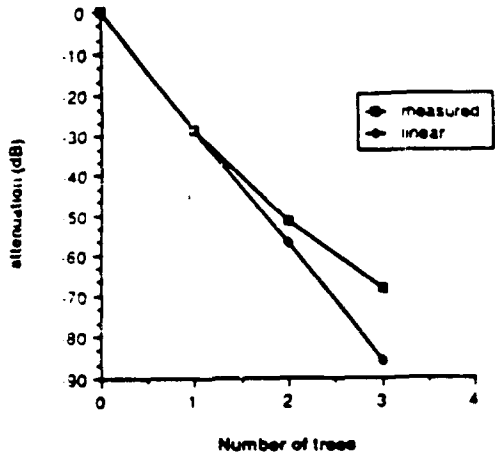

Fig. 6 - Attenuation (dB) for several trees placed in series in the measurement path

3.2 Bistatic Measurements

Similar measurements were conducted in the bistatic mode for a single tree to gain information about bistatic scattering of a tree as a function of the azimuth angle ϕ (see Fig. 7). With the transmitter remaining fixed in location and orientation and the tree remaining fixed in location, the receiver was moved to several locations on the perimeter of a circle as shown in Fig. 7. At each location, the received signal was measured as the tree was made to rotate about its axis. Plots of the power measured versus rotation angle of the tree for $\phi = 90^0$ are shown in Fig. 8. The single-frequency pattern is quite different from that averaged over a bandwidth of 2 GHz.

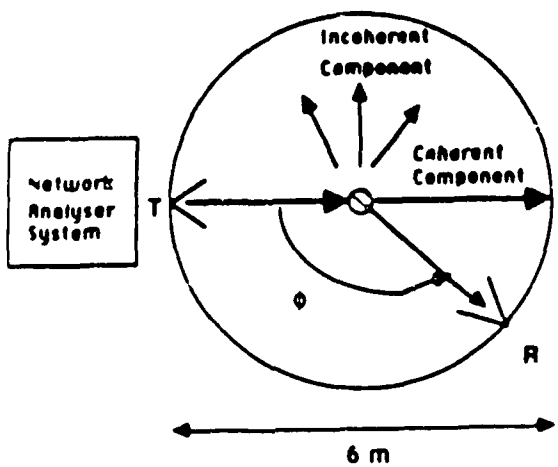

Fig. 7 - Bistatic Measurement Set-Up (top view)

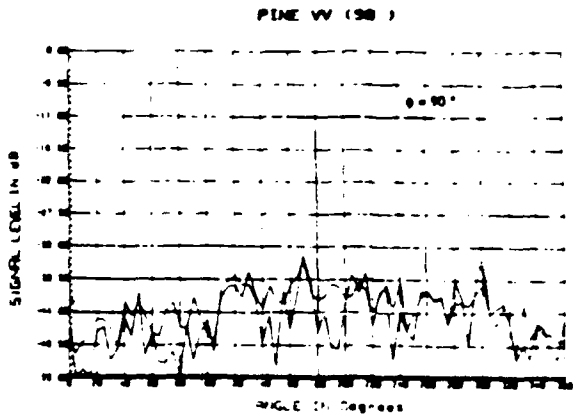

Fig. 8 - Attenuation vs. rotating angle for the pine tree ($\phi = 90°$)

For line-of-sight free-space propagation conditions (calibration configuration), one can use the Friis transmission formula to define the calibration power.

$$P_c = P_t\, G_t\, G_r \left(\frac{\lambda}{4\pi R}\right)^2 \qquad (1)$$

where R is the distance between the two antennas The radar equation for bistatic scattering is given by

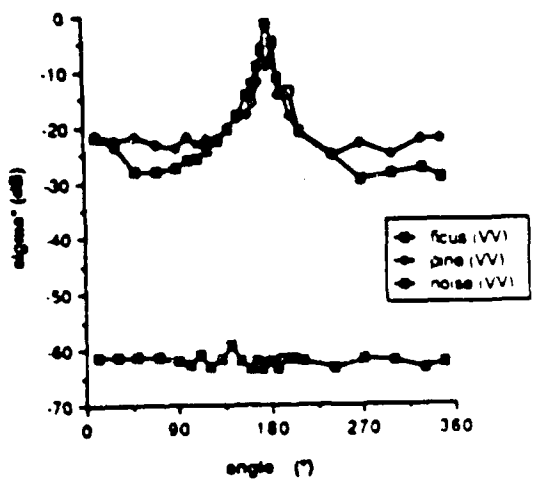

Fig 9 - Bistatic Scattering Measurement for VV polarization as a function of azimuth angle ϕ

$$P_r = P_t G_t G_r \frac{\lambda^2}{(4\pi)^3 R_t^2 R_r^2} \sigma \qquad (2)$$

where $R_t = R_r = R$ 2, and σ is the bistatic radar cross-section of the target. As mentioned earlier, the total projected area of the beam on the tree is about 0.02 m^2. Since the beam is within the crown and covers a good number of scatterers (the foliage can be described as a collection of randomly oriented scatterers), the area-extensive form of the radar equation can be used:

$$P_r = 16 P_t \frac{G_t G_r \lambda^2}{(4\pi)^3 R^4} A \sigma^0 \qquad (3)$$

where A is the illuminated area. Combining (2) with (3) leads to

$$\frac{P_r}{P_c} = \beta^2 \sigma^0 \text{ or } \sigma^0 (dB) = \frac{P_r}{P_c} (dB) - \beta^2 (dB)$$

where β is the antenna beamwidth (3^0)

Figures 9-11 show plots of σ^0 as a function of azimuth angle ϕ for VV polarization, HH polarization, and HV polarization, respectively. For the pine tree (VV polarization), the attenuation at $\phi = 180^0$ is larger than at 170^0 and 190^0. This is because the trunk of the tree exhibits strong attenuation for the V-polarized wave (E parallel to the trunk) in the forward scattering direction. In general, the like-polarized patterns have narrower main lobes in the forward scattering direction ($\phi = 180^0$) than those of the cross-polarized patterns. For VV polarization, the bistatic scattering pattern was carried out from $\phi = 10^\circ$ to $\phi = 350^\circ$. Surprisingly, despite of difference in canopy structure, the two types of trees exhibit comparable bistatic scattering patterns.

4. CONCLUSION

The data presented in this paper demonstrates the utility of transmission and bistatic scattering data for developing an understanding of the nature of the scattering that takes place in an anisotropic inhomogeneous medium such as foliage. In future phases of this program, additional data will be acquired and appropriate scattering models will be developed and examined.

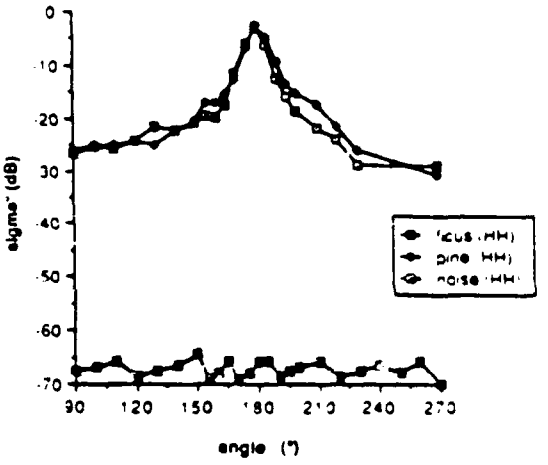

Fig. 10 - Bistatic Scattering Measurement for H
polarization as a function of azimuth angle

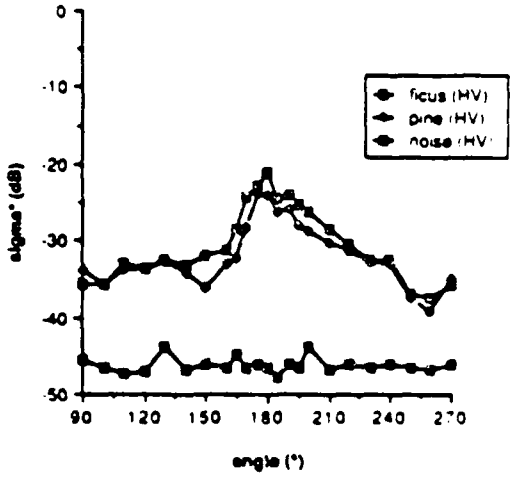

Fig. 11 - Bistatic Scattering Measurement for HV
polarization as a function of azimuth angle

ACKNOWLEDGMENTS

The authors would like to thank Roger de Roo for his help in the measurements.

REFERENCES

[1] Ulaby, F.T., R.K. Moore, A.K. Fung, Microwave Remote Sensing, Active and Passive, vol. III, Artech House, 1986, pp. 1882-1892.

[2] Currie, N.C., F.B. Dyer, E.E. Martin, "Millimeter Foliage Penetration Measurements", 1976 Int. IEEE Antennas and Propag. Soc. Symp. Digest, Amherst, MA.

[3] Graf G., B. Roce, "Radar Scattering from a solitary fir tree", Proc. of IGARSS' 82 Symposium, Munchen, June 1982.

[4] Violette E.J., R.H. Espeland, F. Schwering, "Vegetation loss Measurements at 9.6, 28.8 and 57.6 GHz through a Pecan Orchard in Texas", CECOM-83-2-, U.S. Army Communications Electronics Command, Fort Monmouth, NJ, March 1983.

[5] Ulaby, F.T., T.F. Haddock, J.R. East and V.V. Liepa, "Millimeter-wave Network Analyzer Based Scatterometer", Proc. of IGARSS '86 Symposium, Zurich, Sept. 1986.

[6] Ulaby, F.T., M.A. El-Rayes, "Microwave Dielectric Spectrum of Vegetation, Part II: Dual Dispersion Model", submitted for publication in IEEE Trans. on Geosc. and Remote Sensing, 1987.

[7] Hallikainen M.T., F.T. Ulaby, T.E. van Deventer, "Extinction Behavior of Dry Snow in the 18 to 90 GHz range", Proc. of IGARSS '87 Symposium, Ann Arbor, May 1987.

Millimeter-Wave Bistatic Scattering From Ground and Vegetation Targets

FAWWAZ T ULABY, FELLOW, IEEE, TAHERA E VAN DEVENTER, STUDENT MEMBER, IEEE, JACK R EAST, MEMBER, IEEE, THOMAS F HADDOCK, MEMBER, IEEE, AND MICHAEL EUGENE COLUZZI, STUDENT MEMBER, IEEE

Abstract—A 35-GHz bistatic radar system was used to measure the attenuation through trees and the bistatic scattering pattern of tree foliage. The data was found to be in good agreement with a first-order multiple scattering model. Measurements were also made to study the angular variation of the bistatic scattering coefficient of a smooth sand surface, a rough sand surface, and a gravel surface. The measurements, which were made for HH, HV, and VV polarization configurations over a wide range of the azimuth angle ϕ and the scattering angle θ_s, provide a quantitative reference for the design and use of millimeter-wave bistatic radar systems.

I. Introduction

THERE IS A dearth of data available on the millimeter-wave backscattering properties of terrain surfaces, but by comparison, bistatic data is almost nonexistent. The only bistatic data of note were measured in the late 1950's at 1.15 GHz [1] and in the mid-1960's at 10 GHz [2]. The scarcity of bistatic data is due, in part, to the fact that bistatic radar measurements are more difficult to make than monostatic measurements, and this is especially true at millimeter wavelengths.

This paper documents the results of an experimental investigation conducted to examine the extinction and bistatic scattering behavior of trees and the bistatic scattering patterns of smooth and rough ground surfaces, all made at 35 GHz.

II. Measurement System

The data reported in this paper were acquired by the 35-GHz channel of the millimeter-wave polarimeter (MMP) [3] operated in the bistatic mode (Fig. 1). The MMP includes a swept-frequency source driven by a HP 8510A vector network analyzer. It sweeps in frequency from 2 to 4 GHz. The signal is sent to the transmitter section and is upconverted to 34–36 GHz using a mixer and fixed-frequency Gunn source operating at 32 GHz. The RF signal is transmitted by a lens-corrected horn antenna with a beamwidth of 4.2°. The transmitter section also contains a fixed-frequency source operating at 10.7 GHz. Part of the swept 34–36 GHz transmitted signal is sampled by a directional coupler and then mixed with the third harmonic of the 10.7 GHz using a harmonic downconverter to produce a 2–4 GHz swept frequency signal for the reference port of the HP 8511A frequency converter (port a, in Fig. 1). The receiver section consists of another antenna and another harmonic downconverter. A sample of the 10.7-GHz signal transmitted from the transmitter section to the receiver section through a 10-m-long low-loss coaxial cable serves as the local oscillator signal at the receiver. Thus, all cables connecting the transmitter section and the receiver section with the HP 8510A (and associated peripherals) carry 2–4 GHz signals and the cable connecting the transmitter to the receiver carries a 10.7-GHz signal. This design arrangement makes it possible to operate the radar system in a bistatic mode while maintaining phase coherence between the transmitted and received signals. A summary of the system characteristics is given in Table I.

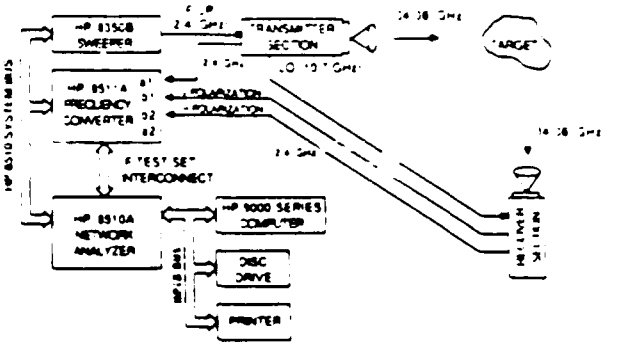

Fig. 1. Block diagram of the 35-GHz channel of the MMP when operated in the bistatic mode.

The system was used in a laboratory setting for measuring the power scattered from trees and from sand and gravel surfaces, as discussed next.

III. Measurement of Foliage Attenuation and Bistatic Scattering

Two types of measurements were conducted for trees: 1) transmission measurements to determine the attenuation rate versus the number of trees in the transmission path, and 2) bistatic scattering measurements to evaluate the azimuthal variation of the bistatic scattering coefficient. The configurations used are sketched in Fig. 2. In both cases, the transmitter and receiver antennas were mounted on poles at the same height above the ground and

Manuscript received October 9, 1987; revised December 30, 1987.

The authors are with the Department of Electrical Engineering and Computer Science, The University of Michigan, Ann Arbor, MI 48109-2122.

IEEE Log Number 8820213.

0196-2892/88/0500-0229$01.00 © 1988 IEEE

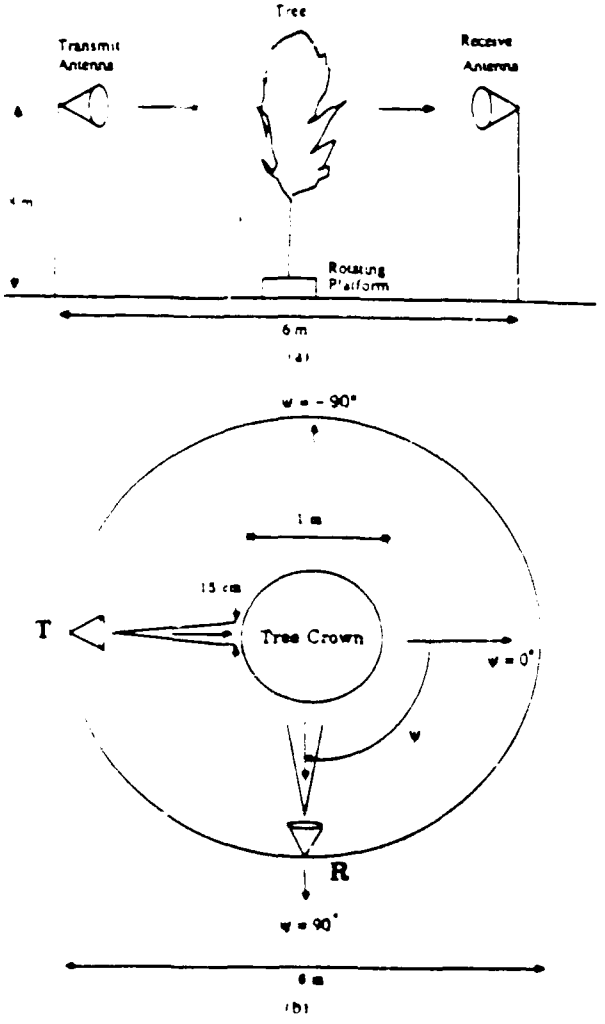

Fig. 2. Configurations used for measuring (a) foliage attenuation and (b) bistatic scattering from trees. For measurements involving more than one tree in the transmission path, the distance between the transmitter and receiver antennas was increased to 8 m.

TABLE I
CHARACTERISTICS OF THE MMP SYSTEM

Frequency	34–36 GHz in 494 steps of [illegible] each
RF Bandwidth	Variable from 1 to 2 GHz
Polarization	HH, HV, VV, VH
Transmit Antenna Beamwidth	4.2°
Receive Antenna Beamwidth	4.2° for Attenuation Measurements 12° for Bistatic Scattering Measurements
Polarization Isolation	> 45 dB

the transmitter remained stationary throughout both experiments. Because the beamwidths of both transmit and receive antennas were on the order of 4.2°, an infrared beam was used (prior to placing the trees in the transmission path) to insure proper antenna alignment.

Two distinctly different types of trees were selected for examination in this study: Ficus and Arbor Vitae (Fig. 3). The Ficus tree (Ficus Nitida-Green Gem) has small, flat, simple leaves approximately 10 cm² in area (Fig. 4). The

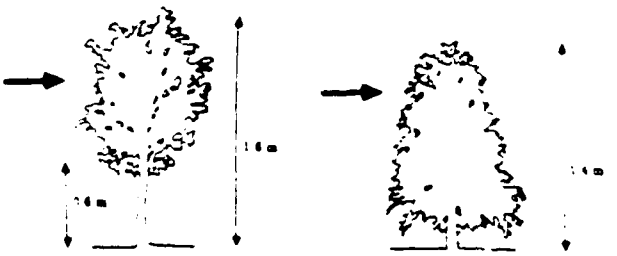

Fig. 3. Sketches of tree architectures.

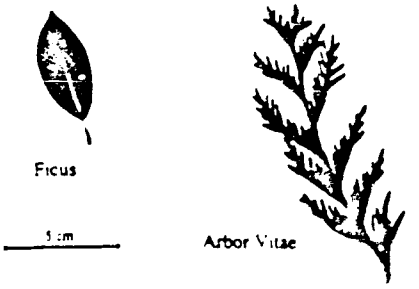

Fig. 4. Photographs of a Ficus leaf and an Arbor vitae branch.

TABLE II
FOLIAGE INFORMATION

	Ficus	Arbor Vitae
Tree Height (above platform)	1.6 m	1.4 m
Crown Width	1.0 m	0.6 m
Trunk diameter @ 1 m height	4 cm	2 cm
Leaf Moisture Content	0.74	0.55
Dielectric Constant at 35 GHz	16 − j11	11 − j6
Leaf Biomass (kg/m³)	2.4	—

Arbor Vitae had a branching trunk arrangement and a conical crown of short upwardly spreading branches. Its needles were approximately 1.5–3 mm in length (Fig. 4). Additional information about these trees is given in Table II. The complex dielectric constants of the leaves and trunk at 35 GHz were estimated by extending 1–20 GHz dielectric measurements that were made using a coaxial probe [4] to 35 GHz by applying a dielectric model that was recently developed for vegetation [5]. Over the experiment duration, the trees were kept in pots and did not undergo major changes; however, differences as large as ±5 dB were observed between transmission measurements made a week apart. These variations are attributed to the loss of a few leaves and to possible changes in moisture content.

A. Single-Tree Attenuation Measurements

For the single-tree experiments, the tree was placed on a rotating platform at 3 m from the transmit and receive antennas. The antennas were placed at an identical height of 1.8 m that provided transmission through the central region of the crown. The crown was approximately [illegible] in diameter for the Arbor Vitae tree and 1 m for the Ficus. Thus, the distance between each of the antennas and the outer edge of the tree crown was about 2 m. The [illegible]

this spacing was sufficient to satisfy the far-field condition, transmission measurements were made for several locations of the tree between the two antennas extending from one extreme of placing the center of the tree only 2 m from the transmit antenna and 4 m from the receive antenna up to the opposite extreme of placing the center of the tree at 2 m from the receive antenna. The transmission loss was found to be approximately independent of the tree's location between the two antennas (variation $\cong$ 2 dB).

The received signal was first measured with no trees present in the transmission path. This provided the free-space reference level P_0. Then, with the tree standing on a rotatable platform placed midway between the two antennas, the received power was measured as a function of rotation angle over 360°. The area of the tree illuminated by the antenna beam was a circle approximately 15 cm in diameter (and 0.02 m^2 in area) which was well within the crown of the tree. The attenuation A is related to the received power P through

$$P = P_0 e^{-A} \tag{1}$$

and in decibels

$$A(dB) = 4.34\,A = 10 \log (P_0/P). \tag{2}$$

Plots of the measured attenuation versus rotation angle are shown in Fig. 5(a) for the Ficus tree and in Fig. 5(b) for the Arbor Vitae tree. We observe that $A(dB)$ exhibits large fluctuations, particularly for the Ficus tree, which are attributed to the physical asymmetry of the trees. For each tree, two plots are shown, one corresponding to CW measurements at 35 GHz and another corresponding to measurements of the received power when averaged over a 2-GHz band centered at 35 GHz. The difference between the single-frequency data and the 2-GHz averaged attenuation is on the order of only 0.3 dB. This indicates that the transmitted wave is essentially totally coherent, and that the relative contribution of multiple scattering is negligible. In contrast, for bistatic scattering at an azimuth angle $\Psi = 90°$ (with Ψ as defined in Fig. 2(b)), frequency averaging produces results that are significantly different from single-frequency results (as discussed later in connection with Fig. 6) because the bistatically scattered signal, being a result of diffuse scattering, is essentially incoherent in nature.

Table III presents a summary of the attenuation results, including the mean values of the measured attenuation and the calculated standard-deviation to mean ratio. For the Ficus tree, the mean attenuation is approximately the same for both horizontal (H) and vertical (V) polarizations, but for the Arbor Vitae tree the mean attenuation for vertical polarization, $A_V(dB)$, is 6.5 dB greater than $A_H(dB)$. The wave polarization is defined as V when the E field is in the vertical direction, and as H when E is in the plane parallel to the ground surface. The higher attenuation for [illegible] fact that its branches and needles were oriented more along the vertical direction than along the horizontal, in contrast with the Ficus tree whose leaves were essentially randomly oriented.

B. Propagation Model

Except for the main trunk, tree foliage consists primarily of randomly distributed leaves (or needles) and branches, most of which are much larger than the wavelength in size (at millimeter wavelengths), have complex shapes, and are characterized by a quasi-uniform orientation distribution. These properties suggest that whereas individual scattering elements may exhibit highly complex and polarization-dependent scattering patterns, an elemental volume dV containing many of these elements is likely to exhibit propagation and scattering properties that are weakly polarization-dependent and characterized by a relatively simple scattering pattern. This prediction is supported by the observations made in this study that show that measurements of both the transmission through and the bistatic scattering from trees exhibit comparable results for H and V polarizations.

The random nature of the tree foliage supports the use of transport theory [6] for modeling wave propagation through the canopy [7]. We shall consider the foliage to be comprised of randomly distributed particles with number density N (number of particles per unit volume) and average extinction, total scattering, and bistatic scattering cross sections σ_e, σ_s, and σ_{bs}, respectively. By *average*, we mean that

$$\sigma_e = \frac{1}{N} \int_0^\infty \sigma_e(D)\, n(D)\, dD \tag{3}$$

where $n(D)$ is the particle size distribution and $\sigma_e(D)$ is the extinction cross section of a particle of size D. Similar definitions apply to σ_s and σ_{bs}, as discussed by Ishimaru in [6, p. 74].

The bistatic scattering cross section σ_{bs} is assumed to be azimuthally symmetric with respect to the forward-scattering direction ($\Psi = 0°$ in Fig. 2(b)). Thus

$$\sigma_{bs}(\Psi) = \sigma_s g(\Psi) \tag{4}$$

and since

$$\sigma_s = \frac{1}{4\pi} \int_{4\pi} \int \sigma_{bs}(\Psi)\, d\Omega \tag{5}$$

the scattering pattern $g(\Psi)$ has to satisfy the condition

$$\frac{1}{4\pi} \int_{4\pi} \int g(\Psi)\, d\Omega = 1. \tag{6}$$

In their analysis of millimeter-wave propagation through trees, Schwering and Johnson [7] proposed a scattering pattern of the form

$$g(\Psi) = \alpha f(\Psi) + (1 - \alpha)$$

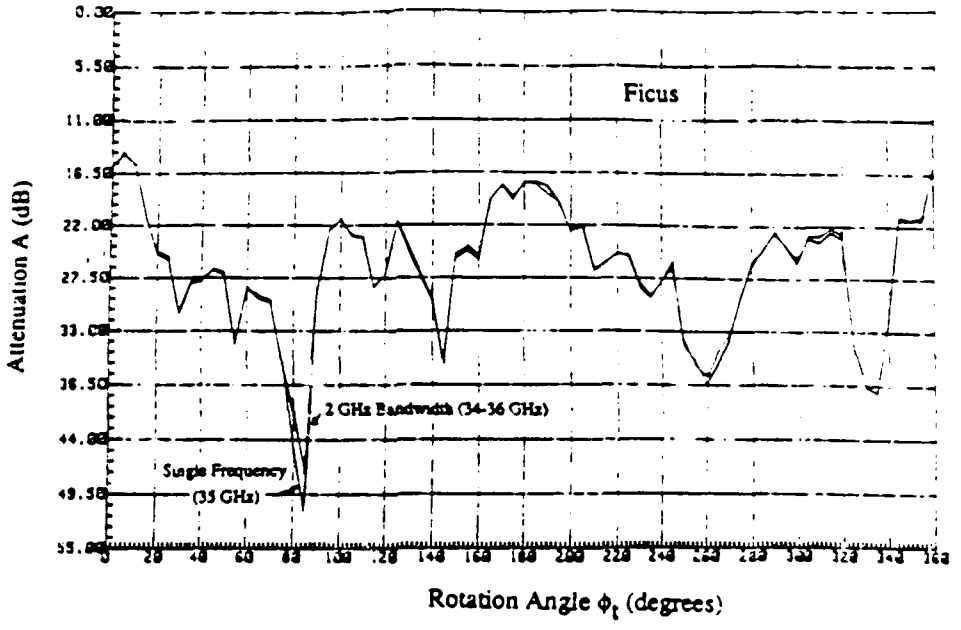

(a)

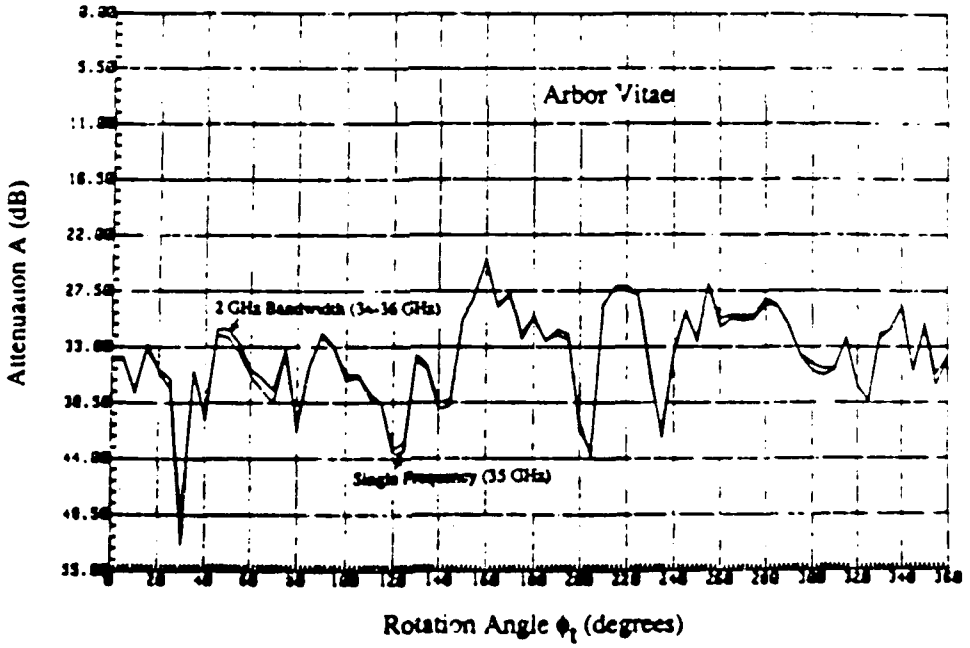

(b)

Fig. 5. Measured attenuation versus tree rotation angle (measured relative to an arbitrary starting position) for (a) Ficus and (b) Arbor Vitae. The wave polarization was vertical.

TABLE III
SUMMARY OF SINGLE-TREE ATTENUATION MEASUREMENTS FOR HORIZONTAL (H) AND VERTICAL (V) POLARIZATIONS

Measured Parameters	Ficus		Arbor Vitae	
	H	V	H	V
Mean Attenuation, A (dB)	38.8	37.1	38.1	34.4
Standard Deviation/Mean, σ_A	1.86	1.88	0.93	0.96
Extinction Coefficient κ_e (dB/m)	38.8	37.1	38.1	43.2

where $f(\Psi)$ is the forward lobe of the scattering pattern and $(1 - \alpha)$ is its isotropic background. They further proposed a Gaussian function for $f(\Psi)$. As we will discuss later, we measured the bistatic scattering from a tree and determined the pattern of $g(\Psi)$ experimentally. The results suggest a function of the form

$$f(\Psi) = 2(1 + \beta_1^{-2})e^{-\Psi^2}$$

where β_s is the effective beamwidth of the forward lobe and is related to the half-power beamwidth β_s' by $\beta_s' = 1.4\,\beta_s$. The multiplying coefficient of the above function was obtained by satisfying the condition given by (6).

An additional function of interest is the normalized scattering pattern

$$g_n(\Psi) = \frac{g(\Psi)}{g(0)} = \frac{2\alpha(1 + \beta_s^2)\, e^{-\Psi^2/\beta_s^2} + (1 - \alpha)}{2\alpha(1 + \beta_s^2) + (1 - \alpha)}. \quad (9)$$

C. Transmission

For line of sight propagation along the forward direction ($\Psi = 0$) with no trees present in the propagation path, the received power is given by

$$P_0 = P_t G_{t0} G_{r0} \left(\frac{\lambda}{8\pi R}\right)^2 \quad (10)$$

where P_t is the transmitted power, G_{t0} and G_{r0} are the gains of the transmit and receive antennas, λ is the wavelength, and $2R$ is the distance between the two antennas. When we place a tree of crown diameter d between the transmit and receive antennas, the foliage attenuates the incident intensity as well as generates some forward-scattered intensity through diffuse bistatic scattering. The received power is given by

$$P = P_c + P_d \quad (11)$$

where P_c is the coherent component (also called the reduced incident intensity) given by

$$P_c = P_0 e^{-\kappa_e d} \quad (12)$$

and P_d is the diffuse component. In (12), κ_e is the extinction coefficient (or extinction cross section per unit volume) of the foliage and is related to σ_e by

$$\kappa_e = N\sigma_e, \quad NPm^{-1}. \quad (13)$$

In his book on wave propagation in random media, Ishimaru [6] provides the basic formulation for relating the diffuse intensity P_d to the scattering properties of the medium. Schwering and Johnson [7] extended the formulation by developing an elaborate model that accounts for all orders of multiple scattering in the form of a series solution. In the present analysis, we shall adopt their model, but we shall limit the formulation to the first-order solution, which takes the form

$$P_d = P_0 q e^{-\kappa_e d}\left[\exp(\kappa_e \alpha \omega d) - 1\right] \quad (14)$$

where ω is the scattering albedo of the foliage medium

$$\omega = \frac{\kappa_s}{\kappa_e} = \frac{N\sigma_s}{N\sigma_e} = \frac{\sigma_s}{\sigma_e} \quad (15)$$

and q is a weighting factor related to the scattering pattern $g(\Psi)$ and the radiation pattern of the receive antenna. For a receive antenna with a Gaussian pattern of the form

$$G_r(\theta_s) = G_{r0} \exp(-\theta_s^2/\beta_a^2) \quad (16)$$

the factor q is given by

$$q = \frac{\beta_a^2(1 + \beta_s^2)}{2\beta_s^2} \quad (17)$$

where θ_s is the antenna angle measured from the boresight direction and β_a is the effective antenna beamwidth ($\beta_a = 0.6\,\beta_a'$ where β_a' is the half-power beamwidth). The above expression for q was derived by integrating the bistatically scattered intensity over the antenna pattern and is valid only if β_a is significantly smaller than β_s. (For the experiments discussed in the next section, $\beta_a \cong 2°$ and $\beta_s \cong 10°$.)

Upon inserting (12) and (14) in (11), we get

$$P = P_0 e^{-\kappa_e d}\left\{1 + q\left[\exp(\kappa_e \alpha \omega d) - 1\right]\right\}. \quad (18)$$

For a highly directive receive antenna, such that $\beta_a \ll \beta_s$, and $\kappa_e d$ not very large, P_d is much smaller than P_c and $P \cong P_c$. When this condition is satisfied, the attenuation is $A(dB) = 4.34\,\kappa_e d$. As d increases, the diffuse component, which accounts for multiple scattering in the medium, becomes more important relative to the coherent component and eventually becomes the dominant term. Thus

$$A(dB) = 10 \log (P_0/P)$$

$$= -10 \log\left\{e^{-\kappa_e d}\left[1 + q(e^{\kappa_e \alpha \omega d} - 1)\right]\right\} \quad (19)$$

$$\cong 4.34\,\kappa_e d, \quad \text{for } q\left[e^{\kappa_e \alpha \omega d} - 1\right] \ll 1 \quad (20)$$

$$\cong 4.34\,\kappa_e d(1 - \alpha\omega) - 10 \log q, \quad \text{for } \kappa_e d \gg 1. \quad (21)$$

The expression for $A(dB)$ given by (19) includes four unknown parameters: κ_e, ω, α, and q. Actually, the parameter q is a *proxy* for β_s (because the only other parameter in (17) is the antenna beamwidth β_a, which usually is a known quantity). To determine the values of four independent parameters from experimental measurements, we need to conduct at least four nonredundant experiments. This was done by measuring $A(dB)$ for one tree, two trees, three trees, and four trees placed in the propagation path. The trees were placed very close to one another, simulating a continuous canopy. The distance between the transmit and receive antennas was increased to about 8 m. To measure the average attenuation for two trees, 72 measurements were made corresponding to that many combinations of azimuth positions of the two trees; the combinations were selected by a random number generator from 360 × 360 possible combinations. A similar procedure was used for measuring the attenuation of three trees and four trees. The experiment was conducted for Ficus trees only. The results, which are discussed in detail in Section III-C, confirm the general dependence of $A(dB)$, as given by (19), on the foliage depth d and are in agreement with the experimental results reported by Violette *et al.* [8], but it was not possible to obtain ...

values for the unknown parameters because of variations in A (dB) associated with physical variations among the four trees. It was not possible to make transmission measurements for more than four trees because the attenuation measured for four trees (which was 82 dB) was only 10 dB above the receiver noise level and, therefore, the addition of another tree would have placed the received power below the noise level.

To solve this problem, we decided to complement the transmission measurements with bistatic scattering measurements, as described in Section III-C. The formulation needed for analyzing the bistatic measurements is given next.

In an effort to learn more about the transmission and bistatic scattering properties of foliage, bistatic scattering measurements were conducted as a function of the bistatic angle Ψ defined in Fig. 2(b). The transmit and receive antennas were at the same height above the ground, and their beams always pointed in the horizontal plane and always intersected at the center of the circle, which was also the center of the rotatable platform on which the tree was placed. Proper alignment of the antennas' boresight directions was realized (prior to inserting the tree) using infrared guns mounted onto the transmitter and receiver platforms and an infrared detector connected to a vertical pole placed at the center of the circle.

With the transmitter remaining fixed in location and orientation and the tree remaining fixed in location, the receiver was moved to several locations on the perimeter of the circle (Fig. 2(b)). For the vertical-transmit vertical-receive polarization configuration (VV), the measurements were conducted over the range from $\Psi = -170°$ to $\Psi = 170°$, but for the HH and HV polarization configurations, the angular range was limited to $\Psi = -90°$ to $+90°$. At each receiver position, the tree was made to rotate about its vertical axis through 360° in discrete increments of 5°. The received power $P(\phi_i)$ was recorded at each of 72 positions comprising a complete rotation over the tree's azimuth angle ϕ_i. Sample plots of the received power for $\Psi = 90°$ are shown in Fig. 6. We observe that the single-frequency plot and the plot representing the received power averaged over a 2-GHz bandwidth are poorly correlated with one another, in stark contrast with the $\Psi = 0°$ observations discussed earlier in connection with Fig. 5. Bistatic scattering at an azimuth angle of 90° is a result of diffuse scattering, which is incoherent in nature (does not preserve phase information), and therefore the received signal will decorrelate with frequency separation. Consequently, frequency averaging helps reduce the variability (of the received signal) caused by phase interference effects; the standard-deviation to mean ratio of the measured power is 1.2 for the single-frequency (35-GHz) data, in comparison to 0.8 for the 2-GHz averaged data (34–36 GHz). Because of the greater precision provided by frequency averaging, all bistatic scattering measurements were conducted in that mode. Each bistatic scattering data point presented in the remainder of this section is based on measurements of the mean value of the received power $\bar{P}$ with the averaging being performed over both the angle ϕ, (by rotating the tree about its axis over 72 positions) and frequency (over a 2-GHz bandwidth).

Now, we shall consider the power received at an angle Ψ as a result of bistatic scattering by the volume formed by the intersection of the beams of the transmit and receive antennas. The sketch shown in Fig. 7 has been drawn at the correct relative scale so as to show the size of the intersection region relative to the dimensions of the tree crown. For an elemental volume dV located at point B in Fig. 7, part of the power incident upon it in the indicated direction is bistatically scattered in the direction of the receive antenna at an angle (Ψ) relative to the incident direction. The differential power arriving at the receive antenna due to scattering by the element dV at the position vector $\bar{r}$ is proportional to $N\sigma_{bi}(\bar{r}, \Psi) \exp[-\tau_1(\bar{r}) - \tau_2(\bar{r})]$, where $\sigma_{bi}(\bar{r}, \Psi)$ is the bistatic scattering cross section, and $\tau_1(\bar{r})$ and $\tau_2(\bar{r})$ are the attenuation functions associated with propagation through the foliage to the element at $\bar{r}$ (points A to B in Fig. 7) and again from that element to the receiver (points B to C), respectively. If we consider first-order multiple scattering contributions only and we regard the gains of the two antennas as constant over their respective beamwidths, the radar equation takes the form [6, p. 73]

$$P(\Psi) = P_t G_{t0} G_{r0} \frac{\lambda^2 N}{(4\pi)^3} \cdot \iiint_{\substack{\text{Scattering} \\ \text{Volume}}} \frac{\sigma_{bi}(\bar{r}, \Psi) e^{-[\tau_1(\bar{r}) + \tau_2(\bar{r})]}\, dV}{R_t^2(\bar{r})\, R_r^2(\bar{r})} \quad (22)$$

where $R_t(\bar{r})$ and $R_r(\bar{r})$ are the distances from the transmit and receive antennas to the volume element at position $\bar{r}$. We shall assume that $\sigma_{bi}(\bar{r}, \Psi)$ is uniform throughout the foliage-intersection-volume and that it is a function of Ψ only. In that case, the ratio of (22) to (10) yields

$$\frac{P(\Psi)}{P_0} = \frac{R^2 N}{\pi} \sigma_{bi}(\Psi)\, I(\Psi) \quad (23)$$

where $I(\Psi)$ is the illumination integral

$$I(\Psi) = \iiint_{\substack{\text{Intersection} \\ \text{Volume}}} \frac{\exp[-\kappa_e(d_1(\bar{r}) + d_2(\bar{r}))]\, dV}{R_t^2(\bar{r})\, R_r^2(\bar{r})} \quad (24)$$

κ_e is the extinction coefficient, d_1 is the path length in the foliage traversed by the incident beam as it propagates to the element at $\bar{r}$, and d_2 is similarly defined for the power scattered by the element toward the receiver. In Fig. 8, d_1 and d_2 correspond to the distances between points A and B and between B and C, respectively. From (23), the bistatic scattering cross section per unit volume is

$$N\sigma_{bi}(\Psi) = \frac{P(\Psi)}{P_0} \cdot \frac{\pi}{R^2 I(\Psi)} \quad (25)$$

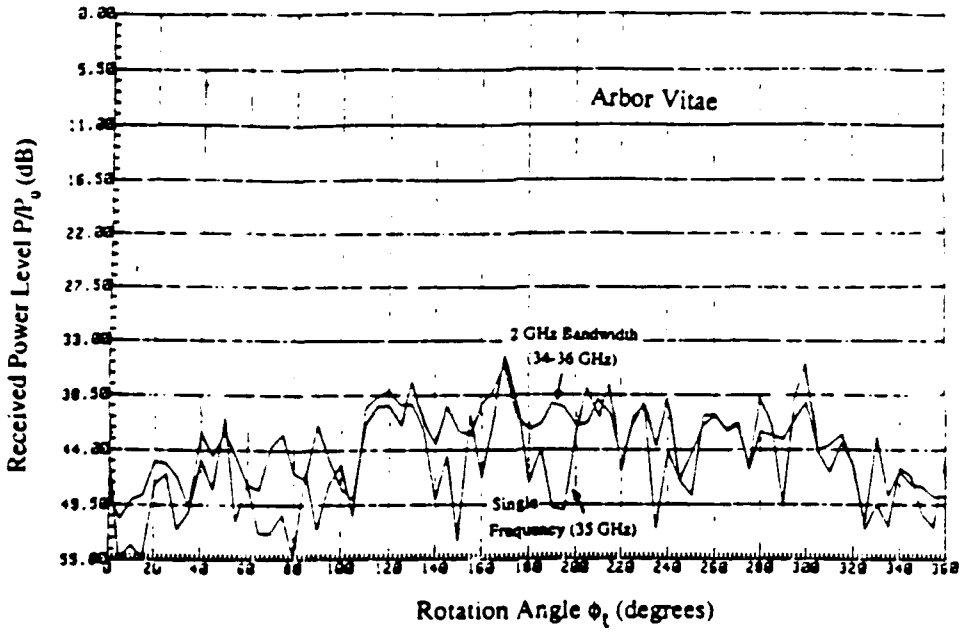

Fig. 6. Measured received power versus tree rotation angle for an azimuth bistatic angle $\Psi = 90°$. The wave polarization was vertical.

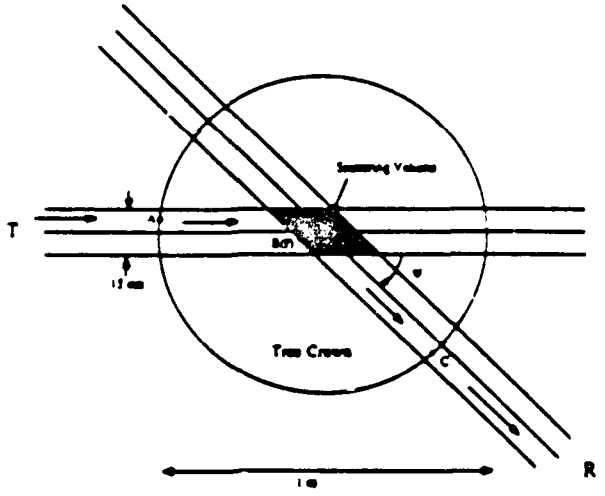

Fig. 7. Top view of the tree crown showing the scattering volume formed by the intersection of the transmit and receive antenna beams.

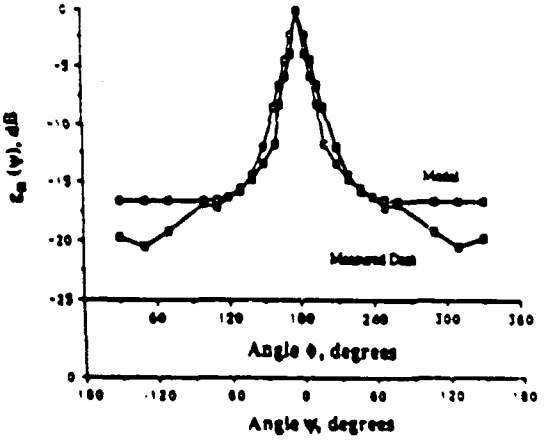

Fig. 8. Bistatic scattering pattern $\kappa_e g(\Psi)$, as determined from the measured bistatic scattering experiments. The curve labeled "Model" is based on fitting the function given by (9) to the data.

If we use (8) to replace $N\sigma_{bs}(\Psi)$ with $N\sigma_t g(\Psi)$ and then replace $N\sigma_t$ with κ_e, we end up with

$$\kappa_e g(\Psi) = \frac{P(\Psi)}{P_0} \cdot \frac{\pi}{R^2 I(\Psi)}. \tag{26}$$

C. Estimation of Foliage Propagation Parameters

With regard to (26), P_0 is the (calibration) power measured with the two antennas boresighted towards one another, $P(\Psi)$ is the power measured when the receiver is at angle Ψ, $R = 3m$ is the radius of the circle, and $I(\Psi)$ is the illumination integral given by (24). If the extinction coefficient κ_e is known, we can compute $I(\Psi)$ numerically for the specific geometry and antenna patterns associated with the measurements of $P(\Psi)$. Hence, we can 1) compute $\kappa_e g(\Psi)$, as a function of Ψ, 2) compare the shape of the pattern to that described by the theoretical function given by (6), (7) and if the agreement is good, we can then estimate κ_e, α, and β_t.

At first examination, it would appear that the success of this procedure would hinge on having *a priori* knowledge of κ_e. Based on the transmission measurements for one tree, we can make an initial estimate of κ_e by ignoring the contribution of diffuse scattering and using (20) to determine κ_e. Such an estimate may be smaller than the true value of κ_e, but not larger. Furthermore, careful examination of the illumination integral $I(\Psi)$ reveals that a

small change in κ_e causes the level of the overall pattern of $I(\Psi)$ to change but has a minor influence on its shape. Hence, using the initial estimate of $\kappa_e = 5.2$ Np m^{-1}, it should be possible to determine the shape of the resultant pattern $g(\Psi)$. This exercise led to the results shown in Fig. 8, which shows the normalized function $g(\Psi)$ as derived from the measured data following the procedure outlined above, and also shows a plot of the function given by (9) with its parameters having been selected to best fit the experimentally derived function. The good overall agreement between the two functions indicates that the functional form given by (7) is appropriate for $g(\Psi)$. Moreover, the fit allows us to obtain reasonable estimates of α and β and an initial estimate of κ_s. With β already known, we can compute q using (17). If we then insert α and q in (19) and replace ω with κ_s/κ_e, we end up with an expression for $A(dB)$ that has only one unknown parameter κ_s. By comparing the expression to the measured values of $A(dB)$ for each of the four transmission cases (one tree, two trees, ..., four trees), we obtain four values for κ_s. We then use the average value as a new input into the computation of $g(\Psi)$ and κ_s.

After repeating the above process through two cycles, we obtained the following results

$$\kappa_e = 5.22 \text{ Np m}^{-1}$$

$$\kappa_s = 4.7 \text{ Np m}^{-1}$$

$$\omega = 0.9$$

$$\alpha = 0.38$$

$$\beta_s = 0.17 \text{ rad} = 9.5°$$

and the theoretical curve shown in Fig. 9.

The preceding results support the validity of the first-order multiple-scattering propagation model given in Section III-B and provide a quantitative picture of the bistatic scattering pattern of tree foliage at 35 GHz.

IV Bistatic Scattering Measurements for Sand and Gravel

The arrangement used for making measurements of the bistatic scattering coefficient of sand and gravel surfaces is illustrated in Fig. 10; the incidence angle θ_i is between the surface normal and the boresight direction of the transmit antenna, a similar definition applies to the scattering angle θ_s, and the azimuth angle ϕ is defined as the azimuth angle of the boresight direction of the receive antenna. The $\phi = 0$ direction (x-axis) is chosen to coincide with the azimuth direction of the transmit antenna. When using narrow-beam transmit and receive antennas, it is difficult to achieve perfect overlap of their footprints on the target surface. To avoid measurement inaccuracies that may be caused by imprecise pointing of the transmit and receive antennas, a broad-beam antenna was used for reception and a narrow-beam antenna was used for transmission. The transmit antenna had a beamwidth of 4.2°, compared to 15° for the beam of the receive antenna.

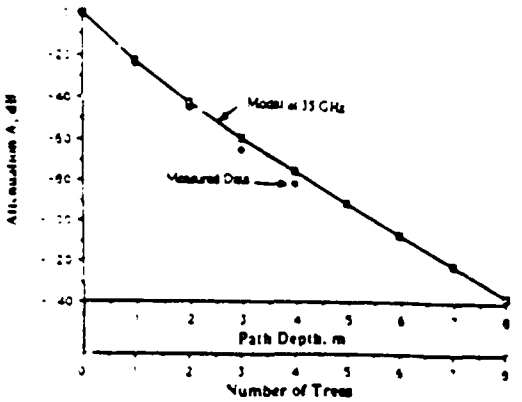

Fig. 9. Comparison of measured attenuations with theoretical model. Note the nonlinear dependence on path length (1.32 dB for one tree and 4.2 dB for four trees).

Thus, the power arriving at the receive antenna is essentially the result of scattering by the area illuminated by the transmit antenna.

The bistatic scattering measurements were comprised of two major experiments. In the first experiment, both θ_i and θ_s were maintained constant at 66° and the azimuth angle ϕ was varied from 10° to 180°. At a nominal range of 3.2 m between the target and the transmit and receive antennas, the area illuminated by the transmit antenna was an ellipse with minor and major axes of 24 and 50 cm, respectively. The target material (sand or gravel) was placed in a "sandbox" at the center of a circle approximately 5 m in diameter. The sandbox, whose surface had dimensions of 1.2 m × 1.2 m, was much larger in surface area than the footprint of the transmit antenna. The floor area surrounding the sandbox was covered with absorbing material.

The purpose of the second experiment was to extend the results of the first experiment by examining the variation of the bistatic scattering coefficient $\sigma^\circ(\theta_i, \theta_s, \phi)$ as a function of both θ_s and ϕ for a fixed value of θ_i, namely 60°. The rationale for choosing $\theta_i = 66°$ in the first experiment and 60° in the second one will be discussed later.

A. Calibration

The radar equation for the bistatic scattering case is given by

$$P = P_t \frac{G_{0t} G_{0r} \lambda^2}{(4\pi)^3} \int \frac{g_t(\theta_t)\, g_r(\theta_r)}{R_t^2 R_r^2} \sigma^\circ \, dA \qquad (27)$$

where P_t is the transmitted power; G_0 is maximum gain of the (transmit or receive) antenna; $g(\theta)$ is the normalized radiation pattern; R is the range to the target; the subscripts t and r stand for transmit and receive, respectively; θ is the antenna angle relative to the boresight direction, and dA is an element of area. Assuming σ° is approximately constant over the angular range of the transmit antenna beamwidth, the preceding equation is

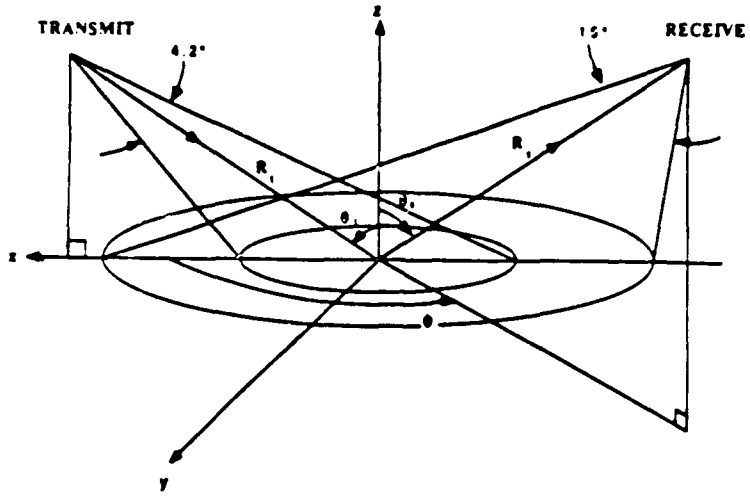

Fig. 10. Geometry of the bistatic scattering arrangement.

be rewritten as

$$P = P_r \frac{G_{r0} C_{r0}}{(4\pi)^3} \lambda^2 \sigma^\circ I \tag{28}$$

where

$$I = \int \frac{g_t(\theta_t)\, g_r(\theta_r)}{R_t^2 R_r^2}\, dA \tag{29}$$

is the illumination integral, which is readily computable from knowledge of the antennas' radiation patterns and the measurement geometry. Because the beamwidth of the transmit antenna is much smaller than that of the receive antenna, the illumination integral is governed primarily by $g_t(\theta_t)$.

The system was calibrated by measuring the power received with the transmit and receive antennas pointing at each other along their boresight directions. This provides the reference level P_0 given by (10). Combining (10) with (28) provides the expression

$$\sigma^\circ = \left(\frac{\pi}{R^2 I}\right)\left(\frac{P}{P_0}\right). \tag{30}$$

An alternative calibration approach is to measure the power reflected from a flat metal plate in the specular direction (i.e., the plate is oriented such that $\theta_t = \theta_r$ and its surface normal is in the plane containing the boresight directions of the two antennas). If the plate is much larger than the 3-dB footprint of the transmit antenna pattern, image theory leads to the same expression given by (10) if $2R$ is replaced with $R_t + R_r$. The two calibration approaches were found to yield results that agree with one another within a difference of 1 dB.

Using the metal plate as a specular reflector, the azimuth pattern of the transmit antenna was measured by moving the receive antenna in azimuth in steps of 2°. The results, shown in Fig. 11, are in close agreement with the pattern measured at an antenna range. Actually, the plot

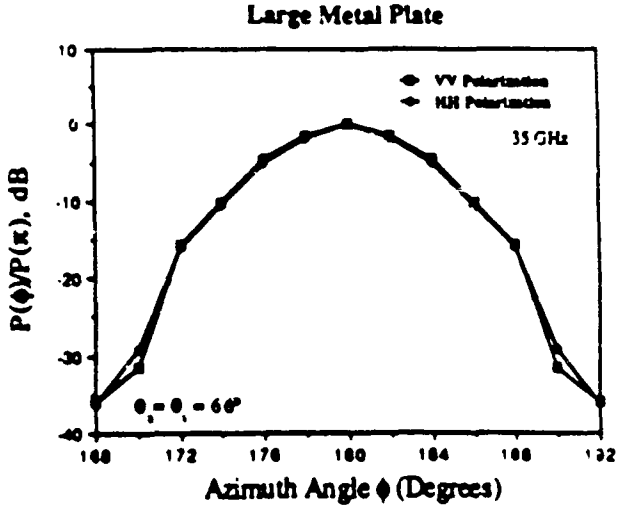

Fig. 11. Measured power reflected from the metal plate (normalized to the power reflected in the specular direction) as a function of the azimuth angle φ.

is a product of the radiation patterns of the transmit and receive antennas, but the receive antenna pattern is much wider than that of the transmit antenna and, therefore, its effect on the shape of the product pattern is secondary in importance.

B. Noise Performance and Measurement Precision

The radar system used in this study had been designed to step in frequency from 34 to 36 GHz in 401 steps. By Fourier-transforming the frequency response of the received signal to the time domain, it is possible to gate the time response such that reflections from objects other than the target area are filtered out. This procedure led to a noise-equivalent level for σ° equal to −45 dB. The lowest σ° value presented in this paper is −35 dB, corresponding to a signal-to-noise ratio of 10 dB.

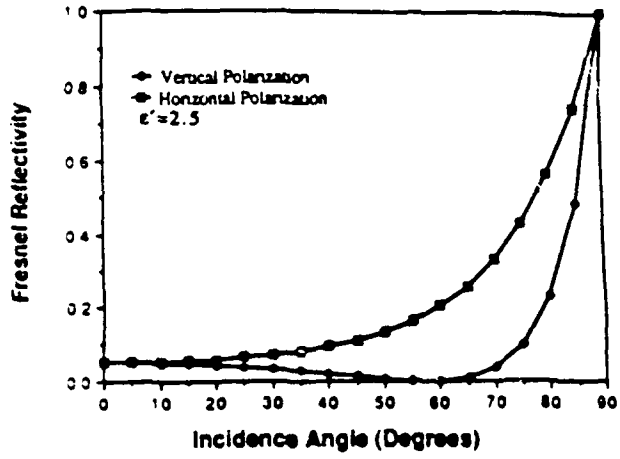

Fig. 12. Calculated Fresnel reflectivity for sand.

According to Rayleigh fading statistics, the ratio of the standard deviation s to the mean value $\bar{\sigma}^\circ$ associated with a radar measurement of a random target is given by

$$\frac{s}{\bar{\sigma}^\circ} = \frac{1}{\sqrt{N}} \tag{31}$$

where N is the total number of independent samples included in the measurement of σ° [9]. In the present study, 10 spatially independent samples were measured by rotating the target to different positions while always pointing the transmitted beam off-center such that its footprint is positioned halfway between the center and the edge of the box. For 10 independent samples, $s/\bar{\sigma}^\circ \cong 0.3$. This is very close to the values measured experimentally and presented in another paper in this issue [9].

C. Target Characteristics

The targets examined in this investigation included two sand surfaces and a coarse gravel surface. The first sand surface was prepared to be flat and smooth and the second one was artificially roughened to generate a randomly distributed, slightly rough surface. Based on measurements of two transects of the surface height profile, the rms height is estimated to be smaller than 0.1 cm for the smooth surface and about 1.67 cm for the slightly rough surface. The latter surface consisted of smooth undulations with no significant small scale structure; the undulations looked like randomly oriented plane facets approximately 10 cm in diameter. The gravel consisted of stones that had relatively smooth surfaces and ranged in size from 1-2 cm in diameter.

The depth of the material placed in the wooden box was selected such that it was equal to twice the penetration depth δ_p. The complex dielectric constant of the sand material was measured at 10 GHz as $\epsilon = 2.5 - j\,0.03$. The sand was totally dry. Hence, its ϵ at 35 GHz is not expected to be different from its value at 10 GHz. This leads to $\delta_p = 7.5$ cm at 35 GHz. The sandbox was filled with sand to a depth of 15 cm, or two penetration depths. The two-way attenuation for a depth equal to $2\,\delta_p$ is 17 dB. Thus, contributions from depths greater than 15 cm may be neglected. This conclusion was verified experimentally by measuring the received power from the sand layer as a function of layer thickness.

D. Bistatic Scattering From Smooth Sand

The first question that needed to be addressed was, "How close to a specular surface is a visually smooth sand surface at 35 GHz?" The scattering function for a specular surface is a delta function; for a given incidence angle θ_i, power is reflected only in the direction corresponding to $\theta_s = \theta_i$ and $\Phi = 180°$. Moreover, the reflected signal is totally coherent in nature. As the surface departs from perfectly smooth, the magnitude of the coherent scattering component decreases and incoherent scattering becomes present in addition.

To answer the question we posed above, we first computed the Fresnel reflectivity Γ for sand (with $\epsilon = 2.5 - j\,0.03$) as a function of the incidence angle θ, for both H and V polarizations (Fig. 12). We wanted to choose θ_i such that the ratio $\Gamma_H(\theta_i)/\Gamma_V(\theta_i)$ is large so it would be easy to measure, and yet we did not want θ_i to be too large because that would make the pointing geometry difficult to arrange. In our first experiment we chose $\theta_i = 66°$, at this angle, $\Gamma_H(66°) = 0.27$ (or -5.7 dB) $\Gamma_V(66°) = 0.014$ (or -18.5 dB) and the ratio $\Gamma_H/\Gamma_V = 19.3$ (or 12.8 dB).

With $\theta_i = 66°$, the received power was measured along the specular direction first for the smooth sand surface and then for a perfectly conducting flat plate placed on top of the sand surface. The signal reflected from the sand surface was lower than that reflected from the metal plate by 6.4 dB for H polarization and by 18.4 dB for V polarization. Thus, the measured reflectivity Γ_H and Γ_V [illegible] smooth sand surface are respectively only 0.[illegible] and [illegible]

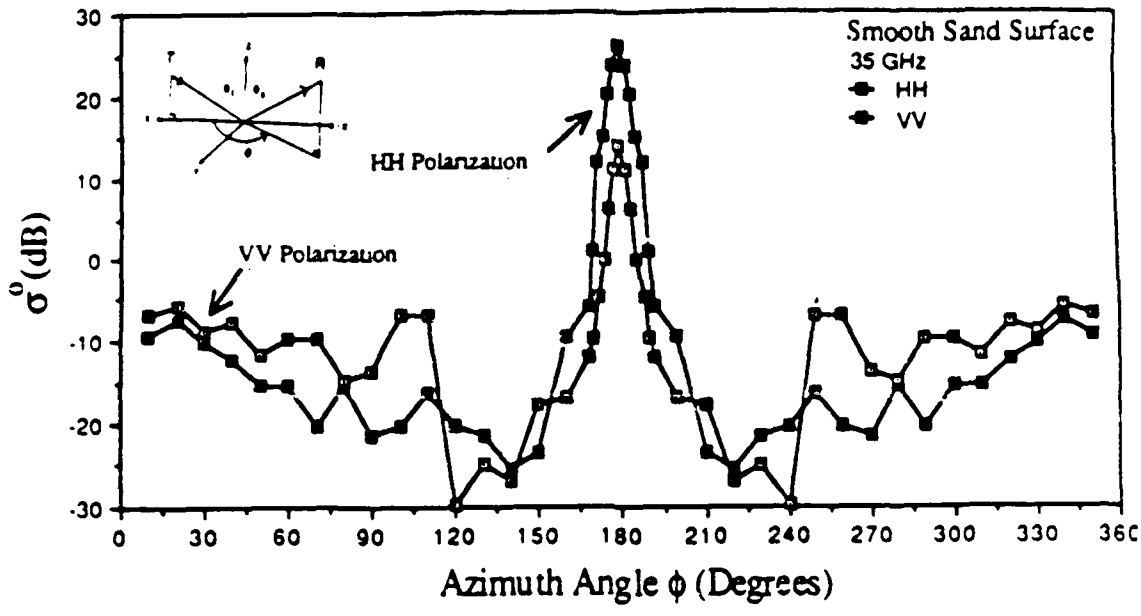

Fig. 13. Measured bistatic scattering pattern of a smooth sand surface with $\theta_i = \theta_s = 66°$.

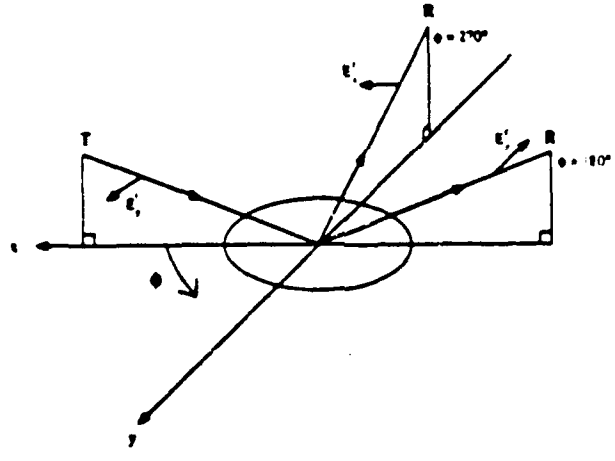

Fig. 14. The electric field of a horizontally polarized transmitted wave is in the x direction. A horizontally polarized antenna located at $\phi = 270°$ can receive waves whose $\bar{E}$ fields are in the x direction.

lower in level than their theoretical counterparts for a specular surface. In other words, a "visually" smooth sand surface is also electromagnetically smooth with regard to reflection along the specular direction at 35 GHz.

Fig. 13 shows measured values of the bistatic scattering coefficient $\sigma^\circ(\theta_s, \theta_s, \phi)$ plotted as a function of ϕ for $\theta_s = \theta_s = 66°$. The plots cover the range from 10° to 350°, although the actual measurements covered only the range from 10° to 180° and the remaining part is a mirror image. We observe that in the specular direction, σ_{HH} is larger than σ_{VV} by 12 dB, but outside the main lobe region, σ_{VV} tends to be slightly larger than σ_{HH}.

In our second experiment, we fixed θ_i at 60° and measured $\sigma^\circ(\theta_s, \theta_s, \phi)$ as a function of ϕ for $\theta_s = \theta_i$ (essentially replicating the previous experiment) and as a function of θ_s at each of two values of ϕ, namely 180° and 270°. Also, the measurements included observations with HV polarization, in addition to HH and VV polarizations. The polarization orientation is defined with respect of the frame of reference of the transmit or receive antenna. Thus, HH polarization, for example, refers to a transmitted wave whose $\bar{E}$-field points along the x direction (Fig. 14) and to a receive antenna oriented to receive waves whose $\bar{E}$-field is along the x direction when

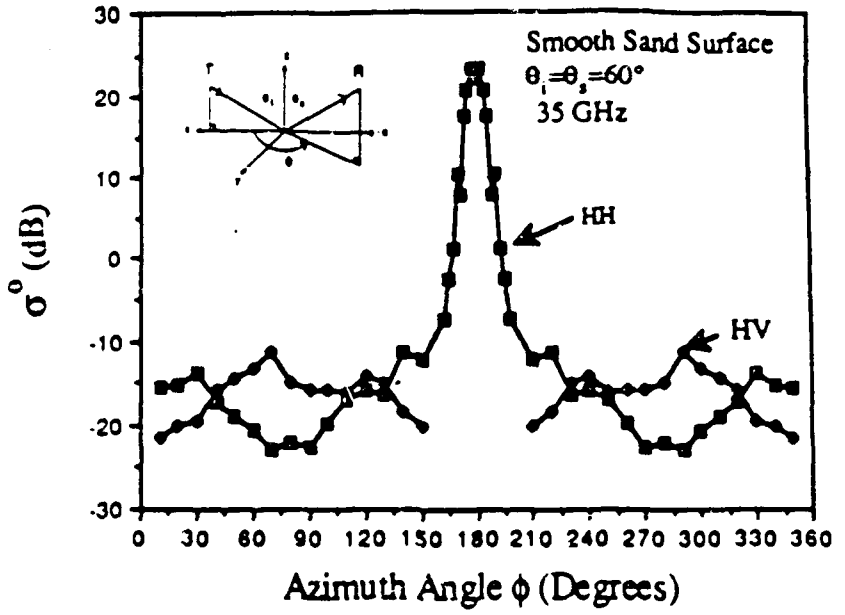

(a)

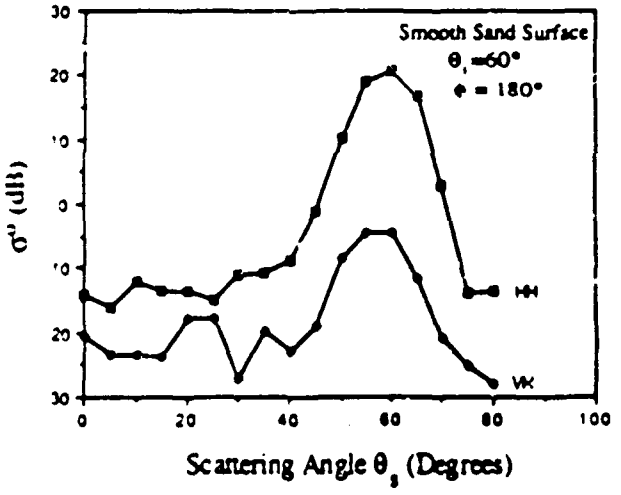

(b)

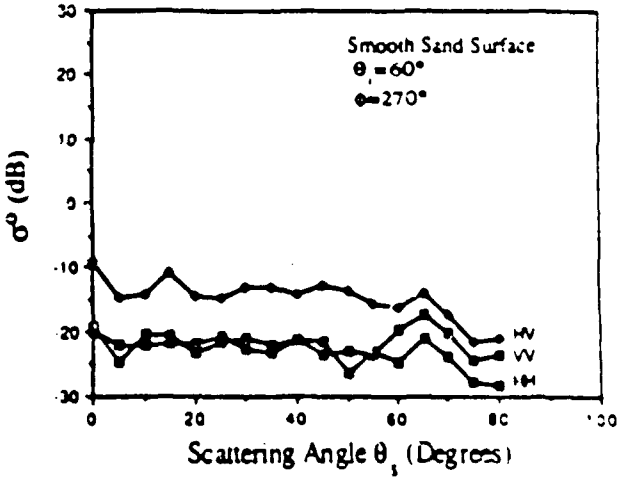

(c)

Fig. 15. Bistatic scattering from a smooth sand surface with $\theta_i = 60°$. (a) azimuth variation with $\theta_s = 60°$. (b) scattering angle variation with $\phi = 180°$, and (c) scattering angle variation with $\phi = 270°$ and (d) a contour plot as a function of θ_s and ϕ.

270° and along the $\hat{y}$ direction when $\phi = 180°$. This means that at $\phi = 90°$ we should expect stronger cross-polarized scattering than like-polarized scattering. Our expectation was confirmed by the results shown in Fig. 15(a). σ°_{HV} is much smaller than σ°_{HH} for ϕ between 150° and 210° (actually σ°_{HV} could not be measured at $\phi = 180°$ because it is lower than σ°_{HH} by more than the 30-dB depolarization isolation factor of the antenna), but σ°_{HV} is larger than σ°_{HH} for $\phi = 60°$-90° (and 270°-300°). Fig. 15(b) and (c) depicts the variation of $\sigma^\circ(\theta_s, \theta_i, \phi)$ with θ_s at $\phi = 180°$ and 270°. Fig. 15(d) shows a contour plot of σ° as a function of both θ_s and ϕ. The plot was generated using simple interpolation between the one-dimensional profiles shown in parts (a)-(c) of Fig. 15.

E. Bistatic Scattering From Rough Sand and Gravel

The like-polarized (HH and VV) bistatic scattering patterns of the rough sand and gravel surfaces (Figs. 16(a) and 17(a)) exhibit significantly lower levels in the specular direction and their main lobes are broader than the

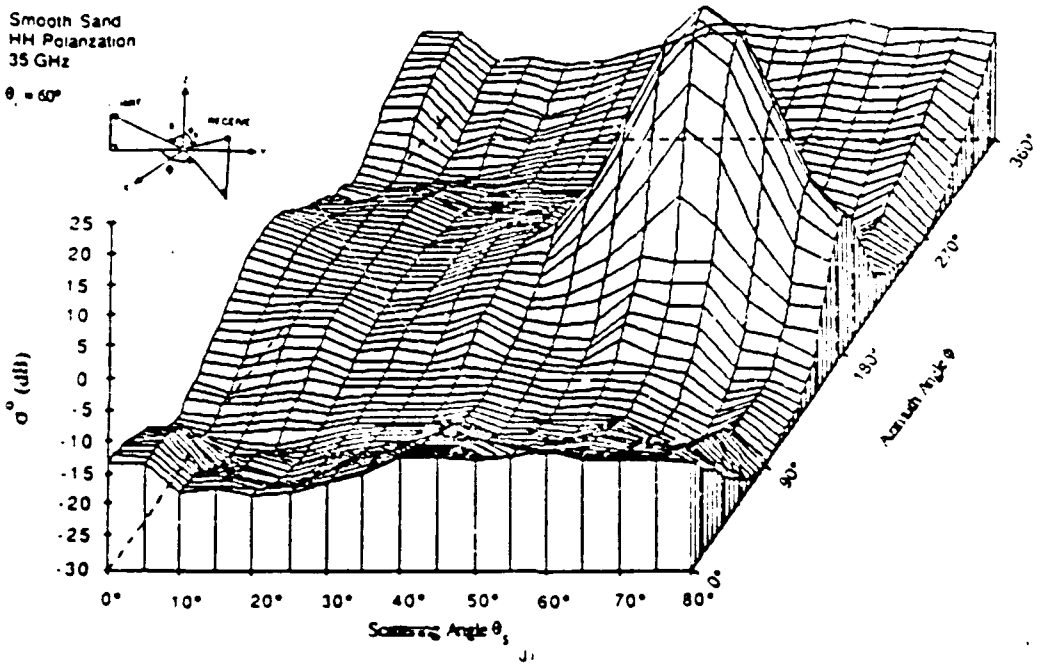

Fig. 4 (Continued)

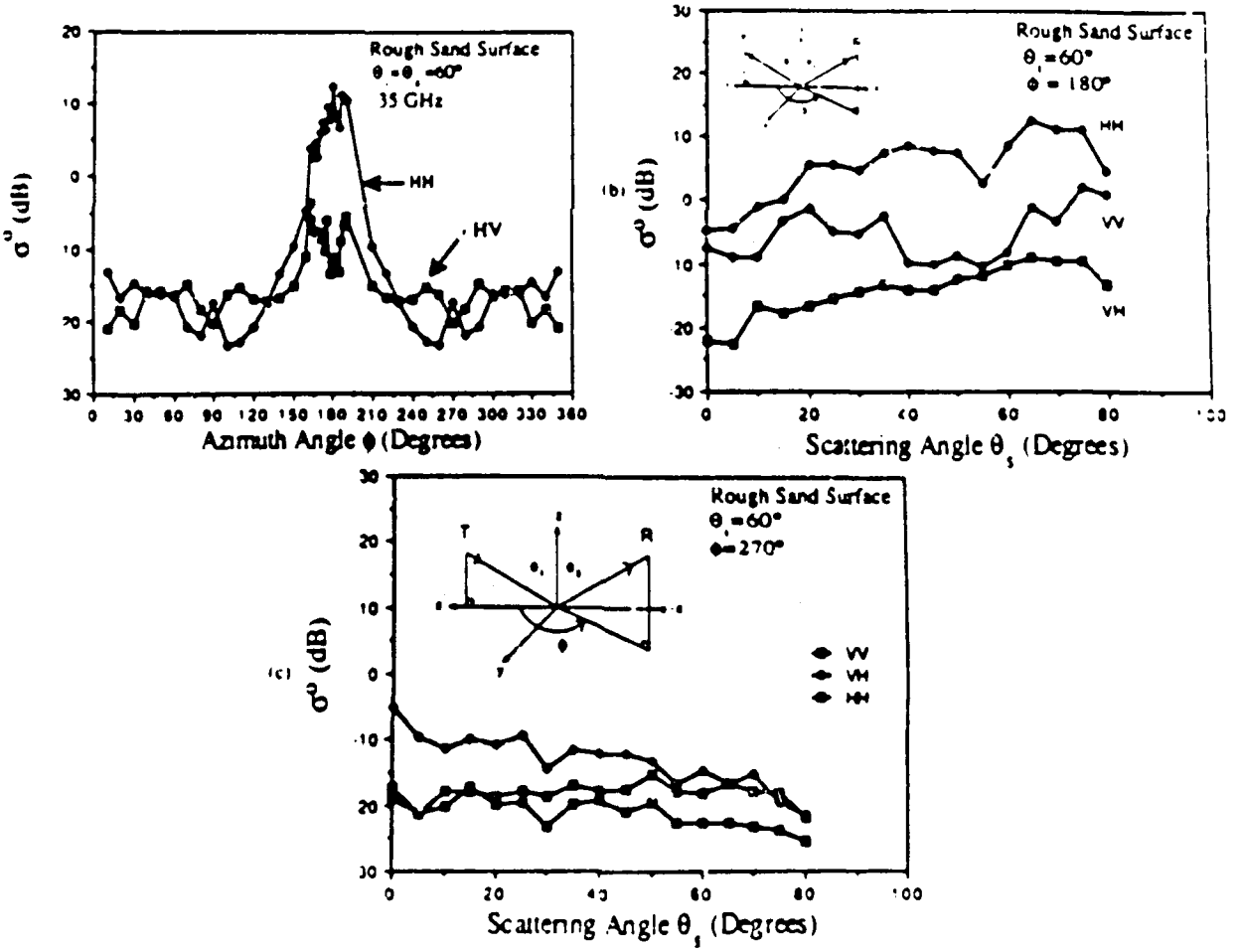

Fig. 10. Bistatic scattering from a rough sand surface with $\theta_i = 60°$: (a) azimuth variation with $\theta_s = 60°$, (b) bistatic scattering angle variation with $\phi = 180°$, and (c) bistatic scattering angle variation with $\phi = 270°$.

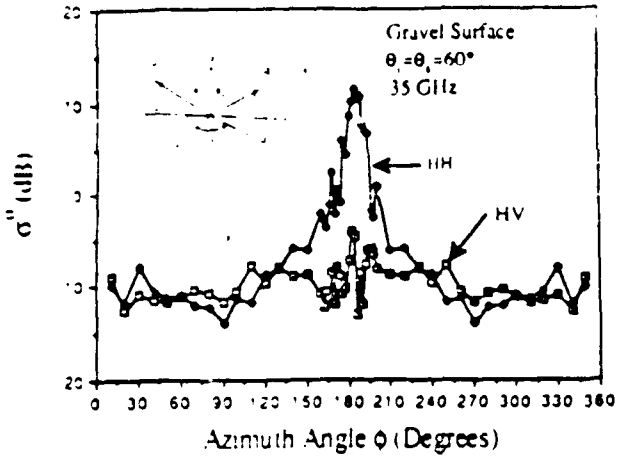

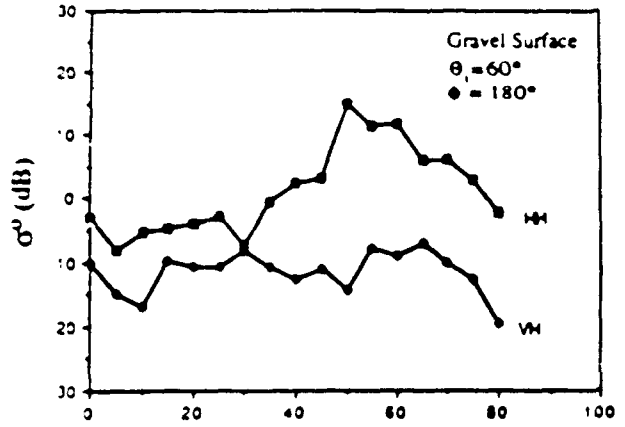

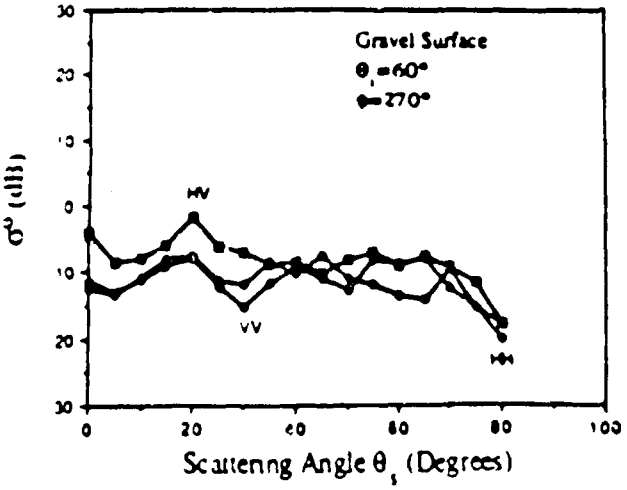

Fig. 7. Bistatic scattering from a gravel surface with $\theta_i = 60°$ at 35 GHz (a) with variation with θ_s in the principal plane, (b) with variation with θ_s in the HH and VH scattering angle variation with $\phi = 270°$.

patterns of the smooth sand surface. However, along the specular direction, the difference between σ_{HH} (dB) and σ_{VV} (dB) is approximately the same for both the smooth and rough sand surfaces.

V. Concluding Remarks

The prime objectives of this phase of the millimeter-wave bistatic scattering study had been to develop calibrated instruments, establish measurement approaches, and acquire samples of bistatic scattering data for a variety of targets and target conditions. This paper provides a summary of how these objectives were realized and the major conclusions drawn from the experimental observations. The next step will involve the execution of carefully planned experiments designed to evaluate the dependence of the bistatic scattering coefficient $\sigma^0(\theta_i, \theta_s, \phi)$ on specific target characteristics, such as the dielectric constant and the roughness parameters of the surface. Data from such experiments will then be used to guide the testing and development of theoretical scattering models.

References

[1] R. L. Cosgriff, W. H. Peake, and R. C. Taylor, "Terrain scattering properties for sensor system design," Ohio State Univ. Rep. 71 (1960).

[2] W. H. Peake and T. L. Oliver, "The response of terrestrial surfaces at microwave frequencies," Air Force Avionics Lab., Wright Patterson AFB, OH, TR AFAL TR 70-301, (1971).

[3] F. T. Ulaby, T. F. Haddock, J. East, and M. W. White, "A microwave network analyzer based scatterometer," *IEEE Trans. Geosci. Remote Sensing*, vol. 26, no. 1, pp. 75-81, Jan. 1988.

[4] M. El Rayes and F. T. Ulaby, "Microwave dielectric spectrum of vegetation part I: experimental observations," *IEEE Trans. Geosci. Remote Sensing*, vol. GE-25, no. 5, pp. 541-549, Sept. 1987.

[5] F. T. Ulaby and M. A. El Rayes, "Microwave dielectric spectrum of vegetation, part II: Dual dispersion model," *IEEE Trans. Geosci. Remote Sensing*, vol. GE-25, no. 5, pp. 550-557, Sept. 1987.

[6] A. Ishimaru, *Wave Propagation and Scattering in Random Media*, vol. 1. New York: Academic, 1978, ch. 7.

[7] F. Schwering and R. A. Johnson, "A transport theory model for millimeter wave propagation in woods and forests," *J. Electromagnetic Waves and Applications with Matter*, vol. 1, pp. 209-235.

[8] E. J. Violette and R. H. Espeland, "Vegetation and measurements at 9.6, 28.8, and 97.6 GHz through a pecan tree orchard and a grass field," Naval Ocean Systems Center, Kaneohe, HI, Tech. Rep. 1010, Mar. 1984.

[9] F. T. Ulaby, T. F. Haddock, and R. T. Austin, "Fluctuation statistics of millimeter wave scattering from distributed targets," *IEEE Trans. Geosci. Remote Sensing*, vol. 26, no. 1, pp. 75-81, Jan. 1988.

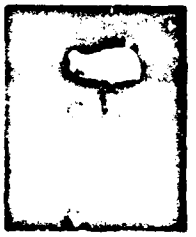

Fawwaz T. Ulaby (M'68-SM'74-F'81) was born in Damascus, Syria, on February 4, 1943. He received the B.S. degree in physics from the American University of Beirut, Lebanon, in 1964, and the M.S.E.E. and Ph.D. degrees in electrical engineering from the University of Texas, Austin, in 1966 and 1968, respectively.

From 1968 to 1984 he was a Professor in the Electrical Engineering Department at the University of Kansas, Lawrence, where he was named Distinguished Professor and Director of the Kansas Center for Research, where he was Director of the Remote Sensing Laboratory. He is currently with the Radiation Laboratory and Department of Electrical and Computer Engineering, University of Michigan, Ann Arbor. His current research interests involve microwave remote sensing of terrain using active and passive microwave remote sensing. He is co-author of the three books ... and A. K. Fung. He is a consultant to the three ...

Remote Sensing: Active and Passive (Reading, MA: Addison-Wesley). In addition, he is coeditor of the *Manual of Remote Sensing*, 2nd ed., vol. I (American Society of Photogrammetry).

Dr. Ulaby is a member of Eta Kappa Nu, Tau Beta Pi, and Sigma Xi. He has been named the Executive Editor for IEEE TRANSACTIONS ON GEOSCIENCE AND REMOTE SENSING, 1984–1985, and was the Geoscience and Remote Sensing Society's Distinguished Lecturer for 1987. He was named an IEEE Fellow in 1980 "for contributions to the application of radar to remote sensing for agriculture and hydrology." He received the GRS Society's Outstanding Service Award in 1982, and its Distinguished Service Award in 1983. In 1984, he also received a Presidential Citation for Meritorious Service from the American Society of Photogrammetry. He received the University of Kansas Chancellor's Award for Excellence in Teaching in 1980, the University of Kansas Gould Award for "distinguished service to higher education" in 1973, and the Eta Kappa Nu MacDonald Award as an "outstanding electrical engineering professor in the United States of America" in 1975.

•

Tahera E. van Deventer (S'87) was born in Hillerod, Denmark, on October 3, 1961. She received the Diplome Universitaire de Technologie from the Institut Universitaire de Technologie de Marseille (I.U.T.), France, in 1982, and the B.S.E. and M.S.E. degrees in electrical engineering from The University of Michigan, Ann Arbor, in 1985 and 1986, respectively. She is currently working toward the Ph.D. degree on the subject of scattering and attenuation by nonlinear media such as vegetation and snow.

She worked in the acoustic field for Bruel & Kjaer from 1982 to 1983. She is a member of Tau Beta Pi and Eta Kappa Nu.

•

Jack R. East (S'70–M'72) received the B.S.E., M.S., and Ph.D. degrees from the University of Michigan, Ann Arbor.

He is now an Associate Research Scientist in the Solid-State Electronics Laboratory of The University of Michigan, working in the area of microwave- and millimeter-wave solid-state devices.

Thomas F. Haddock (M'86) was born in Washington, DC, on November 2, 1949. He received the B.A. degree in mathematics and the M.S. and Ph.D. degrees in physics from the University of Michigan, Ann Arbor, in 1972, 1977, and 1984, respectively.

From 1984 to 1985 he was Manager of Development Projects at Applied Intelligent Systems, a machine vision firm involved in real-time optical, infrared, and X-ray vision systems. He is currently with the Radiation Laboratory and the Department of Electrical Engineering and Computer Science, University of Michigan. He has conducted research in the fast flux density variations of quasi-stellar objects at a wavelength of 12.5 mm. Other research has included development of real-time alphanumeric character recognition algorithms and ultrasonic weld inspection algorithms. Prior to receiving the Ph.D. degree, he worked as Applications Engineer for Sams/3M, a manufacturer of heart-lung machines and cardiac assist devices, where he developed electrodes for manufacturing applications. His current research interests are millimeter-wave scattering and emission from natural targets.

Dr. Haddock is a member of the American Astronomical Society.

•

Michael Eugene Coluzzi (S'85) was born in Santa Monica, CA, on August 30, 1962. He received the B.S.E.E. degree in 1984 from UCLA. In 1987 he was awarded the M.S.E.E. degree from the University of Michigan in 1987 where he was appointed a Teaching Assistantship and conducted research in the area of remote sensing.

He worked at ITT Gilfillan in the area of receiver development for radars between 1984 and 1986.

LIMETER-WAVE BISTATIC RADAR MEASUREMENTS OF SAND AND GRAVEL

F. T. Ulaby, T. F. Haodock, and M. E. Coluzzi

Radiation Laboratory
Department of Electrical Engineering
and Computer Science
The University of Michigan
Ann Arbor, MI 48109-2122, USA

ABSTRACT

Bistatic radar measurements were conducted for sand and gravel surfaces to evaluate the variation with azimuth angle and polarization configuration for various surface roughnesses. The measurements were made at 35 GHz using the Millimeter-Wave Polarimeter (MMP) system. With the transmit and receive antennas oriented to observe the target at the same incidence angle ($\theta_i = \theta_s$), the received power was recorded as a function of the azimuth angle ϕ over the range from 10° to 180° (specular direction). A second experiment is planned, which will consist of measurements at $\phi = 180°$ as a function of θ_s for specific incidence angles θ_i. Assuming the scattering pattern of the target can be modeled as a product of an azimuth pattern $f(\phi)$ and an elevation pattern $f(\theta_i, \theta_s)$, the two sets of measurements provide an estimate of the bidirectional scattering function of the target. Such a function is far superior for evaluating the validity and degree of applicability of theoretical scattering models than the traditional approach of only testing the backscatter response as a function of incidence angle.

Keywords: Radar, bistatic scattering, millimeter-wave systems.

I. INTRODUCTION

Compared to the volume of backscattering data available for both point and distributed targets, bistatic data is almost nonexistent. The only bistatic data of note were measured in the late 1950's at 1.15 GHz [1] and in the mid-1960's at 10 GHz [2]. The scarcity of bistatic data is in part due to the fact that bistatic radar measurements are more difficult to make than monostatic measurements. From the standpoint of testing and evaluating the applicability of theoretical scattering models, however, the availability of bistatic data provides two additional degrees of freedom. In the backscatter case, the incidence angle θ_i and scattered angle θ_s are equal, and the azimuth angle between the incident and scattered directions, ϕ, is zero. Hence, for an azimuthally symmetric randomly distributed target, which most terrain surfaces are, the backscattering coefficient is a function of only one directional variable, θ_i. In the bistatic case, all three angles (θ_i, θ_s, and ϕ) are independent variables. If bistatic data are available to characterize the bidirectional scattering function of a target, the process of developing a scattering model appropriate to the target or class of targets under consideration and the testing of these models would be greatly facilitated.

This paper describes an attempt to calibrate a 35 GHz scatterometer system and to use it to make bistatic scattering measurements for sand and gravel surfaces.

II. SYSTEM DESCRIPTION

The block diagram shown in Fig. 1 depicts the basic elements of the Millimeter-Wave Polarimeter (MPP) system when operated in the bistatic mode. Details of the system description are given in [3]. For the purposes of the present study, the system was operated at 35 GHz and used to make HH- and VV-polarized measurements over a wide range of the azimuth angle ϕ. The arrangement used is illustrated in Fig. 2; the angle θ_i is between the surface normal of the target's surface and the boresight direction of the transmit antenna, a similar definition applies to the scattering angle θ_s, and the azimuth angle ϕ is defined as the azimuth angle of the boresight direction of the receive antenna (the x-axis is chosen such that the azimuth angle of the transmit direction is zero). To avoid measurement errors associated with the pointing of the transmit and receive antennas such that their footprints always overlap perfectly, a broad-beam

This work was supported by Army Research Office Contract DAAG29-85-K-0220.

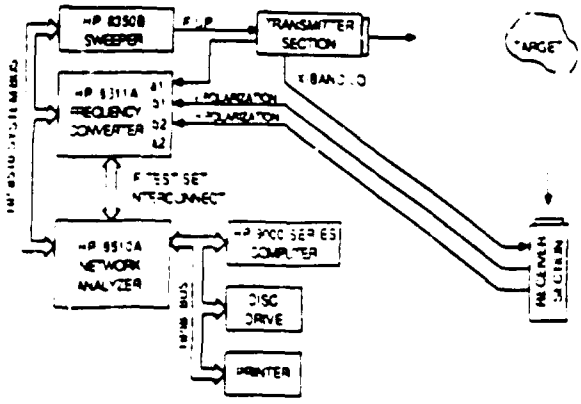

Fig. 1 Block diagram of the MMP operating in the bistatic mode.

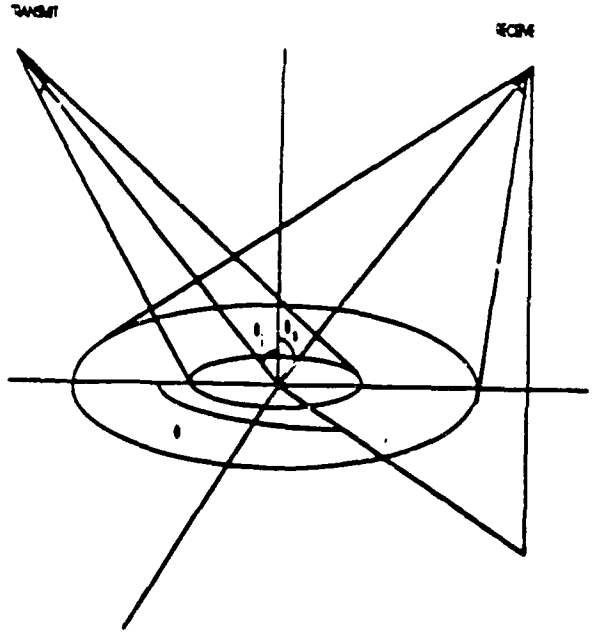

Fig. 2 Geometry of the bistatic measurement problem.

a tenna was used for reception and a narrow-beam antenna was used for transmission. The transmit antenna had a beamwidth of 3°, compared to about 15° for the receive antenna. At a nominal distance of 3.2 m between the target and the transmit and receive antennas, the illuminated area for $\theta_i = \theta_s = 66°$ is 17 cm x 42 cm for the transmit beam and 85 cm x 200 cm for the receive beam.

The radar equation for the bistatic case is given by:

$$P_r = P_t \lambda^2 \frac{G_{t0} G_{r0}}{(4\pi)^3} \int \frac{g_t(\theta_t)\, g_r(\theta_r)}{R_t^2 R_r^2} \sigma^\circ \, dA \quad . \quad (1)$$

where P_t is the transmitted power; G_0 is maximum gain of the (transmit or receive) antenna, $g(\theta)$ is the normalized radiation pattern; R is the range to the target; the subscripts t and r stand for transmit and receive, respectively; θ is the antenna angle relative to the boresight direction; σ° is the bistatic scattering coefficient of the target, and dA is an element of area. Assuming σ° is approximately constant over the angular range of the transmit antenna beamwidth, the preceding equation may be rewritten as:

$$P_r = P_t \lambda^2 \frac{G_{t0} G_{r0}}{(4\pi)^3} \sigma^\circ \, I \quad . \quad (2)$$

where I, the illumination integral, may be computed from knowledge of the antennas' radiation patterns and the measurement geometry.

A. Calibration

The system was calibrated by measuring the received power with the transmit and receive antennas pointing at each other along their boresight directions. If this is referred to as the calibration signal P_c,

$$P_c = P_t \frac{\lambda^2 G_{t0} G_{r0}}{(4\pi R_c)^2} \quad . \quad (3)$$

where R_c is the distance between the two antennas, then

$$\frac{P_r}{P_c} = \left(\frac{R_c^2 I}{4\pi} \right) \sigma^\circ \quad . \quad (4)$$

An alternate calibration approach is to measure the reflected power from a flat metal plate in the specular direction (i.e. the plate is oriented such that $\theta_i = \theta_s$ and its surface normal is in the plane containing the boresight directions of the two antennas). If the plate is much larger than the footprint of the transmit antenna pattern, image theory leads to the same expression given by (3) if R_c is replaced with $R_t + R_r$. The two calibration approaches were found to yield results that agree with one another within an accuracy range of about 1 dB.

Using the metal plate as a specular reflector, the azimuth pattern of the transmit antenna was measured by moving the receive antenna in azimuth in steps of 2°. The results are shown in Fig. 3. Actually the plot is a product of the radiation patterns of the transmit and receive antennas, but the receive antenna pattern is

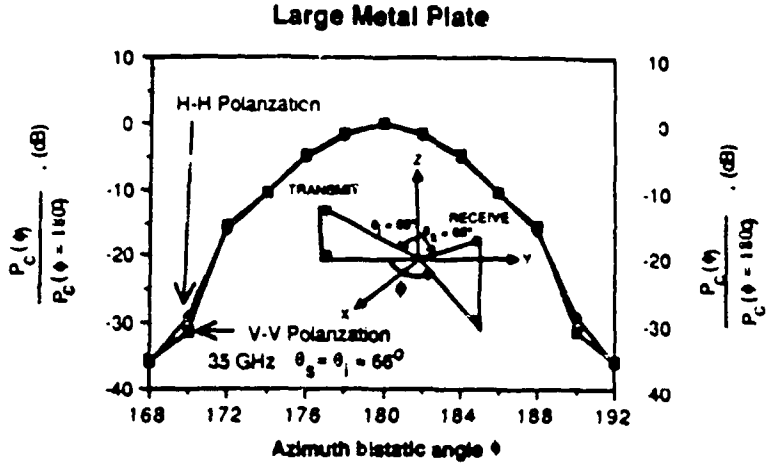

Fig. 3 Azimuth pattern of the transmit antenna determined from measurements of the power reflected by a large metal plate.

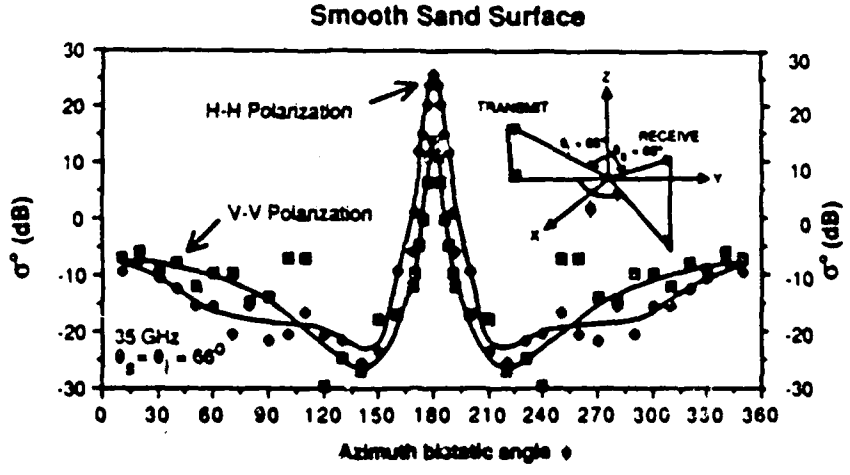

Fig. 4 Measured bistatic scattering pattern of a smooth sand surface.

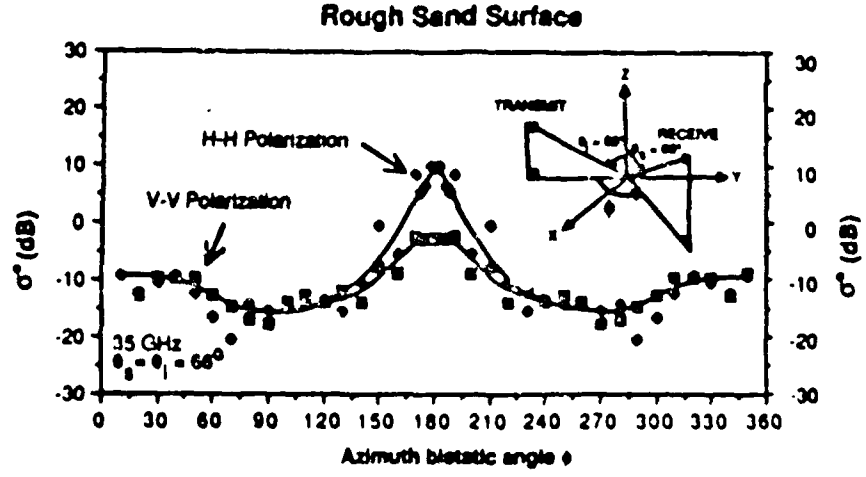

Fig. 5 Measured bistatic scattering pattern of a rough sand surface.

much wider than that of the transmit antenna, and hence its effect on the shape of the product pattern is secondary in importance.

B. Noise Performance

The radar system is designed to step in frequency from 34 GHz to 36 GHz in 401 steps. The 2-GHz bandwidth provides two major advantages. By Fourier-transforming the frequency response to the time domain, it is possible to gate the time response to correspond to reflections from the target area alone, thereby eliminating reflections from other targets or objects in the test area. This procedure led to a noise-equivalent level for σ° equal to -45 dB. When absorbing material was used to cover the target area, the reflected power corresponded to $\sigma^\circ = -25$ dB. This is because the test was performed for $\theta_i = \theta_s = 66^\circ$ and $\phi = 90^\circ$. Away from normal incidence, the reflection performance of absorbing materials deteriorates rapidly for large values of θ. As a data-quality test, only values of σ° larger than -35 dB, which corresponds to a signal-to-noise ratio of at least 10 dB, are considered acceptable for further processing and analysis.

C. Measurement Precision

The second major advantage derived from using the 2-GHz bandwidth is that by averaging the received signal over such a wide bandwidth, the precision with which σ° is measured is greatly improved. According to Rayleigh fading statistics, the ratio of the standard deviation s to the mean value $\bar{\sigma}^\circ$ associated with a radar measurement of a target is given by

$$\frac{s}{\bar{\sigma}^\circ} = \frac{1}{\sqrt{N}} . \qquad (5)$$

where N is the total number of independent samples included in the measurement of σ°. Frequency averaging over a 2-GHz bandwidth provides approximately five independent samples for the geometry used in this study. The calculation leading to $N_f \cong 5$ is based on the expressions given in [4].

In addition to frequency averaging, spatial averaging was used by rotating the target about its own axis. This led to 10 independent spatial samples. Hence, $N = N_f N_s \cong 50$, and $s/\bar{\sigma}^\circ \cong 0.14$.

III. RESULTS

A. Target Characteristics

The targets examined in this phase of the program included two sand surfaces and a coarse gravel surface. The first sand surface was prepared to be flat and smooth and the second one was artificially roughened to generate a randomly distributed, slightly rough surface. Based on measurements of two transects of the surface height profile, the r.m.s. height is estimated to be smaller than 0.1 cm for the smooth surface and about 1.67 cm for the slightly rough surface. The latter surface consisted of smooth undulations with no small scale structure; the undulations looked like randomly oriented plane facets approximately 10 cm in diameter. The stones in the gravel had diameters ranging from 1 to 2 cm.

The target material (sand and gravel) was placed in a "sand box" at the center of a circle approximately 5 m in diameter. The sand box could be rotated about its axis. The sand box was several times larger than the the size of the antenna footprint at the target surface. The depth of material placed in the box was determined through calculations and verified experimentally. The dielectric constant of the sand was measured at 10 GHz as

$$\epsilon \cong 2.5 - j0.03 . \qquad (6)$$

The sand was totally dry. Hence, the dielectric constant of the sand at 35 GHz is not expected to be different from that at 10 GHz. The penetration depth for $\epsilon''/\epsilon' << 1$ is given by

$$\delta_p = \frac{\lambda\sqrt{\epsilon'}}{2\pi\epsilon''} \cong 7.5 \text{ cm} . \qquad (7)$$

The sandbox was filled with sand to a height of 15 cm, or two penetration depths. The two-way attenuation for $z = 2\delta_p$ is 17 dB. Thus, contributions from depths greater than 15 cm may be neglected. The fact that this was a valid conclusion was verified experimentally by measuring the received power from the sand layer as a function of layer thickness.

The stones comprising the gravel had a permittivity $\epsilon' = 4.6$ at 10 GHz. The thickness of the gravel layer used in this study was 15 cm also.

B. Bistatic Scattering From Smooth Sand

The first question that needed to be addressed was: How close to a specular surface is a "visually" smooth sand surface at 35 GHz? The scattering function for a specular surface is a delta function; for a given incidence angle θ_i, power is reflected only in the direction corresponding to $\theta_s = \theta_i$ and $\phi = 180^\circ$. Moreover, the reflected signal is totally coherent in nature. As the surface departs from perfectly smooth, the magnitude of the coherent scattering component decreases and incoherent scattering becomes present in addition.

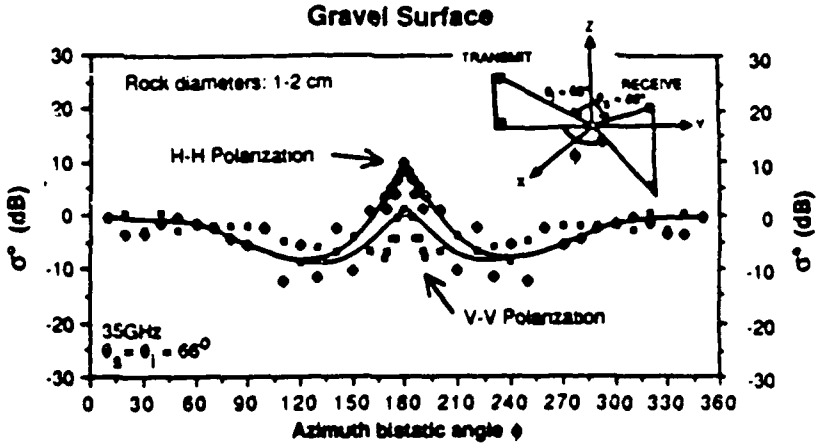

Fig. 6 Measured bistatic scattering pattern of a gravel surface.

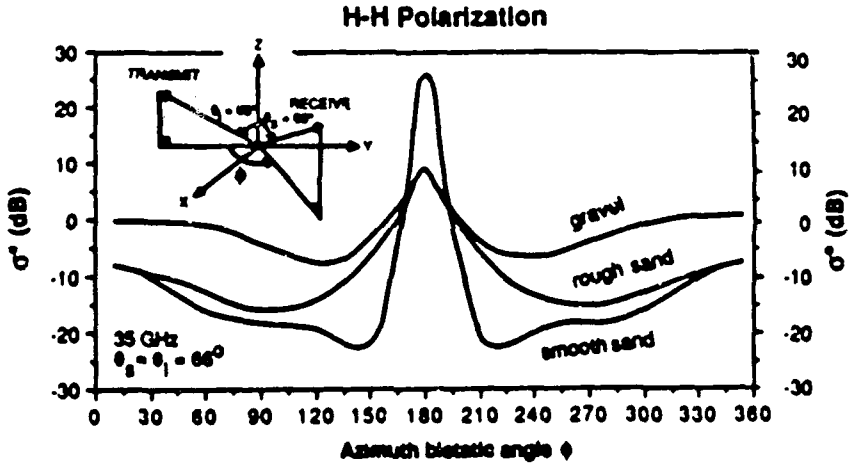

Fig. 7 Comparison of the measured bistatic scattering patterns for the smooth sand surface, rough sand surface, and the gravel surface for HH polarization.

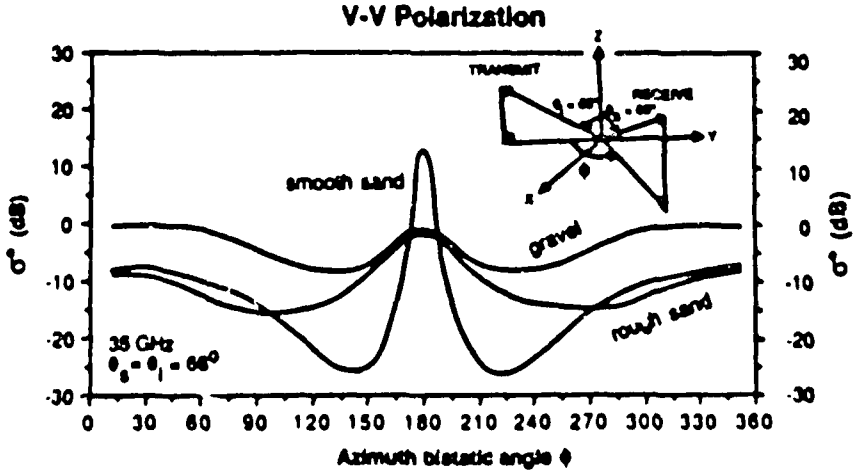

Fig. 8 Comparison of the measured bistatic scattering patterns for the smooth sand surface, rough sand surface, and the gravel surface for VV polarization.

With $\theta_i = 66°$, the received power was measured along the specular direction first for the smooth sand surface and then for a perfectly conducting flat plate placed on top of the sand surface. The signal reflected from the sand surface was lower than that reflected from the metal plate by 6.4 dB for H polarization and by 18.4 dB for V polarization. For a specular sand surface, the difference in level should be equal to $\Gamma_H^s(66°)$ for H polarization and equal to $\Gamma_V^s(66°)$ for V polarization, where $\Gamma^s(66°)$ is the Fresnel reflectivity at $\theta_i = 66°$. For a sand surface with ε as given by equation (6), $\Gamma_H^s(66°) = 0.27$ and $\Gamma_V^s(66°) = 0.014$. The corresponding values in dB are $\Gamma_H^s = -5.7$ dB and $\Gamma_V^s = -18.5$ dB. Thus, the measured reflectivities Γ_H and Γ_V are 0.7 dB and 0.1 dB lower in level than their specular counterparts. In other words, a "visually" smooth sand surface is also electromagnetically smooth with regard to reflection along the specular direction at 35 GHz.

Figure 4 shows measured values of the bistatic scattering coefficient $\sigma^\circ(\theta_i, \theta_s, \phi)$ plotted as a function of ϕ for $\theta_i = \theta_s = 66°$. The plots cover the range from 10° to 350°, although the actual measurements covered only the range from 10° to 180°. We observe that in the specular direction, σ°_{HH} is larger than σ°_{VV} by 12 dB, but outside the main-lobe region, σ°_{VV} tends to be slightly larger than σ°_{HH}.

C. Bistatic Scattering From Rough Sand Surface

The bistatic scattering patterns of the slightly rough sand surface (Fig. 5) exhibit significantly lower levels than the smooth sand surface along the specular direction, by about 17 dB, but the ration $\sigma^\circ_{HH}/\sigma^\circ_{VV}$ remains the same (12 dB) as for the smooth surface. Outside the main lobe region, σ° of the slightly rough surface is generally higher in level than that of the smooth surface and the levels are about the same for the two polarizations.

D. Bistatic Scattering From Gravel

The scattering patterns shown in Fig. 6 for gravel are somewhat similar to those observed for the rough surface except that the difference between σ°_{HH} and σ°_{VV} are for gravel than for the sand surface (8.5 dB compared to 12 dB).

For purposes of comparison of the bistatic data measured for the three surfaces discussed above, Figs. 7 and 8 show the HH-polarization and VV-polarization curves presented earlier in Figs. 4-6.

IV. CONCLUSIONS

The material presented in this paper represents the first phase of a new program designed to establish the bistatic scattering behavior of natural surfaces. The primary tasks realized so far include system calibration and noise performance evaluation and preliminary attempts to analyze the azimuthal variation of the bistatic scattering patterns of smooth and rough surfaces. In future phases of the program, bistatic patterns will be measured as a function of all three angles (θ_i, θ_s, and ϕ) for many types of distributed surfaces. Additionally, appropriate scattering models will be developed as a function of the dielectric and geometrical parameters of the targets.

REFERENCES

[1] Cosgriff, R. L., W. H. Peake, and R. C. Taylor, "Terrain Scattering Properties for Sensor System Design" Report 181, Ohio State University, 1960.

[2] Peake, W. H. and T. L. Oliver, "The Response of Terrestrial Surfaces at Microwave Frequencies," TR AFAL-JR-70-301, Air Force Avionics Lab Wright-Patterson AFB, Ohio, 1971.

[3] Ulaby, F. T., T. F. Haddock, J. East and M. W. Whitt, "A Millimeter-wave Network Analyzer Based Scatterometer," Submitted for publication in *IEEE Transactions on Geoscience and Remote Sensing*, 1987.

[4] Ulaby, F. T., R. K. Moore, and A. K. Fung, Microwave Remote Sensing, Vol II, Addison Wesley, 1982, pp. 782-783.

Accepted for publication in Radio Science

MILLIMETER WAVE SCATTERING MODEL FOR A LEAF

K. Sarabandi, F.T. Ulaby, and T.B.A. Senior

Radiation Laboratory, Electrical Engineering and Computer Science Department,

University of Michigan, Ann Arbor

Abstract

At millimeter wave frequencies a typical leaf is a significant fraction of a wavelength in thickness, and its nonuniform dielectric profile now affects the scattering. To provide a simple and efficient method for predicting the scattering, two types of physical optics approximations are examined. The first approximates the volume polarization current by the current which would exist in an infinite dielectric slab with the same profile, while the second (and simpler) one employs the surface current which, on the infinite slab, produces the known reflected field. It is shown that the first method is superior, and provided the actual dielectric profile is used, it predicts the scattered field to an accuracy which is adequate for most practical purposes.

slab, produces a plane wave identical to the reflected field, and this is the surface current physical optics (SCPO) approximation.

For an electrically thin leaf or plate, the two approximations are indistinguishable, but as the thickness (or frequency) increases, the predicted scattering differs in most directions, and by comparison with the results of a moment method solution of the volume integral equation, it is shown that VIPO is superior. In addition, for a two layer material, it is no longer adequate to treat the plate as homogeneous one having an average dielectric constant. Provided the actual dielectric profile of a leaf is simulated, it appears that VIPO can predict the scattering behavior of a leaf to an accuracy that is sufficient for most practical purposes at millimeter wavelengths.

2 Structure of a Leaf

The structure of a typical vegetation leaf is shown in Fig.1. The type and number density of cells may vary as a function of depth into the leaf which, in turn, results in a nonuniform dielectric profile. The effect of this nonuniformity becomes observable at higher frequencies where the thickness of the leaf is comparable to the wavelength.

Leaves contain two types of photosynthetic cells: *palisade parenchyma*, consisting of column-shaped cells in which most photosynthesis takes place, and *spongy parenchyma*, which consist of irregularly shaped cells with large spaces between them. Because a large part of the vegetation material is water, its dielectric con-

as 4 dB at 140 GHz.

3 Physical Optics Approximations

At microwave frequencies where a typical leaf is no more than about $\lambda_0/50$ in thickness with lateral dimensions comparable to or larger than the wavelength, the scattering properties can be accurately predicted using the physical optics approximation applied to a resistive sheet model of a leaf [Sarabandi et al, 1988]. In effect, the leaf is modeled as an infinitesimally thin layer, but as the frequency increases, it is necessary to take the leaf thickness in to account. There are now two types of physical optics approximation that can be employed. The standard one is the surface current (SCPO) approach in which an infinite dielectric slab is replaced by an equivalent sheet current that produces a plane wave identical to the reflected wave of the slab. This current is then used as an approximation to the equivalent surface current over the upper surface of a finite dielectric plate. Alternatively, the induced (volume) polarization current in the plate can be approximated by the current in the infinite dielectric slab, and we shall refer to this as the volume integral physical optics (VIPO) method. It is more accurate than the SCPO method, although the latter is more convenient to use for evaluating the scattered field.

To illustrate the two procedures, consider a dielectric plate consisting of a homogeneous dielectric of thickness d_1 and relative permittivity ϵ_1 atop a second material of thickness $d_2 - d_1$ and relative permittivity ϵ_2. The plate occupies the region $-\frac{a}{2} \leq y \leq \frac{a}{2}$, $-\frac{b}{2} \leq y \leq \frac{b}{2}$, and $-d_2 \leq z \leq 0$ as shown in Fig. 2, and is

and

$$\Gamma = \frac{C_+ R_1 + C_- e^{2ik_{1z}d_1}}{C_+ + C_- R_1 e^{2ik_{1z}d_1}}. \tag{5}$$

The corresponding results for a single layer of thickness d_1 and relative dielectric constant ϵ_1 can be obtained by putting $d_2 = d_1$ and $k_{2z} = k_{1z}$, implying $B_2 = B_1$ and $A_2 = A_1$.

Given a volume distribution of electric current J in free space, the corresponding Hertz vector is

$$\Pi(\bar{r}) = \frac{iZ_0}{4\pi k_0} \int_V \mathbf{J}(\bar{r}') \frac{e^{ik_0|\bar{r}-\bar{r}'|}}{|\bar{r}-\bar{r}'|} dv, \tag{6}$$

where $Z_0 (= 1/Y_0)$ is the free space impedance, and the resulting field is

$$\mathbf{E}(\bar{r}) = \nabla \times \nabla \times \Pi(\bar{r}),$$

$$\mathbf{H}(\bar{r}) = -ik_0 Y_0 \nabla \times \Pi(\bar{r}).$$

In the far zone of the current distribution

$$\Pi(\bar{r}) \approx \frac{e^{ik_0 r}}{k_0 r} \frac{iZ_0}{4\pi k_0} \int_V \mathbf{J}(\bar{r}') e^{-ik_0 \hat{r}\cdot\bar{r}'} dv, \tag{7}$$

and

$$\mathbf{E}(\bar{r}) \approx -k_0^2 \hat{r} \times \hat{r} \times \Pi(\bar{r}). \tag{8}$$

In the dielectric slab the volume current J is the polarization current

$$\mathbf{J} = -ik_0 Y_0 (\epsilon_j - 1) E_y \hat{y}. \tag{9}$$

where E_y has the value appropriate to each layer ($j = 1, 2$), and when this is inserted into (6) and the integration carried out over the volume occupied by

produces a plane wave identical to the field reflected from the dielectric slab. As evident from the impulse function $\delta(z)$ in (16), the current is located at the upper surface of the slab, and when (16) is inserted into (6) we find

$$\Pi^{SCPO} \approx \hat{y}\frac{e^{ik_0 r}}{k_0 r}\cdot\frac{-i}{2\pi}\cos\theta_0\Gamma ab\frac{\sin X}{X}, \tag{17}$$

and the far field amplitude is then

$$S_E^{SCPO}(\theta_s,\theta_0) = \hat{y}\frac{-ik_0^2}{2\pi}\cos\theta_0\Gamma ab\frac{\sin X}{X}. \tag{18}$$

In the specular ($\theta_s = -\theta_0$) and backscattering ($\theta_s = \theta_0$) directions it can be verified that (14) and (18) are identical, but in the other directions the two approximations differ.

In the case of H polarization for which

$$\mathbf{H}^i = \hat{y}e^{ik_0(x\sin\theta_0 - z\cos\theta_0)} \tag{19}$$

the analysis is similar. With H_y represented as shown in (2), the various coefficients (now indicated by primes) differ from those for E polarization in having k_{1z} replaced by k_{1z}/ϵ_1 and k_{2z} replaced by k_{2z}/ϵ_2 everywhere except in the exponents. The induced polarization current then has two components and is given by

$$\mathbf{J} = -ik_0Z_0(\epsilon_j - 1)(E_x\hat{x} + E_z\hat{z}). \tag{20}$$

where $E_x = (ik_0\epsilon_j)^{-1}Z_0\partial H_y/\partial z$ and $E_z = -(ik_0\epsilon_j)^{-1}Z_0\partial H_y/\partial x$ have the values appropriate to each layer ($j = 1, 2$). The Hertz vector can be computed using (6), and for the scattered field $\mathbf{H}^s$, the far field amplitude is found to be

$$S_H^{VIPO}(\theta_s,\theta_0) = \hat{y}\frac{k_0^3 ab}{4\pi}\frac{\sin X}{X}(\cos\theta_s F_1' - \sin\theta_s F_2'). \tag{21}$$

4 Numerical Results

To illustrate the difference between the VIPO and SCPO approximations we consider a homogeneous (single layer) plate of thickness $d_2 = \lambda_0/4$ with $\epsilon_2 = \epsilon_1 = 3 + i0.1$. For an E-polarized plane wave incident at 30 degrees, the amplitude and phase of S^{VIPO}/S^{SCPO} are given in Figs. 3 and 4, and these show that the difference increases away from the specular and backscattering directions. At a fixed scattering angle, the difference increases with the electrical thickness of the plate up to the first resonance and then decreases. To test their accuracy the two approximations have been compared with the results of a moment method solution of the volume integral equation. The particular code used is a two-dimensional one which was extended to three dimensions by assuming that the induced currents are independent of the y coordinate. Since the dielectric constant of most vegetation materials is high, it is necessary to have the cell sizes very small, and one consequence of this is the need to compute the matrix elements extremely accurately, especially for H polarization. For a $2\lambda_0$ square plate formed from the above-mentioned layer and illuminated by an E-polarized plane wave at normal incidence, the two approximations are compared with the moment method solution in Fig. 5, and the superiority of VIPO is clear.

In the case of a thin plate the two approximations are indistinguishable. This is illustrated in Fig. 6 showing the VIPO expression (14) and the moment method solution for a $2\lambda_0$ square plate of thickness $d_2 = \lambda_0/50$ for E polarization. The plate is a homogeneous one having $\epsilon = 13 + i12$ corresponding to the average

al [1987] the leaf can be modeled as a resistive sheet using an average value for the permittivity. If the physical optics approximation is then applied, the resulting scattering is attributed to a surface current, and this method is equivalent to the SCPO approximation. At higher frequencies, however, the thickness and structure of a leaf are more significant. At 100 GHz and above a leaf is a considerable fraction of a wavelength in thickness, and in spite of the reduced sensitivity to water content, the nonuniformity affects the scattering.

For a two-layer model of a leaf, the SCPO approximation has been compared with the volume integral (VIPO) approximation. When the leaf is thin the two approximations are identical and in good agreement with data obtained from a moment method solution of the integral equation, but as the electrical thickness increases, the two approximations diverge in all directions except the specular and (for E polarization) backscattering ones. Although the VIPO approximation is more complicated, its accuracy is greater, and the agreement with the moment method data is better using a two-layer model than when a single layer of average permittivity is employed.

For most practical purposes it would appear that VIPO in conjunction with an accurate dielectric profile of a leaf provides an adequate approximation to the scattering at millimeter wavelengths. As our knowledge of the profile increases, it may be desirable to use a multi-layer model which could even simulate a continuous, nonuniform profile, and a convenient way of doing this is described in the Appendix. We also note that at frequencies for which the leaf thickness is comparable to $\lambda_m/2$

References

[1] Le Vine, D.M., A. Snyder, R.H. Lang, and H.G. Garter, Scattering from thin dielectric disks, *IEEE Trans. Antennas Propag.*, 33, 1410-1413, 1985.

[2] Sarabandi, K., T.B.A. Senior, and F.T. Ulaby, Effect of curvature on the backscattering from a leaf, *J. Electromag. Waves and Applics.*, 2, 653-670, 1988.

[3] Senior, T.B.A., K. Sarabandi, and F.T. Ulaby, Measuring and modeling the backscattering cross section of a leaf, *Radio Sci.*, 22, 1109-1116, 1987.

[4] Senior, T.B.A., and J.L. Volakis, Sheet simulation of a thin dielectric layer, *Radio Sci.*, 22, 1261-1270 1987.

[5] Willis, T.M., H. Weil, and D.M. Le Vine, Applicability of physical optics thin plate scattering formulas for remote sensing, *IEEE Trans. Geosci. Remote Sensing*, 26, 153-160, 1988.

where $\mathbf{J}_{\overline{m}}$ is the total electric current supported by the resistive sheet, and

$$\hat{\mathbf{n}} \times \{\hat{\mathbf{n}} \times [\mathbf{H}^+ + \mathbf{H}^-]\} - \frac{iY_0}{k_0}\hat{\mathbf{n}} \times \frac{\partial}{\partial n}[\mathbf{E}^+ + \mathbf{E}^-] = -2R_m^s \mathbf{J}_m^s \qquad \text{(A4)}$$

$$\mathbf{J}_m^s = -\hat{\mathbf{n}} \times [\mathbf{E}^+ - \mathbf{E}^-] \qquad \text{(A5)}$$

where $\mathbf{J}_m^s$ is the total magnetic current supported by the conductive sheet. The superscripts $^{+,-}$ refer to the upper $(+)$ and lower $(-)$ sides of the sheet, and $\hat{\mathbf{n}}$ is the unit vector outward normal to the upper side.

A2 Scattering by a Stack of N Planar Sheets

Consider a stack of N infinite planar combined sheets all parallel to the xy plane of a Cartesian coordinate system (x, y, z) as depicted in Fig. A1. The top sheet is in the $z = 0$ plane and the m^{th} sheet is located at $z = -d_m$, where $d_1 = 0$. The space between the m^{th} and $(m+1)^{th}$ sheets is referred to as region m, and we note that region 0 $(z > 0)$ and region $N(z < -d_n)$ are semi-infinite free space. A plane wave whose plane of incidence is parallel to the xz plane impinges on the stack of sheets from above. From the symmetry of the problem, all the field vectors are independent of y (i.e., $\frac{\partial}{\partial y} = 0$), as a result of which the field components in each region can be separated into $E-$ and $H-$polarized waves which are the dual of each other.

In the case of E polarization the incident field is given by (1) and the field

expressed as (excluding the phase factor $e^{ik_0 \sin\theta_0 x}$)

$$J_m^E = \hat{y} 2Y_0 \cos\theta_0 e^{ik_0 \cos\theta_0 d_m} \left[1 - \frac{1+\Gamma_m^E}{1+e^{2ik_0\cos\theta_0(d_{m+1}-d_m)}\Gamma_m^E}\right] \cdot \prod_{\ell=1}^{m-1} \left(\frac{1+\Gamma_{\ell-1}^E}{1+e^{2ik_0\cos\theta_0(d_{\ell+1}-d_\ell)}\Gamma_\ell^E}\right). \tag{A8}$$

The total reflection coefficient in region 0 ($\Gamma_E(\theta) = \Gamma_0^E$) can be evaluated from the recursive relation (A7) by noting that $\Gamma_N^E = 0$ (the region N is semi-infinite). The total transmission coefficient can also be obtained from (A7) as follows:

$$T_E(\theta) = \frac{C_N^i}{C_0^i} = \prod_{m=1}^{N} \left[\frac{1+\Gamma_{m-1}^E}{1+e^{2ik_0\cos\theta_0(d_{m+1}-d_m)}\Gamma_m^E}\right] \tag{A9}$$

Unlike the E-polarized case where the magnetic current is zero, an H-polarized wave excites a magnetic current in the y direction and the tangential electric and magnetic fields are both discontinuous across the combined sheets. For H polarization the tangential field vectors in region m can be obtained by applying the duality relationships to (A6). In this case the amplitudes of the travelling in $-z$ and $+z$ directions are denoted by B_m^i and B_m^r respectively. By applying the boundary conditions (A2)-(A5) at the m^{th} sheet and denoting the reflection coefficient in region m by

$$\Gamma_m^H = \frac{B_m^r}{B_m^i} e^{-2ik_0\cos\theta_0 d_{m+1}},$$

after some algebraic manipulation we obtain

$$\Gamma_{m-1}^H = \frac{(Q_m P_m - 1) - (1-P_m)(Q_m - 1)\Gamma_m^H e^{2ik_0\cos\theta_0(d_{m+1}-d_m)}}{-(1+P_m)(1+Q_m) + (1-Q_m P_m)\Gamma_m^H e^{2ik_0\cos\theta_0(d_{m+1}-d_m)}} \tag{A10}$$

$$B_m^i = \frac{(Q_m - 1) + (1+Q_m)\Gamma_{m-1}^H}{-(1+Q_m) + (1-Q_m)\Gamma_m^H e^{2ik_0\cos\theta_0(d_{m+1}-d_m)}} B_{m-1}^i \tag{A11}$$

leads to

$$\Pi(\bar{r}) \approx \frac{e^{ik_0 r}}{ik_0 r}\frac{jZ_0}{4\pi}\int_{-a/2}^{a/2}\int_{-b/2}^{b/2}\Big(\sum_{m=1}^{N} \mathbf{J}_m(\bar{r}')e^{ik_0\cos\theta_s d_m}\Big)e^{ik_0\sin\theta_s x'}dx'dy',$$

$$\Pi^*(\bar{r}) \approx \frac{e^{ik_0 r}}{ik_0 r}\frac{jY_0}{4\pi}\int_{-a/2}^{a/2}\int_{-b/2}^{b/2}\Big(\sum_{m=1}^{N} \mathbf{J}_m^*(\bar{r}')e^{ik_0\cos\theta_s d_m}\Big)e^{ik_0\sin\theta_s x'}dx'dy'. \tag{A16}$$

Using the physical optics approximation, the currents obtained for the infinite sheets are substituted into (A16) to find the scattered fields. For E and H polarizations the far field amplitudes are

$$\mathbf{S}_E(\theta_s,\theta_0) = \hat{y}\frac{j}{4\pi}k_0^2 ab Z_0\Big(\sum_{m=1}^{N}\mathbf{J}_m^E e^{ik_0\cos\theta_s d_m}\Big)\frac{\sin X}{X}, \tag{A17}$$

$$\mathbf{S}_H(\theta,\theta_0) = \hat{y}\frac{j}{4\pi}k_0^2 ab\Big[\sum_{m=1}^{N}(\cos\theta_s \mathbf{J}_m^H + Y_0\mathbf{J}_m^{H*})e^{ik_0\cos\theta_s d_m}\Big]\frac{\sin X}{X}. \tag{A18}$$

where, as before, $X = \frac{ka}{2}(\sin\theta_s + \sin\theta_0)$. In the backscattering ($\theta_s = \theta_0$) and specular ($\theta_s = -\theta_0$) directions the summation term in (A17) reduces to a telescopic series resulting in

$$\sum_{m=1}^{N}\mathbf{J}_m^E e^{ik\cos\theta_0 d_m} = 2Y_0\cos\theta_0 C_0^r = 2Y_0\cos\theta_0\Gamma_E(\theta_0), \tag{A19}$$

and backscattering cross section is then

$$\sigma_E(\theta_0,\theta_0) = 4\pi\frac{(ab)^2}{\lambda^2}\cos^2\theta_0\,|\,\Gamma_E(\theta_0)\,|^2\,\frac{\sin^2(ka\sin\theta_0)}{(ka\sin\theta_0)^2}. \tag{A20}$$

Also, for H polarization

$$\begin{aligned}\textstyle\sum_{m=1}^{N}(\cos\theta_0 J_m^H + Y_0 J_m^{H*})e^{ik_0\cos\theta_0 d_m} &= -2\cos\theta_0\textstyle\sum_{m=1}^{N}(B_{m-1}^r - B_m^r)\\ &= -2\cos\theta_0 B_0^r = -2\cos\theta_0\,\Gamma_H(\theta_0),\end{aligned} \tag{A21}$$

List of Figures

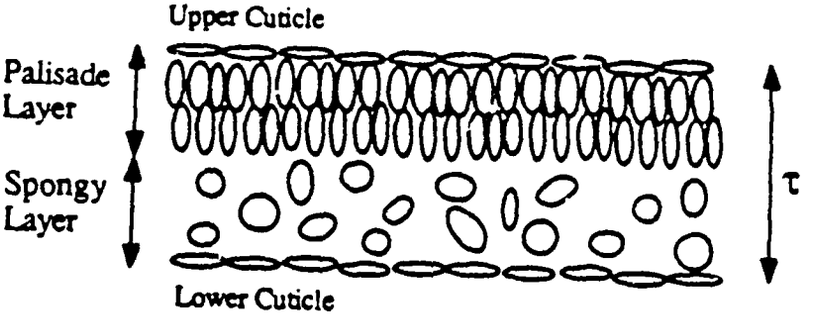

Figure 1: The structure of a typical vegetation leaf.

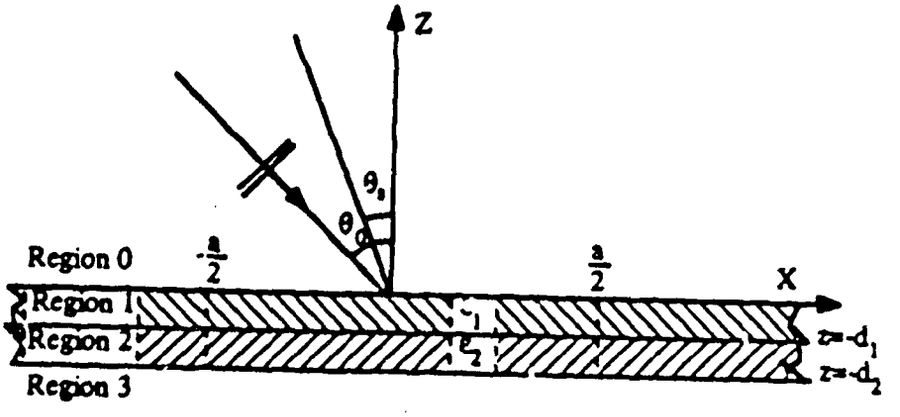

Figure 2: The geometry of the scattering of a plane wave from a two-layer dielectric slab.

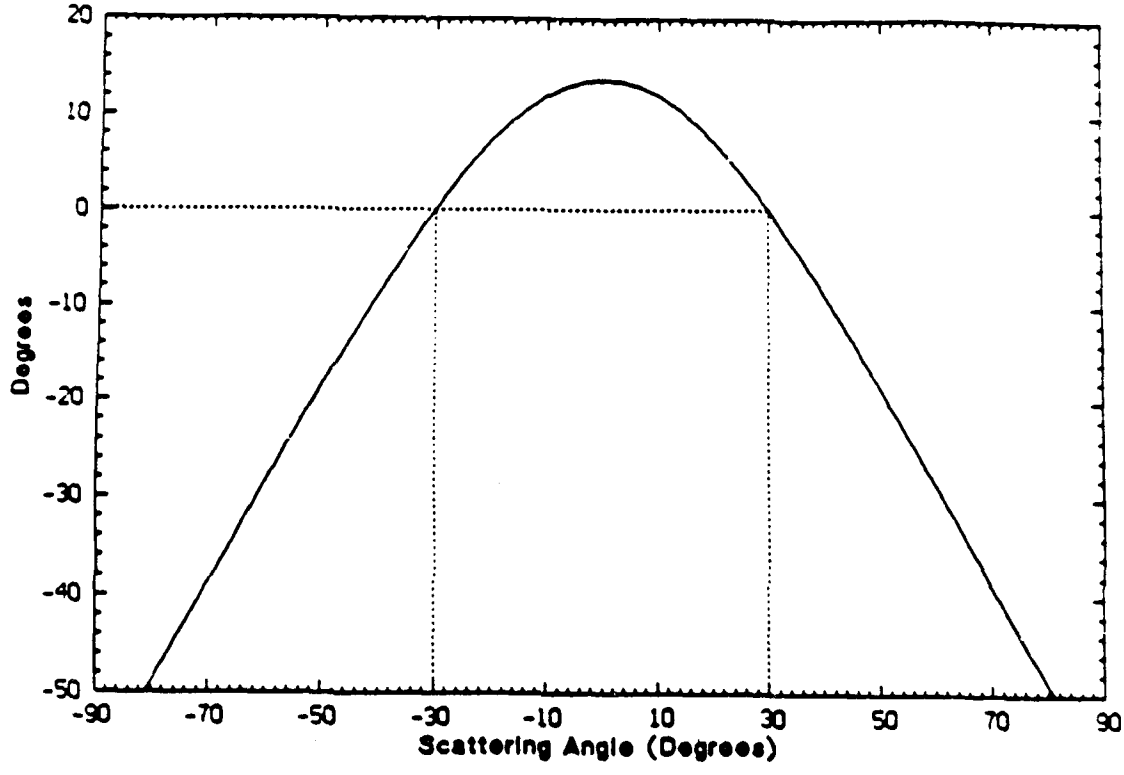

Figure 4: Phase of the ratio of the bistatic far field amplitude of VIPO to SCPO for E polarization of a dielectric plate with $d_2 = \lambda_0/4$ and $\epsilon_1 = \epsilon_2 = 3 + i0.1$ at $\theta_0 = 30$ degrees.

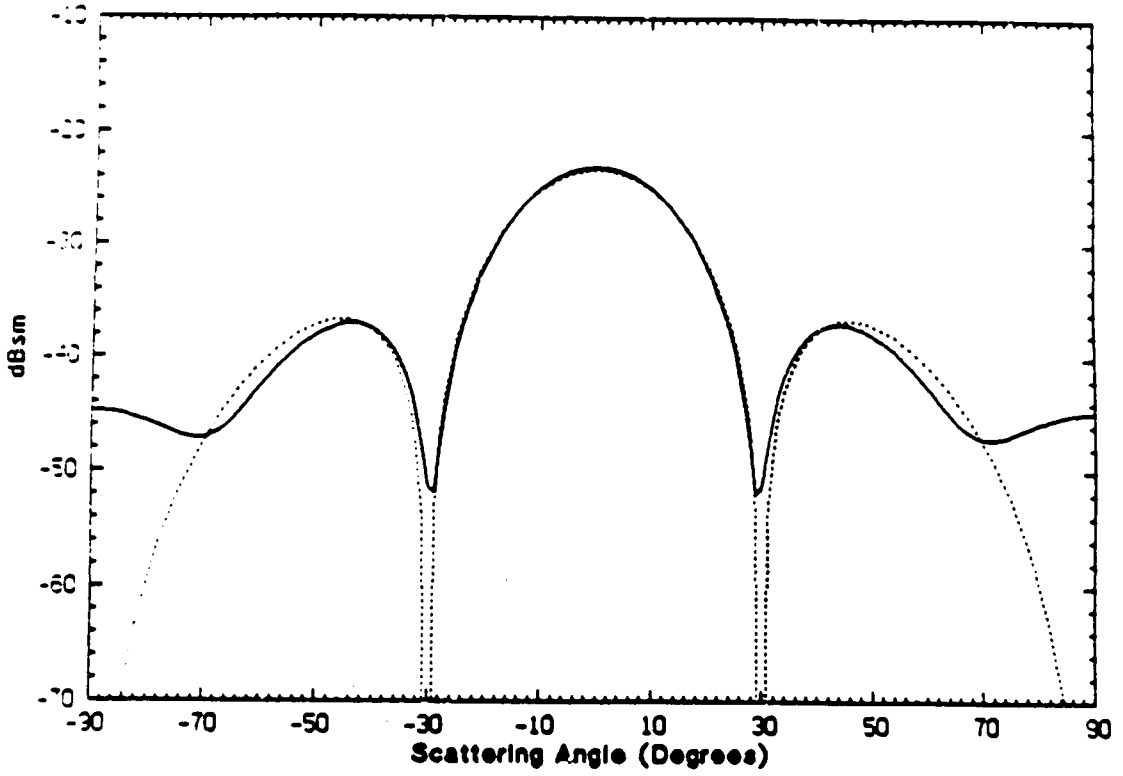

Figure 6: The bistatic cross section area of a $2\lambda_0 \times 2\lambda_0$ plate for E polarization with $d_z = \lambda_0/50$ and $\epsilon_{avg} = 13 + i12$ at normal incidence: (——) moment method solution, (- - -) VIPO or SCPO.

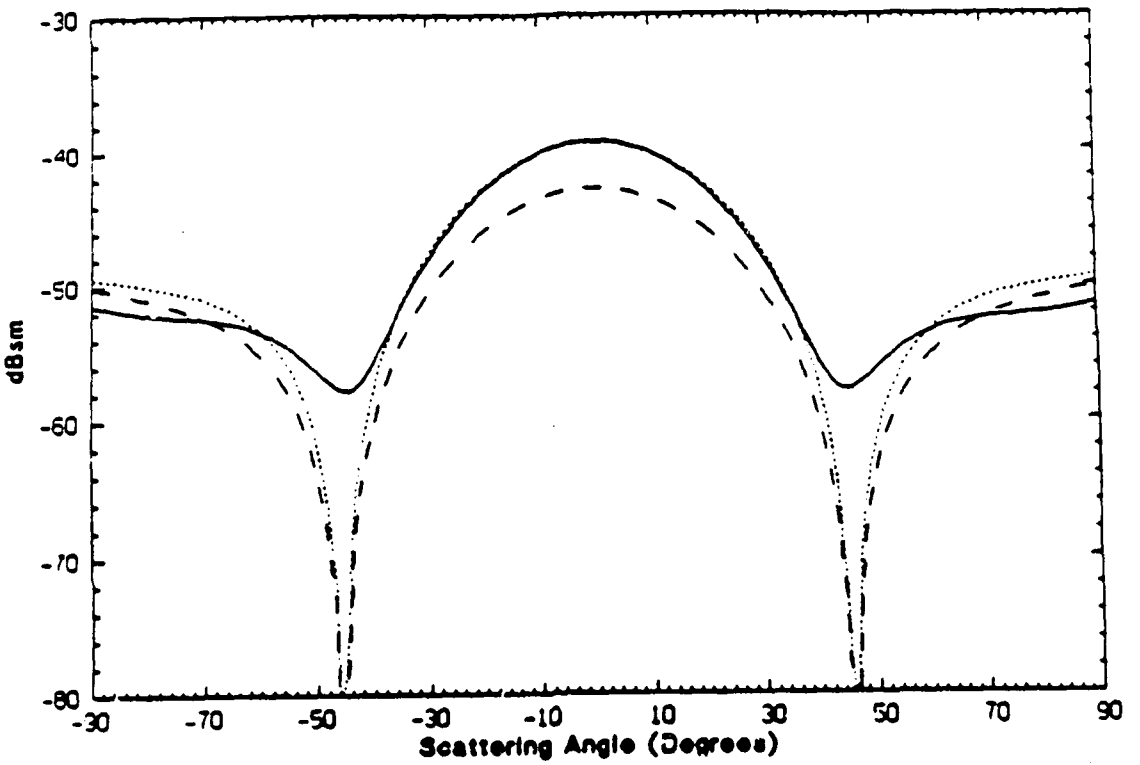

Figure 8: The bistatic cross section of a $1.4\lambda_0 \times 2\lambda_0$ plate for E polarization with $d_2 = 2d_1 = 0.5mm$ and f =140 GHz at normal incidence: (——) moment method solution with $\epsilon_1 = 5 + i4$, $\epsilon_2 = 2 + i1$, (- - -) VIPO with $\epsilon_1 = 5 + i4$, $\epsilon_2 = 2 + i1$, (– –) VIPO with $\epsilon_2 = \epsilon_1 = 3.5 + i2.5$.

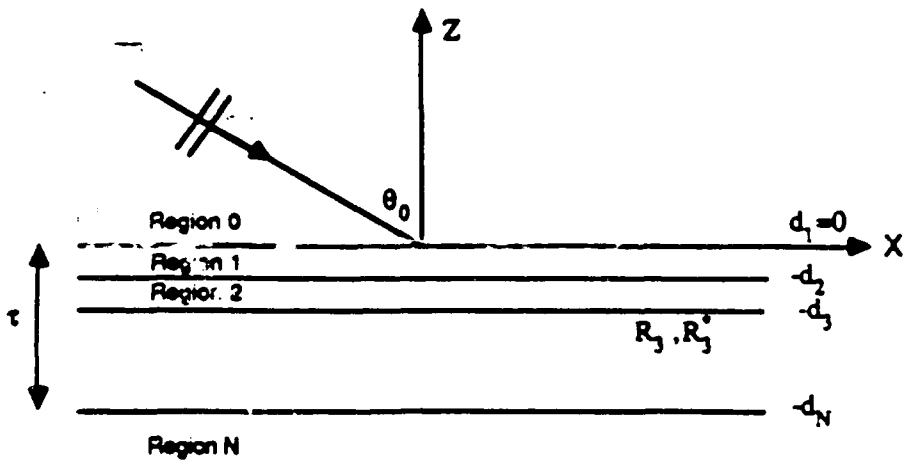

Figure A-1: Layer of N combined sheets simulating infinite dielectric slab.

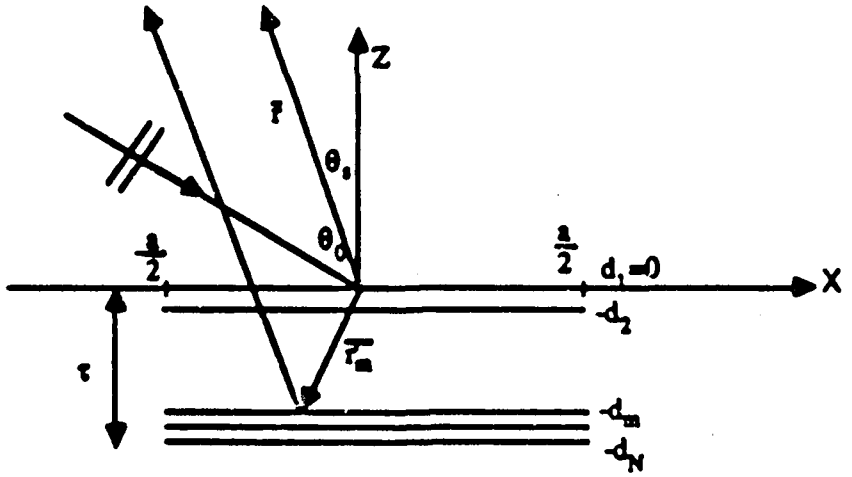

Figure A-2: The geometry of the scattering of a plane wave from a finite N-layer combined-sheet.

MEASUREMENT AND MODELING OF MILLIMETER-WAVE SCATTERING FROM TREE FOLIAGE

F.T. Ulaby, T.H. Haddock, and Y. Kuga
Radiation Laboratory
University of Michigan
Ann Arbor, Michigan 48109

ABSTRACT

Because the constituent elements of a tree canopy, namely the leaves, needles, branches, and trunks, have complex geometries with curvatures and surface roughness scales that are comparable to or larger than the wavelength at millimeter-wavelengths, the traditional approach used to compute the phase function of the vegetation volume is totally impractical. In this paper we propose a relatively simple model for characterizing the phase function on the basis of direct experimental data. The model is used in conjunction with a solution of the radiative transfer equation to predict the backscattering behavior of tree canopies. The model is found to provide very good agreement with radar observations made of 35, 94, and 140 GHz.

This work was supported by U.S. Army Research Office contract DAAG29-85-K-0020.

Vegetation Scattering at Millimeter Wavelengths

1. INTRODUCTION

The leaves, needles, branches, and trunks comprising a vegetation canopy are lossy dielectric structures with complex geometries. Whereas it may be acceptable to approximate a leaf as a thin, flat disc at centimeter and longer wavelengths, such a treatment is invalid at millimeter wavelengths because the leaf curvature and its thickness are comparable to or larger than λ. Similar statements can be made with regard to the size and surface roughness of branches and other components of a vegetation plant or tree. Consequently, it is very difficult, if not impossible, to use numerical quadrature techniques for solving the vector radiative transfer equation [Ulaby et al., 1986; Tsang et al., 1985] to compute the radar backscattering coefficient of vegetation at millimeter wavelengths. The problems encountered are: (1) it is not possible to compute the scattering phase function of the vegetation volume because accurate models for the scattering matrices of the scattering elements (curved leaves, rough-surface branches, etc.) are not available at millimeter wavelengths, and even if such models were available, the numerical computations that would have to be performed to obtain the phase function (which involve integration over size and orientation parameters) would be extremely expensive, and (2) when the phase function has a complicated dependence on the bistatic scattering angles, it is very difficult to compute the solution of the radiative transfer problem beyond the first order. Hence, an alternate approach is needed for computing the radar backscatter from vegetation at millimeter wavelengths.

In this paper we shall propose a relatively simple model for characterizing the phase function of vegetation canopies at millimeter wavelengths, and then use it in a second-order solution of the radiative transfer equation to compute radar

backscattering from trees. Model results are compared with radar backscatter measurements for tree canopies at 35, 94, and 140 GHz.

2. PHASE MATRIX

Except for the main trunk, tree foliage consists primarily of randomly distributed leaves (or needles) and branches, most of which are much larger than the wavelength in size (at millimeter wavelengths), have complex shapes, and are characterized by a quasi-uniform orientation distribution. These properties suggest that whereas individual scattering elements may exhibit highly complex and polarization-dependent scattering patterns, an elemental volume dV containing many of these elements is likely to exhibit propagation and scattering properties that are weakly polarization-dependent and characterized by a relatively simple scattering pattern. This prediction is supported by experimental observations made by Ulaby et al. [1988] which show that bistatic scattering from trees exhibits comparable results for horizontal and vertical polarizations.

The random nature of the tree foliage supports the use of radiative transfer theory [Ishimaru, 1978] for modeling millimeter wave propagation in the canopy [Ulaby et al., 1988; Schwering et al., 1988]. In the radiative transfer model, the formulation is given in terms of the phase function $P(\theta_s, \phi_s; \theta_i, \phi_i)$ relating the specific intensity scattered by a unit volume of the scattering medium into the direction (θ_s, ϕ_s) to the specific intensity incident upon the unit volume from the direction (θ_i, ϕ_i), with both sets of orientation angles being defined with respect to a reference coordinate $(\hat{x}, \hat{y}, \hat{z})$. The phase matrix represents the average Stokes matrix of the particles constituting the unit volume. To relate P to the properties of the medium, we start by considering scattering by a single particle. For a plane wave with electric field vector $\mathbf{E}^i$ incident upon the particle in the direction $\hat{k}_i = (\theta_i, \phi_i)$, the far-field wave scattered by the particle in the direction $\hat{k}_s = (\theta_s, \phi_s)$ is a spherical wave with field vector $\mathbf{E}^s$. The vertical and

horizontal polarization components or E^s at a range r from the scatterer are related to the components of the incident field through the scattering matrix $S(\theta_s, \phi_s; \theta_i, \phi_i)$ of the particle Ulaby et al., [1986],

$$\begin{bmatrix} E_v^s \\ E_h^s \end{bmatrix} = \frac{e^{ik_o r}}{r} S \begin{bmatrix} E_v^i \\ E_h^i \end{bmatrix}. \quad (1)$$

The matrix S is given by four scattering amplitudes,

$$S(\hat{k}_s, \hat{k}_i) = \begin{bmatrix} S_{vv} & S_{vh} \\ S_{hv} & S_{hh} \end{bmatrix}. \quad (2)$$

For a specified scattered/incident polarization combination, the bistatic scattering cross section of the particle is defined in terms of the ratio of the scattered to incident power densities. For *vh* polarization, for example,

$$\sigma_{vh}(\hat{k}_s, \hat{k}_i) = \left[4\pi r^2 . |E_v^s|^2 / |E_h^i|^2 \right] = 4\pi |S_{vh}|^2. \quad (3)$$

When considering an elementary volume containing N randomly distributed particles per unit volume, we can characterize bistatic scattering by the volume in terms of the bistatic scattering cross section per unit volume (or bistatic scattering coefficient)

$$\kappa_{vh} = N < \sigma_{vh} >$$
$$= 4\pi N < |S_{vh}|^2 >, \qquad (4)$$

where < > denotes ensemble average.

The vector radiative transfer equation is formulated in terms of the specific intensity vector I defined through the modified Stokes parameters I_v, I_h, U, and V as follows:

$$I\, d\Omega = \begin{bmatrix} I_h \\ I_v \\ U \\ V \end{bmatrix} d\Omega = \frac{1}{\eta} \begin{bmatrix} < |E_v|^2 > \\ < |E_h|^2 > \\ 2\mathrm{Re} < E_v E_h^* > \\ 2\,\mathrm{Im} < E_v E_h^* > \end{bmatrix}. \qquad (5)$$

For an elementary volume of length ds illuminated, in the general case, from all directions $\hat{k}_i$ by incident intensity $I^i(\hat{k}_i)$, the intensity scattered in the direction $\hat{k}_s$ is given by

$$I^s(\hat{k}_s) = \int\int_{4\pi} ds\; P\,(\hat{k}_s, \hat{k}_i)\; I^i(\hat{k}_i)\, d\Omega_i \qquad (6)$$

where P is the phase matrix given by

$$\mathbf{P}\ (\hat{\mathbf{k}}_s, \hat{\mathbf{k}}_i) = \begin{bmatrix} P_{11} & P_{12} & P_{13} & P_{14} \\ P_{21} & P_{22} & P_{23} & P_{24} \\ P_{31} & P_{32} & P_{33} & P_{34} \\ P_{41} & P_{42} & P_{43} & P_{44} \end{bmatrix}$$

whose elements are related to those of **S** by

$$\mathbf{P}(\hat{\mathbf{k}}_s, \hat{\mathbf{k}}_i) = N \left[\begin{array}{c|c|c|c} \langle |S_{vv}|^2 \rangle & \langle |S_{vh}|^2 \rangle & \langle Re(S_{vv} S_{vh}^*) \rangle & -\langle Im(S_{vv} S_{vh}^*) \rangle \\ \langle |S_{hv}|^2 \rangle & \langle |S_{hh}|^2 \rangle & \langle Re(S_{hv} S_{hh}^*) \rangle & -\langle Im(S_{hv} S_{hh}^*) \rangle \\ 2\langle Re(S_{vv} S_{hv}^*) \rangle & 2\langle Re(S_{vh} S_{hh}^*) \rangle & \langle Re(S_{vv} S_{hh}^* + S_{vh} S_{hv}^*) \rangle & -\langle Im(S_{vv} S_{hh}^* - S_{vh} S_{hv}^*) \\ 2\langle Im(S_{vv} S_{hv}^*) \rangle & 2\langle Im(S_{vh} S_{hh}^*) \rangle & \langle Im(S_{vv} S_{hh}^* + S_{vh} S_{hv}^*) \rangle & \langle Re(S_{vv} S_{hh}^* - S_{vh} S_{hv}^*) \end{array}\right] \tag{7}$$

3. PROPOSED PHASE MATRIX

The 16 elements of **P** can be readily computed provided we know (1) the number density N, (2) the probability density functions for the sizes, shapes and orientations of the particles, and (3) the dielectric properties of the particles, and additionally we have available appropriate models for computing the scattering matrices of the particles. In most cases, this information is not available for terrain surfaces and volumes, which forces investigators to estimate the physical parameters of the canopy and to treat the canopy constituents as spheres, cylinders, and discs.

These approximations lead to errors, and because the number of parameters involved is large, it is difficult to assess the sources of error.

3.1 PHASE MATRIX IN THE SCATTERING PLANE

Instead of using the first approach described above to compute the elements of the phase matrix P, we propose to use a semi-empirical approach based on experimental measurements. Ulaby et al. [1988] used a 35-GHz bistatic radar system to examine the scattering patterns of small trees under Laboratory conditions. Two types of experiments were conducted: (1) transmission measurements to determine the extinction coefficient κ_e for horizontal and vertical polarizations and (2) bistatic scattering measurements in the plane of scattering (defined to be the plane containing the incident and scattered directions and orthogonal to the polarization planes of the waves [Chandrasekhar, 1960]) to evaluate the angular variations of the like- and cross-polarized bistatic scattering cross sections per unit volume $\kappa_{vv}(\psi)$, $\kappa_{vh}(\psi)$, $\kappa_{hv}(\psi)$, and $\kappa_{hh}(\psi)$, where ψ is the angle shown in Fig. 1. While the transmitter remained in one location with the beam pointing at the crown section of the tree, the receiver was moved in discrete steps around a circle in the horizontal plane with the tree at its center. At each receiver location, defined by the angle ψ, the average received power was measured and then used to compute $\kappa_{vv}(\psi)$, $\kappa_{vh}(\psi)$, $\kappa_{hv}(\psi)$, and $\kappa_{hh}(\psi)$. The averaging process was realized by placing the tree on a rotating platform and measuring the received power (for a given receiver location) as the tree was rotated over 360°.

Two distinctly different types of trees were selected for examination: Ficus and Arbor Vitae (Fig. 2). The Ficus tree had small, flat, simple leaves approximately 10 cm^2 in area, whereas the Arbor Vitae tree had a branching trunk arrangement with branches supporting needles approximately 1.5 - 3 mm in length. More detailed

information about these test trees and the measurement procedure is given in Ulaby et al., [1988].

The major conclusions derived from the experimental observations that pertain to the present study are:

(1) For both types of trees, the like-polarized scattering patterns, $\kappa_{vv}(\psi)$ and $\kappa_{hh}(\psi)$, were approximately the same, and a similar result was observed for $\kappa_{vh}(\psi)$ and $\kappa_{hv}(\psi)$. Thus,

$$\kappa_{hh}(\psi) \simeq \kappa_{vv}(\psi) \triangleq \kappa_1(\psi) \tag{8}$$

$$\kappa_{hv}(\psi) \simeq \kappa_{vh}(\psi) \triangleq \kappa_2(\psi) . \tag{9}$$

(2) In spite of the fact that the two trees were markedly different in terms of the shapes and sizes of their scattering elements (leaves, needles, branches), both exhibited similar scattering patterns. Figures 3 and 4 shows plots of the measured values of $\kappa_1(\psi)$ and $\kappa_2(\psi)$ for the two types of trees. Also shown are plots calculated using the expressions discussed below.

The scattering coefficient κ_s^h for a h-polarized incident intensity is given by

$$\kappa_s^h = \frac{1}{4\pi} \iint_{4\pi} \left[\kappa_{hh}(\hat{\kappa}_s) + \kappa_{vh}(\hat{\kappa}_s) \right] d\Omega_s, \tag{10}$$

and a similar expression can be defined for κ_s^v. In view of (8) and (9), we shall set $\kappa_s^h = \kappa_s^v = \kappa_e$.

Assuming azimuthal symmetry with respect to the forward scattering direction ($\psi = 0$), the like- and cross-polarized scattering coefficients can be expressed as

$$\kappa_1(\psi) = \kappa_s g_1(\psi), \tag{11}$$

$$\kappa_2(\psi) = \kappa_s g_2(\psi), \tag{12}$$

and to satisfy (10), the sum of $g_1(\psi)$ and $g_2(\psi)$ has to satisfy the relation

$$\frac{1}{2}\int_0^{\pi}\left[g_1(\psi) + g_2(\psi)\right]\sin\psi\, d\psi = 1 \ . \tag{13}$$

In view of the shapes of the measured patterns (Figs. 3 and 4), $g_1(\psi)$ and $g_2(\psi)$ can each be described as the sum of a relatively weak isotropic component and a Gaussian-shaped, strong and narrow forward-scattering lobe $f(\psi)$,

$$g_1(\psi) = \left[\alpha_1 f_1(\psi) + (1-\alpha_1)\right] C$$
$$= \left[\alpha_1 \left(\frac{2}{\beta_1}\right)^2 \exp\left[-\left(\frac{\psi}{\beta_1}\right)^2\right] + (1-\alpha_1)\right] C \tag{14}$$

$$g_2(\psi) = \left[\alpha_2 f_2(\psi) + (1-\alpha_2)\right](1-C)$$
$$= \left[\alpha_2 \left(\frac{2}{\beta_2}\right)^2 \exp\left[-\left(\frac{\psi}{\beta_2}\right)^2\right] + (1-\alpha_2)\right](1-C) \tag{15}$$

where β_1 and β_2 are the effective beamwidths of the like- and cross-polarized forward scattering lobes. These expressions have the following properties:

(a)

$$\frac{1}{2}\int_0^{\pi} g_1(\psi)\,\sin\psi\,d\psi = C \qquad (16)$$

(b)

$$\frac{1}{2}\int_0^{\pi} g_2(\psi)\,\sin\psi\,d\psi = 1 - C \qquad (17)$$

(c)

$$\int_0^{\pi} \alpha\, f(\psi)\sin\psi\,d\psi \Big/ \int_0^{\pi} (1-\alpha)\sin\psi\,d\psi = \alpha/(1-\alpha). \qquad (18)$$

The sum of properties (a) and (b) satisfies (13), the ratio (1-C)/C represents the ratio of total scattered cross-polarized energy to total scattered like-polarized energy, and the ratio $(1-\alpha)/\alpha$ represents the ratio contained in the isoptropic component to the energy contained in the main lobe.

The "calculated" plots shown in the Figs. 3 and 4 are based on (11), (12), (14), and (15), with the values of the parameters selected to provide good agreement between the measured and calculated plots.

Now let us return to the phase matrix given by (7). The element P_{11} is given by

$$\begin{aligned} P_{11}(\psi) &= N\langle |S_w|^2 \rangle \\ &= \frac{N}{4\pi}\langle\sigma_w\rangle = \frac{1}{4\pi}\kappa_w(\psi) \\ &= \frac{\kappa_s}{4\pi}\, g_1(\psi). \end{aligned} \qquad (19)$$

Similary, it is easy to show that

$$P_{22}(\psi) = P_{11}(\psi),$$

and

$$P_{12}(\psi) = P_{21}(\psi) = \frac{\kappa_s}{4\pi} g_2(\psi). \tag{20}$$

Next, we shall make certain assumptions to simplify the remaining terms.

Let us consider the term P_{13} in P,

$$\begin{aligned} P_{13} &= N < \mathrm{Re}\,(S_{vv} S_{vh}^{*}) > \\ &= N < \mathrm{Re}\,(|S_{vv}| e^{j\phi_{vv}} |S_{vh}| e^{-j\phi_{vh}}) > \\ &= N < |S_{vv}||S_{vh}| \cos(\phi_{vv} - \phi_{vh}) > \\ &= N < |S_{vv}||S_{vh}| > < \cos(\phi_{vv} - \phi_{vh}) > \end{aligned} \tag{21}$$

where ϕ_{vv} is the phase of the scattering amplitude S_{vv} (and similar definitions apply for the other scattering amplitudes). In the last step of (21) it was assumed that the magnitude $|S_{vv}|\,|S_{vh}|$ and the phase difference $(\phi_{vv} - \phi_{vh})$ are independent random variables. According to 35-GHz radar measurements of the backscattering from rocks [Whitt and Ulaby, 1988] and 1.25 GHz polarimatric data extracted from airborne radar images of forested areas, the phase difference $(\phi_{vv} - \phi_{vh})$ is uniformly distributed over $[0, 2\pi]$. Hence, the average value of $\cos(\phi_{vv} - \phi_{vh})$ is zero, and therefore $P_{13} = 0$. Similarly, all terms in P involving the product of a like-polarized scattering amplitude and cross-polarized scattering amplitude may be set equal to zero.

It was also observed (in the same investigations) cited above that the phase difference ($\phi_{vv} - \phi_{hh}$) corresponding to the product of the like-polarized scattering amplitudes has a Gaussian-like dsitribution centered at 0°. We shall, therefore, adopt the approximations $< \cos (\phi_{vv} - \phi_{hh}) > \simeq 1$ and $< \sin (\phi_{vv} - \phi_{hh}) > \simeq 0$. Furthermore, in view of (8), we shall assume that $< |S_{vv}| \; |S_{hh}| > \simeq < |S_{vv}|^2 >$. Hence, for the terms involving ($S_{vv} S_{hh}^*$), we have

$$\begin{aligned} N < \mathrm{Re} (S_{vv} S_{hh}^*) > &= N < |S_{vv}| \, |S_{hh}| \cos (\phi_{vv} - \phi_{hh}) > \\ &= N < |S_{vv}| \, |S_{hh}| > < \cos (\phi_{vv} - \phi_{hh}) > \\ &= N < |S_{vv}|^2 > \\ &= P_{11} \end{aligned} \tag{22}$$

and

$$N < \mathrm{Im} (S_{vv} S_{hh}^*) > = 0 \tag{23}$$

Upon incorporating the preceding results in (11), we obtain the simplified matrix

$$P (\psi) = \frac{\kappa_s}{4\pi} \begin{bmatrix} g_1 & g_2 & 0 & 0 \\ g_2 & g_1 & 0 & 0 \\ 0 & 0 & g_1+g_2 & 0 \\ 0 & 0 & 0 & g_1-g_2 \end{bmatrix} \tag{24}$$

with g_1 and g_2 as given by (14) and (15), respectively.

3.2 PHASE MATRIX FOR ANY INCIDENT AND SCATTERED DIRECTIONS

The phase matrix $P(\psi)$ in Eq. 24 is obtained in terms of the scattering angle ψ as shown in Fig. 1. If the incident direction is (θ_i, ϕ_i) and the scattered direction is (θ_s, ϕ_s), denoted by points $P_1(\theta_i, \phi_i)$ and $P_2(\theta_s, \phi_s)$ in the polar coordinate system shown in Fig. 5, the plane of scattering contains the triangle OP_1P_2 and the scattering angle ψ is given by the angle P_1OP_2. The radiative transfer equation, on the other hand, is written in terms of the polar angles θ and ϕ. We need to obtain a new phase matrix in terms of θ and ϕ in order to use it in the radiative transfer equation. The details of the transformation from $P(\psi)$ to $P(\theta_s, \phi_s; \theta_i, \phi_i)$, which involves linear transformations through angles γ_1 and $\pi - \gamma_2$, are described in Chandrasekhar [1960]. The transformed phase matrix is given by

$$\mathbf{P}(\theta_s, \phi_s; \theta_i, \phi_i) = \mathbf{L}(\pi - \gamma_2)\ \mathbf{P}(\psi)\ \mathbf{L}(-\gamma_1) \tag{25}$$

where $\mathbf{L}$ is a linear transformation given by

$$\mathbf{L}(\gamma) = \begin{vmatrix} \cos^2\gamma & \sin^2\gamma & \frac{1}{2}\sin 2\gamma & 0 \\ \sin^2\gamma & \cos^2\gamma & -\frac{1}{2}\sin 2\gamma & 0 \\ -\sin 2\gamma & \sin 2\gamma & \cos 2\gamma & 0 \\ 0 & 0 & 0 & 1 \end{vmatrix} \tag{26}$$

The angles γ_1 and γ_2 are defined in Fig. 5.

Introducing the abbreviations

$$(\ell,\ell) = \cos\gamma_1 \cos\gamma_2 - \sin\gamma_1 \sin\gamma_2 \tag{27a}$$

$$(\ell, r) = -\cos\gamma_1 \sin\gamma_2 + \sin\gamma_1 \cos\gamma_2 \tag{27b}$$

$$(r, \ell) = \sin\gamma_1 \cos\gamma_2 + \cos\gamma_1 \sin\gamma_2 \tag{27c}$$

$$(r, r) = \cos\gamma_1 \cos\gamma_2 + \sin\gamma_1 \sin\gamma_2 \tag{27d}$$

We can write the phase matrix as

$$P(\theta_s,\phi_s;\theta,\phi) = \frac{\kappa_s}{4\pi}\begin{bmatrix} g_1(\psi)(\ell,\ell)^2 + g_2(\psi)(\ell,r)^2 & g_1(\psi)(r,\ell)^2 + g_2(\psi)(r,r)^2 \\ g_1(\psi)(r,\ell)^2 + g_2(\psi)(r,r)^2 & g_1(\psi)(\ell,\ell)^2 + g_2(\psi)(\ell,r)^2 \\ 2[g_1(\psi)(\ell,\ell)(r,\ell)+g_2(\psi)(r,r)(\ell,r)] & -2[g_1(\psi)(r,\ell)(\ell,\ell)+g_2(\psi)(r,r)(\ell,r)] \\ 0 & 0 \end{bmatrix}$$

$$\begin{bmatrix} -g_1(\psi)(r,\ell)(\ell,\ell) + g_2(\psi)(r,r)(\ell,r) & 0 \\ g_1(\psi)(r,\ell)(\ell,\ell) - g_2(\psi)(r,r)(\ell,r) & 0 \\ g_1(\psi)[(\ell,\ell)^2 - (r,\ell)^2] + g_2(\psi)[(r,r)^2 - (\ell,r)^2] & 0 \\ 0 & g_1(\psi) - g_2(\psi) \end{bmatrix} \tag{28}$$

Using the cosine and sin laws of a spherical triangle, we can write (ℓ,ℓ), (r,r), (r,ℓ), and (ℓ,r) in terms of θ_s, ϕ_s, θ_i and ϕ_i.

$$(\ell,\ell) = \frac{\sin^2(\phi_i - \phi_s)}{\sin^2\psi} \sin\theta_s \sin\theta_i (\cos\psi - 1) - \cos(\phi_i - \phi_s) \qquad (29a)$$

$$(r,r) = \frac{\sin^2(\phi_i - \phi_s)}{\sin^2\psi} \sin\theta_s \sin\theta_i (\cos\psi + 1) - \cos(\phi_i - \phi_s) \qquad (29b)$$

$$(r,\ell) = \left\{ (\sec\theta_i + \sec\theta_s) \left[\sin(\phi_i - \phi_s) \left(1 + \frac{\sin\theta_s \sin\theta_i \cos\psi \cos(\phi_i - \phi_s)}{\sin^2\psi}\right)\right]\right.$$

$$\left. - \frac{\sin(\phi_i - \phi_s)}{\sin^2\psi} \left[\sin^2\theta_i \sec\theta_i + \sin^2\theta_s \sec\theta_s\right]\right\} \qquad (29c)$$

$$(\ell,r) = \left\{ (\sec\theta_i - \sec\theta_s) \left[\sin(\phi_i - \phi_s) \left(1 + \frac{\sin\theta_s \sin\theta_i \cos\psi \cos(\phi_i - \phi_s)}{\sin^2\psi}\right)\right]\right.$$

$$\left. - \frac{\sin(\phi_i - \phi_s)}{\sin^2\psi} \left[\sin^2\theta_i \sec\theta_i - \sin^2\theta_s \sec\theta_s\right]\right\} \qquad (29d)$$

where

$$\cos\psi = \cos\theta_s \cos\theta_i + \sin\theta_s \sin\theta_i \cos(\phi_i - \phi_s) \qquad (30)$$

4. RADIATIVE TRANSFER MODEL

At millimeter wavelengths, the penetration depths of foliage rarely exceeds 1m. Hence, it would be reasonable to neglect the backscatter contribution of the underlying ground surface, and in the case of most vegetation canopies it may also be possible to treat the canopy as semiinfinite in depth. In this section we seek an expression for the vector specific intensity $\mathbf{I}^s$ scattered from a forest canopy characterized by a phase matrix of the form given by (28). To this end, we shall develop a first-order solution and a second-order solution of the radiative transfer equation and then compare the results with the exact solution (based on numerical computations using the quadrature method) and with experimental data.

The vegetation canopy is modeled as a continuous, statistically homogeneous, horizontal layer of vertical extent d. The layer has diffuse upper and lower boundaries (Fig. 6) at $z=0$ and $z=-d$, respectively, and it is illuminated by an intensity

$$\mathbf{I}^i = \mathbf{I}_0 \, \delta(\cos\theta - \cos\theta_0)\, \delta(\phi - \phi_0) \tag{31}$$

incident upon the upper boundary in the direction $(\pi - \theta_0, \phi_0)$. Upon solving the radiative transfer equation to obtain an expression for the intensity $\mathbf{I}^s(\theta_s, \phi_s)$ scattered in any direction (θ_s, ϕ_s), we can set $\theta_s = \theta_0$ and $\phi_s = \pi + \phi_0$, which corresponds to scattering in the backward direction, to compute the backscattering coefficient from the equation

$$\sigma^o_{pq}(\theta_0) = \frac{4\pi \cos\theta_0 \, I^s_p(\theta_0, \pi + \phi_0)}{I^i_q(\pi - \theta_0, \phi_0)} \tag{32}$$

where $p, q = v$ or h polarization.

4.1 Radiative Transfer Equations

When formulating the radiative transfer problem for bounded media, the standard practice is to split the intensity vector into upward-going $\left(I^{+}(\theta_s, \phi_s, z)\right)$ downward-going $\left(I^{-}(\pi - \theta_s, \phi_s, z)\right)$ components, noting that θ_s varies between 0 and $\pi/2$ [Ulaby et al., 1986]. In the vegetation layer, the intensity $I^{+}(\theta_s, \phi_s, z)$ travelling in the upward direction (θ_s, ϕ_s) and the intensity $I^{-}(\pi - \theta_s, \phi_s, z)$ traveling in the downward direction $(\pi - \theta_s, \phi_s)$ must satisfy the coupled radiative transfer equations .

$$\frac{d}{dz} I^{+}(\mu_s, \phi_s, z) = -\frac{\kappa_e}{\mu_s} I^{+}(\mu_s, \phi_s, z) + F^{+}(\mu_s, \phi_s, z) \tag{33a}$$

$$-\frac{d}{dz} I^{-}(-\mu_s, \phi_s, z) = -\frac{\kappa_e}{\mu_s} I^{-}(-\mu_s, \phi_s, z) + F^{-}(-\mu_s, \phi_s, z) \tag{33b}$$

where κ_e is the extinction coefficient of the vegetation medium, $\mu_s = \cos\theta_s$, and $-\mu_s = \cos(\pi - \theta_s)$. The source functions $F^{+}(\mu_s, \phi_s, z)$ and $F^{-}(-\mu_s, \phi_s, z)$ account for directing the energy incident upon an elemental volume from all directions into the direction (θ_s, ϕ_s) and $(\pi - \theta_s, \phi_s)$, respectively, and are given by

$$F^{+}(\mu_s, \phi_s, z) = \frac{1}{\mu_s}\left[\int_0^{2\pi}\int_0^{1} P(\mu_s, \phi_s; \mu_i, \phi_i)\, I^{+}(\mu_i, \phi_i, z)\, d\Omega_i + \int_0^{2\pi}\int_0^{1} P(\mu_s, \phi_s; -\mu_i, \phi_i)\, I^{-}(-\mu_i, \phi_i, z)\, d\Omega_i\right] \tag{34a}$$

$$F^{-}(-\mu_s, \phi_s, z) = \frac{1}{\mu_s}\left[\int_0^{2\pi}\int_0^{1} P(-\mu_s, \phi_s; \mu_i, \phi_i)\, I^{+}(\mu_i, \phi_i, z)\, d\Omega_i + \int_0^{2\pi}\int_0^{1} P(-\mu_s, \phi_s; -\mu_i, \phi_i)\, I^{-}(-\mu_i, \phi_i, z)\, d\Omega_i\right] \quad (34b)$$

where $d\Omega_i = d\mu_i\, d\phi_i = \sin\theta_i\, d\theta_i\, d\phi_i$, and $P(\mu_s, \phi_s; \mu_i, \phi_i)$ is the phase matrix of the vegetation layer relating the intensity incident (upon a unit volume in the medium) in the direction (θ_i, ϕ_i) to the intensity scattered in the direction (θ_s, ϕ_s). The phase matrix is defined by (28).

The solution to differential equations (33a) and (33b) can formally be expressed as

$$I^{+}(\mu_s, \phi_s, z) = e^{-\kappa_e(z+d)/\mu_s} I^{+}(\mu_s, \phi_s, -d) + \int_{-d}^{z} e^{-\kappa_e(z-z')/\mu_s} F^{+}(\mu_s, \phi_s, z')\, dz' \quad (35a)$$

$$I^{-}(-\mu_s, \phi_s, z) = e^{-\kappa_e z/\mu_s} I^{-}(-\mu_s, \phi_s, 0) + \int_{z}^{0} e^{\kappa_e(z-z')/\mu_s} F^{-}(-\mu_s, \phi_s, z')\, dz'. \quad (35b)$$

Because there is no reflection at the (diffuse) air-vegetation boundaries at $z = 0$ and $z = -d$, the following boundary conditions must be satisfied:

$$I^{-}(-\mu_s, \phi_s, 0) = I_0\, \delta(\mu_s - \mu_0)\, \delta(\phi_s - \phi_0) \quad (36a)$$

$$I^{+}(\mu_s, \phi_s, -d) = 0. \quad (36b)$$

and because F^+ and F^- are themselves integral functions of I^+ and I^-, we have to use numerical techniques involving segmentation in z and (θ, ϕ) in order to obtain an exact solution for $I^s = I^+ (\theta_s, \phi_s, z = 0)$. While this may be usefull, particularly for comparing with results based on approximate solutions, the numerical technique does not provide much insight with regard to the relative importance of various scattering contributions. Hence, we shall use the iterative technique to develop expressions for the first-order and second-order solutions of (35a) and (35b) and then compare their results with the exact results of the numerical solution. The assumptions underlying the iterative technique is that the medium is weakly scattering; i.e., the scattering albedo $\omega = \kappa_s / \kappa_e << 1$. At millimeter wavelength, $\omega \simeq 0.6 - 0.9$ for vegetation [3], and therefore the condition is not satisfied. Nonetheless, we shall now proceed with the iterative technique and then evaluate its usefulness in a later section.

4.2 First-Order Solution

We start with the zeroth-order solutions, which are obtained by setting P=0 in (34a) and (34b), which renders $F_0^+ = F_0^- = 0$ in (35a) and (35b), where the zero subscript denotes zero order. Using the boundary conditions given by (34) and (35), the zeroth-order specific intensities are given by

$$I_0^+ (\mu_s, \phi_s, z) = 0 \tag{37a}$$

$$I_0^- (-\mu_s, \phi_s, z) = e^{\kappa_e z/\mu_s} I_0 \delta (\mu_s - \mu_0) \delta (\phi_s - \phi_0) \tag{37b}$$

The zeroth-order solution corresponds to propagation of the coherent wave through the medium with scattering ignored, except for its contribution to extinction. To

obtain the first-order solution, we first need to insert (37a) and (37b) into (34a) and (34b) to compute the first-order source function F_1^+ and F_1^-, and then insert the results in (35a) and (35b). This process leads to

$$I_1^+(\mu_s, \phi_s, z) = \frac{e^{-\kappa_e z/\mu_s}}{\mu_s \kappa_1}\left[e^{\kappa_1 z} - e^{\kappa_1 d}\right] P(\mu_s, \phi_s; -\mu_0, \phi_0)\, I_0 \tag{38}$$

$$I_1^-(-\mu_s, \phi_s, z) = e^{\kappa_e z/\mu_0} I_0\, \delta(\mu_s - \mu_0)\, \delta(\phi_s - \phi_0)$$

$$+ \frac{e^{\kappa_e z/\mu_s}}{\mu_s \kappa_2}\left[1 - e^{\kappa_2 z}\right] P(-\mu_s, \phi_s; -\mu_0, \phi_0)\, I_0 \tag{39}$$

where

$$\kappa_1 \triangleq \kappa_e (1/\mu_0 + 1/\mu_s) \tag{40}$$

$$\kappa_2 \triangleq \kappa_e (1/\mu_0 - 1/\mu_s)\,. \tag{41}$$

The first-order solution for the backscattering coefficient can be obtained by setting $z = 0$, $\mu_s = \mu_0$, and $\phi_s = \pi + \phi_0$ in (38) and then inserting the result in (32). These steps lead to the expression

$$\sigma_w^0(\theta_0) = \frac{4\pi \cos\theta_0}{2\kappa_e}\left[1 - e^{-2\kappa_e d \sec\theta_0}\right]\left[\mathbf{P}(\mu_0, \pi+\phi_0; -\mu_0, \phi_0)\right]_{11}$$

$$= \frac{\kappa_s \cos\theta_0}{2\kappa_e}\left[1 - e^{-2\kappa_e d \sec\theta_0}\right] g_1(\pi) \qquad (42)$$

where $[\mathbf{P}]_{11}$ is the 11 element of $\mathbf{P}$ and $g_1(\pi)$ is given by (14) with $\psi = \pi$.

Similarly, the other principal-polarization backscattering coefficients are given by

$$\sigma_{hh}^0(\theta_0) = \sigma_w^0(\theta_0)$$

$$\sigma_{hv}^0(\theta_0) = \sigma_{vh}^0(\theta_0) = \frac{\kappa_s \cos\theta_0}{2\kappa_e}\left[1 - e^{-2\kappa_e d \sec\theta_0}\right] g_2(\pi). \qquad (43)$$

For a thick canopy such that $(2\kappa_e d \sec\theta_0) >> 1$, the term in the second square bracket in (42) and (43) reduces to 1.

4.3 Second-Order Solution

The second order solution for the backscattered intensity at the surface $I_2^+(\theta_0, \pi+\phi_0, 0)$, can be obtained by (1) replacing (θ_s, ϕ_s, z) in (38) and (39) with (θ_i, ϕ_i, z'), (2) inserting the resultant expressions in (34a) and (34b) to obtain $F_1^+(\mu_s, \phi_s, z')$ and $F_1^-(-\mu_s, \phi_s, z')$, and (3) then inserting those expressions in (35a) and (4) finally replacing (μ_s, ϕ_s, z) with $(\mu_0, \pi+\phi_0, 0)$. This process leads to

$$I_2^+(\theta_0, \pi+\phi_0, 0) = \int_d^0 e^{\kappa_e z'/\mu_0} F_1^+(\mu_0, \pi+\phi_0, z')\, dz' \qquad (44)$$

with

$$F_1^+(\mu_0, \pi + \phi_0, z) = \frac{1}{\mu_0}\left[e^{\kappa_e z/\mu_0}\, P(\mu_0, \pi + \phi_0; -\mu_0, \phi_0)\, I_0\right.$$

$$+ \int_0^{2\pi}\int_0^1 \frac{e^{-\kappa_e z/\mu_1}}{\mu_1 \kappa_3}\left[e^{\kappa_3 z} - e^{-\kappa_3 d}\right] P(\mu_0, \pi + \phi_0; \mu_1, \phi_1)\, P(\mu_1, \phi_1; -\mu_0, \phi_0)\, I_0\, d\Omega_1$$

$$\left. + \int_0^{2\pi}\int_0^1 \frac{e^{\kappa_e z/\mu_1}}{\mu_1 \kappa_4}\left[1 - e^{\kappa_4 z}\right] P(\mu_0, \pi + \phi_0, -\mu_1, \phi_1)\, P(-\mu_1, \phi_1; -\mu_0, \phi_0)\, I_0\, d\Omega_1\right] \quad (45)$$

where

$$\kappa_3 \triangleq \kappa_e\left(\frac{1}{\mu_1} + \frac{1}{\mu_0}\right) \quad (46)$$

$$\kappa_4 \triangleq \kappa_e\left(\frac{1}{\mu_0} - \frac{1}{\mu_1}\right) \quad (47)$$

Using (14), (15) and (28) to define **P**, the integrals can be evaluated numerically, and the computed intensity I_2^+ can be inserted in (32) to compute σ_{pq}^0 for any $p, q =$ *v* or *h* polarizations.

5. MODEL BEHAVIOR AND EXPERIMENTAL OBSERVATIONS

Using the phase matrix given by (28) with the parameters measured for the Ficus tree, the co-polarized (co-pol) and cross-polarized (x-pol) backscattering coefficients were computed for a variety of canopy conditions in accordance with (a) the first-order solution of Section 4.2, (b) the second-order solution of Section 4.3, and (c) the exact numerical solution using the quadrature gradient technique [Ulaby et al., 1986]. Figure 7 shows the variation of σ^o with the albedo $\omega = \kappa_s / \kappa_e$, for a canopy with an optical thickness $\tau = \kappa_e d = 1$ Np. For an error within 1 dB of the numerical solution, the first-order solution is useful up to $\omega \simeq 0.4$ for the co-pol component but is not at all useful for the x-pol component, and the second-order solution is useful up to $\omega \simeq 0.85$ for the co-pol component but only useful up to $\omega \simeq 0.5$ for the x-pol component. If we relax the error margin to 2 dB for the x-pol component, the useful range of ω may be extended up to 0.85 for the second-order solution.

The dependence on optical thickness is illustrated in Fig. 8 for all three solutions. For all intents and purposes, σ^o is independent of τ for $\tau \geq 1$ Np. This condition is almost always satisfied for tree canopies at millimeter wavelengths.

Comparison of the model behavior with experimental data is provided in Fig. 9 which shows measurements of σ^o as a function of incidence angle for a canopy of Spruce trees at 35 GHz and a canopy of Bur Oak trees at 94, and 140 GHz.

The canopies had continuous crown sections, the trees were about 10m in height, and the leaves had a moisture content of 53% in the case of the Spruce trees and 27% for the Bur Oak trees. The computations are based on the second-order solution using the Ficus phase-function model shown in Fig. 3. The only free parameter used in attempting to match the model results with the data is the albedo ω, which was chosen to be equal to 0.6 at 35 GHz, 0.8 at 94 GHz, and 0.95 at 140 GHz. Similar results were obtained in attempting to match the model to experimental

observations for (horizontally) continuous canopies comprised of other types of trees. This observation is not surprising in view of the strong similarity noted earlier between the bistatic scattering patterns shown in Fig. 3 and 4 for two trees with very dissimilar tree architectures. In other words, the proposed model appears to apply to a wide range of tree types of continuous-crown canopies, with the only major parameter controlling the levels of the co-pol and x-pol backscattering responses being the albedo ω. In turn, ω is strongly dependent on the wavelength and probably dependent on leaf moisture content. Further study is needed to establish the dependence of ω on these two parameters.

6. CONCLUSIONS

Using the phase matrix model proposed in this study, radiative transfer theory appears to provide excellent agreement with experimental observations of the backscatter from tree canopies at 35, 94, and 140 GHz. The only free parameter used in matching the model to data is the scattering albedo ω which appears to depend on only two parameters, the wave frequency and the leaf moisture content. The roles of shape and size of the tree leaves or needles and the tree branch architecture appear to be secondary in importance. Further study is needed to establish the exact dependence of ω on moisture content and frequency.

REFERENCES

Chandrasekhar, S., *Radiative Transfer*, Dover Publications, New York, 1960, pp. 34-35.

Ishimaru, A., *Wave Propagation and Scattering in Random Media*, Vol. 1, Academic Press, New York, 1978, Ch. 7.

Schwering, F.K., E.J. Violette, and R.H. Espeland, "Millimeter-Wave Propagation in Vegetation: Experiments and Theory," *IEEE Transactions on Geoscience and Remote Sensing*, Vol. 26, May, 1988, pp. 355-367.

Tsang, L., J.A. Kong, and R.T. Shin, *Theory of Microwave Remote Sensing*, John Wiley and Sons, New York, 1985, Ch. 3.

Ulaby, F.T., R.K. Moore, and A.K. Fung, *Microwave Remote Sensing*, Vol. III, Artech House, Dedham, Massachusetts, 1986, Ch. 13.

Ulaby, F.T., T.E. van Deventer, J.R. East, T.F. Haddock, and M.E. Coluzzi, "Millimeter-Wave Bistatic Scattering From Ground and Vegetation Targets," *IEEE Transactions on Geoscience and Remote Sensing*, Vol. 26, May, 1988, pp. 229-243.

Whitt, M.W., and F.T. Ulaby, "Millimeter-Wave Polarimetric Measurements of Artificial and Natural Targets," *IEEE Transactions on Geoscience and Remote Sensing*, Vol. 26, September, 1988, pp. 563-574.

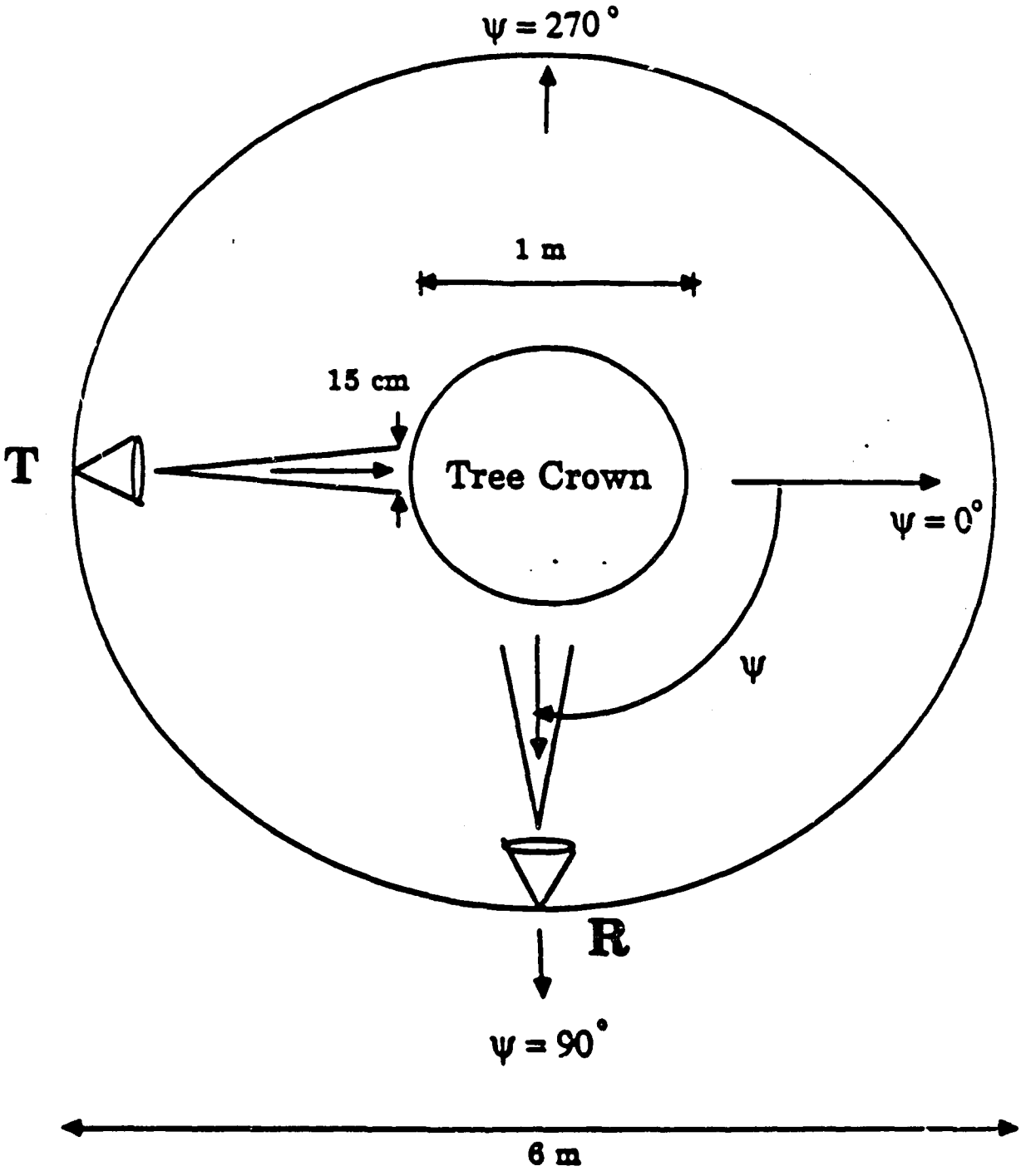

Figure 1. Configuration used for measuring bistatic scattering from tree foliage. The tree was placed on a rotating platform, the transmitter was in a fixed location, and the reciever could be set at any angle ψ

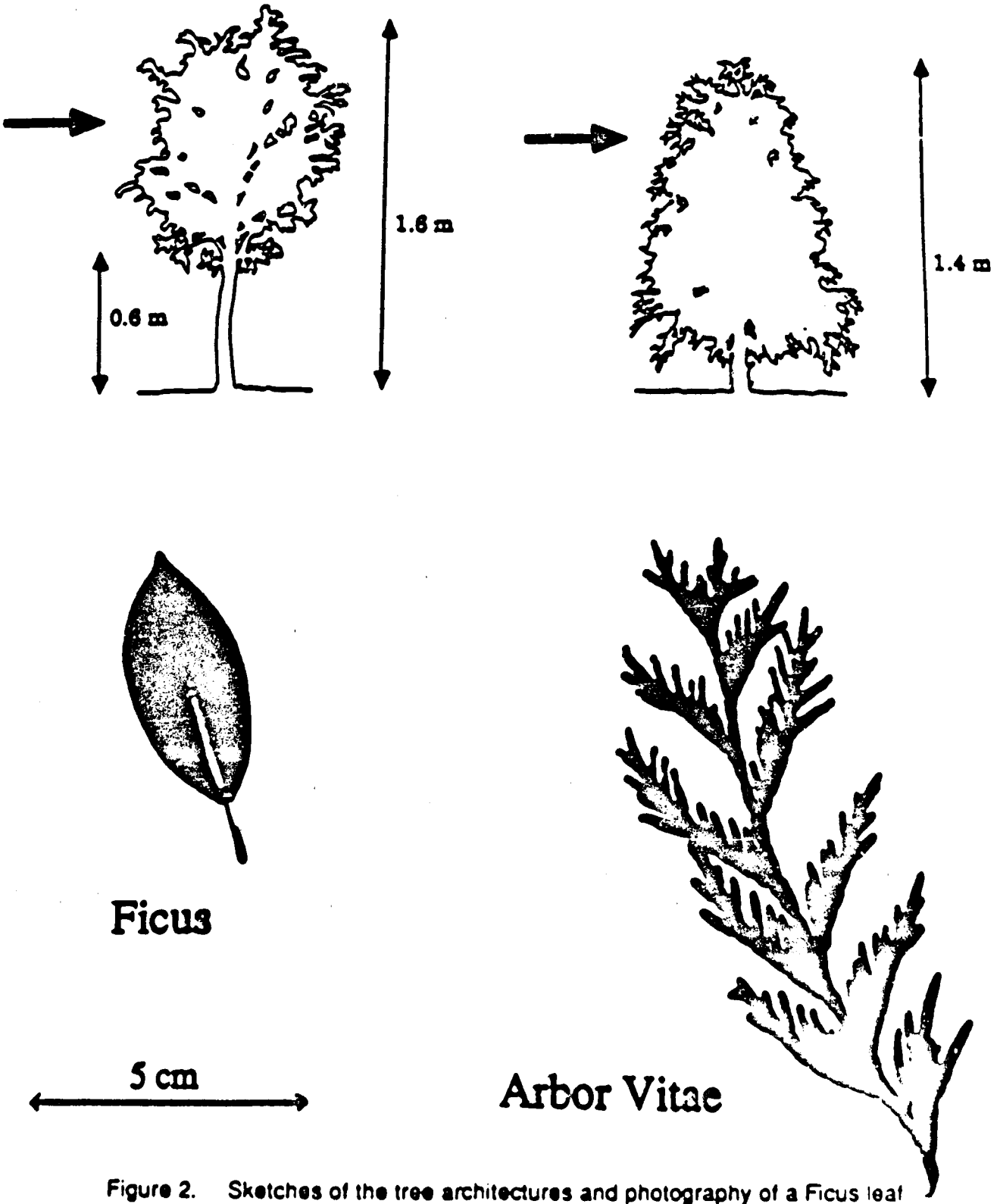

Figure 2. Sketches of the tree architectures and photography of a Ficus leaf and an Arbor Vitae branch.

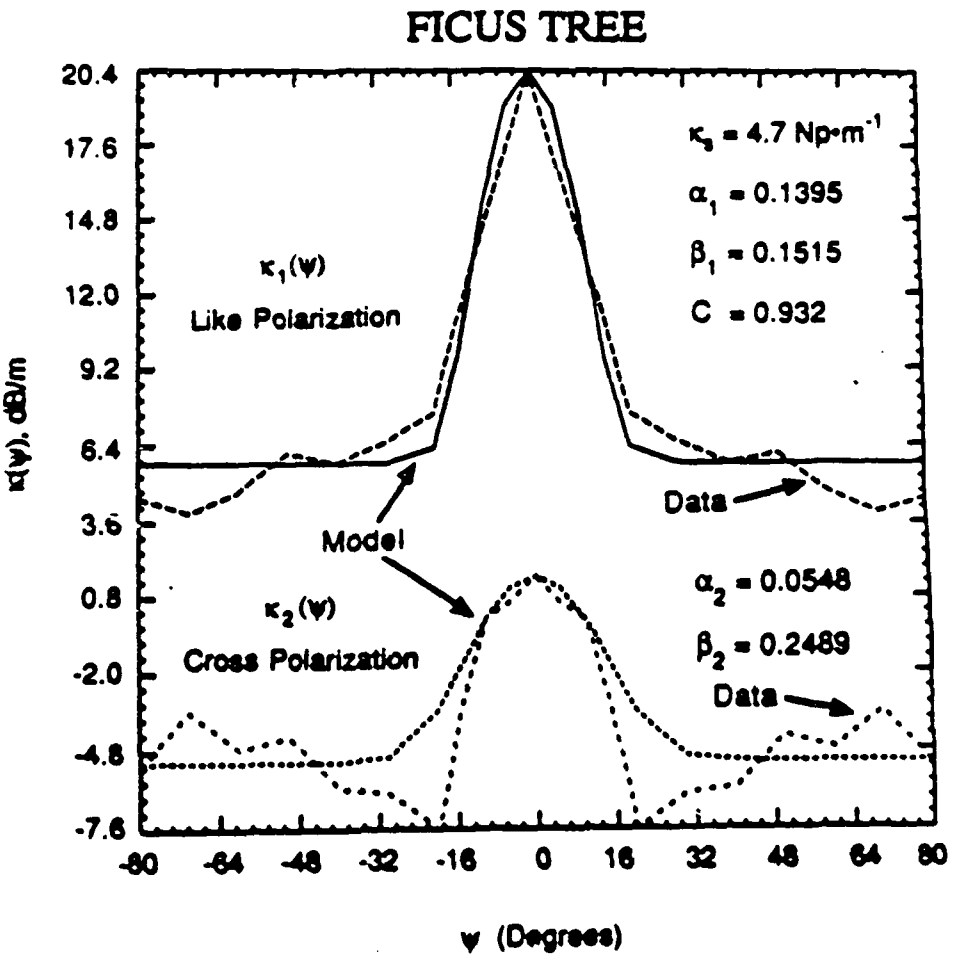

Figure 3. Comparison of measured bistatic scattering cross section per unit volume for Ficus tree foliage with calculations based on the model functions given by (14) and (15).

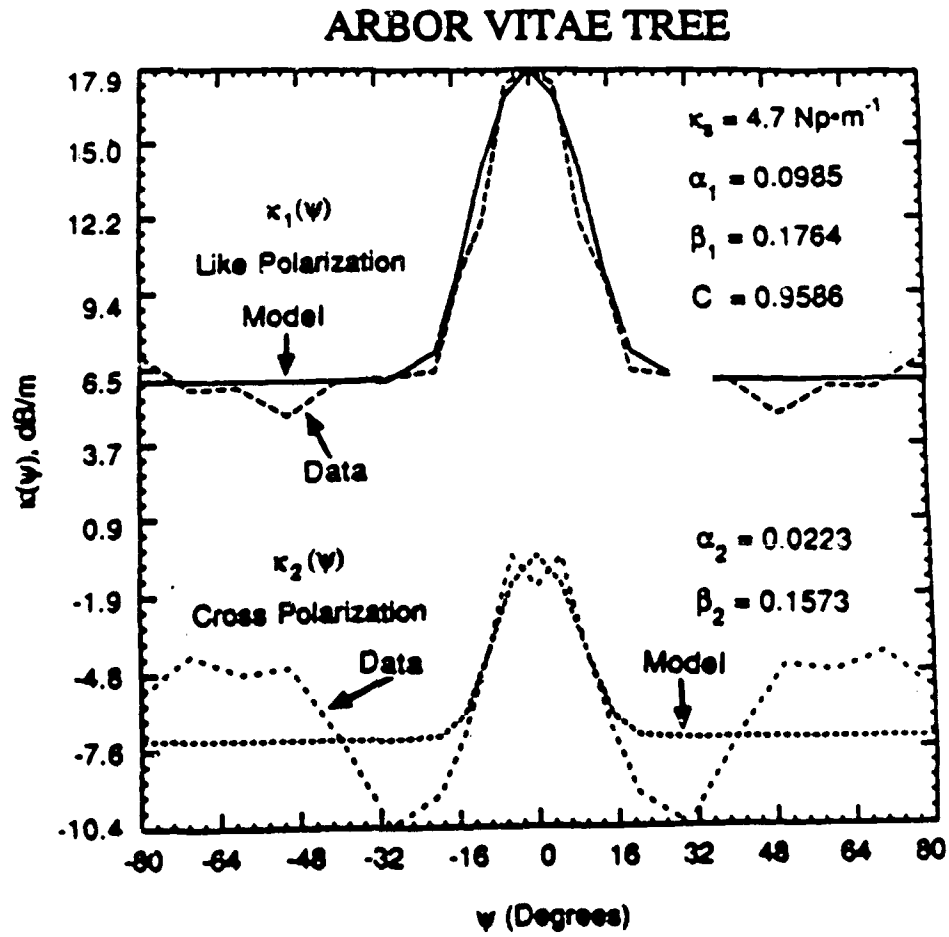

Figure 4. Comparison of measured bistatic scattering cross section per unit volume for Arbor Vitae tree foliage with calculations based on the model functions given by (14) and (15).

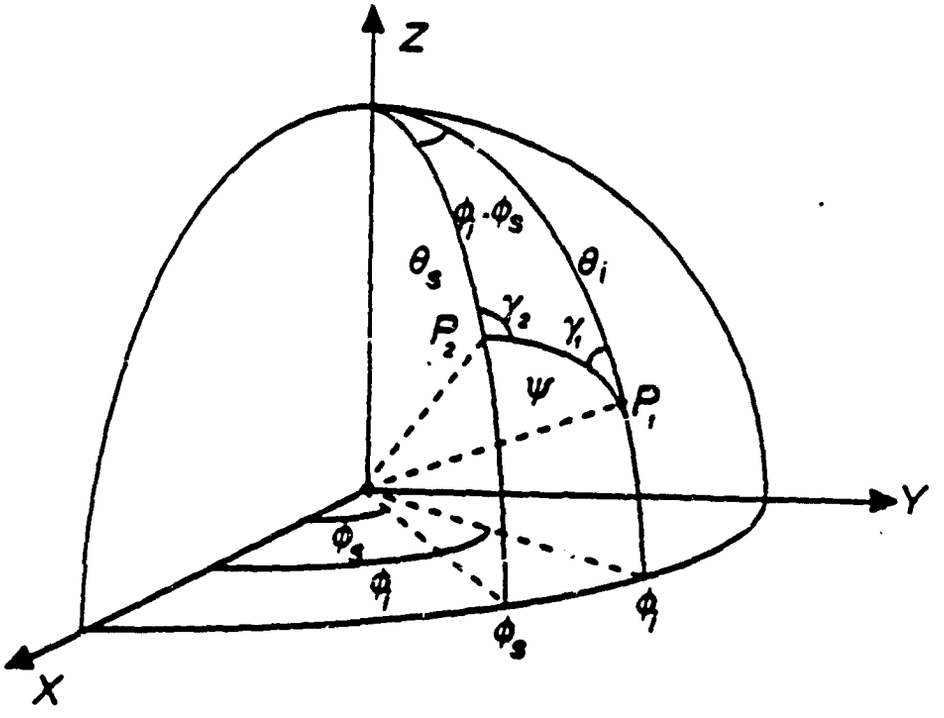

Figure 5. Coordinate system showing the incident and scattered angles, (θ_i, ϕ_i) and (θ_s, ϕ_s), and their relation to ψ.

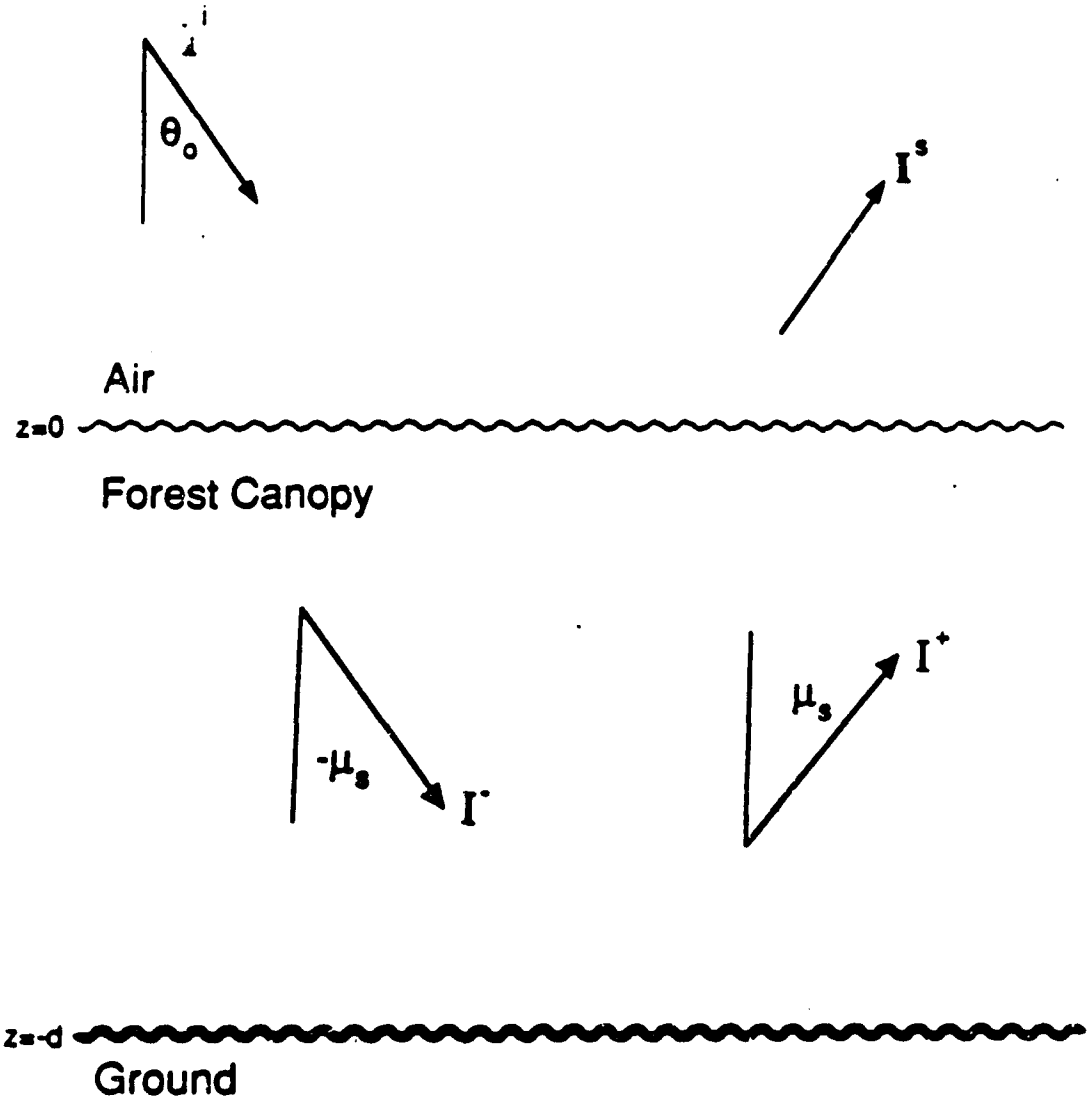

Figure 6. Geometry of the scattering problem.

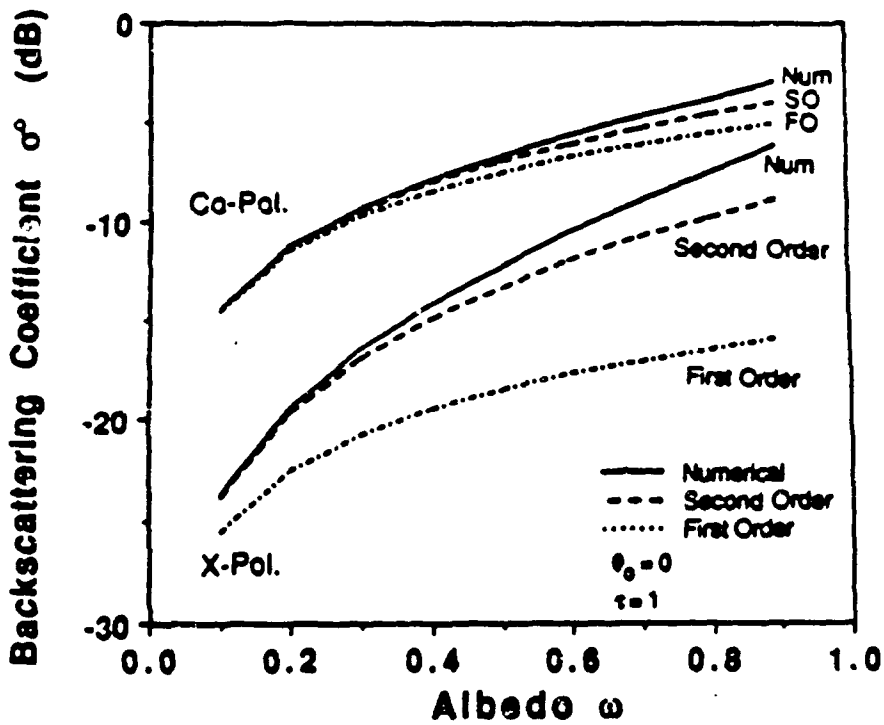

Figure 7. Backscattering coefficient as a function of albedo at normal incidence, computed with the first order, second order, and numerical solutions.

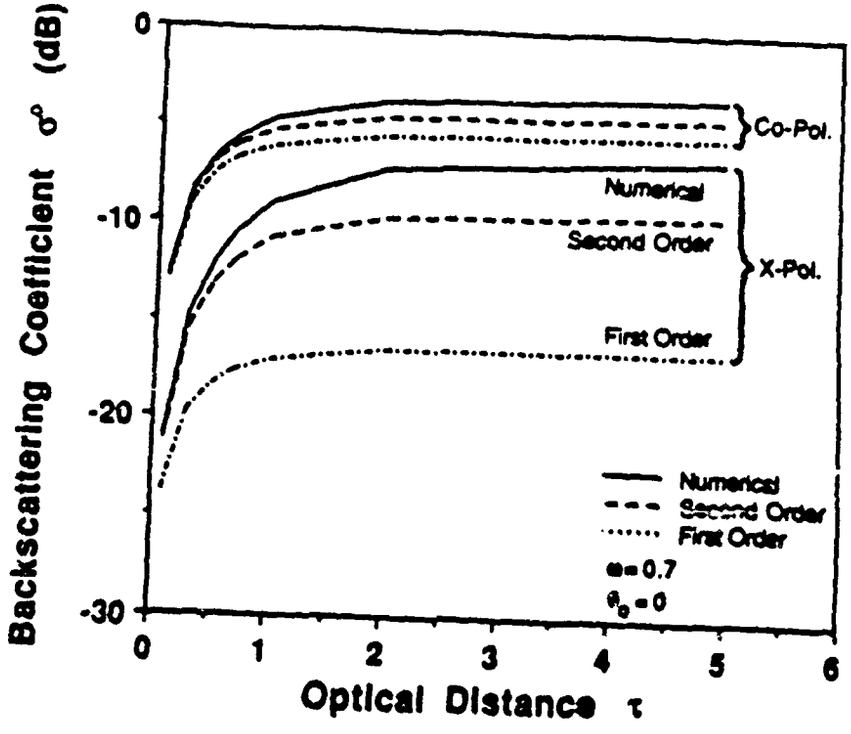

Figure 8. Variation of backscattering coefficient with optical thickness τ.

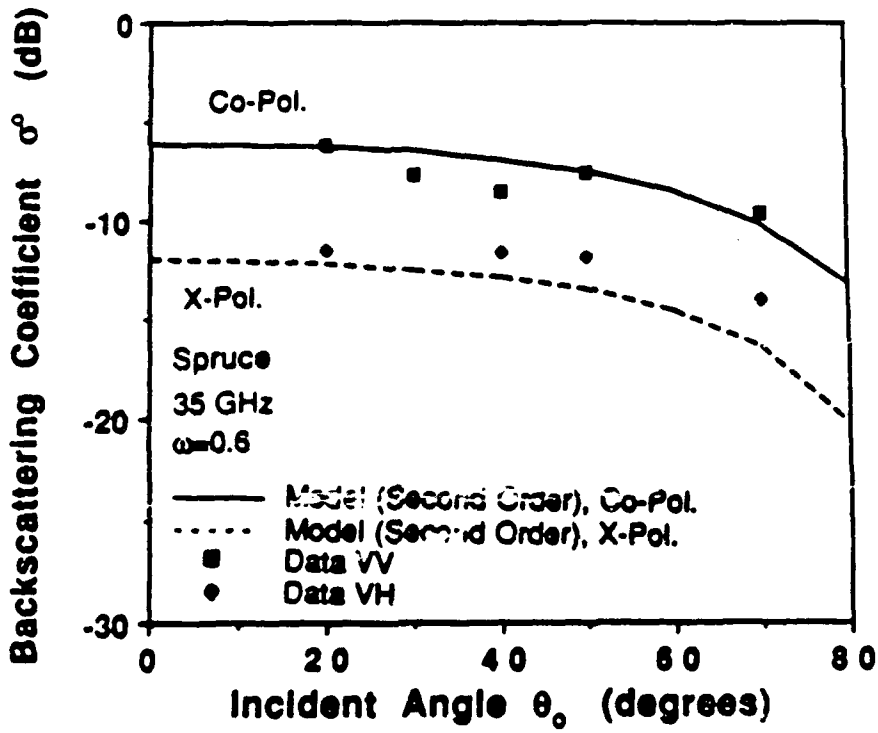

(a) 35 GHz

Figure 9. Comparison of theory with experimental observations at (a) 35 GHz for a canopy of Spruce trees and at (b) 94 GHz and (c) 140 GHz for a canopy of Bur Oak trees.

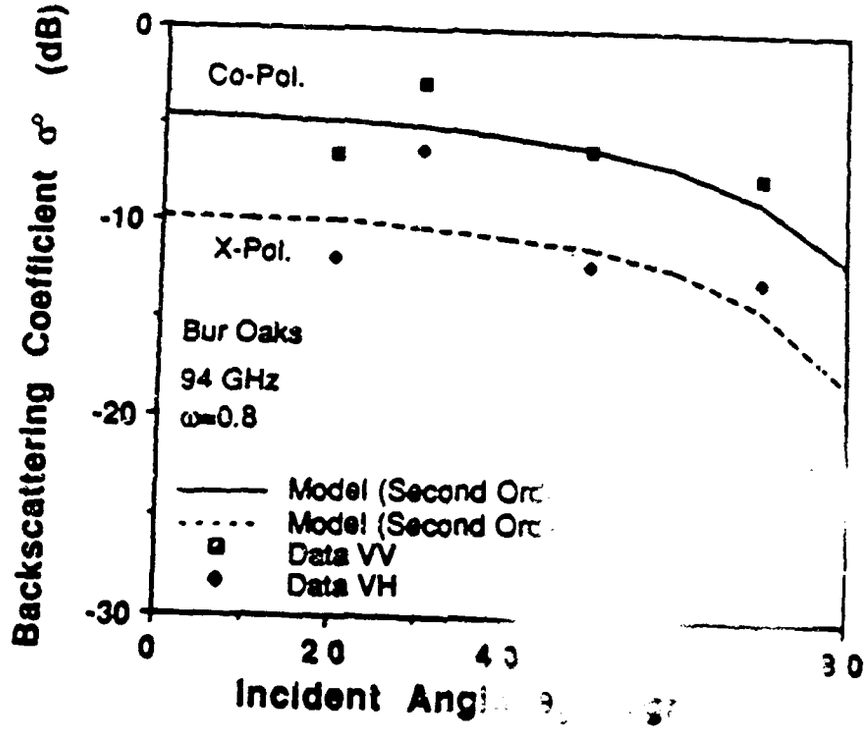
Backscattering Coefficient σ° (dB)
0
-10
-20
-30
Co-Pol.
X-Pol.
Bur Oaks
94 GHz
ω=0.8
Model (Second Orc
Model (Second Orc
Data VV
Data VH
0
20
40
30
Incident Angl

(b) 94 GHz

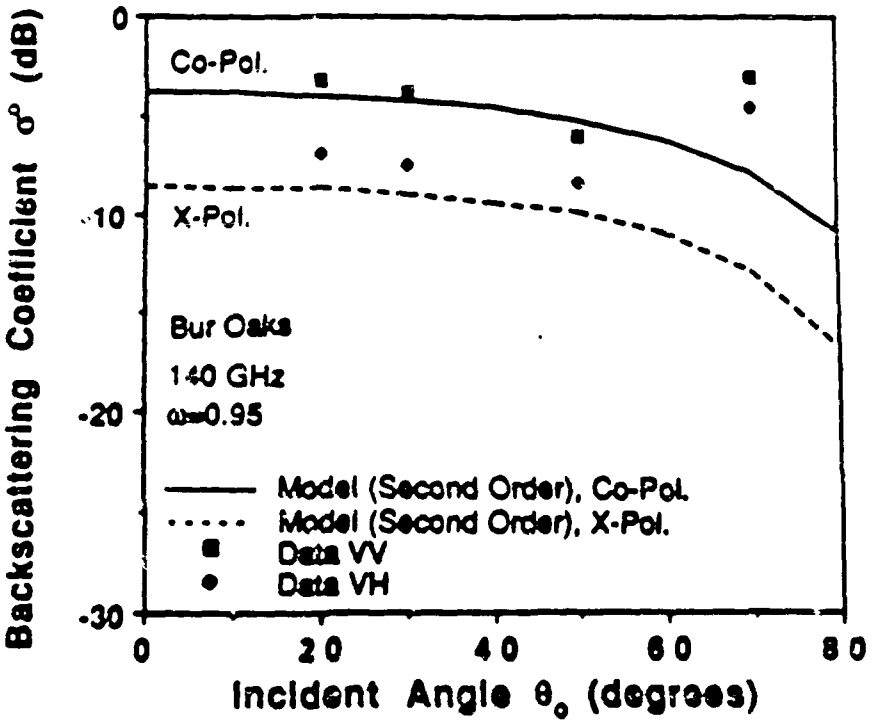
Backscattering Coefficient σ° (dB)
0
-10
-20
-30
Co-Pol.
X-Pol.
Bur Oaks
140 GHz
ω=0.95
Model (Second Order), Co-Pol.
Model (Second Order), X-Pol.
Data VV
Data VH
0
20
40
60
80
Incident Angle θ0 (degrees)

(c) 140 GHz

MILLIMETER-WAVE RADAR SCATTERING FROM SNOW PART I–RADIATIVE TRANSFER MODEL WITH QUASI-CRYSTALLINE APPROXIMATION

Yasuo Kuga, Richard T. Austin, Thomas F. Haddock and Fawwaz T. Ulaby

Radiation Laboratory, Department of Electrical Engineering and Computer Science,
University of Michigan, Ann Arbor, MI

Abstract

Millimeter-wave remote sensing of ground snow has attracted considerable interest in recent years. Because the size of the snow ice particle is comparable to the wavelength in the millimeter-wave region, we can no longer use a simple Rayleigh phase function or the small particle approximation usually used at microwave frequencies for calculating the extinction coefficient. In this paper we developed a model for MMW scattering from snow using the vector radiative transfer theory and a Mie phase function. Assuming snow to consist of randomly distributed spherical particles embedded in a mixture of

air and water, the vector radiative transfer theory is solved using the discrete ordinate method. The extinction coefficient is calculated by the quasi-crystalline approximation. The backscattering coefficient is calculated for different liquid water contents at 35, 95 and 140 GHz. We show that the backscattering coefficient is sensitive to liquid water content at 35 GHz, but the sensitivity decreases at 95 and 140 GHz.

I. INTRODUCTION

Although several papers have appeared recently documenting the results of millimeter-wave (MMW) radar observations of snow-covered terrain [1-11], the interaction mechanisms responsible for the observed radar response are not well understood at the present time. At millimeter wavelengths, snow is a highly lossy medium, particularly when wet; consequently, the penetration depth is only on the order of a few centimeters [1,2]. For dry snow, the attenuation is dominated by scattering because the ice particles are comparable to the wavelength in size, and for wet snow both absorption and scattering are important.

The physical parameters that exhibit the strongest importance on the radar backscatter from snow are snow surface roughness, crystal size, snow depth, and the liquid-water profile with depth. This paper, which in part I of a two-paper sequence, provides a radiative transfer model for characterizing MMW scatering from snow, using the quasi-crystalline approximation [14] to compute the extinction coefficient of the snow medium. Part II describes the results of experiments conducted at 35, 94, and 140 GHz, and includes comparison between theory and experiment for certain cases.

II. SNOW MODEL

In our snow model, we assume ground snow to consist of spherical ice particles embedded in a background medium. Liquid water, when present, is included as part of the background medium. The size of the water inclusion is usually much smaller than the wavelength for millimeter-wave remote sensing. Therefore, it is reasonable to assume that the water is uniformly distributed in the snow and the dielectric constant of water can be included as a part of the background. Thus, the wet snow medium is modeled in terms of ice crystals in a "wet air" background. It is also possible to consider the snow as lossy particles in a thin film of water surrounded by air, in which case the dielectric constant of the water inclusions is part of the dielectric constant of the lossy particles. This approach is inappropriate, however, because the liquid water in snow usually occupies the spaces between adjacent ice crystals rather than coat the crystals [1].

From ground-truth data, we know that the ice particles have an average diameter on the order of 0.1-2 mm and their shapes are round but non-spherical. In our model we treat the snow ice

particles as spheres with a normal size distribution with an average diameter of 1 mm and a standard deviation of 0.2 mm. The values of the dielectric constant of the ice particles needed in this study were obtained from [15] and are listed in Table 1. Also from the ground-truth data measured in conjunction with the experimental observations reported in Part II, the volume concentration of snow is approximately 40% and the snow depth is 0.45 m. These values are used in our model.

A. Background Absorption by Water Inclusion

The imaginary part of the background dielectric constant is directly related to the background absorption coefficient. We use a dielectric mixing formula to calculate the background dielectric constant, and we assume that scattering by the water particles to be much smaller than absorption. The absorption coefficient κ_{ag} of the background medium is given by

$$k_{ag} = 2Imag(k_b)(1-f) \quad (1)$$

$$= 2k_o Imag(\sqrt{\epsilon_b})(1-f) \quad (2)$$

where k_o is the free space wavenumber, ϵ_b is the background dielectric constant, and f is the volume fraction of ice particles. To obtain the dielectric constant of the background, which is a mixture of air and water, we use the Van Santen mixing formula [1],

$$\epsilon_b = 1 + \frac{m_v}{3}(\epsilon_w - 1) \sum_{u=a,b,c} \left[\frac{1}{1 + A_u(\frac{\epsilon_w}{\epsilon_b}) - 1} \right] \quad (3)$$

where ϵ_w is the dielectric constant of water, m_v is the volumetric snow wetness, and A_u is the depolarization factor which depends on the shape of the water droplet.

If the water droplet is spherical, A_u is constant and given by $A_u = 1/3$, but the water particles in snow are usually non-spherical and they change shape with the amount of liquid water present [1]. If the liquid water level is low, known as the pendular regime, the values of A_u are close to those for a needle. On the other hand, if the liquid water level is high, known as the funicular regime, the values of A_u are close to those for a disk. The transition from the pendular to funicular regime occurs at around $m_v = 2.5\%$ [1].

In our calculation of ϵ_b, therefore, we used three different sets of values for A_u depending on the values of m_v. The results for ϵ_b are listed in Table 1 at 35, 95 and 140 GHz.

B. Scattering Characteristics of Ice Particles

The scattering characteristics of ice particles are calculated using the Mie solution [13,14]. The background dielectric constant is assumed to be the real part of ϵ_b listed in Table 1. The imaginary part of ϵ_b is not used because of the difficulty in calculating the Mie solution when the imaginary part of the normalized dielectric constant is negative. The average total and absorption cross-sections are shown in Table 1.

C. Extinction Coefficient of Dry Snow

When snow is dry, the attenuation at MMWS is mainly due to scattering by the snow particles. In a sparsely distributed medium in which the correlation between particles can be neglected, the effective field approximation (EFA) can be applied and the extinction coefficient is linearly proportional to the concentration of particles [14]. Ground snow, however, has a volume fraction of 10 to 40% and the dielectric constant of ice is much larger than that of the background medium. Hence, the independent scatterers assumption is inappropriate for snow because it is necessary that the correlation between adjacent ice particles to be considered[14]. Two important phenomena that must be considered in a dense medium like snow are the backscattering-enhancement effect and the decrease of the extinction coefficient when the density is high [14,17-23].

Backscattering enhancement is caused by the constructive interference of two waves propagating in opposite directions and is important only in the backscattering direction, when the phase difference of the two waves is zero [14,20-23]. The backscattering enhancement effect has been observed for both randomly distributed discrete particles and very rough surfaces. The importance of the backscattering enhancement has been recognized in optics and solid state physics, but its significance in microwave and millimeter-wave remote sensing has not yet been evaluated. Since the angular width of the backscattering enhancement pattern is much less than 1 degree for discrete particles, the backscattering enhancement effect is not observable if the detector's field-of-view is large. In most microwave and millimeter-wave systems, the receiving cone of the antenna is much larger than 1 degree and the observation configuration is not truly monostatic.

Hence, the backscattering-enhancement effect is probably not significant and may be ignored, at least to first-order.

When the volume fraction of particles is more than 1%, the extinction coefficient is no longer linearly proportional to the number density. The derivation from the linear relationship applicable at low densities is related to the size parameter, dielectric constant and volume fraction of particles. Extensive experimental and theoretical studies on the extinction coefficient in a dense medium have been conducted in recent years [14,18,19]. The theoretical models include Twersky's model, the perturbation solution with hole-correction, the quasi-crystalline approximation (QCA) with Percus-Yevick pair correlation function, and the quasi-crystalline approximation with coherent potential (QCA-CP). Twersky's model is simple but it is applicable only for small particles. The formula based on the hole-correction is valid if the volume fraction is much less than 10%. For higher concentrations, QCA and QCA-CP with the Percus-Yevick pair correlation function have been shown to be effective [14].

In the millimeter-wave region where the size parameter is close to 1, we cannot use a small particle approximation. We need to solve the QCA numerically [14]. We calculated the extinction coefficient of snow using the QCA with the Percus-Yevick pair distribution function at 35, 95 and 140 GHz. The results are listed in Table 1. When the volume fraction f is 0.4, the extinction coefficients given by QCA are only 6.5 % of those calculated according to the EFA at 35 GHz and similar percentages apply at 95 and 140 GHz. The optical distance, which is defined as $\tau = (\kappa_e + \kappa_{ag})d$, is shown in Fig. 1 as a function of liquid water content for both EFA and QCA.

According to recent extinction measurements conducted for dry snow at 35 and 95 GHz [2], the extinction coefficient was found to exhibit a strong dependence on snow type. The reported values of the extinction coefficient covered the range between 0.96 and 15.4 ($\frac{Np}{m}$) at 35 GHz and between 1.9 and 30.7 ($\frac{Np}{m}$) at 95 GHz, with estimated median values of about 3.7 ($\frac{Np}{m}$) at 35 GHz and 19 ($\frac{Np}{m}$) at 95 GHz. The median value at 95 GHz is close to that comprised using the QCA method, but the median extinction coefficient at 35 GHz is much higher than that computed according to the QCA method.

If the optical distance is greater than 5, the backscattering coefficient of dry snow becomes essentially independent of the optical distance (in the millimeter-wave region). For a snow

thickness of 0.45 m and extinction coefficient of 19 ($\frac{Np}{m}$), the optical distance is already more than 8 at 95 GHz. Therefore, the exact value of extinction coefficient is not important at 95 and 140 GHz. However, an accurate estimate of the extinction coefficient is important at 35 GHz because τ is smaller. In our model calculations, we used extinction coefficients of 3.7 ($\frac{Np}{m}$) at 35 GHz and 19 ($\frac{Np}{m}$) at 95 GHz, which seem to offer the best fit to the experimental data. Due to the lack of measured extinction-coefficient data at 140 GHz, we will use the value calculated by the QCA model.

III. RADIATIVE TRANSFER THEORY

Microwave remote sensing of ground snow has been studied by many researchers in the past [1,14]. The model is usually based on the radiative transfer theory, and the Rayleigh phase function is used for modeling the ice particles. This is a good approximation for microwave remote sensing because the ice-particle size is much smaller than the wavelength. For millimeter-wave remote sensing, where the ice particle size is comparable to the wavelength, the Mie phase function must be used instead.

In a dense medium like snow, we need to modify the conventional radiative transfer theory to take into account the correlation between particles. A dense-media radiative transfer theory was recently developed using the Dyson equation with QCA-CP and the Bethe-Salpeter equation under the ladder approximation of correlated scatterers [14,17,18]. The form of the dense-media radiative transfer theory is the same as the conventional radiative transfer theory and, therefore, the same numerical techniques can be used for its solution [18,24,25,26]. The difference between the conventional radiative transfer theory and the dense-media radiative transfer theory is the extinction rate, which can be obtained by the QCA-CP and the new form of the albedo. The phase function is still the single particle phase function, which can be approximated by the Rayleigh phase function when the particles are small in size compared to the wavelength.

In this paper we shall use a modified version of the conventional radiative transfer model, but the formulation is not as rigid as the one given in [18]. We will use the measured extinction coefficient instead of the one obtained by the effective field approximation. This seems to give the best fit to the experimental data. The background dielectric constant of the snow layer will be obtained by the QCA and the real part will be used for calculating the reflectivity and transmissivity. The

phase function will be calculated using the Mie theory. Unlike the dense-media radiative transfer theory, the albedo will not depend on the medium concentration The background absorption will be calculated using a mixing formula and included in the total extinction coefficient. This will effectively reduce the albedo when the liquid water content increases in the background.

A. Problem Formulation

We consider a plane parallel medium containing spherical particles as shown in Fig. 2. A linearly polarized wave, which can be either vertically or horizontally polarized, is obliquely incident with incident angles θ_o and ϕ_o. The dielectric constants of media 1, 2, and 3 may be different. In our model medium 1 is air, medium 2 is snow, and medium 3 is the ground. We assume ϵ_1 and ϵ_3 do not change with temperature, but ϵ_2 (the background dielectric constant of medium 2) varies in response to changes in liquid water content of the snow layer.

The formulation of the radiative transfer theory for an oblique incident case has been derived previously in terms of the Fourier series expansion for the Stokes vectors [25]. If the incident wave is normally incident and linearly polarized, only two terms in the Fourier series are necessary, but the oblique incident case requires all the components of the Fourier series [25]. In this paper we will briefly describe the formulation. The details can be found elsewhere [24,25].

For convenience we will use the modified Stokes parameters (I_1, I_2, U, V),

$$\begin{aligned} I_1 &= \langle E_1 E_1^* \rangle \\ I_2 &= \langle E_2 E_2^* \rangle \\ U &= 2Re\langle E_1 E_2^* \rangle \\ V &= 2Im\langle E_1 E_2^* \rangle \end{aligned} \tag{4}$$

where E_1 and E_2 are the electric field in the $\hat{\theta}$ and $\hat{\phi}$ directions. The equation of transfer for the incoherent specific intensity I propagating in the $\hat{s}$ direction (Fig. 2) is given by

$$\frac{d[I(\bar{r},\hat{s})]}{ds} = -\kappa_e[I(\bar{r},\hat{s})] - \kappa_{as}[I(\bar{r},\hat{s})] + \kappa_s \int_{4\pi} d\omega'[S][I(\bar{r},\hat{s}')] + \kappa_e[I_i] \tag{5}$$

where

$$[I] = \begin{pmatrix} I_1 \\ I_2 \\ U \\ V \end{pmatrix} = 4 \times 1 \text{ incoherent specific intensity matrix,}$$

$[S]$ = $[S_{ij}] = 4 \times 4$ Mueller matrix,

$[I_i]$ = 4×1 incident specific intensity matrix (defined later by (13)).

The Mueller matrix (which also is called the scattering matrix) is expressed in terms of the scattering amplitudes f_{11}, f_{12}, f_{21}, and f_{22} [Ishimaru]:

$$[S] = \frac{1}{\langle \sigma_t \rangle} \begin{pmatrix} \langle |f_{11}| \rangle^2 & \langle |f_{12}| \rangle^2 & Re\langle f_{11} f_{12}^* \rangle & -Im\langle f_{11} f_{12}^* \rangle \\ \langle |f_{21}| \rangle^2 & \langle |f_{22}| \rangle^2 & Re\langle f_{21} f_{22}^* \rangle & -Im\langle f_{21} f_{22}^* \rangle \\ 2Re\langle f_{11} f_{21}^* \rangle & 2Re\langle f_{12} f_{22}^* \rangle & Re\langle f_{11} f_{22}^* + f_{12} f_{21}^* \rangle & -Im\langle f_{11} f_{22}^* - f_{12} f_{21}^* \rangle \\ 2Im\langle f_{11} f_{21}^* \rangle & 2Im\langle f_{12} f_{22}^* \rangle & Im\langle f_{11} f_{22}^* + f_{12} f_{21}^* \rangle & Re\langle f_{11} f_{22}^* - f_{12} f_{21}^* \rangle \end{pmatrix} \tag{6}$$

where $\langle\rangle$ denotes ensemble averaging over the particle size distribution and $\langle \sigma_t \rangle$ is the average extinction cross section of the particles. In terms of the optical distance τ and the extinction coefficient κ_e, the equation of transfer becomes

$$\mu \frac{d[I(\tau, \hat{s})]}{d\tau} = -[I(\tau, \hat{s})] + \frac{\kappa_e}{\kappa_e'} \int_{4\pi} d\omega' [S][I(\tau, \hat{s}')] + \frac{\kappa_e}{\kappa_e'} [I_i] \tag{7}$$

with

$$\mu = \cos\theta,$$

$$
\begin{aligned}
d\omega' &= d\mu' d\phi', \\
d\tau &= \mu \kappa_e' ds, \\
\kappa_e' &= \kappa_e + \kappa_{ag}
\end{aligned} \tag{8}
$$

Absorption by the background medium (wet air) is now included in κ_e' in Eq. 7. If the background absorption is zero, Eq. 7 reduces to Eq. 2 in [25]. However, if κ_{ag} is not zero, κ_{ag} acts like an additional loss term in the particle's extinction cross section.

$$
\frac{\kappa_e}{\kappa_e'} = \frac{\kappa_e}{\kappa_e + \kappa_{ag}}. \tag{9}
$$

In a sparse medium with number density N and $\kappa_e = N\sigma_t$, the above equation becomes:

$$
\frac{\kappa_e}{\kappa_e'} = \frac{\langle \sigma_t \rangle}{\langle \sigma_t \rangle + \frac{\kappa_{ag}}{N}}. \tag{10}
$$

This form is similar to the albedo of a single particle which is defined as

$$
W_o = \frac{\sigma_s}{\sigma_t} = \frac{\sigma_s}{\sigma_s + \sigma_a} \tag{11}
$$

where σ_s and σ_a are the particle's scattering and absorption cross-sections. If we define the effective albedo as

$$
W_o' = \frac{\sigma_s}{\sigma_t + \frac{\kappa_{ag}}{N}} \tag{12}
$$

we observe that it decreases as the background absorption increases. For example, the effective albedo of dry snow at 95 GHz is $W_o' = 0.99$. If the background is wet and the snow wetness is 5%, the effective albedo becomes $W_o' = 0.69$. A similar calculation at 35 GHz shows that W_o' decreases from 0.95 for dry snow to $W_o' = 0.09$ for a snow wetness of 5%. In our model we assume $\frac{\kappa_s}{\kappa_e'}$ to be independent of the density and given by Eq. 9. For calculating the optical distance and the reflection coefficients, however, we used QCA to obtain the effective propagation

constant of the snow. We chose this approach because if QCA is used for calculating $\frac{\sigma_e}{\sigma_s}$, the backscattering coefficient becomes very small for slightly wet snow and it does not agree with the experimental data. Our approach seems to give a reasonable fit to this experimental data. One problem with our approach is that when τ becomes small, the intensity of the dry snow may become less than that of the wet snow. For MMW remote sensing, however, τ is large and this deficiency is not critical.

B. Incident Specific Intensity for Vertical Polarization

Because of reflection at the boundaries, we have upward and downward traveling incident waves

$$[I_i] = [I_i^+] + [I_i^-] \tag{13}$$

where $[I_i^+]$ is for $\mu > 0$ and $[I_i^-]$ is for $\mu < 0$. For a vertically polarized incident wave $I_o[1000]^t$ incident along the direction (μ_o, o), $[I_i^+]$ is given in terms of the reduced incident intensity I_{ri}^+ by

$$\begin{aligned}
[I_i^+] &= \int [S][I_{ri}^+] d\omega' \\
&= I_o C_p \int [S] \begin{pmatrix} 1 \\ 0 \\ 0 \\ 0 \end{pmatrix} \delta(\mu' - \mu_o)\delta(\phi') e^{-\frac{\tau}{\mu_o}} d\mu' d\phi' \\
&= I_o C_p \begin{pmatrix} F_{11} \\ F_{21} \\ F_{31} \\ F_{41} \end{pmatrix}_{\mu=\mu_o} e^{-\frac{\tau}{\mu_o}}
\end{aligned} \tag{14}$$

with

$$F_{11} = \frac{\langle |f_{11}|^2 \rangle}{\langle \sigma_t \rangle}, F_{21} = \frac{\langle |f_{21}|^2 \rangle}{\langle \sigma_t \rangle}, F_{31} = \frac{2Re\langle f_{11} f_{21}^* \rangle}{\langle \sigma_t \rangle}, F_{41} = \frac{2Im\langle f_{11} f_{21}^* \rangle}{\langle \sigma_t \rangle}, \tag{15}$$

$\mu_o = \cos\theta_o, \phi_o = 0$; $F_{11}, F_{21}, F_{31}, F_{41}$ are evaluated at $\mu = \mu_o$;

$$C_p = \frac{T_{12}}{1 - R_{23}R_{21}\exp(-\frac{2\tau_o}{\mu_o})}, \tag{16}$$

$$T_{12} = \frac{n_2 \cos\theta_2}{n_1 \cos\theta_1}|t_{12}^v|^2 \tag{17}$$

$$R_{21} = |r_{21}^v|^2, \tag{18}$$

$$R_{23} = |r_{23}^v|^2, \tag{19}$$

where the superscript v denotes vertical polarization and r_{ij}^v and t_{ij}^v are the Fresnel reflection and transmission coefficients at boundary ij,

$$r_{ij}^v = \frac{n_j \cos\theta_i - n_i \cos\theta_j}{n_j \cos\theta_i + n_i \cos\theta_j} \tag{20}$$

$$t_{ij}^v = \frac{2n_j \cos\theta_i}{n_j \cos\theta_i + n_i \cos\theta_j} \tag{21}$$

The reflected incident specific intensity $[I_i^-]$ is given by

$$\begin{aligned}
[I_i^-] &= \int [S][I_{ri}^-]d\omega' \\
&= I_o C_p R_{23} \int [S] \begin{pmatrix} 1 \\ 0 \\ 0 \\ 0 \end{pmatrix} \delta(\mu' + \mu_o)\delta(\phi')d\mu' d\phi' \exp(-\frac{2\tau_o - \tau}{\mu_o}) \\
&= I_o C_p R_{23} \begin{pmatrix} F_{11} \\ F_{21} \\ F_{31} \\ F_{41} \end{pmatrix}_{\mu=-\mu_o} \exp(-\frac{2\tau_o - \tau}{\mu_o}).
\end{aligned} \tag{22}$$

C. Incident Specific Intensity for Horizontal Polarization

For a horizontally polarized incident wave given by $I_o[0100]^T$, $[I_i^+]$ is given by

$$[I_i^+] = I_o C_p \begin{pmatrix} F_{12} \\ F_{22} \\ F_{32} \\ F_{42} \end{pmatrix}_{\mu=\mu_o} \exp(-\frac{\tau}{\mu_o}) \tag{23}$$

with

$$F_{12} = \frac{\langle |f_{12}|^2 \rangle}{\langle \sigma_t \rangle}, F_{22} = \frac{\langle |f_{22}|^2 \rangle}{\langle \sigma_t \rangle}, F_{32} = \frac{2Re\langle f_{12} f_{22}^* \rangle}{\langle \sigma_t \rangle}, F_{42} = \frac{2Im\langle f_{12} f_{22}^* \rangle}{\langle \sigma_t \rangle}. \tag{24}$$

The reflected for horizontal polarization is given by

$$[I_i^-] = I_o C_p R_{23} \begin{pmatrix} F_{12} \\ F_{22} \\ F_{32} \\ F_{42} \end{pmatrix}_{\mu=-\mu_o} \exp(-\frac{2\tau_o - \tau}{\mu_o}). \tag{25}$$

The qualities C_p and R_{23} in (23) and (24) are given by the same expressions given previously for the vertical polarization case, except for replacing the superscript v with h everywhere and using

$$r_{ij}^h = \frac{n_i \cos\theta_i - n_j \cos\theta_j}{n_i \cos\theta_i + n_j \cos\theta_j} \tag{26}$$

$$t_{ij}^h = \frac{2n_i \cos\theta_i}{n_i \cos\theta_i + n_j \cos\theta_j} \tag{27}$$

D. Outline of the Solution

The boundary condition for the incoherent specific intensity $[I]$ is that the inward intensities at the upper and lower boundaries are given by

$$[I(\tau = o, -\mu) = [R_{21}(-\mu)][I(\tau = o, \mu)], -1(\mu(0 \tag{28}$$

$$[I(\tau = \tau_o, -\mu)] = [R_{23}(\mu)][I(\tau = \tau_o, \mu)], 0(\mu(1 \tag{29}$$

where $[R_{21}(\mu)]$ and $[R_{23}(\mu)]$ are reflectively matrices given by generic forms

$$[R_{ij}(\mu)] = \begin{pmatrix} |r_{ij}^v|^2 & 0 & 0 & 0 \\ 0 & |r_{ij}^h|^2 & 0 & 0 \\ 0 & 0 & Re(r_{ij}^v r_{ij}^{h*}) & -Im(r_{ij}^v r_{ij}^{h*}) \\ 0 & 0 & Im(r_{ij}^v r_{ij}^{h*}) & Re(r_{ij}^v r_{ij}^{h*}) \end{pmatrix} \tag{30}$$

It is possible to eliminate the ϕ dependence from Eq. 7 and obtain a new equation in terms of τ and μ [1,14,24,25]. First we expand $[I],[S]$ and $[F]$ in Fourier series in ϕ. For the plane wave case, we can show that all Fourier components of the equation of transfer are independent of each other, and for the vertically and horizontally polarized incident waves, the first two terms of the stokes vector are even functions of ϕ and the last two terms are odd functions of ϕ. The incoherent specific intensity is given by the sum of all Fourier terms,

$$[I] = \sum_{m=o}^{\infty} [I]_m \cos m\phi + \sum_{m=1}^{\infty} [I]_m \sin m\phi \tag{31}$$

We can obtain the equation of transfer for each Fourier component. For the Fourier component $m = 0$ and a vertically polarized incident wave.

$$\mu \frac{d[I]_o}{d\tau} = -[I]_o + \frac{\kappa_e}{\kappa_e'} \int_{-1}^{1} [L]_o [I]_o d\mu' + \frac{\kappa_e}{\kappa_e'} C_p [F^+]_o e^{-\frac{\tau}{\mu_o}} + \frac{\kappa_e}{\kappa_e'} C_p R_{23} [F^-]_o e^{-\frac{2\tau_o - \tau}{\mu_o}} \tag{32}$$

where

$$[I]_o = \begin{bmatrix} I_{o1} \\ I_{o2} \end{bmatrix}, [L]_o = [S_1]_o^a, [F^+]_o = \begin{bmatrix} F_{11} \\ F_{21} \end{bmatrix}_{\mu=\mu_o}, [F^-]_o = \begin{bmatrix} F_{11} \\ F_{21} \end{bmatrix}_{\mu=-\mu_o} \tag{33}$$

For $m)0$

$$\mu \frac{d[I]_m}{d\tau} = -[I]_m + \frac{\kappa_e}{\kappa_e'} \int_{-1}^{1} [L]_m [I]_m d\mu' + \frac{\kappa_e}{\kappa_e'} C_p [F^+]_m e^{-\frac{\tau}{\mu_o}} + \frac{\kappa_e}{\kappa_e'} C_p R_{23} [F^-]_m e^{-\frac{2\tau_o - \tau}{\mu_o}} \tag{34}$$

where

$$[I]m = \begin{pmatrix} I_{m1} \\ I_{m2} \\ U_m \\ V_m \end{pmatrix}, [F^+]_m = \begin{pmatrix} F_{11} \\ F_{21} \\ F_{31} \\ F_{41} \end{pmatrix}_{\mu=\mu_o}, [F^-]_m = \begin{pmatrix} F_{11} \\ F_{21} \\ F_{31} \\ F_{41} \end{pmatrix}_{\mu=-\mu_o}, [L]_m = \begin{pmatrix} [S_1]^a_m & [S_2]^b_m \\ -[S_3]^b_m & [S_4]^a_m \end{pmatrix} \quad (35)$$

The equation of transfer given by Eq. 32 and 34, together with the boundary conditions given by Eq. 28 and 29, constitute the complete mathematical formulation of the problem. An analytical solution of the integro-differential equation given by Eq. (32) and (34) is not available, but it is possible to solve the equation of transfer numerically by several techniques. In this study we use the discrete ordinate method. The details of these techniques are given in [24] and [25]. Once $[I]_o$ and $[I]_m$ have been found, the total incoherent specific intensity emerging from the layer at a point above the air-snow boundary can be computed from

$$[I] = [T_{21}] \left\{ \sum_{m=o}^{\infty} \begin{pmatrix} I_1 \\ I_2 \\ 0 \\ 0 \end{pmatrix} \cos m\phi + \sum_{m=1}^{\infty} \begin{pmatrix} 0 \\ 0 \\ U \\ V \end{pmatrix} \sin m\phi \right\} \quad at \quad \tau = 0 \qquad (36)$$

where $[T_{21}]$ is the transmissivity matrix of the upper boundary. If the incident angle is larger than the critical angle, $[T_{ij}] = 0$; otherwise, it is given by

$$[T_{ij}] = \frac{n_j^3 \cos\theta_j}{n_i^3 \cos\theta_i} \begin{pmatrix} |t^v_{ij}|^2 & 0 & 0 & 0 \\ 0 & |t^h_{ij}|^2 & 0 & 0 \\ 0 & 0 & Re(t^v_{ij} t^{h*}_{ij}) & -I_m(t^v_{ij} t^{h*}_{ij}) \\ 0 & 0 & Im(t^v_{ij} t^{h*}_{ij}) & Re(t^v_{ij} t^{h*}_{ij}) \end{pmatrix} \qquad (37)$$

where t_{ij} is given by (21) for vertical polarization and by (27) for horizontal polarization.

Once the specific intensity has been computed for a vertically polarized incident wave, the backscattering coefficients of the snow-volume for vv and hv polarizations can be obtained from the first and second elements of $[I]$

$$\sigma_{sv}^{vv} = 4\pi \cos\theta_o I_1$$
$$\sigma_{sv}^{hv} = 4\pi \cos\theta_o I_2 \qquad (38)$$

IV. SURFACE SCATTERING AT BOUNDARIES

In the millimeter-wave region, most natural surfaces, such as ground snow, are rough compared to the wavelength. Surface scattering at the snow-ground interface is not important for millimeter-wave remote sensing because of the large amount of attenuation in the snow layer, however, the scattering at the air-snow interface becomes important when snow is wet and the volume fraction of ice particles is high.

If the top surface is rough, the incident wave transmitted into the snow layer is no longer a plane wave. Hence, we need to consider the interaction between surface scattering and volume scattering. This interaction has been examined in the literature [1, 14] for a Rayleigh layer bounded by a Kirchhoff rough surface interface. Based on these studies, we can ignore the influence of the rough surface on the wave transmitted into the snow layer because, as we have shown in Table 1, the effective index of refraction of the snow layer is around 1.3. However, we have to account for the direct backscatter from the rough surface, which we can add incoherently to the volume backscattering distribution dervied in the preceeding section [26].

Two widely used techniques for analyzing surface scattering are the Kirchhoff approximation and the small perturbation method [1,14]. If a surface has a large rms slope, we can obtain a simple expression using the Kirchhoff stationary phase approximation. Assuming that the surface characteristics can be modeled by a Gaussian correlation function, we can write the co-polarized backscattering coefficient of the snow surface as

$$\sigma_{gg} = \frac{|r(0)|^2 \exp(-\frac{\tan^2\theta_o}{2m^2})}{2m^2 \cos^4\theta_o} \qquad (39)$$

where θ_o is the incident angle, m is the rms slope, and $r(0)$ is the Fresnel reflection coefficient evaluated at normal incidence. The Kirchhoff approximation does not produce depolarization in the backscatter direction. Therefore, the total-snow backscattering coefficient is

$$\sigma_{ts}^{vv} = \sigma_{sv}^{vv} + \sigma_{ss}$$
$$\sigma_{ts}^{hh} = \sigma_{sv}^{hh} + \sigma_{ss}$$
$$\sigma_{ts}^{hv} = \sigma_{ts}^{vh} = \sigma_{sv}^{vh} = \sigma_{sv}^{hv} \quad (40)$$

V. RESULTS

In this section we shall discuss the variation of the backscattering coefficient with snow wetness (Liquid water content), snow thickness, and angle of incidence, and we shall graduate the contribution of surface scattering to the total backscattering coefficient. All calculations were preferred for a snow layer with an ice volume fraction of 0.4 containing ice particles characterized by a normal size distribution with a mean diameter of 1mm and a standard deviation of 0.2mm. The snow surface is assumed to have a rms shape $m = 0.5$.

Evaluation of the Fourier components of (36) led to the conclusion that it is necessary to include only the first four components in the computation of the scattered intensity I because the contributions of the higher order components are negligibly small. Moreover, except when the snow layer is dry and its thickness is only a few centimeters, the effects of reflections by the underlying ground surface may be ignored.

A. Surface Scattering Contribution

The plots shown in Fig. 3 depict the 35-GHz variation of the snow-volume backscattering coefficient σ_{sv} with liquid water content for a 0.45-m thick snow layer at the incident angle $\theta_o = 40°$. An additional curve is shown for the co-polarized case representing the total-snow backscattering coefficient σ_{ts}, which includes σ_{sv} and the surface contribution σ_{ss}. We observe that σ_{sv} decreases rapidly with increasing liquid water content due to the corresponding increase in background absorption. The rate of decrease of the cross-polarized component is much higher than the rate for the co-polarized component, indicating less multiple scattering as the medium becomes highly absorptive. Because we use spherically shaped ice particles in the mode, single scattering does not produce depolarization; the depolarized return is caused exclusively by multiple scattering.

For dry snow ($m_v = 0$), the contribution of surface scattering, σ_{ss}, is negligibly small in comparison with σ_{sv}. However, σ_{ss} increases with increasing m_v and becomes comparable in magnitude with σ_{sv} at $m_v = 5\%$. These observations pertain to 35 GHz. Similar calculations made at 95 and 140 GHz indicate that $\sigma_{ss} << \sigma_{sv}$ even at $m_v = 5\%$. Thus, surface scattering may not be included at these higher frequencies.

The variation of the backscattering coefficient with liquid water content at 95 and 140 GHz is shown in Fig. 4. Compared with the 35-GHz results, σ_{sv} decreases with liquid water content at a much slower rate, and the cross-polarized component remains significant in magnitude even at high liquid water contents, indicating strong volume scattering with snow layer. Although the background absorption coefficient κ_{ag} is approximately twice as large at 95 GHz than its value at 35 GHz (see Table 1), the effect of the background absorption on the total backscattered signal is less important at 95 GHz than at 35 GHz because the scattering cross section of the ice particle is much larger at 95 GHz, as a result of which multiple scattering becomes dominant in comparison to absorption. As was noted earlier, at 95 GHz the effective albedo of the snow volume decreases from 0.99 for dry snow to 0.69 for wet snow with $m_v = 5\%$, compared to a corresponding decrease from 0.95 to 0.09 at 35 GHz. At 140 GHz, the effective albedo decreases from 0.99 for dry snow to 0.90 for $m_v = 5\%$.

B. Angular Variation

The angular variation shown in Fig. 5 is very close to a $\cos\theta$ - dependence for both co- and cross- polarized scattering coefficients. The co-polarized response represents both hh and vv polarizations because according to the model calculations, there is little difference between the two responses. This $\cos\theta$ - like variations was also observed at 95 and 140 GHz.

C. Variation with Snow Thickness

Figure 6 shows the response of the backscattering coefficient to snow thickness at 35 and 95 GHz for $\theta_o = 40°$. Two wetness conditions are shown. In all cases, the minimum thickness considered in the model calculations was 5 cm. For dry snow, σ_{vs} increases rapidly with increasing snow thickness, particularly for cross polarization, until it approaches a saturation level beyond which the increase becomes very gradual.

D. Simulation of Diurnal Response

Let us consider a diurnal cycle during which the liquid water content of a 0.45-m thick snow layer exhibits the variation shown in Fig. 7a, which is Gaussian shaped with a peak value of 2%. In fact the wetness need not be uniform in depth because the radar response is essentially controlled by the wetness of the very surface layer (as long as the layer is not dry and the snow contains a subsurface layer with non-zero wetness).

Figures 7b, 7c and 7d show the corresponding diurnal radar response at 35, 95, and 140 GHz. All cases include both the co- and cross-polarized responses. As expected, the radar diurnal responses are approximately mirror images of the liquid-water diurnal variation, with 35 GHz exhibiting the greatest dynamic range and 140 GHz exhibiting the smallest.

VI. CONCLUSIONS

Using radiative transfer theory, we developed a reasonably and computationally efficient, uncomplicated, model for relating the backscattering coefficient of snow at millimeter wavelengths to the physical properties of the snow layer. According to the mode, snow-surface roughness is unimportant when the snow is dry, but when the snow is wet snow-surface roughness is important at 35 GHz but not at the higher frequencies examined in this paper (95 and 140 GHz).

Within an error of about 1 dB, the backscattering coefficient σ_{ts} varies with incidence angle as $\cos\theta_0$ for both the co-polarized and cross-polarized configurations at all millimeter-wave frequencies and liquid water contents considered in this study. The effective penetration depth of the snow medium is strongly dependent on frequency and the liquid water content. At 35 GHz, the effective penetration depth decreases from about 30cm for dry snow down to about 1.5cm for m_v = 5%. At 95 and 140 GHz, the penetration depth of dry snow is 5cm and 1cm, respectively. The backscattering coefficient decreases with increasing liquid water content, with 35 GHz exhibiting the strongest sensitivity to liquid water variations and 140 GHz exhibiting the weakest.

VII. REFERENCES

1. F. T. Ulaby, R. K. Moore, and A. K. Fung, Microwave Remote Sensing Vol. I, II, and III, Addison-Wesley, 1981.

2. M. Hallikainen,"Scattering properties of snow in the 10 to 90 GHz range," Proceeding of ISAP, pp. 667-670, 1985.

3. R. T. Austin, T. F. Haddock, and F. T. Ulaby, "An investigation of the diurnal variation of backscatter from snow at millimeter-wave frequencies," unpublished report, University of Michigan, 1988.

4. W. H. Stiles and F. T. Ulaby, "The active and passive microwave response to snow parameters: Part I- Wetness, J. Geophys. Res., 85, pp. 1037-1044, 1980.

5. M. Hallikainen, F. T. Ulaby and M. Abdelrazik, "The dielectric behavior of snow in the 3 to 37 GHz range," 1984 IEEE Intl. Geosci. Remote Sensing Symp. (IGARSS'84) Digest, Strasbourg, France, 27-30 August, pp. 169-176.

6. D. T. Hayes, U. H. W. Lammers, and R. A. Marr, "Scattering from snow backgrounds at 35, 98, and 140 GHz," RADX-TR-84-69, Rome Air Development Center Report, 1984.

7. Special issue, IEEE Trans. on Geoscience and Remote Sensing, Vol. 26, No. 3, May 1988.

8. E. P. Baars and H. Essen, "Millimeter-wave backscatter measurements on snow- covered terrain," IEEE Trans. Geoscience and Remote Sensing, Vol. 26, No. 3, pp 282-299, May 1988.

9. L. D. Williams, J. G. Gallagher, D. E. Sugden, and R. V. Birnie, "Surface snow properties effects on millimeter-wave backscatter," IEEE Trans. Geoscience and Remote Sensing, Vol. 26, No. 3, pp. 300-306, May 1988.

10. J. Nemarich, R. J. Wellman, and J. Lacombe, "Backscatter and attenuation by falling snow and rain at 96, 140 and 225 GHz, IEEE Trans. Geoscience and Remote Sensing, Vol. 26, No. 3, pp 319-329, May 1988.

11. N. C. Currie, J. D. Echard, M. J. Gary, A. H. Green, T. L. Lane, and J. M. Trostel, "Millimeter-wave measurements and analysis of snow-covered ground," IEEE Trans. Geoscience and Remote Sensing, Vol. 26, No. 3, pp 307-318, May 1988.

12. S. Chandrasekhar, Radiative Transfer, Clarendon, Oxford, 1950.

13. A. Ishimaru, Wave Propagation and Scattering in Random Media Vol. I and II, Academic Press, New York, 1978.

14. L. Tsang, J. A. Kong, and R. T. Shin, Theory of Microwave Remote Sensing, Wiley, New York, 1985.

15. C. Matzler and U. Wegmuller, "Dielectric properties of fresh water ice at microwave frequencies," J. Phy. D: Applied Physics, Vol. 20, pp. 1623-1630, 1987.

16. F. T. Ulaby, T. F. Haddock, J. R. East, and M. W. Whitt, "A millimeter-wave network analyzer based scatterometer," IEEE Trans. Geoscience and Remote Sensing, Vol. 26, No. 1, pp. 75-81, 1988.

17. L. Tsang and A. Ishimaru, "Radiative wave equations for vector electromagnetic propagation in dense nontenuous media," J. of Electromagnetic Waves and Applications, Vol. 1, No. 1, pp. 52-72, 1987.

18. B. Wen, L. Tsang, D. P. Winebrenner, and A. Ishimaru, "Dense medium radiative transfer theory: Comparison with experiment and application to microwave remote sensing and polarimetry," submitted to IEEE Trans. Geoscience and Remote Sensing.

19. A. Ishimaru and Y. Kuga, "Attenuation constant of coherent field in a dense distribution of particles," J. Opt. Soc. Am., Vol. 72, pp.1317-1320, 1982.

20. Y. Kuga and A. Ishimaru, "Retroreflectance from a dense distribution of spherical particles," Journal of the Optical Society of America, A-1, 831-835, 1984.

21. L. Tsang and A. Ishimaru, "Backscattering enhancement of random discrete scatterers," Journal of the Optical Society of America, A-1, 836-839, 1984.

22. M. van Albada and A. Lagendijk, "Observation of weak localization of light in a random medium," Phys. Rev. Lett. 55, 2692-2695, 1985.

23. P. E. Wolf and G. Maret, "Weak localization and coherent backscattering of photon in disordered media," Phys. Rev. Lett. 55, 2696-2699, 1985.

24. R. L-T Cheung and A. Ishimaru, "Transmission, backscattering, and depolarization of waves in randomly distributed spherical particles," Applied Optics, Vol. 21, No. 20, 3792-3798, 1982.

25. A. Ishimaru, R. Woo, J. W. Armstrong, and D. C. Blackman,"Multiple scattering calculations of rain effects," Radio Science, Vol. 17, No. 6, 1425-1433, 1982.

26. Q. Ma, A. Ishimaru, P. Phu and Y. Kuga, "Transmission, bidirectional reflectance and depolarization of an optical wave for a single leaf," submitted to Radio Science.

FIGURE CAPTIONS

Figure 1. Optical distance τ versus liquid water content m_v at 35 and 95 GHz. Snow depth is 0.45 m, the ice volume fraction is 0.4, and average ice particle direction is 1 mm. EFA is the effective field approximation and QCA is the quasi-crystalline approximation.

Figure 2. Geometry showing the snow model.

Figure 3. Backscattering coefficients σ_{vv} and σ_{hh} versus m_v at 35 GHz. Symbols are the calculated values based on the radiative transfer theory. Solid lines are 3rd order polynomial curve fit to calculated results. The incidence angle is $\theta_o = 40°$ and the incident wave is vertically polarized. The rms slope of the snow surface is $m = 0.5$.

Figure 4. Backscattering coefficient σ_{vv} versus m_v at 95 and 140 GHz. Symbols are the calculated values based on the radiative transfer theory. Solid lines are 3rd order polynomial curve fit to calculated results. The incident angle is $\theta_o = 40°$ and the incident wave is horizontally polarized.

Figure 5. Backscattering coefficient σ_{vv} versus incident angle at 35 GHz for 0.45 m thick layer.

Figure 6. Backscattering coefficient σ_{vv} versus snow thickness. The incident angle is $\theta_o = 40°$ and the incident wave is vertically poplarized.

Figure 7(a). Model for the liquid water content variation in time. $m_v = W_{peak} \exp[-(t - 13.85)^2/\sigma^2$ where W_{peak} is the peak value $W_{peak} = 2\%$, t is time in hours and σ is the standard deviation $\sigma = 2$. (b), (c) and (d) are the diurnal variation of the backscattering coefficient σ_{vv} at 35, 95 and 140 GHz.

Table 1 Dielectric and propagation properties of a snow medium with ice volume fraction f=0.4, average ice particle diameter of 1mm, and number density N=7.64x10^8.

35 GHz ε_{ice} = 3.15+i0.003, σ_t =1.2x10^{-8}, σ_a =5x10^{-10}, κ_e(EFA)=8.24 (Np/m)

m_v (%)	ε_b Real	Imag.	κ_{ag} (Np/m)	K (QCA) (Np/m) Real	Imag.	Re[n(QCA)]	κ_e(QCA) (Np/m)
0	1	0	0	930	0.269	1.268	0.538
1	1.0427	0.0129	5.56	942	0.267	1.285	0.534
2	1.104	0.0532	22.2	958	0.264	1.307	0.528
3	1.1776	0.0869	35.2	977	0.262	1.332	0.524
4	1.2405	0.1268	50.0	992	0.259	1.353	0.518
5	1.3046	0.1723	66.2	1007	0.257	1.373	0.514

95 GHz ε_{ice} = 3.15+i0.0085, σ_t =5.89x10^{-7}, σ_a =4.28x10^{-9}, κ_e(EFA)=402 (Np/m)

m_v (%)	ε_b Real	Imag.	κ_{ag} (Np/m)	K (QCA) (Np/m) Real	Imag.	Re[n(QCA)]	κ_e(QCA) (Np/m)
0	1	0	0	2562	11.35	1.2884	22.69
1	1.0296	0.0138	16.2	2582	10.91	1.298	21.82
2	1.0626	0.0397	45.9	2604	10.43	1.3095	20.86
3	1.1055	0.0697	78.7	2632	9.84	1.323	19.68
4	1.141	0.0961	107.2	2654	9.39	1.335	18.78
5	1.1765	0.1244	136.6	2676	8.95	1.346	17.9

140 GHz ε_{ice} = 3.15+i0.012, σ_t =.95x10^{-6}, σ_a =2.33x10^{-8}, κ_e(EFA)=1331 (Np/m)

m_v (%)	ε_b Real	Imag.	κ_{ag} (Np/m)	K (QCA) (Np/m) Real	Imag.	Re[n(QCA)]	κ_e(QCA) (Np/m)
0	1	0	0	3876	56.58	1.32	113.15
1	1.0254	0.0115	20	3891	54.95	1.326	109.9
2	1.0534	0.0307	52.67	3909	53.94	1.331	107.9
3	1.0883	0.0540	91.15	3933	53.36	1.339	106.7
4	1.1181	0.0741	123.38	3955	53.2	1.347	106.4
5	1.1482	0.0953	156.54	3977	53.1	1.354	106.3

m_v : liquid water content by volume, ε_b :background dielectric constant, κ_{ag}: background absorption coefficient, K(QCA):propagation constant in the snow layer obtained by QCA, Re[n(QCA)]: real part of the effective index of refraction obtained by QCA, κ_e(QCA) :extinction coefficient of ice particles obtained by QCA, κ_e(EFA) :extinction coefficient of ice particles obtained by EFA. σ_t and σ_a :total and absorption cross-sections of ice particles obtained by EFA.

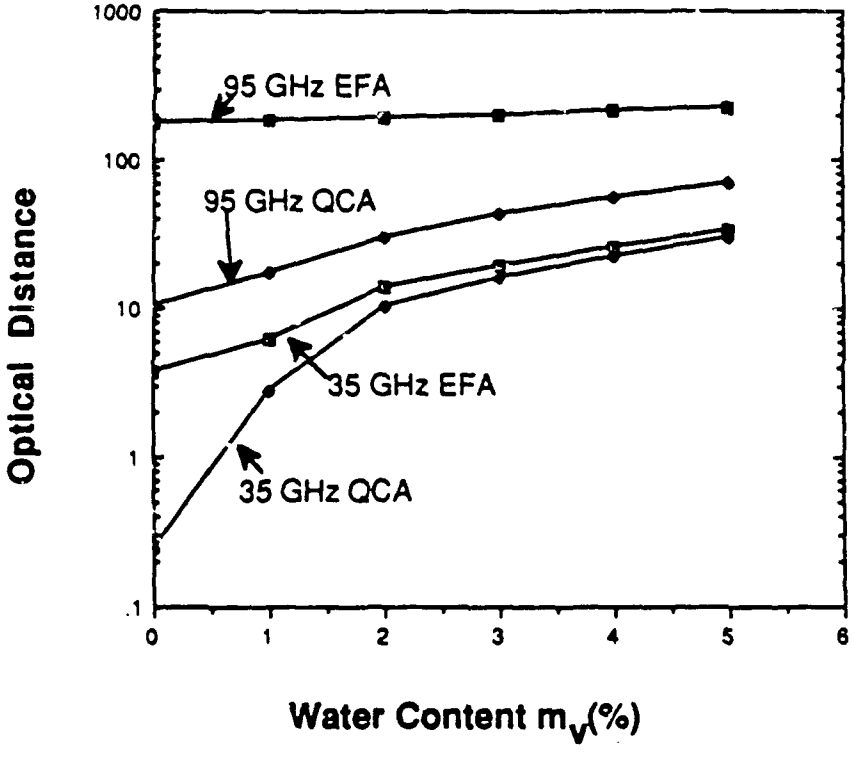
1000
100
10
1
.1
0
1
2
3
4
5
6
95 GHz EFA
95 GHz QCA
35 GHz EFA
35 GHz QCA
Optical Distance
Water Content m_v(%)

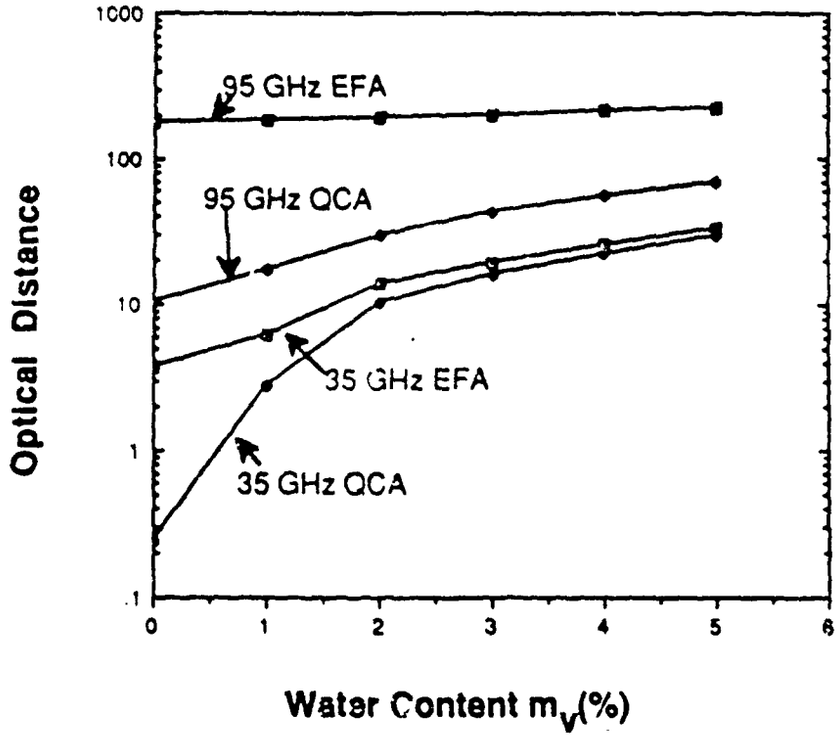
1000
100
10
1
.1
0
1
2
3
4
5
6
95 GHz EFA
95 GHz QCA
35 GHz EFA
35 GHz QCA
Optical Distance
Water Content m_v(%)

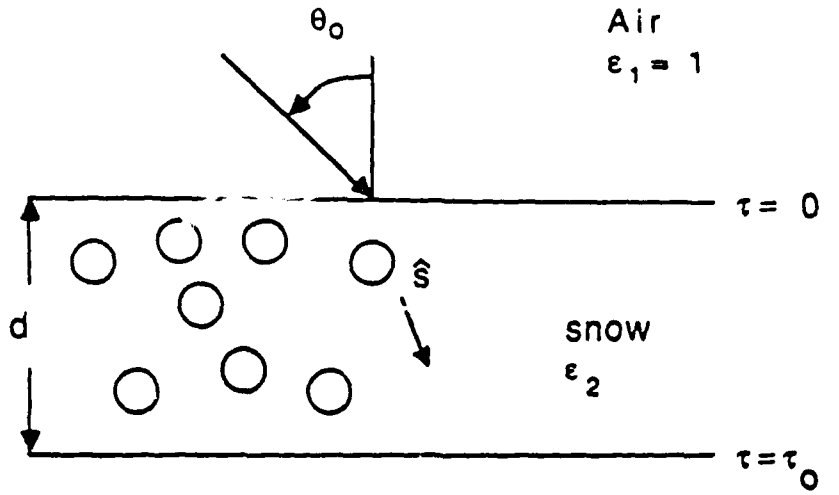
θ_o
Air
$\varepsilon_1 = 1$
$\tau = 0$
$\hat{s}$
d
snow
ε_2
$\tau = \tau_o$
ground
$\varepsilon_3 = 3.17$

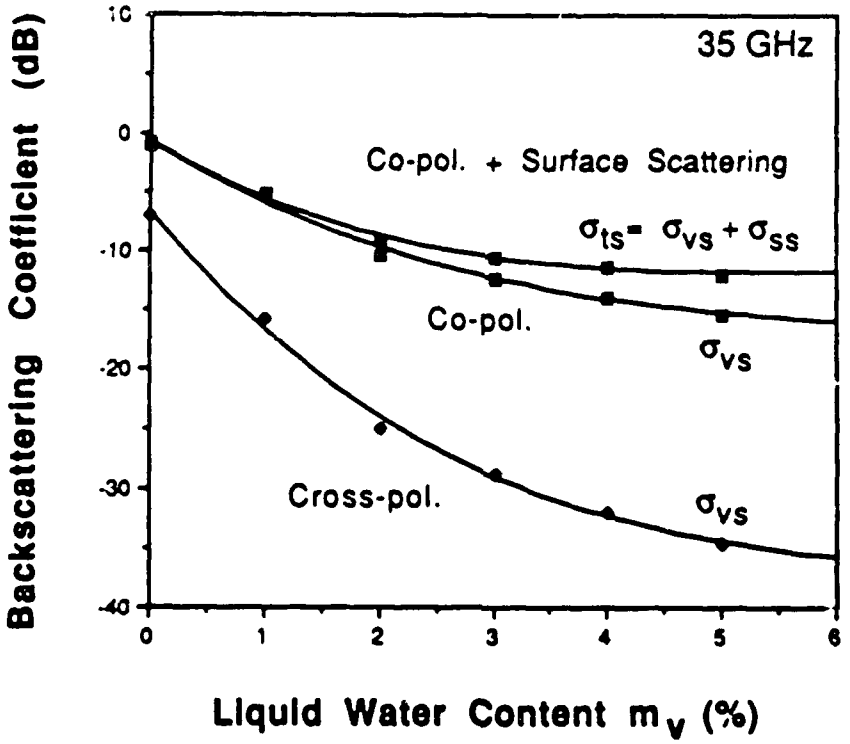
35 GHz
Co-pol. + Surface Scattering
$\sigma_{ts} = \sigma_{vs} + \sigma_{ss}$
Co-pol.
σ_{vs}
Cross-pol.
σ_{vs}
Backscattering Coefficient (dB)
10
0
-10
-20
-30
-40
0
1
2
3
4
5
6
Liquid Water Content m_v (%)

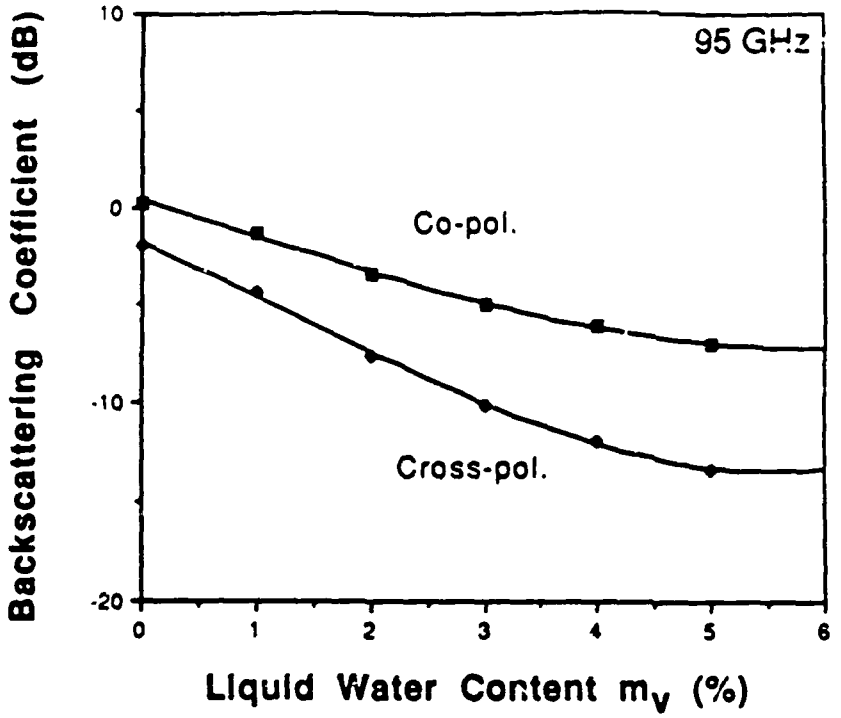
95 GHz
Co-pol.
Cross-pol.
Backscattering Coefficient (dB)
10
0
-10
-20
0
1
2
3
4
5
6
Liquid Water Content m_v (%)

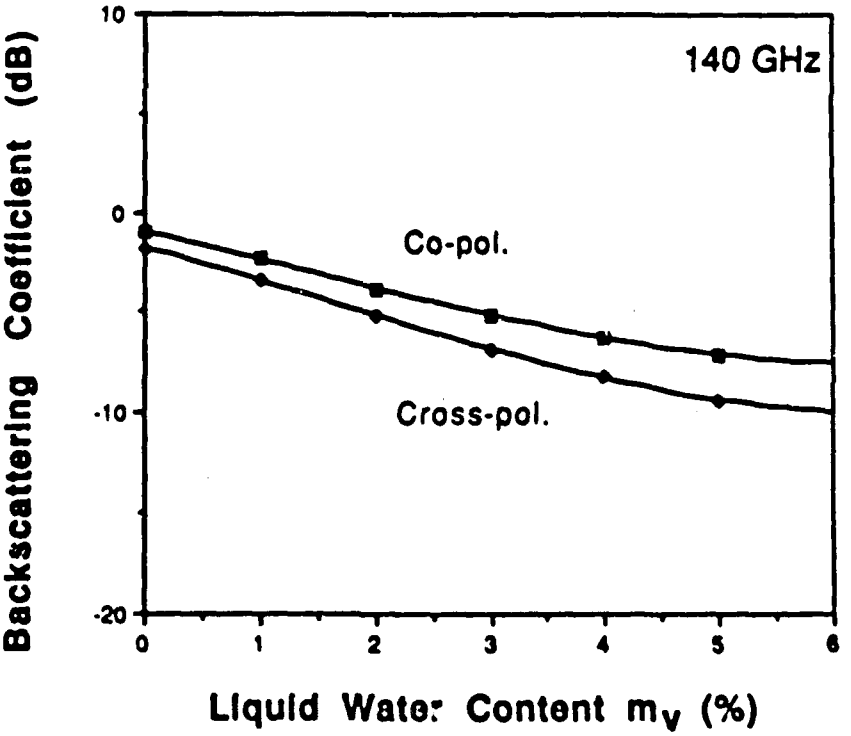
140 GHz
Co-pol.
Cross-pol.
Backscattering Coefficient (dB)
10
0
-10
-20
0
1
2
3
4
5
6
Liquid Water Content m_v (%)

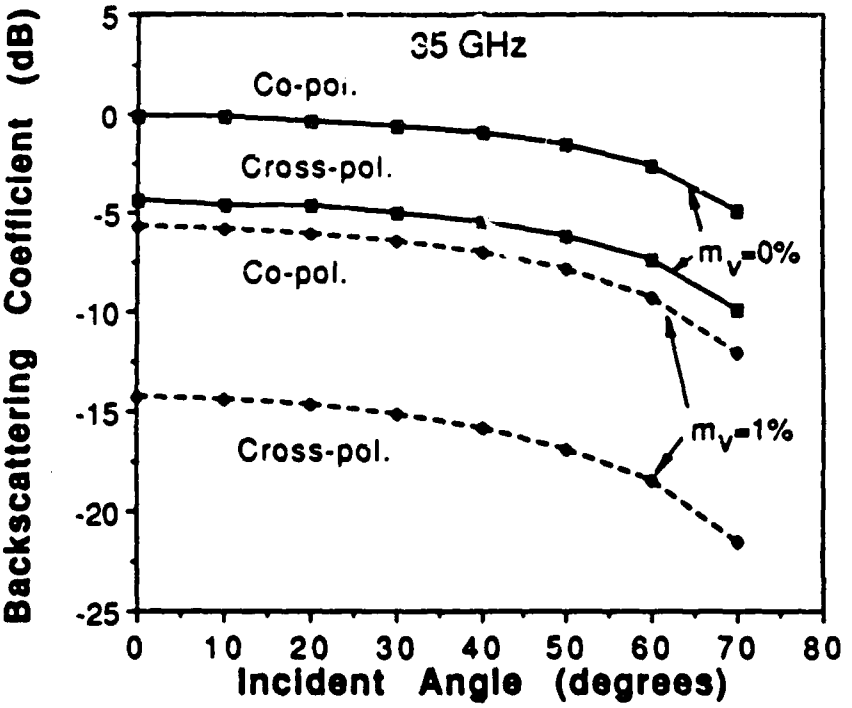
35 GHz
Co-pol.
Cross-pol.
Co-pol.
Cross-pol.
m_v=0%
m_v=1%
Backscattering Coefficient (dB)
5
0
-5
-10
-15
-20
-25
0
10
20
30
40
50
60
70
80
Incident Angle (degrees)

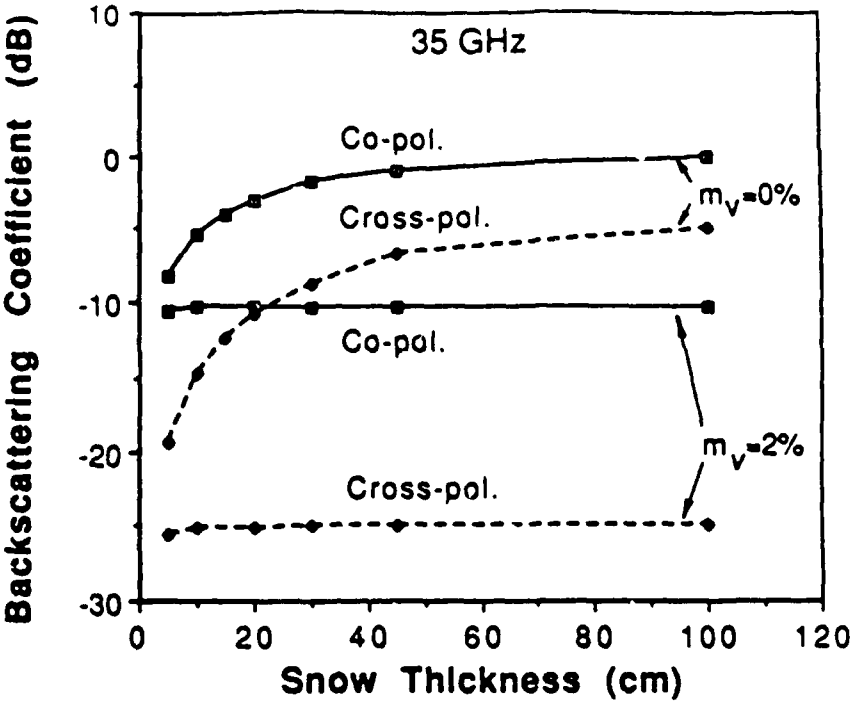
35 GHz
Co-pol.
Cross-pol.
m_v=0%
Co-pol.
Cross-pol.
m_v=2%
Backscattering Coefficient (dB)
10
0
-10
-20
-30
0
20
40
60
80
100
120
Snow Thickness (cm)

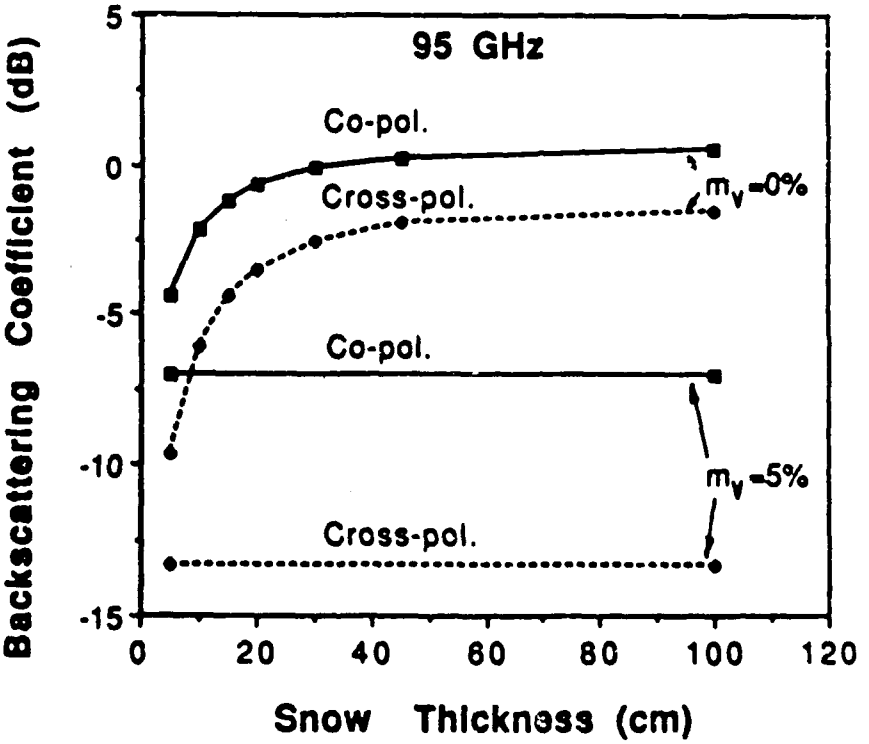
95 GHz
Co-pol.
Cross-pol.
m_v=0%
Co-pol.
m_v=5%
Cross-pol.
Backscattering Coefficient (dB)
5
0
-5
-10
-15
0
20
40
60
80
100
120
Snow Thickness (cm)

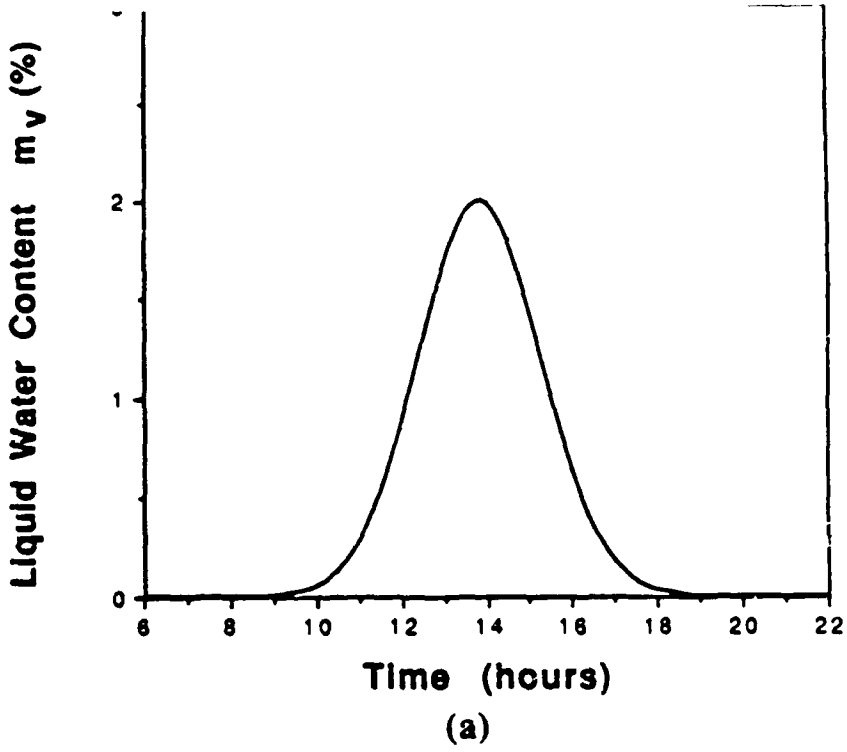
Liquid Water Content m_v (%)
0
1
2
6
8
10
12
14
16
18
20
22
Time (hours)

(a)

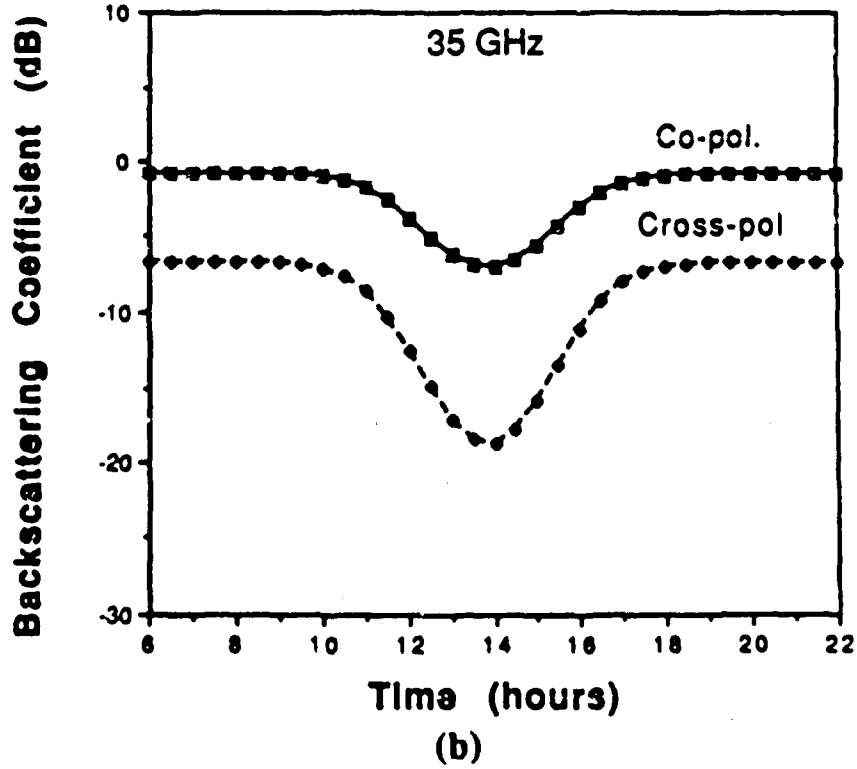
35 GHz
Co-pol.
Cross-pol
Backscattering Coefficient (dB)
10
0
-10
-20
-30
6
8
10
12
14
16
18
20
22
Time (hours)

(b)

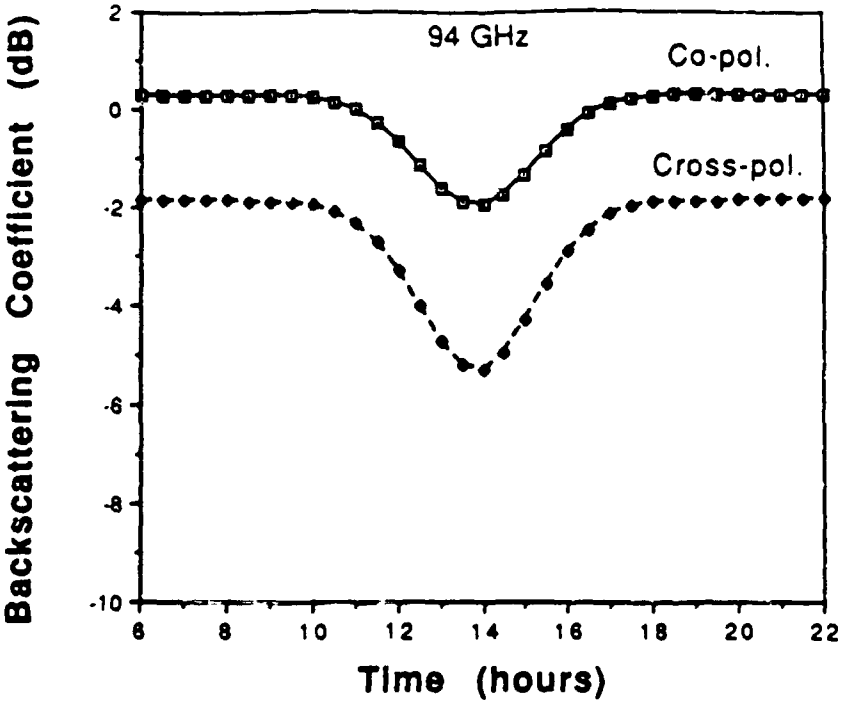
94 GHz
Co-pol.
Cross-pol.
Backscattering Coefficient (dB)
2
0
-2
-4
-6
-8
-10
6
8
10
12
14
16
18
20
22
Time (hours)

(c)

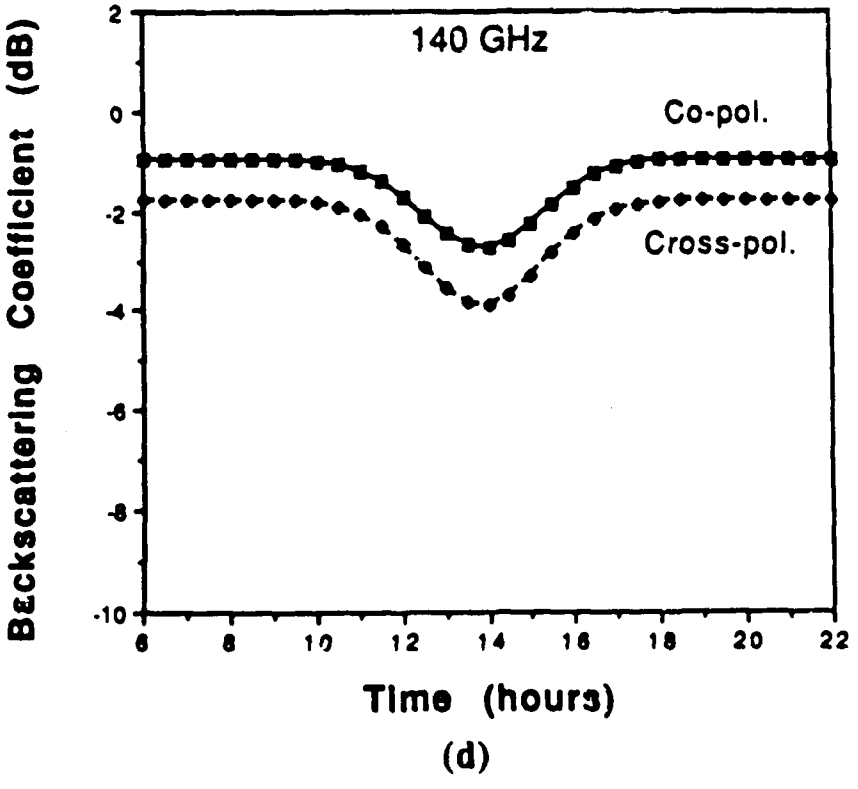
140 GHz
Co-pol.
Cross-pol.
Backscattering Coefficient (dB)
2
0
-2
-4
-6
-8
-10
6
8
10
12
14
16
18
20
22
Time (hours)

(d)

REPORT DOCUMENTATION PAGE

1a. REPORT SECURITY CLASSIFICATION Unclassified	1b. RESTRICTIVE MARKINGS
2a. SECURITY CLASSIFICATION AUTHORITY	3. DISTRIBUTION / AVAILABILITY OF REPORT Approved for public release; distribution unlimited.
2b. DECLASSIFICATION / DOWNGRADING SCHEDULE	
4. PERFORMING ORGANIZATION REPORT NUMBER(S)	5. MONITORING ORGANIZATION REPORT NUMBER(S) ARO 22844.13-GS
6a. NAME OF PERFORMING ORGANIZATION Radiation Laboratory, University of Michigan, Ann Arbor, MI 48109 6b. OFFICE SYMBOL (If applicable)	7a. NAME OF MONITORING ORGANIZATION U. S. Army Research Office
6c. ADDRESS (City, State, and ZIP Code) Ann Arbor, Michigan 48109	7b. ADDRESS (City, State, and ZIP Code) P. O. Box 12211 Research Triangle Park, NC 27709-2211
8a. NAME OF FUNDING / SPONSORING ORGANIZATION U. S. Army Research Office 8b. OFFICE SYMBOL (If applicable)	9. PROCUREMENT INSTRUMENT IDENTIFICATION NUMBER DAAG29-85-K-0220
8c. ADDRESS (City, State, and ZIP Code) P. O. Box 12211 Research Triangle Park, NC 27709-2211	10. SOURCE OF FUNDING NUMBERS PROGRAM ELEMENT NO. / PROJECT NO. / TASK NO. / WORK UNIT ACCESSION NO
11. TITLE (Include Security Classification) Millimeter Wave Radar Clutter Program	
12. PERSONAL AUTHOR(S) Fawwaz T. Ulaby	
13a. TYPE OF REPORT Final	13b. TIME COVERED FROM 10/85 TO 9/89
14. DATE OF REPORT (Year, Month, Day) 1989, October 30	15. PAGE COUNT 204
16. SUPPLEMENTARY NOTATION The view, opinions and/or findings contained in this report are those of the author(s) and should not be construed as an official Department of the Army position, policy, or decision, unless so designated by other documentation.	
17. COSATI CODES FIELD / GROUP / SUB-GROUP	18. SUBJECT TERMS (Continue on reverse if necessary and identify by block number) Millimeter waves, Radar scattering, Terrain Clutter

19. ABSTRACT (Continue on reverse if necessary and identify by block number)

See Reverse side

20. DISTRIBUTION / AVAILABILITY OF ABSTRACT ☐ UNCLASSIFIED/UNLIMITED ☐ SAME AS RPT. ☐ DTIC USERS	21. ABSTRACT SECURITY CLASSIFICATION Unclassified
22a. NAME OF RESPONSIBLE INDIVIDUAL	22b. TELEPHONE (Include Area Code) / 22c. OFFICE SYMBOL

DD FORM 1473, 84 MAR

83 APR edition may be used until exhausted.
All other editions are obsolete.

ABSTRACT

This final report provides a summary of the results realized from the research activities conducted under the sponsorship of U.S. Army Research Office Contract DAAG29-85-K-0220, entitled "Millimeter Wave Radar Clutter Program". The overall goal of the progam was to conduct experimental measurments and develop theoretical models to improve our understanding of electromagnetic wave interaction with terrain at millimeter wavelengths. The work was divided into five major tasks. Tasks 1 involved the construction of calibrated scatterometer systems at 35, 94, and 140 GHz. In designing, constructing, and testing these systems, a great deal was learnt about system-design trade-offs and system stability requirements, and new calibration techniques were developed. The scatterometer systems were then used in support of the remaining tasks. The objective of Task 2 was to evaluate the effects of signal fading on the radar backscatter from terrain. Based on experiments conducted from asphalt and snow-covered surfaces, it was determined that the Rayleigh fading model is applicable at millimeter wavelengths, and a model was developed to show how frequency averaging can be used to reduce signal fading fluctuations. Task 3 involved the development of a model that relates the transmission loss of dry snow to crystal size in the 18-90 GHz region. In Task 4, we examined the character of bistatic scattering from surfaces of various surface roughness and from two types of trees. The bistatic data for trees proved instrumental in the development of a radar model for scattering from tree foliage at millimeter wavelengths, which was one component of Task 5. The other component of Task 5 involved the development of a model for snow. (AW)